

REPORT DOCUMENTATION PAGE				Form Approved OMB No. 0704-0188	
Public reporting burden for this collection of information is estimated to average 1 hour per response, including the time for reviewing instructions, searching existing data sources, gathering and maintaining the data needed, and completing and reviewing the collection of information. Send comments regarding this burden estimate or any other aspect of this collection of information, including suggestions for reducing the burden, to Department of Defense, Washington Headquarters Services, Directorate for Information Operations and Reports (0704-0188), 1215 Jefferson Davis Highway, Suite 1204, Arlington, VA 22202-4302. Respondents should be aware that notwithstanding any other provision of law, no person shall be subject to any penalty for failing to comply with a collection of information if it does not display a currently valid OMB control number. PLEASE DO NOT RETURN YOUR FORM TO THE ABOVE ADDRESS.					
1. REPORT DATE (DD-MM-YYYY) 08-08-2006		2. REPORT TYPE Final Report		3. DATES COVERED (From – To) 30 September 2002 - 12-Sep-06	
4. TITLE AND SUBTITLE Hazards and Possibilities of Optical Breakdown Effects Below the Threshold for Shockwave and Bubble Formation			5a. CONTRACT NUMBER FA8655-02-1-3047		
			5b. GRANT NUMBER		
			5c. PROGRAM ELEMENT NUMBER		
6. AUTHOR(S) Dr. Alfred Vogel			5d. PROJECT NUMBER		
			5d. TASK NUMBER		
			5e. WORK UNIT NUMBER		
7. PERFORMING ORGANIZATION NAME(S) AND ADDRESS(ES) Medical Laser Center Luebeck Peter Monnik Weg #4 Luebeck D-23562 Germany				8. PERFORMING ORGANIZATION REPORT NUMBER N/A	
9. SPONSORING/MONITORING AGENCY NAME(S) AND ADDRESS(ES) EOARD PSC 821 BOX 14 FPO 09421-0014				10. SPONSOR/MONITOR'S ACRONYM(S)	
				11. SPONSOR/MONITOR'S REPORT NUMBER(S) SPC 02-4047	
12. DISTRIBUTION/AVAILABILITY STATEMENT Approved for public release; distribution is unlimited.					
13. SUPPLEMENTARY NOTES					
14. ABSTRACT Femtosecond laser pulses enable the creation of spatially extremely confined chemical, thermal, and mechanical effects in biological media and other transparent materials via free-electron generation through nonlinear absorption. The principle mechanisms of femtosecond laser interaction with biomaterials are not only relevant for nanosurgery with tightly focused laser pulses but also for applications such as intrastromal corneal refractive surgery or presbyopia treatment where the laser pulses are focused at smaller numerical apertures. A significant advancement has been made in models of optical breakdown in biomaterials from this project, specifically from the understanding of specific absorption properties of the biomolecules or strains contained in the aqueous medium.					
15. SUBJECT TERMS EOARD, Laser Safety, laser-induced damage					
16. SECURITY CLASSIFICATION OF:			17. LIMITATION OF ABSTRACT UL	18, NUMBER OF PAGES 95	19a. NAME OF RESPONSIBLE PERSON ROBERT N. KANG, Lt Col, USAF
a. REPORT UNCLAS	b. ABSTRACT UNCLAS	c. THIS PAGE UNCLAS			19b. TELEPHONE NUMBER <i>(Include area code)</i> +44 (0)20 7514 4437

Hazards and possibilities of optical breakdown effects below the threshold for shock wave and bubble formation

AFOSR International Research Initiative Project SPC 024047

Grant FA8655-02-1-3047

Final Report

July 2006

Primary Investigator: Prof. Dr. Alfred Vogel, Ph.D.

Organization: Medical Laser Center Luebeck, and
Institute of Biomedical Optics, University of Luebeck

Address: Peter-Monnik-Weg 4, D-23562 Luebeck, Germany

Phone: + 49-451-500-6504 **FAX:** + 49-451-505486

e-mail: vogel@mll.mu-luebeck.de

Country: Germany

In accordance with Defense Federal Acquisition Regulation 252.227-7036, Declaration of Technical Data Conformity (Jan 1997), the Contractor, Prof. Dr. Alfred Vogel, hereby declares that, to the best of its knowledge and belief, the technical data delivered herewith under Contract No. FA8655-02-1-3047 is complete, accurate, and complies with all requirements of the contract.

I certify that there were no subject inventions to declare as defined in FAR 52.227-12, during the performance of this contract.

DATE: 12 September 2006

Name and Title of Authorized Official: Prof. Dr. Alfred Vogel

CONTENTS

1 INTRODUCTION: OPTICAL BREAKDOWN THRESHOLD, AND THE CHANGE OF LASER MATTER INTERACTION WITH INCREASING IRRADIANCE	1
2 BACKGROUND: USE OF ULTRASHORT LASER PULSES FOR CELL SURGERY, REFRACTIVE SURGERY, AND GENERATION OF PHOTONIC STRUCTURES	3
2.1 Cell surgery	3
2.2 Historical development of cell surgery	4
2.3 Femtosecond laser-induced ocular effects and creation of photonic structures	5
3 MODELING AND EXPERIMENTAL INVESTIGATIONS OF FEMTOSECOND BREAKDOWN AT LARGE NA IN THE LOW DENSITY PLASMA REGIME	6
3.1 Outline of the modeling efforts	6
3.2 Plasma formation	7
3.2.1 <i>Qualitative picture</i>	7
3.2.2 <i>Numerical simulations</i>	9
3.2.3 <i>Evolution of free-electron density and breakdown thresholds</i>	12
3.2.4 <i>Low-density plasmas in bulk media</i>	14
3.3 Irradiance- and free-electron distribution within the focal volume	15
3.3.1 <i>Shape of the focal volume</i>	15
3.3.2 <i>Irradiance- and electron density distribution within the focal volume</i>	16
3.4 Chemical effects of low-density plasmas	17
3.5 Temperature evolution during pulse series	19
3.5.1 <i>Calculation of temperature distribution</i>	19
3.5.2 <i>Evolution of the temperature distribution</i>	20
3.5.3 <i>Comparison with cw irradiation of linear absorbers</i>	22
3.6 Thermoelastic stress generation and stress-induced bubble formation	22
3.6.1 <i>Calculation of stress distribution and bubble formation</i>	22
3.6.2 <i>Evolution of the stress distribution</i>	24
3.6.3 <i>Threshold for stress-induced bubble formation</i>	28
3.6.4 <i>Cavitation bubble dynamics</i>	30
3.6.5 <i>Experimental determination of the bubble formation threshold and bubble size</i>	34
3.6.6 <i>Comparison between experimentally determined and calculated bubble size</i>	38
4 FEMTOSECOND BREAKDOWN IN THE HIGH DENSITY PLASMA REGIME	40
4.1 Cavitation bubble radius and conversion of laser energy into bubble energy	40
4.2 Luminescent femtosecond plasmas with large energy density	41
4.3 Future experimental work and modeling	42

5	TIME-RESOLVED IMAGING OF FEMTOSECOND BREAKDOWN	44
5.1.	Schlieren techniques for the visualization of low-density plasmas	44
5.2.	Test of Hoffman contrast and dark-field technique on laser-induced pressure transients in air	48
5.3.	Investigation of femtosecond laser-induced low-density plasmas	50
6	INFLUENCE OF LINEAR ABSORPTION ON OPTICAL BREAKDOWN	51
6.1.	Extension of the numerical model of optical breakdown to include thermal electron emission	51
6.1.1	<i>Modeling approach</i>	51
6.1.2	<i>Results</i>	52
6.1.3	<i>Discussion</i>	58
6.2.	Modeling of optical breakdown considering both thermal electron emission and linear absorption	59
6.2.1	<i>Results</i>	59
6.2.2	<i>Discussion</i>	68
6.3.	Influence of linear absorption on multiphoton ionization	70
7	IMPLICATIONS FOR LASER EFFECTS ON BIOLOGICAL CELLS AND TISSUES	71
7.1	Femtosecond pulse trains at MHz repetition rates with energies below the threshold for bubble formation	72
7.2	Femtosecond pulses at kHz repetition rates with energies above the bubble formation threshold	73
7.3	Comparison with long-pulsed and cw irradiation	74
7.4	Potential hazards from low-density plasmas in multiphoton microscopy and second harmonic imaging	75
8	SUMMARY AND CONCLUSIONS	77
9	PUBLICATION YIELD OF THE PROJECT	79
10	REFERENCES	80
11	ACKNOWLEDGEMENTS	91

1 INTRODUCTION: OPTICAL BREAKDOWN THRESHOLD, AND THE CHANGE OF LASER MATTER INTERACTION WITH INCREASING IRRADIANCE

We found in previous theoretical studies that femtosecond plasma formation involves a gradual increase of free electron density with irradiance [Vog01, Vog02]. To understand the potential of femtosecond pulses for highly localized material processing and modification of biological media, one therefore needs to include the irradiance range *below* the optical breakdown threshold as much as for superthreshold irradiances. This is the scope of the present work.

To properly set the stage for such investigations, we first need to address the terminology used. While “plasma” in gases is usually defined as mixture of free electrons and ions, for dielectric solids or liquids the term stands for the presence of a large number of quasi-free electrons in the conduction band. Correspondingly, “plasma formation,” and “optical breakdown” denote the processes leading to the excitation of these electrons into the conduction band. The expression “optical breakdown threshold” denotes a certain number density of free electrons that is associated with a critical change of physical effects in the irradiated material. Although its precise definition is of particular importance, the actual use of the term in the literature on plasma formation is often quite arbitrary and inconsistent.

Experimental criteria for optical breakdown are plasma luminescence, cavitation bubble formation, and transmission loss. Which criterion is best suited in the context of material processing and surgery? The criterion of plasma luminescence is of little practical use because for femtosecond breakdown it can usually not be observed even when the free electron density is already large enough to cause ablation or cavity formation. A certain absorption loss is also not necessarily linked to a change in the laser-material interaction and its use to define the breakdown threshold would thus be quite arbitrary. As we will see in section 3, cavity formation demarcates the transition from chemical effects of free electrons to disruption, i.e. it defines the onset of a new regime of laser material interaction. Therefore, we consider bubble formation to be the most meaningful and universal criterion for optical breakdown.

In numerical simulations, optical breakdown is commonly identified with the irradiance producing the critical free electron density where the plasma frequency equals the laser frequency and the plasma becomes reflective. However, this definition is not well founded because i) it does not relate to any experimental threshold criterion, and ii) the corresponding irradiance it is not even proportional to the irradiance correlated with any experimental criterion. This complicates the comparison between calculated and experimentally determined threshold values.

Noack and Vogel (1999) have shown that a given value of the free electron density reached during a fs laser pulse and a ns laser pulse corresponds to entirely different energy densities in both cases. In fs breakdown, a large free electron density is required to produce a large plasma energy density because only one “set” of free electrons is produced during the pulse. By contrast, in ns breakdown a dynamic equilibrium between free electron generation and recombination evolves during the laser pulse, which results in the same energy density at much lower values of free electron density and temperature. By contrast, the energy density required for bubble formation is similar for both pulse durations. Hence, it makes no sense to use the same value of the free electron density when measured breakdown thresholds for different pulse durations are compared with calculated values.

This statement is also true when threshold for the same pulse duration but different wavelengths are compared. For UV ns pulses, the free electron density increases gradually with irradiance, similar to femtosecond breakdown [Vog01a], and a small bubble can be formed once the plasma energy density is sufficiently large for a phase transition. This is already possible at relatively small free electron densities. By contrast, for IR ns pulses and breakdown in pure media, multiphoton-ionization-mediated generation of the start electrons for avalanche ionization is the decisive hurdle determining the breakdown threshold. Since the irradiance required for a 6-photon process (at 1064 nm and bd in aqueous media) is very large, the subsequent ionization avalanche proceeds very fast and produces a very large free electron density and a large cavitation bubble even at threshold. Thus the simplifying identification of the theoretical bd threshold with a specific critical free electron density will produce erroneous results when experimental threshold data obtained with UV and IR wavelengths are compared to experimental values. Physically meaningful predictions of breakdown threshold must thus be based on modeling of the experimentally used breakdown criterion such in section 3 of this report and not just on the calculation of a certain free electron density.

In this report, we use bubble formation as experimental breakdown criterion but see the real challenge in investigating the change of interaction mechanisms occurring when the irradiance gradually increases from values below this threshold to values above this threshold. This approach is much more difficult and complex than a mere calculation of irradiance thresholds corresponding to a certain free electron density, but has much larger explanatory power for the analysis of the mechanisms underlying tissue ablation, cell surgery and the laser-based creation of photonic structures.

When the grant application was written, emphasis was laid on the investigation of low-density plasmas below the shock wave and bubble formation threshold because previous results suggested that cell surgery using ultrashort laser pulses was performed in this regime. Indeed, this proved to be true for the pioneering work by Koenig and co-workers in which subnanjoule laser pulses from fs oscillators emitting pulse trains with 50-80 MHz repetition rate were used [Koe99a, 01a, 02], as shown in sections 3 and 7. Based on our initial assumption, we modeled plasma formation (employing the full Keldysh model including multiphoton and tunneling ionization, and a refined approach for impact ionization), the temperature evolution and the evolution of the stress distribution. However, we learned in 2004 that nanosurgery could also be performed using amplified fs pulses with kHz repetition rates and energies of a few nanojoules that were likely to be associated with bubble formation [Yan04]. Therefore, we extended the scope of the work to include the modeling and experimental investigation of thermoelastically induced bubble formation, and we show in section 3 that this mechanism is also compatible with nanosurgery. Thus we were able to identify two different modes of nanosurgery (or ‘nanomorphing’ if fs pulses are used to create photonic structures).

When we went even further beyond the original scope of the project to pulse energies well above the threshold of bubble formation, we found that for large NAs luminescent plasmas are observed and very large plasma energy densities are reached (section 4). It became obvious that the physics of femtosecond breakdown at large numerical apertures (NA) is very different from the physics at low NA. There is evidence that the energy density of fs plasmas well above the breakdown threshold is similar to those of ns plasmas. For fs breakdown, in which only one set of free electrons is produced, this indicates the occurrence of very large free electron densities and possibly also very high temperatures. This indicates that efficient laser plasma coupling prevails under circumstances for which it was previously considered to be impossible.

Originally we had planned to use Schlieren photography to prove the existence of low-density plasmas below the bubble formation threshold. The experimental techniques developed for this purpose are described in section 5. However, for the large NAs used in cell surgery and addressed in our modeling and experiments, the region with refractive index changes is smaller than the diffraction limited resolution of any optical imaging system. Therefore, we will use the developed Schlieren methods for future investigations of the transition of breakdown dynamics from large NA to smaller NAs.

Last but not least we addressed in our project the question of how the breakdown threshold and dynamics is changed by linear absorption (i.e. one-photon absorption), a topic that is also beyond the scope of the initial grant application. Heating by linear absorption may lead to thermal emission influencing the evolution of the free electron density, and chromophores allowing for one photon-absorption may facilitate free-electron generation by introducing intermediate steps assisting MPI. The results of an extended model including thermal free electron emission are described in section 6. The model yields reasonable predictions for breakdown thresholds in the presence of linear absorption but the inclusion of thermal emission destroys the self-consistency of a breakdown model that merely addresses the temporal evolution of free electron density but ignores the hydrodynamic effects leading to plasma expansion. Consistency can be restored only by consideration of the coupling between free electron evolution and hydrodynamic effects.

Finally in section 7 we discuss the implications of our modeling results for cell surgery and the creation of photonic structures as well as possible consequences of low-density plasma formation for the safety of nonlinear imaging modalities such as multiphoton microscopy and second harmonic imaging.

2. BACKGROUND: USE OF ULTRASHORT LASER PULSES FOR CELL SURGERY, REFRACTIVE SURGERY, AND GENERATION OF PHOTONIC STRUCTURES

2.1 CELL SURGERY

Nonlinear absorption of short and ultrashort laser pulses focused through microscope objectives of high numerical aperture (NA) can be used to achieve very fine and highly localized laser effects inside of biological media that are transparent at low irradiance [She84, Vog03, Ven02, Koe99] as well as in the bulk of photonic materials [Sch01, Min01, Wat03, Tac04].

With moderate NAs and nanosecond laser pulses, this possibility has been utilized already in the 1980s for intraocular surgery [Ste86, Vog86]. After the advent of femtosecond lasers, it was employed also for corneal intrastromal refractive surgery [Rat03, Hei03] and for the creation of corneal flaps in excimer laser refractive surgery (LASIK) [Rat03, Hei03, Juh99, Han04]. However, with moderate NAs, the spatial distribution of the deposited energy is influenced by nonlinear self-focusing, normal group velocity dispersion, and plasma-defocusing leading to filamentation and streak formation in the biological material [She84, Wat03, Vog96, Hei02, Liu03, Mao04, Kas04, Kol04, Arn05]. Diffraction at the aperture of the optical system may also contribute to streak formation [Fuc05]. The nonlinear propagation effects become ever more important when the laser pulse duration is reduced and a larger laser power is required to produce optical breakdown. Therefore, it is not possible to achieve highly localized energy deposition when femtosecond pulses are focused into the bulk of transparent media at low NA. Plasma-mediated femtosecond laser nano-processing requires focusing at very large numerical apertures – not only to minimize the diffraction limited focus diameter but also to avoid filamentation. Self-focusing occurs when a critical power is exceeded, regardless which focusing angle is used. By contrast, optical breakdown requires an irradiance threshold to be surpassed. With increasing numerical aperture the spot size becomes smaller and thus the power that is necessary to overcome the threshold irradiance decreases. Beyond a certain numerical aperture, the breakdown power is smaller than the critical power for self-focusing, and localized energy deposition on a sub-micrometerscale can be achieved. For femtosecond optical breakdown in water and glass this was found to be the case for $NA \geq 0.9$ [Sch01].

Recent years have seen a continuous rise of interest in micro- and nanosurgery on a cellular and subcellular level. One important application is the separation of individual cells or other small amounts of biomaterial from heterogeneous tissue samples for subsequent genomic or proteomic analysis. Sensitive analytical techniques such as polymerase chain reaction (PCR) enable the analysis of very small amounts of materials [Sai88, Mar93, Bus00] which allows for ever more specific investigations of cell constituents and their function. Key technologies for sample preparation are laser microdissection (LMD) [Ise76, Mei76] and subsequent laser pressure catapulting (LPC) of the dissected specimens into a vial for further analysis [Sch98a, Sch98b, Lah00, Lor04]. A related technique is laser-induced cell lysis and catapulting of the cell content into a micropipet for time-resolved capillary electrophoresis [Sim98, Rau04]. Laser microbeams have also been applied to dissect chromosomes [Ber81, Lia93, Gre99, Koe01], fuse cells [Sat92, Sch94] and for laser-assisted fertilization or hatching by ablation of the outer egg membrane (zona pellicula), a novel method for in-vitro-fertilization [Sch94, Nee92, Ant96, Rin96, Man01]. Laser-induced transient permeabilisation of the cell membrane is of great interest for a gentle transfection of genes and transfer of other substances into specific cell types [Tsu84, Kur86, Tao87, Pal96, Kra98, Bue98, Sou00, Shi01, Schn02, Tir02, Moh03, Zei03, Pat05].

Laser-generated inactivation of specific proteins or cell organelles together with an analysis of the induced deviations from the normal development provides information about the function of the respective proteins and organelles and can be utilized to study cell proliferation, embryonal development, or stress-induced reaction pathways. Two complementary strategies for functional studies have been followed: In the ‘systemic’ approach, specific proteins are targeted by means of antibodies attached to metallic nanoparticles or chromophores [Hue99, Jay99]. When the antibody-absorber conjugates have bound to the target protein(s), the entire cell or group of cells is exposed to a short-pulsed laser beam. Protein inactivation occurs through linear absorption of the laser irradiation in the nanoparticles or chromophores, respectively, resulting in thermo-mechanical or photochemical destruction of the target proteins regardless of their localisation within the cell [Jay99, Hue01, Bec02, Pit03, Yao05]. In the ‘local’ approach, which is investigated in the present paper, one or a few specific target structures are irradiated by a tightly focused laser beam that dissects, alters, or inactivates the material within the focal region. When suitable laser parameters are used, the laser energy is deposited via non-linear absorption, and surgery can be performed at any desired location within a cell or a small organism, regardless of their linear absorption properties.

2.2 HISTORICAL DEVELOPMENT OF CELL SURGERY

Historically, light inactivation of cells or cell organelles was first attempted in 1912 by Tschachotin using 280-nm irradiation from a magnesium spark imaged by a microscope objective on a 5 μm wide spot on the cell [Tsch12]. This type of apparatus was in the 1950s highly refined by Bessis and Nomarski, and the resolution increased into the sub-micrometer regime [Bes60, Mor69]. However, these instruments required very long exposure times. After the advent of the laser, a high-brightness light source was available that enabled to reduce the exposure time into the microsecond range [Bes62]. First experiments on mitochondrial inactivation were performed using free-running ruby laser pulses with about 500 μs duration that were focused into a 5 μm spot [Amy 65, Sto66]. Later, chromosomal dissection was demonstrated using argon laser irradiation with 20-30 μs duration [Ber69, Ber71]. Owing to the good quality of the argon laser beam and the shorter wavelength, it could be focused into a much smaller spot than the multimode emission of the initial ruby lasers. It is important to note that microsecond pulses are still ‘long’ in the context of cell surgery. We shall see in section 5.3 that for large numerical apertures during pulses longer than about 10 μs a stationary temperature distribution similar to that produced by continuous wave (cw) irradiation evolves around the laser focus. Long-pulsed irradiation from cw lasers is still used by various researchers [Rin96, Pal96, Schn02, Pat05, Sto89], especially for cell membrane permeabilisation, or perforation of the zona pellucida. A drawback of the quasi-cw irradiation is that the energy deposition is based on linear (i.e. one photon) absorption and thus requires staining of target structures with vital dyes [Amy65, Sto66, Ber69], unless laser powers larger than 1 W are used [Ber71], or wavelengths employed that are well absorbed even in unstained biologic material [Rin96, Pat05, Sto89].

Soon after the introduction of the laser microbeam, researchers began to use also short-pulsed laser irradiation, mostly with wavelengths in the UV region of the optical spectrum and with durations of a few nanoseconds [Ise76, Mei76, Sch98a, Sch98b, Ber81, Gre99, Sat92, Sch94, Kas98, Bue98, Shi01, Moh03, Bes71, Cal83, Kho00, Col04]. It was found that short laser pulses enable localized energy deposition at arbitrary locations without external sensitizing agents, even though the ablation threshold can still be lowered by staining of the target structures [Koe01, Bue98, Moh03, Bot04, Sac05]. With nanosecond pulses, energies between 0.25 μJ and 250 μJ were required to produce the desired ablative effect, depending on the laser wavelength, beam profile, numerical aperture, and the quality of the optical scheme used for coupling the laser beam into the microscope. Use of UV wavelengths that are well absorbed by biomolecules yielded lower ablation thresholds than the use of visible or near IR irradiation under similar focusing conditions. Recently, it was demonstrated that pulsed laser microdissection relies on plasma formation supported by linear absorption, and that this is associated with violent mechanical effects (shock wave emission and cavitation bubble formation) reaching well beyond the region of energy deposition [Ven02, Lor04]. Pulse energies in the microjoule range typical for nanosecond laser microbeams can therefore severely affect the cell viability.

In search for finer effects, researchers employed first picosecond pulses that could produce intracellular dissections with energies of 70-140 nJ [Lia93, Ais93], and later femtosecond pulses that enabled to lower the ablation threshold to an energy range between 0.4 nJ and a few nanojoules [Koe99, Yan04]. Due to the low energy threshold for plasma formation [Vog99, Noa99], femtosecond pulses can create very fine effects with a spatial extent below the optical diffraction limit. This has been demonstrated in chromosomes [Koe99, Koe01], various other cell organelles [Sac05, Mel03, Wat04, Hei05, She05], small organisms [Yan04, Sup05, Chu05], and tissues [Zei03, Koe02, Rie05]. Sub-diffraction limited resolution can be achieved because the nonlinear absorption diminishes the volume into which the laser energy is deposited. While for nanosecond pulses the optical breakdown threshold depends strongly on the linear absorption at the laser focus, femtosecond optical breakdown exhibits a much weaker dependence on the absorption coefficient of the target material [Ora96]. This facilitates the targeting of arbitrary cellular structures. Because the wavelength dependence of femtosecond breakdown is weak [Vog01], IR wavelengths that can penetrate deeply into the tissue can be used without compromising the precision of tissue effects as is the case with ns pulses [Ven02, Kra98]. Moreover, when pulses from a fs oscillator are used, it becomes possible to combine nonlinear material modification with nonlinear imaging techniques based on 2-photon fluorescence excitation or second harmonic generation [Tir02, Sac05, Yan04, Sup05, Koe02]. Additional progress was possible through the use of modern gene fusion products such as green fluorescent proteins (GFP) which permit the visualization and ablation of cellular structures that are below the resolution of a light microscope [Bot04, Yan04, Sup05, Kho97]. The above advances allow for an unprecedented precision of aiming, surgery, and of the analysis of the created immediate and long-term effects. This potential of fs and ps pulses has been utilized in a variety of functional studies to elucidate the mechanisms of chromosome separation during cell division [Lia93, Kho00, Ais93, Gri03], induce highly localized DNA damage [Mel03], measure the biophysical properties of the cytoskeleton and mitochondria [She05, Col05], stimulate calcium waves in living cells [Smi01], demonstrate nerve regeneration after axotomy within a living *C. elegans* worm [Yab04], map thermosensation in *C. elegans* [Chu05], and to shed light on morphogenetic movements in embryonal development [Ber81, Sup05].

2.3 FEMTOSECOND LASER-INDUCED OCULAR EFFECTS AND CREATION OF PHOTONIC STRUCTURES

The principle mechanisms of femtosecond laser interaction with biomaterials described above are not only relevant for nanosurgery with tightly focused laser pulses but also for applications such as intrastromal corneal refractive surgery [Rat03, Hei03, Juh99, Han04] or presbyopia treatment [Rip05] where the laser pulses are focused at smaller numerical apertures. In the latter cases, nonlinear beam propagation must be taken into account, and one needs to bear in mind that the thermoelastic tensile stress amplitude produced by energy deposition into cylindrical volumes differs from those arising from spherical or ellipsoidal volumes [Pal99]. Similar considerations also apply for the analysis of intraocular lesions from ultrashort laser pulses in the context of laser safety [Cai04, Toth97, Roc99].

Besides for nanoprocessing of biological materials, low density plasmas can also be used to modify other transparent materials and enable, for example, the generation of optical waveguides, couplers, or even lasers in bulk glass and fused silica [Sch01, Min01, Wat03, Tac04]. The process of plasma formation in the bulk of other dielectrics like fused silica and glass strongly resembles the process in water [Sch01, Stu96, Len98, Sch03]. Variations are mainly due to differences in the band gap energy, which is 6.5 eV for water but ≈ 4 eV for barium aluminium borosilicate (BBS) and 9.0 eV for fused silica [Len98, Bas95]. The material response to plasma formation will, of course, be modified by the different threshold values for chemical and thermomechanically induced changes. When pulse series with high repetition rate are used, low-density plasmas may lead to the formation of defects or color centers that is associated with a change of the refractive index [Efi98, Her04]. Thermal effects produced through heat accumulation during application of series of femtosecond pulses may also play a role [Sch03, Wat00] but cannot be separated from and are probably dominated by the chemical effects of the free electrons. Thermal effects, and especially the resulting thermo-elastic stresses will play a prominent role for low repetition rates and larger pulse energies [Str02, Pou03, Bha04], where they can even lead to the formation of voids [Gle97, Wat00, Juo04].

3. MODELING AND EXPERIMENTAL INVESTIGATIONS OF FEMTOSECOND BREAKDOWN AT LARGE NA IN THE LOW DENSITY PLASMA REGIME

3.1 OUTLINE OF THE MODELING EFFORTS

The high precision of the femtosecond laser effects is certainly related to the fact that the energy threshold for femtosecond optical breakdown is very low. Calculated breakdown energies for 100 fs pulses focused into water by an objective with NA = 1.3 are as small as 0.6 nJ at 355 nm, 1.6 nJ at 532 nm, and 3.9 nJ at 1064 nm [Vog01]. The low breakdown threshold is, on the other hand, not sufficient to explain the fineness of the laser effects because laser-induced breakdown is generally associated with mechanical effects such as shock wave emission and bubble formation that extend beyond the focal region [Ven02, Vog99a, Vog96b]. We found in previous theoretical studies that plasmas with a large free electron density are produced in a fairly large irradiance range below the breakdown threshold that was defined by a critical free electron density $\rho_{cr} = 10^{21} \text{ cm}^{-3}$ [Vog01, Vog02]. To understand the full potential of femtosecond pulses for highly localized material processing and modification of biological media, one therefore needs to include the irradiance range *below* the optical breakdown threshold. Moreover, one needs to elucidate why the conversion of absorbed laser light into mechanical energy above the breakdown threshold is much smaller than for longer pulse durations [Vog03, Vog99a].

The present study investigates the chemical, thermal, and thermomechanical effects arising from low-density plasmas to explain the mechanisms underlying femtosecond-laser nanosurgery of cells and biological tissues. Two parameter regimes have been established for nanosurgery: One technique uses long series of pulses from fs oscillators with repetition rates in the order of 80 MHz and pulse energies well below the optical breakdown threshold that do not much exceed the energies used for nonlinear imaging [Koe99, Koe01, Tir02, Zei03, Sac05, Sup05, Rie05, Smi01, Oeh00]. The other approach uses amplified pulse series at 1 kHz repetition rate with pulse energies slightly above the threshold for transient bubble formation [Yan04, Wat04, Hei05, She05]. To cover both regimes and to address possible side effects of nonlinear imaging, we investigate plasma formation and plasma-induced effects for an irradiance range reaching from the values used for nonlinear imaging to those producing bubble formation. We consider repetition rates in the kilohertz range where the mechanical and thermal events induced by subsequent pulses are largely independent, and in the megahertz range where accumulative effects are likely to occur.

We use a rate equation model considering multiphoton ionization, tunnel ionization, and avalanche ionization to numerically simulate the temporal evolution of the free electron density during the laser pulse for a given irradiance, and to calculate the irradiance dependence of the free-electron density and volumetric energy density reached at the end of the laser pulse. The value of the energy density created by each laser pulse is then used to calculate the temperature distribution in the focal region after application of a single laser pulse and of series of pulses. The results of the temperature calculations yield, finally, the starting point for calculations of the thermoelastic stresses that are generated during the formation of the low-density plasmas, and of stress-induced bubble formation. All calculations are performed for a numerical aperture of NA = 1.3 and the wavelength of the titanium sapphire laser ($\lambda = 800 \text{ nm}$). Whenever possible, the findings of the numerical simulations are compared to experimental results.

The numerical calculations yield threshold values of the irradiance above which chemical changes in the focal region, a considerable temperature rise, and bubble formation are expected to occur. We found two different mechanisms of bubble formation: At repetition rates in the MHz range, fairly large long-lasting bubbles containing non-condensable gas can be formed by plasma-mediated accumulative heating and chemical disintegration of biomolecules. At lower repetition rates, transient bubbles with lifetimes below 100 ns are created by thermoelastic stresses. Due to the thermoelastic origin of bubble formation, the conversion efficiency from absorbed laser light energy into bubble energy is low, enabling the creation of spatially extremely confined disruptive effects.

A comparison between experimental parameters used for cell surgery and our numerical results (see Section 7) revealed two different modes of femtosecond-laser nanosurgery: Dissection using long pulse trains at MHz repetition rates is mediated by free-electron-induced chemical decomposition (bond breaking) and not related to heating or thermoelastic stresses. With this dissection mode, bubble formation needs to be avoided because the relatively large and long-lasting bubbles cause dislocations far beyond the laser focus. By contrast, intracellular dissection at moderate (kHz) repetition rates relies on the thermoelastically-induced formation of minute transient cavities. Both modes of femtosecond laser nanoprocessing of biomaterials achieve a better precision than cell surgery using cw irradiation.

Femtosecond-laser-produced low density plasmas are thus a versatile tool for the manipulation of transparent biological media and other transparent materials such as glass. However, they may also be a potential source of damage in multiphoton microscopy and higher harmonic imaging.

3.2 PLASMA FORMATION

3.2.1 Qualitative picture

The process of plasma formation through laser-induced breakdown in transparent biological media is schematically depicted in **Figure 1**. It essentially consists of the formation of quasi-free electrons by an interplay of photo-ionization and avalanche ionization.

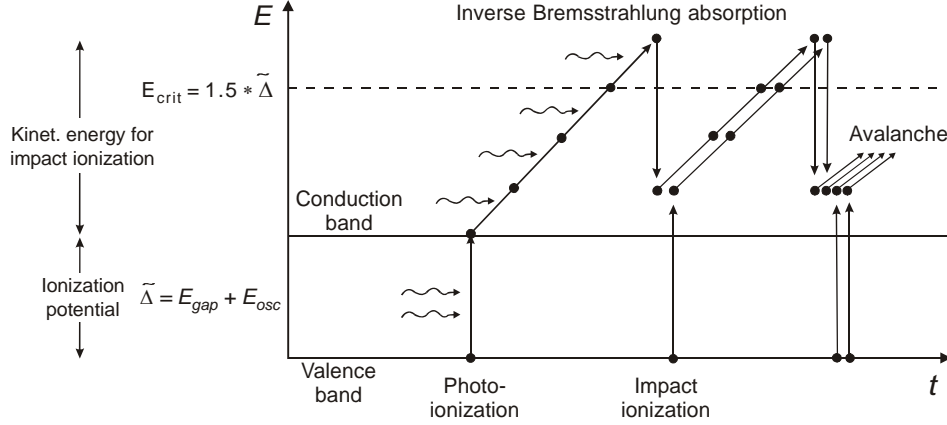


Figure 1: Interplay of photoionization, inverse Bremsstrahlung absorption and impact ionization in the process of plasma formation. Recurring sequences of inverse Bremsstrahlung absorption events and impact ionization lead to an avalanche growth in the number of free electrons. The requirements to satisfy the conservation laws for energy and momentum in impact ionization, and their consequences for plasma formation are discussed in the text.

It has been shown experimentally that the optical breakdown threshold in water is very similar to that in ocular and other biological media [Doc86]. For convenience, we shall therefore focus attention on plasma formation in pure water. Whereas the optical breakdown in gases leads to the generation of free electrons and ions, it must be noted that in condensed matter electrons are either bound to a particular molecule or they are "quasi-free" if they have sufficient kinetic energy to be able to move without being captured by local potential energy barriers. Transitions between bound and quasi-free states are the equivalent of ionization of molecules in gases. To describe the breakdown process in water, Sacchi (1991) has proposed that water should be treated as an amorphous semiconductor and the excitation energy Δ regarded as the energy required for a transition from the molecular $1b_1$ orbital into an excitation band (band gap 6.5 eV) [Wil76, Gra79, Nik83]. We follow this approach. For simplicity, we will use the terms "free electrons" and "ionization" as abbreviations for "quasi-free electrons" and "excitation into the conduction band". Nonlinear absorption of liquid water does actually not only involve ionization but also dissociation of the water molecules [Nik83], but in our model dissociation is neglected to reduce the complexity of the numerical code.

The photon energies at the wavelengths of 1064 nm, 800 nm, 532 nm, and 355 nm investigated in this study are 1.17 eV, 1.56 eV, 2.34 eV, and 3.51 eV, respectively. This means that the energy of six, five, three, and two photons, respectively, is required to overcome the band gap energy $\Delta = 6.5$ eV. The excitation energy into the conduction band can be provided either by photoionization (multiphoton ionization or tunneling [Kel65, Amm86], or by impact ionization [Rea71, Tho81, Arn92, Rid99]. In previous breakdown models, it was often assumed that a free electron could be produced as soon as Δ was exceeded either by the sum of the simultaneously absorbed photons, or by the kinetic energy of an impacting free electron [Noa99, Ken95, Fen97, Tie99]. However, for very short laser pulses where breakdown occurs at large irradiance values, the band gap energy has to be replaced by the effective ionization potential to account for the oscillation energy of the electron due to the electric laser field. The ionization potential of individual atoms is [Kel65]

$$\tilde{\Delta} = \Delta + \frac{e^2 F^2}{4 m \omega^2}, \quad (1)$$

where ω and F denote the circular frequency and amplitude of the electric laser field, e is the electron charge, and $1/m = 1/m_c + 1/m_v$ is the exciton reduced mass that is given by the effective masses m_c of the quasi-free electron in the conduction band and m_v of the hole in the valence band. The second term in equation (1) can be neglected in nanosecond optical breakdown but must be considered in femtosecond optical breakdown where F is orders of magnitude larger.

Multiphoton ionization (MPI) and tunneling are the mechanisms governing photoionization for different field strengths and frequencies of the electromagnetic field. In his classical paper [Kel65], Keldysh introduced a parameter $\gamma = \omega / \omega_t$ to distinguish tunneling and MPI regimes. Here $1/\omega_t$ stands for the tunneling time through the atomic potential barrier which is inversely proportional to the strength of the electromagnetic field. For values $\gamma \ll 1$ as obtained with low frequencies and large field strengths tunneling is responsible for ionization, while for values $\gamma \gg 1$ typical for optical frequencies and moderate field strengths the probability of MPI is much higher than that of tunneling. However, femtosecond optical breakdown requires very high field strengths for which the tunneling time through the atomic potential barrier is extremely short, leading to values $\gamma < 1$ of the Keldysh parameter even for optical frequencies. For $\lambda = 800$ nm, the transition from multiphoton to tunneling ionisation occurs at field strengths of about 100-200 MV/cm, corresponding to irradiances of $1.3 - 2.6 \times 10^{13}$ W/cm² [Arn05, Tie99, Kai00]. Values for the breakdown irradiance for a 100-fs pulse in distilled water (1.1×10^{13} W/cm² for $\lambda = 580$ nm [Vog99a]) are close to this transition. Approximations of the Keldysh theory considering only multiphoton ionization that were used in previous breakdown models [Noa99, Ken95, Fen97] are thus inappropriate for the modeling of femtosecond breakdown, especially for pulse durations ≤ 100 fs.

Once a free electron is produced in the medium, it can absorb photons in a non-resonant process called “inverse Bremsstrahlung” in the course of collisions with heavy charged particles (ions or atomic nuclei) [Rea71]. A third particle (ion/atom) is necessary for energy and momentum to be conserved during absorption, as they cannot both be conserved if only an electron and a photon interact. The electron gains kinetic energy during the absorption of the photon. After a sequence of several inverse Bremsstrahlung absorption events, the kinetic energy is sufficiently large to produce another free electron through impact ionization [Tho81, Arn92, Rid99, Kai00]. Two free electrons with low kinetic energies are now available which can gain energy through inverse Bremsstrahlung absorption (Fig. 1). The recurring sequence of inverse Bremsstrahlung absorption events and impact ionization leads to an avalanche growth in the number of free electrons if the irradiance is high enough to overcome the losses of free electrons through diffusion out of the focal volume and through recombination. The energy gain through inverse Bremsstrahlung must, moreover, be more rapid than the energy loss by collisions with heavy particles occurring without simultaneous absorption of a photon (the fraction of energy lost is proportional to the ratio of the electron and ion masses). The whole process is called “avalanche ionization”, or “cascade ionization”.

For impact ionization to occur, the kinetic energy of the impacting electron must be larger than the effective ionization potential $\tilde{\Delta}$ to satisfy the conservation laws for energy and momentum [Rid99, Kel60, 109]. According to Ridley (1999), the critical energy for bands with parabolic energy dispersion is

$$E_{crit} = \left(\frac{1+2\mu}{1+\mu} \right) \tilde{\Delta}, \quad \text{with } \mu = \frac{m_c}{m_v}. \quad (2)$$

The value of μ depends on the band structure, it is 1 for a symmetric band structure with the Fermi level at the center of the band gap but smaller for semiconductors [Rid99]. Kaiser et. al. assumed $\mu = 1$ for α -SiO₂ [Kai00], and since we did not find information on the value of μ for water, we follow their assumption. This implies that a kinetic energy of $E_{crit} = 1.5 \tilde{\Delta}$ is required for impact ionization [Kai00, Ret04].

The excess energy of $0.5 \tilde{\Delta}$ that remains after impact ionization is distributed among the collision partners [Rid99, Kai00, Stu96]. Thus, each quasi-free electron produced by impact ionization has to gain less energy than $1.5 \tilde{\Delta}$ to reach the critical energy. However, the average energy leading to an impact ionization event is larger than E_{crit} because the impact ionization rate increases with kinetic energy [Arn92, Kai00, Kel60, Ret04]. To consider both factors, we assume that the average energy gain required for a free electron to cause impact ionization is $1.5 \tilde{\Delta}$, as illustrated in Fig. 1. A more detailed consideration of the energy distribution of the free-electron population and of the energy dependence of the ionization rates [Arn92, Kai00, Ret04, Stu96] would require experimental data on collision cross sections that are not available for water.

While strong-field ionization is almost “instantaneous,” there are time constraints on cascade ionization because several consecutive inverse Bremsstrahlung absorption events are necessary for a free electron to pick up the critical energy for impact ionization. For a band gap of 6.5 eV in water and a Keldysh parameter $\gamma = 2$, the effective ionization potential is $\tilde{\Delta} \approx 7.3$ eV, and the average gain in kinetic energy required to enable impact ionization is $(3/2) \tilde{\Delta} \approx 10.95$ eV. When laser irradiation of $\lambda = 800$ nm wavelength with a photon energy of 1.55 eV is used to produce optical breakdown, an electron must undergo at least 8 inverse Bremsstrahlung absorption events before impact ionization can occur. As mentioned above, inverse Bremsstrahlung absorption can only occur during collisions of the electrons with heavy particles. In condensed matter, the time τ between collisions was estimated to be roughly 1 fs [Blo74]. Recent experimental investigations yielded a value of $\tau = 1.7$ fs for fused silica [Sun04]. Based on this value, the minimum time for one doubling sequence of the number of free electrons by cascade

ionization is 13.6 fs even if every collision involves absorption of a photon. A detailed analysis of the time constraints in cascade ionization was presented by Kaiser et. al. (2000) and Rethfeld (2004). They come to the conclusion that cascade ionization plays only a minor role in femtosecond breakdown compared to multiphoton effects – in striking contrast to Joglekar et. al. (2003, 2004) who present some experimental evidence for the opposite statement. However, the time constraints in cascade ionization were not considered in any of the models presented by authors who claim that it dominates femtosecond breakdown [Tie99, Jog03, Jog04].

In our study, we shall combine the Keldysh model for strong-field ionization (including both tunneling and multiphoton absorption) [Kel65] with Shen's, Kennedy's, and Stuart's description of avalanche ionization [She84, Ken95, Stua96] which is based on the Drude model. Other recent studies on femtosecond optical breakdown in transparent dielectrics have followed the same approach [Arn05, Fei04], while Tien et. al. (1999) combined the Keldysh theory with Thornber's model of avalanche ionization (1981). Since the numerical model used by Kaiser et. al. (2000) and Rethfeld (2004) is very complex we consider the time constraints in cascade ionization by simply introducing a retarded time for the calculation of the cascade ionization rates, as described in section 3.2.2.

To obtain a better understanding of the mechanisms of cell surgery using femtosecond pulses, we are interested in the plasmas below and slightly above the optical breakdown threshold. It is evident that a precise delineation of the corresponding irradiance range requires a clear definition of the breakdown threshold. When nano- and picosecond pulses are employed, optical breakdown is accompanied by the formation of a luminous plasma and followed by shock wave emission and cavitation [Vog96a, Vog96b]. At these pulse durations, the plasma luminescence usually serves as experimental breakdown criterion [Ven02, Vog96b]. With shorter laser pulses, there is no plasma luminescence in the visible region of the spectrum, and breakdown in aqueous media is usually detected by observing the formation of a cavitation bubble [Noa99, Ham96]. By contrast, in theoretical investigations the breakdown threshold is defined by the irradiance (or energy) required to produce a certain critical free electron density ρ_{cr} at the laser focus. Mostly, the electron density

$$\rho_{cr}' = \omega^2 \frac{m_c \epsilon_0}{e^2} \quad (3)$$

above which the plasma becomes both strongly reflective and absorbing is used as breakdown criterion [Mao04, Tie99, Kai00, Stu96, Len98]. Here ϵ_0 denotes the vacuum dielectric permittivity. The critical electron density ρ_{cr}' amounts to $0.984 \times 10^{21} \text{ cm}^{-3}$ for $\lambda = 1064 \text{ nm}$, to $3.94 \times 10^{21} \text{ cm}^{-3}$ for $\lambda = 532 \text{ nm}$, and to $8.86 \times 10^{21} \text{ cm}^{-3}$ for 355 nm , respectively. We use a free electron density of $\rho_{cr} = 10^{21} \text{ cm}^{-3}$ as breakdown criterion in our numerical simulations of plasma formation. A constant value was chosen because the experimental threshold criterion (bubble formation) relates to a fixed value of the plasma energy density. In section 3.6.3, threshold values obtained on this basis will be compared with experimental data and calculated values for the onset of stress-induced bubble formation.

Since all calculations are performed for a numerical aperture of $NA = 1.3$, nonlinear propagation effects in the biologic medium can be neglected in the simulations of plasma formation, even for pulse durations as short as 100 fs because Schaffer et. al. showed that these nonlinear effects influence the breakdown threshold only for $NA < 0.9$ [Sch01]. Self-focusing and filamentation may play a role for events well above the breakdown threshold but are not relevant for the pulse energies used in nanosurgery on cells.

In this study, we restrict the modeling to optical breakdown in pure water. In real biological media, the band structure of water is modified by the presence of biomolecules in physiological solution with additional energy levels that may enhance both linear and nonlinear absorption processes. These modifications may lead to a lower threshold for plasma-mediated laser ablation and dissection, especially when exogeneous linearly absorbing dyes are used [Koe01, Bue98, Moh03, Bot04, Sac05]. The consideration of these modifications will be the topic of future work.

3.2.2 Numerical simulations

The time evolution of the electron density ρ_c in the conduction band under the influence of the laser light was calculated using a rate equation of the generic form [Noa99]

$$\frac{d\rho_c}{dt} = \eta_{\text{photo}} + \eta_{\text{casc}} \rho_c - \eta_{\text{diff}} \rho_c - \eta_{\text{rec}} \rho_c^2. \quad (4)$$

The first term represents the production of free electrons mediated by the strong electric field in the laser focus (photoionization via multiphoton and tunneling ionization), the second term represents the contribution of cascade ionization, and the last two terms describe the losses through diffusion of electrons out of the focal volume, and recombination. The cascade ionization rate η_{casc} and the diffusion loss rate η_{diff} are proportional to the number of already produced free electrons, while the recombination rate η_{rec} is proportional to ρ_c^2 , as it involves an interaction

between two charged particles (an electron-hole pair). Even though diffusion and recombination do not play a significant role during femtosecond laser pulses, they were included to enable a comparison to plasma formation by nanosecond pulses.

The temporal evolution of the electron density, $\rho(t)$, was calculated for laser pulses with a Gaussian time variation [Noa99], focused into pure water at a numerical aperture of $NA = 1.3$. At room temperature the initial steady-state ‘free’ electron density in the conduction band resulting from the Boltzmann-Distribution is negligible. Thus the steady-state electron density in the ground state corresponds to the total electron density $\rho_v = 6.68 \times 10^{23} \text{cm}^{-3}$ [Ken95]. For photon energies below the ionization potential, free electrons can be generated by multiphoton or tunnel-ionisation. The time averaged ionisation rate for a field with angular frequency ω and intensity I acting on an electron density $\rho_v - \rho_c$ in the ground state was derived by Keldysh to be [Kel65]

$$\left(\frac{d\rho_c}{dt}\right)_{photo} = \frac{2\omega}{9\pi} \left(\frac{\sqrt{1+\gamma^2}}{\gamma} \frac{m\omega}{\hbar}\right)^{3/2} Q\left(\gamma, \frac{\tilde{\Delta}}{\hbar\omega}\right) \times (\rho_v - \rho_c) \exp\left\{-\pi \left\langle \frac{\tilde{\Delta}}{\hbar\omega} + 1 \right\rangle \times \left[\mathbf{K}\left(\frac{\gamma}{\sqrt{1+\gamma^2}}\right) - \mathbf{E}\left(\frac{\gamma}{\sqrt{1+\gamma^2}}\right) \right] \right\} \left/ \mathbf{E}\left(\frac{1}{\sqrt{1+\gamma^2}}\right) \right\} \quad (5)$$

with

$$Q(\gamma, x) = \sqrt{\pi / 2\mathbf{K}\left(\frac{1}{\sqrt{1+\gamma^2}}\right)} \times \sum_{l=0}^{\infty} \exp\left\{-\pi l \left[\mathbf{K}\left(\frac{\gamma}{\sqrt{1+\gamma^2}}\right) - \mathbf{E}\left(\frac{\gamma}{\sqrt{1+\gamma^2}}\right) \right] \right\} \left/ \mathbf{E}\left(\frac{1}{\sqrt{1+\gamma^2}}\right) \right\} \times \Phi\left\{\left[\pi \left(2\langle x+1 \rangle - 2x + l\right) / 2\mathbf{K}\left(\frac{1}{\sqrt{1+\gamma^2}}\right) \mathbf{E}\left(\frac{1}{\sqrt{1+\gamma^2}}\right) \right]^{1/2}\right\}$$

Here $\langle x \rangle$ represents the integer part of the number x , $\mathbf{K}()$ and $\mathbf{E}()$ denote the elliptic integrals of first and second kind, and $\Phi()$ denotes the Dawson probability integral

$$\Phi(z) = \int_0^z \exp(y^2 - x^2) dy. \quad (6)$$

The Keldysh parameter γ and the effective ionization potential $\tilde{\Delta}$ for creating an electron-hole pair in condensed matter exhibiting a band structure are given by

$$\gamma = \frac{\omega}{e} \sqrt{\frac{c\epsilon_0 m \Delta}{4I}} \quad \text{and} \quad \tilde{\Delta} = \frac{2}{\pi} \Delta \frac{\sqrt{1+\gamma^2}}{\gamma} \mathbf{E}\left(\frac{1}{\sqrt{1+\gamma^2}}\right). \quad (7)$$

Some authors [Ken95, Kai00, Ret04, Jog04] use the expression in equation (1) for the ionization potential of individual atoms instead of equation (7) which Keldysh (1965) derived for solids. For $\gamma \gg 1$, equation (5) reduces to the expression for multiphoton ionisation used in Refs. [Ken95, Noa99], and the ionization potential can be approximated by the band gap energy Δ . Under these circumstances the photoionization rate shows an intensity dependence proportional to I^k , k representing the number of photons required to cross the band gap.

Figure 2 shows the calculated ionisation rate for 780nm as a function of the Keldysh parameter calculated with the complete model in equation (5) and with various approximations. For values $\gamma \ll 1$, the Keldysh multiphoton approximation predicts photoionization rates that are too low by several orders of magnitude, while the prediction of Kennedy’s multiphoton approximation [Ken95, Noa99] are by several orders of magnitude too large.

As soon as free electrons exists in the interaction volume, they gain kinetic energy through inverse Bremsstrahlung absorption of photons and can generate further free-electrons through impact ionisation once their energy exceeds the critical energy described by eq. (2). As explained above, we assume that the average gain of kinetic energy by each electron required to cause an impact ionization event is $E = (3/2) \tilde{\Delta}$. The ionization rate per electron participating in the cascade is then given by [Ken95]

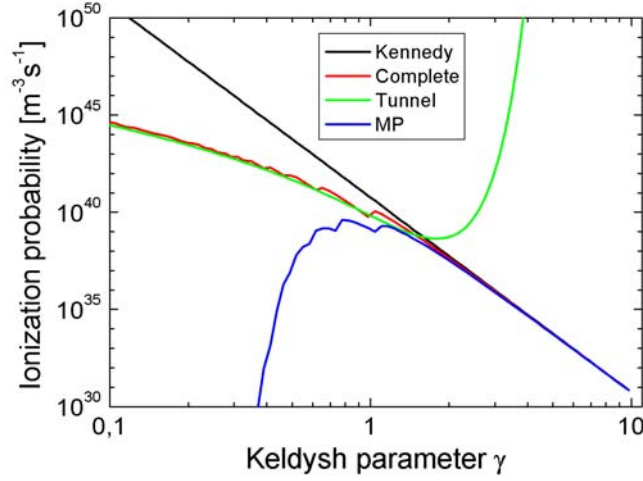


Figure 2: Nonlinear photoionization rate for water at $\lambda = 780$ nm calculated with the complete Keldysh model (pink), Keldysh's approximations in the tunnel limit (green) and the multiphoton limit (violet), and with Kennedy's approximation in the multiphoton limit (blue) [Ken95, Noa99].

$$\eta = \frac{1}{(\omega^2 \tau^2 + 1)} \left[\frac{e^2 \tau}{c n_0 \epsilon_0 m_c (3/2) \tilde{\Delta}} I - \frac{m_c \omega^2 \tau}{M} \right] \quad (8)$$

where τ is the time between collisions, c is the vacuum speed of light, and n_0 the refractive index of the medium at frequency ω . The masses of the electron and the water molecule are m and M , respectively. For large irradiances, the cascade ionization rate is proportional to I .

Two aspects must still be considered to accurately determine the cascade contribution to the free electron density. First, at least one free "seed" electron produced by photoionization is required for the start of the cascade. Therefore, cascade ionisation is only considered if there is at least a 50% probability of having this start electron in the focal volume. Second, it must be taken into account that inverse Bremsstrahlung absorption requires a finite time $\tau_{ion} = \tau n$ which is determined by the mean free time τ (1.7 fs [Sun05]) between electron/molecule collisions and the number n of photons that must be absorbed to gain sufficient energy. Therefore, the contribution of cascade ionization at time t must be evaluated using the electron density created at time $t_{ret} = t - t_{ion}$. A first order approximation of this retardation of the cascade leads to the expression

$$\left(\frac{d\rho_c}{dt} \right)_{casc} = \begin{cases} \frac{\eta}{(1 + \eta t_{ret})} \rho_c & \text{for } \rho_c V \geq 0.5 \\ 0 & \text{for } \rho_c V < 0.5 \end{cases} \quad (9)$$

Free electrons are lost in the interaction volume by diffusion out of the volume V and through recombination. The focal volume was assumed to be ellipsoidal, which corresponds to illumination of the rear aperture of the microscope objective with a plane wave as will be discussed in section 3.3.1. Thus $V = (4/3) \pi a^2 b$ where a and b are the short and long half-axis of the ellipsoidal free-electron distribution described by equation (16) further below. The resulting (negative) ionisation rate due to diffusion is [Ken95, Car59]

$$\left(\frac{d\rho_c}{dt} \right)_{diff} = -\frac{\tau E_{av}}{3 m \Lambda^2} \times \rho_c = -\frac{\tau 5 \tilde{\Delta}}{6 m_c} \left[\frac{6}{a^2} + \frac{2}{b^2} \right] \times \rho_c, \quad (10)$$

where E_{av} is the average kinetic energy of the free electrons, and Λ is the characteristic diffusion length. Free electrons produced by impact ionization possess, on average, a start energy of $(1/2) \tilde{\Delta}$ and produce another free electron through collisional ionization when they reaches a kinetic energy of $2 \tilde{\Delta}$. Thus their mean kinetic energy is $(5/4) \tilde{\Delta}$, leading to the expression on the right side of eq. (10). For the recombination rate, we used an empirical value that was determined by Docchio through inspection of the decay of the plasma luminescence [Doc88]

$$\left(\frac{d\rho_c}{dt} \right)_{rec} = -2 \times 10^{-9} \text{ cm}^3/\text{s} \times \rho_c^2. \quad (11)$$

In reality, recombination of free electrons in water is not a one-step process but consist in hydration of the electron within about 300 fs and subsequent decay of the hydrated state that has an average lifetime of ≈ 300 ns [Nik83].

To obtain the evolution of the free electron density during a Gaussian laser pulse

$$I(t) = I_0 \exp \left[-4 \ln 2 \left(\frac{t}{\tau_L} \right)^2 \right], \quad (12)$$

the total rate equation

$$\frac{d\rho_c}{dt} = \left(\frac{d\rho_c}{dt} \right)_{photo} + \left(\frac{d\rho_c}{dt} \right)_{casc} + \left(\frac{d\rho_c}{dt} \right)_{diff} + \left(\frac{d\rho_c}{dt} \right)_{rec} \quad (13)$$

was solved numerically for various laser pulse peak intensities I using a Runge-Kutta method with adaptive step size control. Separate book-keeping was used for the contribution of eq. (5) to evaluate the influence of multiphoton and cascade ionisation. The breakdown threshold is defined as irradiance I_{rate} required to produce a maximum electron density ρ_{max} during the laser pulse that equals the critical density $\rho_{cr} = 10^{21} \text{ cm}^{-3}$. Besides the time evolution of the electron density, we also assessed the dependence of the maximum electron density on irradiance, by calculating ρ_{max} as a function of I/I_{rate} .

3.2.3 Evolution of free-electron density and breakdown thresholds

The top row of **figure 3** presents the evolution of the free-electron density ρ_c during the laser pulse at the optical breakdown threshold for 6-ns, 1064-nm pulses, and for 100-fs, 800-nm pulses. To facilitate a comparison between the different pulse durations, the time t is normalized with the respective laser pulse duration τ_L . The contribution of photoionization to the total free-electron density is plotted as a dotted line. The bottom row of figure 3 shows how the maximum free electron density achieved during the laser pulse depends on irradiance.

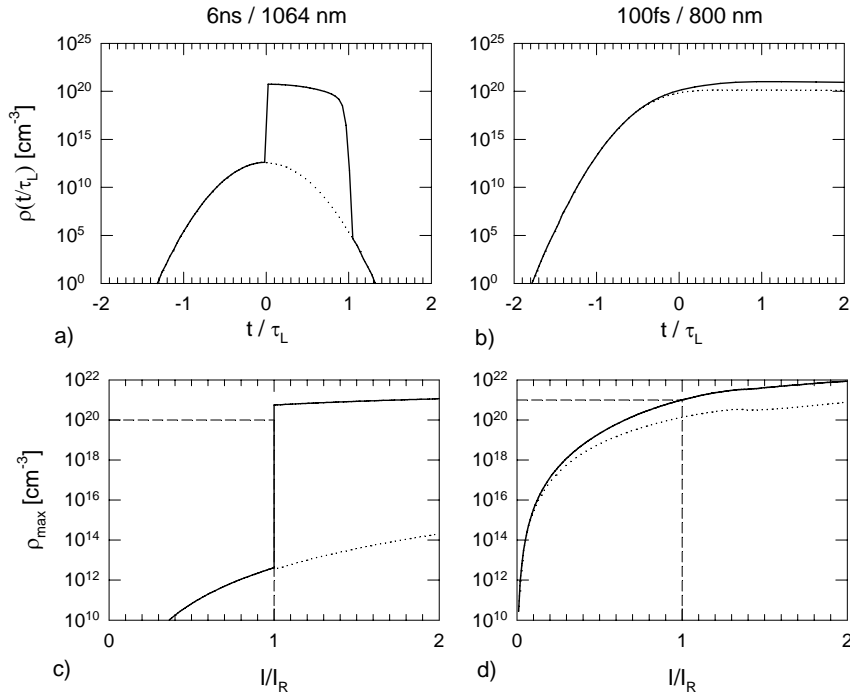


Figure 3: Top row: Evolution of the free-electron density during the laser pulse at the optical breakdown threshold for 6 ns, 1064 nm pulses and for 100 fs, 800 nm pulses. The time t is normalized with respect to the laser pulse duration τ_L . The contribution of multiphoton ionization to the total free-electron density is plotted as a dotted line. Bottom row: Maximum free electron density ρ_{max} achieved during the laser pulse as a function of irradiance, for the same laser parameters. The irradiance I is normalized with respect to the threshold irradiance I_{rate} . The threshold I_{rate} and the corresponding value of ρ_{max} are marked by dotted lines.

It is obvious that the dynamics of plasma formation is extremely different for nanosecond and femtosecond pulses. With nanosecond pulses, no free electrons are formed for irradiance values below the optical breakdown threshold because the irradiance is too low to provide seed electrons by means of multiphoton ionization (Fig 3c). Once the irradiance is high enough to provide a seed electron, the ionization cascade can start. It proceeds very rapidly owing to the high irradiance (Fig. 3a). The electron density shoots up by 9 orders of magnitude within a

small fraction of the laser pulse duration until its rise is stopped by recombination which is proportional to ρ_c^2 . The breakdown threshold is, hence, extremely sharp - either is a highly ionized plasma produced, or no plasma at all. These numerical predictions are supported by the experimental observation that at the threshold of nanosecond optical breakdown with IR laser pulses the transmission of the focal volume drops abruptly to less than 50% of the value without plasma formation [Nah96, Noa98]. The transmission loss for shorter pulse durations is much less abrupt [Vog99a, Nah96, Noa98, Noa98a,c].

With femtosecond pulses, a much higher irradiance is necessary for optical breakdown to be completed during the laser pulse duration than with nanosecond pulses. This favors the generation of free electrons through multiphoton ionization because of its stronger irradiance dependence $\propto I^k$ as opposed to $\propto I$ for the cascade ionization rate (see section 3.2.2). While with nanosecond pulses the total number of free electrons generated through avalanche ionization is 10^9 times larger than the number generated through multiphoton ionization (Fig. 3a), it is only 12 times larger with 100-fs pulses at 800 nm (Fig. 3b). As a consequence of the increasing importance of multiphoton ionization with shorter pulse durations, there is never a lack of seed electrons for avalanche ionization. An avalanche is initiated at irradiance values considerably lower than the breakdown threshold. The free-electron density reached at the end of the avalanche depends on irradiance in a much smoother way (Fig. 3d) than for ns pulses (Fig. 3c). Therefore, one can generate any desired free-electron density by selecting an appropriate irradiance value.

Figure 4 presents threshold values for irradiance, I_{rate} , and radiant exposure, $F_{\text{rate}} = I_{\text{rate}} \times \tau_L$, required to reach a critical free electron density of $\rho_{cr} = 10^{21} \text{ cm}^{-3}$. The thresholds were calculated for various wavelengths and pulse durations ranging from 10 fs to 10 ns. Two regimes can be distinguished: For $\tau_L < 10$ ps, the threshold radiant exposure F_{rate} exhibits only a weak dependence on pulse duration. This reflects the fact that recombination plays only a minor role during ultrashort laser pulses. Therefore, only one set of free electrons is produced that corresponds to an approximately constant energy density within the focal volume. This is in accordance with the experimental threshold criterion of bubble formation that requires a specific energy density, which varies little with laser parameters. By contrast, for longer pulses more than one set of free electrons is produced and recombines during the laser pulse, and it is the threshold irradiance I_{rate} that remains approximately constant, because a minimum irradiance is required to provide the seed electrons for the ionization cascade by multiphoton ionization and to drive the cascade sufficiently fast to reach the critical free electron density within the laser pulse duration. As a consequence, the radiant exposure threshold and plasma energy density increase steeply with increasing pulse duration.

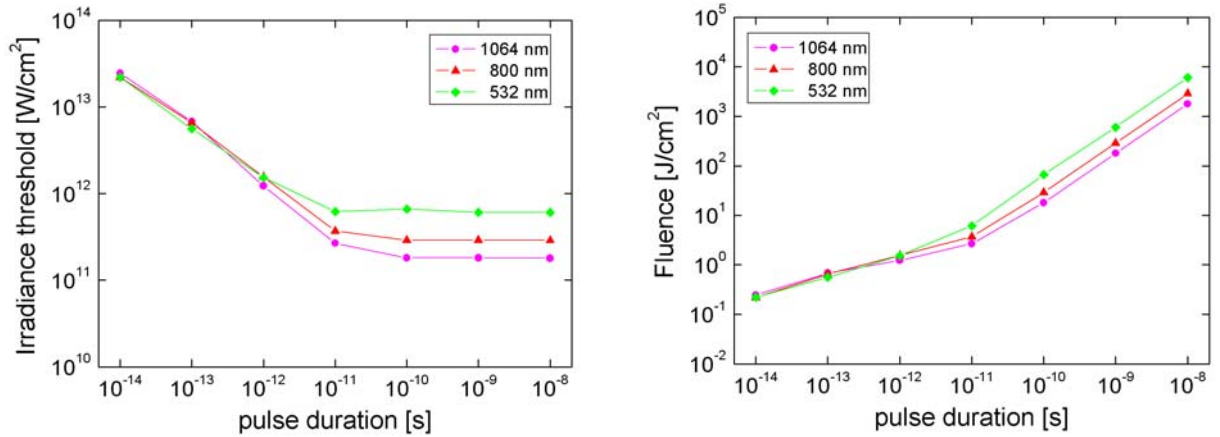


Figure 4: Calculated optical breakdown thresholds ($\rho_{cr} = 10^{21} \text{ cm}^{-3}$) as a function of laser pulse duration for various laser wavelengths.

The predicted form of the $F_{\text{rate}}(\tau_L)$ dependence qualitatively matches experimental observations on the pulse duration dependence of single shot damage thresholds at surfaces of transparent large-band-gap dielectrics [Tie99, Du96] and ablation thresholds of corneal tissue [Juh99, Du94]. Studies in which single shot thresholds at longer pulse durations are mixed with multiple shot thresholds at ultrashort durations show a steeper $F_{\text{rate}}(\tau_L)$ dependence for $\tau_L < 10$ ps both in corneal tissue [Ste89, Nie93] and dielectrics [Stu96, Len98]. The lower thresholds with multiple exposures are due to accumulative effects the possibility of which is explained by the smooth $\rho_{\text{max}}/I_{\text{rate}}$ dependence shown in Fig. 3d.

The predicted wavelength dependence in the picosecond and nanosecond regimes (increasing threshold with decreasing wavelength) seems to be a little surprising at first sight because multiphoton processes occur more easily at shorter wavelengths. However, one needs to keep in mind that the cascade ionization rate increases approximately proportional to the square of the laser wavelength, as evident from Eq. (8).

3.2.4 Low-density plasmas in bulk media

Our numerical calculations for bulk transparent media indicate that it is possible to create low-density plasmas in which the energy density remains below the level that leads to cavity formation in the medium. Experimental evidence for the existence of low-density plasmas was recently provided by Mao et. al. (2004) through measurements of the free electron density in MgO and SiO₂. Free electrons are produced in a fairly large irradiance range below the optical breakdown threshold, with a deterministic relationship between free electron density and irradiance. Low-density plasmas offer the possibility to deliberately produce chemical changes, heating, and thermomechanical effects by varying the irradiance. These effects are very well localized because of the nonlinearity of the plasma formation process which, for sufficiently small irradiances, allows to produce a plasma in a volume that is smaller than the diffraction-limited focus.

For larger irradiances, plasmas in bulk media grow beyond the region of the beam waist, which is not possible for plasma formation at surfaces [Stu96, Jog04, Fei04]. At surfaces, the energy deposition becomes confined to a thin layer of less than 100 nm thickness once the free electron density reaches the critical density because the superficial plasma layer is highly absorbing and reflecting [Stu96, Fei04, Hug75, God77, vdLin96]. By contrast, in bulk media there is no restriction for the region of optical breakdown to spread towards the incoming laser beam with increasing irradiance. At large irradiances, breakdown starts to occur already before the femtosecond pulse reaches the beam waist, and both irradiance and beam propagation are influenced by the plasma generation [Arn05, Ham97]. These effects shield the focal region, enlarge the size of the breakdown region, and limit the free electron density and energy density reached in the entire breakdown volume [Arn05, Vog99a, Fan02a,b, Ray05]. Low density plasmas can, therefore, easily be produced in bulk media while at surfaces the self-induced confinement of plasma formation to a thin layer leads to a rapid rise of free electron density with irradiance, and the irradiance range in which low-density plasmas can be formed is very small [Stu96, Jog04].

The desired chemical or physical effects of low-density plasmas can be most precisely selected if the slope of the $\rho_{\max}(I/I_{\text{rate}})$ curve is small because that offers a large "tuning range" of the irradiance for each effect. **Figure 5** shows that the tuning range increases for shorter laser wavelengths (because of the decreasing order of the multiphoton process).

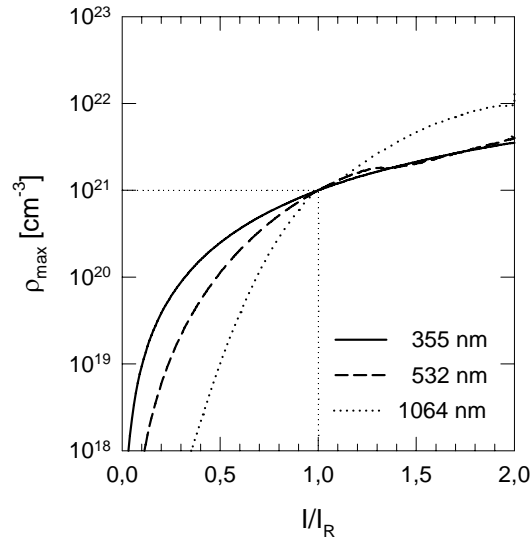


Figure 5: Maximum free electron density as a function of irradiance, $\rho_{\max}(I/I_{\text{rate}})$, for 100 fs pulses at 1064 nm, 532 nm, and 355 nm wavelength. The normalized threshold ($I/I_{\text{rate}} = 1$) and the corresponding value of ρ_{\max} are marked by dotted lines.

3.3 IRRADIANCE- AND FREE-ELECTRON DISTRIBUTION WITHIN THE FOCAL VOLUME

3.3.1 Shape of the focal volume

The temperature and stress distribution in the focal region depend on the distribution of quasi-free electrons produced during femtosecond optical breakdown. Therefore, we must first explore the shape of the irradiance and free-electron density distributions within the focal volume before we can investigate the resulting temperature and stress effects. Because of the nonlinearity of the breakdown process, the free-electron distribution is narrower than the irradiance distribution in the focal volume. A description of their relation will thus also allow to estimate the possible increase of the spatial precision of the laser effects beyond the level achievable with techniques that are based on linear absorption.

The irradiance distribution in the focal volume of a diffraction limited optical system for a focusing angle of $\alpha = 45^\circ$ is reproduced in **figure 6** from the textbook of Born and Wolf (1970) (α is the half angle of the light cone such as used in the definition of the numerical aperture $NA = n_0 \sin\alpha$). The isophotes (contour lines for equal irradiance) reveal that the focal volume in the center of the focal region has an approximately ellipsoidal shape. A similar structure was obtained experimentally when the irradiance distribution in a confocal laser scanning microscope (CLSM) was measured by scanning the tip of a scanning near field optical microscope (SNOM) through the focal region (**Figure 7**), and by a surface plasmon based beam profiling technique [Dit04]. For our numerical simulations, the focal volume will therefore be approximated by an ellipsoid with short axis d and long axis l .

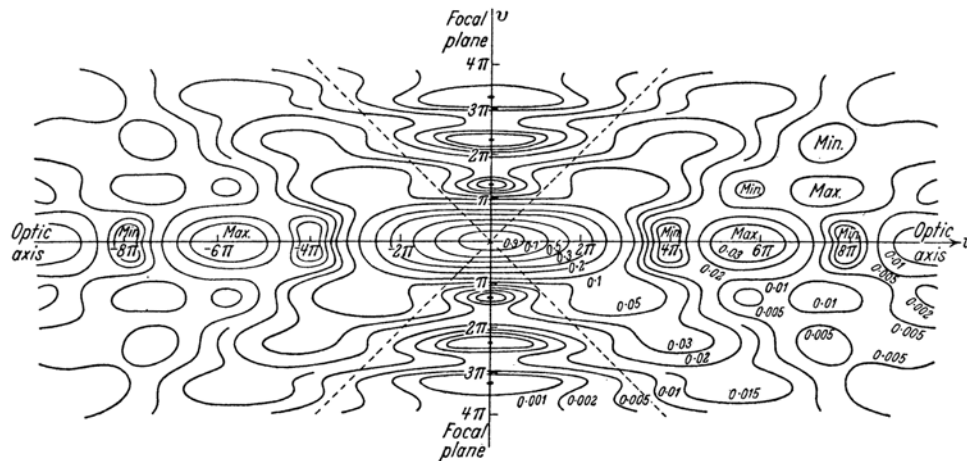


Figure 6: Isophotes (contour lines for equal irradiance) in the focal region of a diffraction limited microscope objective used to focus a plane wave. The dotted lines represent the boundary of the geometrical focus. The focusing angle of $\alpha = 45^\circ$ corresponds to a numerical aperture of $NA = 0.94$ in water. When the figure is rotated around the u -axis, the minima on the v -axis generate the Airy dark rings. The figure is taken from Ref. [Bor70], p. 440.

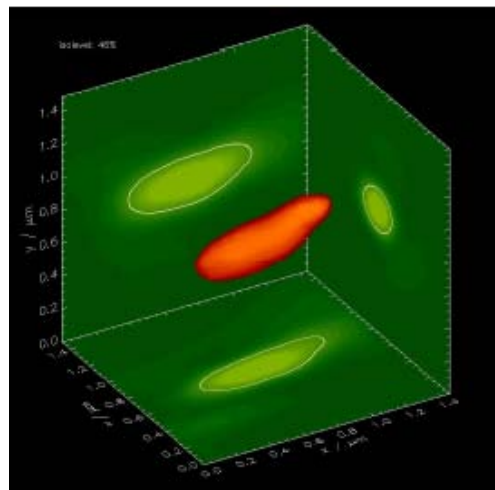


Figure 7: Irradiance distribution in a confocal laser scanning microscope measured by scanning the tip of a scanning near field optical microscope through the focal region of a Zeiss axiovert 100/C-Apo 40x NA = 1.2 water immersion microscope objective. The measurement was performed for a laser wavelength of $\lambda = 488$ nm, the isocontour lines refer to 46% of the maximum irradiance (courtesy of Dr. Jüngel, Carl Zeiss Jena).

The short axis d of the ellipsoid is identified with the diameter of the central maximum of the Airy pattern in the focal plane that is given by

$$d = 1.22 \frac{\lambda}{NA}. \quad (14)$$

The symbol λ refers to the *vacuum* wavelength of light. The refractive index of the medium is contained in the value of the numerical aperture (NA) of the microscope objective. The ratio l/d of the long and short axis can be obtained from the relation

$$\frac{d}{l} = \frac{1 - \cos \alpha}{(3 - 2 \cos \alpha - \cos 2\alpha)^{1/2}} \quad (15)$$

that was derived by Grill and Stelzer for optical setups with a large solid angle [Gri99]. For $NA = 1.3$, which in water corresponds to an angle of $\alpha = 77.8^\circ$, we find $l/d = 2.4$. A similar value is also obtained from the experimental data in Figure 7. For $\lambda = 800$ nm, the above considerations yield focal dimensions of $d = 750$ nm, and $l = 1800$ nm.

3.3.2 Irradiance- and electron density distribution within the focal volume

The mathematical form of the diffraction-limited irradiance distribution in the Fraunhofer diffraction pattern of a microscope objective (Fig. 6) is too complex for convenient computation of the temperature and stress evolution induced by optical breakdown. We approximate the ellipsoidal region of high irradiance in the focus by a Gaussian function

$$I(r, z) = I(0, 0) \exp \left[-2 \left(\frac{r^2}{a^2} + \frac{z^2}{b^2} \right) \right], \quad (16)$$

where r and z are the coordinates in radial and axial direction, respectively, and $a = d/2$ and $b = l/2$ denote the short and long axis of the ellipsoid. The boundaries of the ellipsoid correspond to the $1/e^2$ values of the Gaussian irradiance distribution.

To derive the free-electron distribution $\rho_{\max}(r, z)$ from the irradiance distribution $I(r, z)$, we assume that for femtosecond pulses the free-electron density at the end of the laser pulse is approximately proportional to I^k , where k is the number of photons required for multiphoton ionization. This simplifying assumption corresponds to the low-intensity approximation of the Keldysh theory and neglects the weaker irradiance dependence of avalanche ionization that usually dominates plasma formation during the second half of a laser pulse (Fig. 3b). For $\rho_{\max} \leq 5 \times 10^{20} \text{ cm}^{-3}$, the proportionality $\rho_{\max} \propto I^k$ has been confirmed by the experimental results of Mao et. al. (2004). The spatial distribution of the free-electron density can thus be expressed as

$$\rho_{\max}(r, z) = \rho_{\max}[I(0, 0)] \exp \left[-2k \left(\frac{r^2}{a^2} + \frac{z^2}{b^2} \right) \right]. \quad (17)$$

Figure 8 shows the irradiance and electron density distribution in the focal region according to Eqs. (16) and (17) for $NA = 1.3$ and $\lambda = 800$ nm, for which $k = 5$. Due to the nonlinear absorption process underlying optical breakdown, the free-electron distribution is much narrower than the irradiance distribution. For $\lambda = 800$ nm and breakdown in water, it is narrower by a factor of $\sqrt[5]{5} = 2.24$, which corresponds to a reduction of the affected volume by a factor of 11.2. The diameter of the free-electron distribution at the $1/e^2$ - values amounts to 336 nm, the length to 806 nm.

It is interesting to note that the influence of the nonlinearity of the absorption process in plasma-mediated surgery considerably reduces the gain in spatial resolution that can be achieved by using a shorter wavelength. For example, when a wavelength of 355 nm is used instead of 800 nm, the width of the diffraction-limited irradiance distribution decreases by a factor of 2.25 but the plasma size decreases by a factor of only 1.42 because the order of the multiphoton process is reduced from 5 to 2 and the irradiance distribution is less strongly narrowed in the process of plasma formation. However, the irradiance range leading to low-density plasma formation is much broader for the shorter wavelengths (Fig. 5).

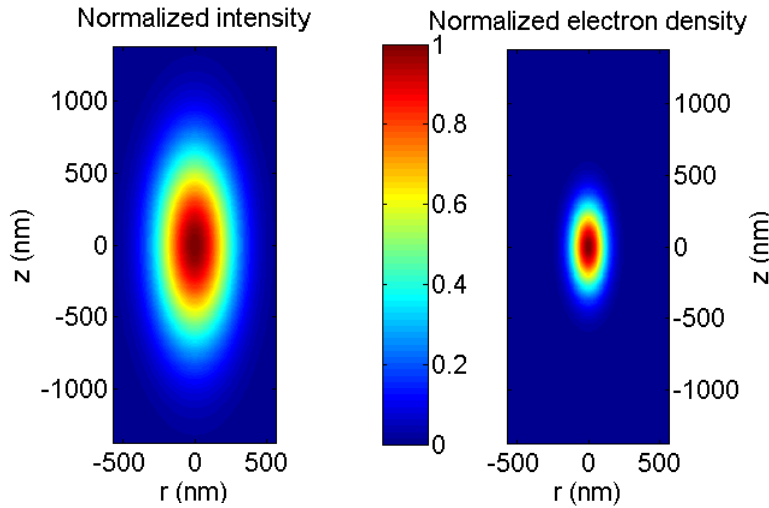


Figure 8: Normalized irradiance distribution (a) and electron density distribution (b) in the focal region for $NA = 1.3$ and $\lambda = 800$ nm that are assumed for the numerical calculations of the temperature and stress evolution induced by femtosecond optical breakdown.

When the laser pulse energy is raised above the optical breakdown threshold, the spatial distribution of the free-electron density broadens because nonlinear absorption of laser light upstream of the laser focus (“plasma shielding”) limits the possible energy density in the vicinity of the beam waist [Vog99a, Nah99, Ham97, Fan02a,b, Ray05]. Moreover, the $\rho(I)$ dependence will strongly deviate from the proportionality to I^k when the critical electron density ρ_{cr} (eq. (3)) is reached above which the plasma becomes highly reflective. Since the reflected light contributes to the plasma formation in the vicinity of the focus center, the electron density distribution is flattened. The critical electron density ρ_{cr} for the change of the optical plasma properties amounts to $0.984 \times 10^{21} \text{ cm}^{-3}$ for $\lambda = 1064$ nm, to $3.94 \times 10^{21} \text{ cm}^{-3}$ for $\lambda = 532$ nm, and to $8.86 \times 10^{21} \text{ cm}^{-3}$ for 355 nm, respectively. We will see in section 3.6.3 that the threshold for bubble formation is close to but still below these values. Therefore, the free-electron distribution depicted in Fig. 8 seems to be a reasonable approximation for the low-density plasma regime and suitable for the calculation of thermoelastic transients leading to bubble formation.

3.4 CHEMICAL EFFECTS OF LOW-DENSITY PLASMAS

Plasma-mediated chemical effects in biological media can be classified into two groups: 1. Changes of the water molecules by which reactive oxygen species (ROS) are created that affect organic molecules, 2. Direct changes of the organic molecules in resonant electron-molecule scattering.

1. The creation of ROS such as OH^* and H_2O_2 through various pathways following ionization and dissociation of water molecules has been investigated by Nikogosyan et. al. (1983) and recently reviewed by Garret et al. (2005). Both oxygen species are known to cause cell damage [Tir01]. Heisterkamp et. al. (2002) later confirmed the dissociation of water molecules during femtosecond laser-induced plasma formation by chemical analysis of the gas content of the bubbles.

2. Capture of electrons into an antibonding molecular orbital can initiate fragmentation of biomolecules [Gar05, Bou00, Hot01, Goh02, Hue03], as shown in **figure 9**. Capture can occur when the electron possesses a “resonant” energy for which there is sufficient overlap between the nuclear wave functions of the initial ground state and the final anion state. For a molecule XY this process corresponds to $e^- + \text{XY} \rightarrow \text{XY}^{*-}$, where the XY^{*-} has a repulsive potential along the X-Y bond coordinate. After a time of 10^{-15} to 10^{-11} s, the transient molecular anion state decays either by electron autodetachment leaving a vibrationally excited molecule (VE), or by dissociation along one, or several specific bonds such as $\text{XY}^{*-} \rightarrow \text{X}^* + \text{Y}^-$ (DA). Various authors describe resonant formation of DNA strand breaking induced by low-energy electrons (3-20 eV) [Bou00, Goh02, Hue03]. Boudaiffa et. al. (2000) found that the maximum single-strand break (SSB) and double-strand break (DSB) yields per incident electron are roughly one or two orders of magnitude larger than those for 10-25 eV photons. It is conceivable that accumulative effects of this kind can lead to a dissociation/dissection of biological structures that are exposed to femtosecond-laser-generated low-density plasmas.

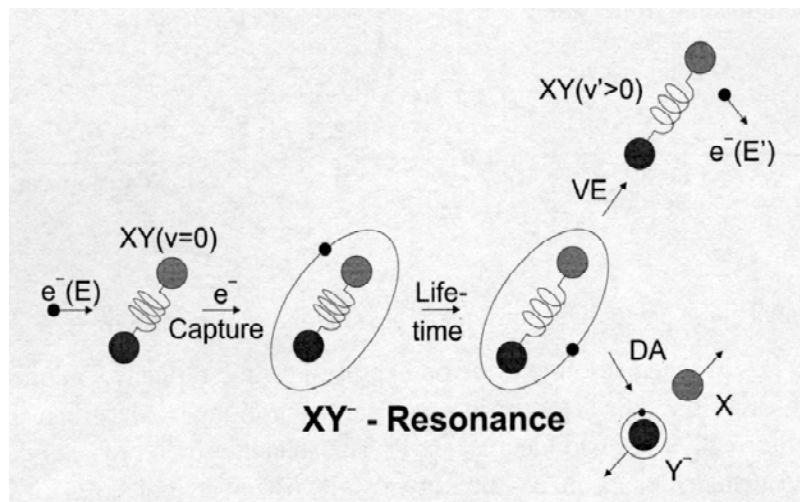


Figure 9: Dynamics of vibrational excitation and dissociative electron attachment in resonant electron-molecule scattering (see text). Reprinted with permission from Ref. [Hot01].

We will now assess the irradiance threshold for chemical changes by low-density plasmas using the plot of free-electron density versus irradiance presented in figure 3d. At NA = 1.3 and 800 nm wavelength, one free electron per focal volume corresponds to a density of $\rho = 2.1 \times 10^{13} \text{ cm}^{-3}$. Our calculations yield the result that this value is reached at an irradiance of $I = 0.26 \times 10^{12} \text{ W cm}^{-2}$ which is 0.04 times the irradiance threshold for breakdown defined as $\rho_c = \rho_{cr} = 10^{21} \text{ cm}^{-3}$. Tirlapur et. al. (2001) experimentally observed membrane dysfunction and DNA strand breaks leading to apoptosis-like cell death after scanning irradiation of PtK2 cells with 800-nm, 90-fs pulses at 80 MHz repetition rate and 7 mW average power (total dwell time 600 μs per cell, i.e. 4.8×10^4 pulses). The average power of 7 mW corresponds to a peak irradiance of $I \approx 0.44 \times 10^{12} \text{ W/cm}^2$ in the focal region, or 0.067 times the calculated breakdown threshold. The observed damage pattern of membrane dysfunction and DNA strand breaks match the effects expected from ROS and free electrons. The damage resembles the type of injury otherwise associated with single photon absorption of UV radiation [Tir01]. However, in Tirlapur's experiments it arose through nonlinear absorption of NIR irradiation and the exposure of cells to low-density plasmas. The relative importance of effects from ROS and free electrons at large irradiances still needs to be investigated.

In some cases, the breaking of a single bond in polymeric biological structures induces a cascade of bond breaking events that may be associated with a dramatic lowering of the apparent laser ablation threshold. For example, EYFP tagged microtubules exhibit an exceptionally low threshold for laser-induced dissection with 76 MHz series of 532-nm, 80-ps pulses (0.01 nJ per pulse) [Bot04], and an exceptionally low threshold was also observed for GFP-labeled microtubules irradiated by 80 MHz series of 880-nm, 100-fs pulses (0.025 nJ per pulse) [Sac05]. The low dissection threshold seems to be related to the dynamic instability between growth and depolymerisation that involves a rapid and self-propagating depolymerisation of the 'open ends' after local breakage of the microtubules [Mit84, Jan02]. Initiation of depolymerization requires breaking of just a single lateral bond which could be induced either by the impact of free electrons in a low-density plasma, or by multiphoton-chemistry, enhanced by the EYFP or GFP labeling, respectively. Since they can be triggered by a single broken bond, these reactions differ from the usual fs laser ablation in the low-density plasma regime that arises as a cumulative effect of many bond breaking events.

The irradiance producing lethal changes when laser pulse series are scanned over *entire* cells ($0.067 \times I_{\text{rate}}$) is slightly higher than the model prediction for the irradiance producing one free electron per pulse in the focal volume ($0.04 \times I_{\text{rate}}$), and about 10 free electrons in the focal volume will be produced by each laser pulse. Considering that the cell is exposed to thousands of pulses during the scanning irradiation, cumulative chemical damage may arise. By contrast, when *locally confined* irradiation is used to achieve knockout of individual cell organelles or intracellular dissection, the irradiance threshold for cell death is considerably higher. The role of plasma-mediated chemical effects for these procedures will be discussed in section 7.1, in comparison to the possible role of thermal and thermomechanical effects.

Recently, non-resonant ultrafast processes of bond breaking induced by large field strength in femtosecond laser pulses have been discussed in the context of laser ablation [Jes03, Bul04]. However, these processes occur at

surfaces where hot electrons can be emitted from the target thus creating a large field among the remaining ions that can cause a Coulomb explosion, and where material decomposed by a strong laser field can freely expand. They are not likely to play a role in the bulk of transparent media, especially not in the low-density plasma regime, i. e. at comparatively low field strengths. Here, chemical changes are rather generated through resonant interactions between quasi-free electrons and molecules.

3.5. TEMPERATURE EVOLUTION DURING PULSE SERIES

3.5.1 Calculation of temperature distribution

The deposition of laser energy into the medium is mediated by the generation and subsequent acceleration of free electrons. The energy carried by the free electrons is transferred to the heavy particles in the interaction volume through collisions and nonradiative recombination processes resulting in a heating of the atomic, molecular and ionic plasma constituents. To assess the time needed to establish an equilibrium temperature, we need to look at the characteristic time for electron cooling (the transfer of kinetic electron energy during collisions) and at the time scale for recombination which in water progresses through hydration of the free electrons. The time constant for electron cooling is in the order of only a few picoseconds [Gar05, Nol97], and the time constant for hydration of free electrons in water is even shorter, about 300 fs [Nik83]. However, the hydrated states possess a relatively long life time of up to 300 ns [Nik83]. In the framework of our model, the different steps are treated as one recombination process according to eq. (11). As the frequency of recombination events is proportional to ρ_e^2 , the recombination time depends on the free-electron density. It takes about 40 ps until the free electron density decreases by one order of magnitude from a peak value of $\rho_e = 10^{20} \text{ cm}^{-3}$, and about 20 ps for a peak value of $\rho_e = 10^{21} \text{ cm}^{-3}$ [Noa99, Vog01]. For low-density plasmas it will thus take between a few picoseconds and tens of picoseconds until a "thermodynamic" temperature is established [Gar05].

The temperature rise can be determined by calculating the volumetric energy density gained by the plasma during the laser pulse. This calculation is particularly easy for femtosecond pulses because the pulse duration is considerably shorter than the electron cooling and recombination times. Therefore, hardly any energy is transferred during the laser pulse, and the energy density deposited into the interaction volume is simply given by the total number density ρ_{max} of the free electrons produced during the pulse multiplied by the mean energy gain of each electron. The mean energy gain of an electron is given by the sum of ionization potential $\tilde{\Delta}$ and average kinetic energy, the latter of which is $(5/4)\tilde{\Delta}$ for free electrons produced by cascade ionization (section 3.2.2). This yields the following simple relation for the plasma energy density ε at the end of the laser pulse:

$$\varepsilon = \rho_{\text{max}} (9/4) \tilde{\Delta} \quad (18)$$

Note that this simple equation neglects the collisional energy transfer before impact ionization that is included in eq. (8) and considered in more detail by more advanced models based on the use of complete collision integrals [Arn05, Kai00]. This may lead to an underestimation of the rise in energy density corresponding to one free electron. On the other hand, eq. (18) treats free electrons produced by multiphoton ionization in the same way as those produced by impact ionization even though they start with zero kinetic energy of electron and hole which will rather overestimate the energy density increase. The temperature rise in the interaction volume after a single laser pulse can then be calculated by $\Delta T = \varepsilon / (\rho_0 C_p)$, where C_p is the heat capacity and ρ_0 the mass density of the medium.

The evolution of the temperature distribution within and around the interaction volume after single 100-fs pulse ($\lambda = 800 \text{ nm}$) during application of series of 100-fs pulses emitted at various repetition rates, and during cw laser irradiation ($\lambda = 514 \text{ nm}$) was calculated by solving the differential equation for heat diffusion with the appropriate Green's function

$$T(x, y, z, t) = \sum_{n=0}^{N-1} \int_0^{\text{Min}(t-n/f, \tau_L)} \int_{-\infty}^{\infty} \int_{-\infty}^{\infty} e^{-2(\frac{x'^2+y'^2}{a^2})-2(\frac{z'^2}{b^2})} \frac{1}{8\pi \rho_0 C_p \kappa (t-n/f-t')} e^{\frac{(x-x')^2+(y-y')^2+(z-z')^2}{4\kappa(t-t')}} dx' dy' dz' dt', \quad (18)$$

where A is the peak density of absorbed power in the irradiated volume, κ the thermal diffusivity, a and b are the short and long half axes of the free-electron density distribution described by Eq. (17) ($1/e^2$ values of electron density), $N = \text{Int}(t \cdot f) + 1$ is the number of pulses which were absorbed until time t , and τ_L is the laser pulse width. The integrals over x' , y' , and z' were solved analytically using *Mathematica* software, whereas the integration over t' was done numerically. We assumed the temporal shape of the laser pulses to be rectangular. We used the values $\rho = 1000 \text{ kg m}^{-3}$ for the density, $C_p = 4187 \text{ J K}^{-1} \text{ kg}^{-1}$ for the heat capacity, and $\kappa = 1.38 \times 10^{-7} \text{ m}^2 \text{ s}^{-1}$ for the heat diffusivity of water [Kuc91].

3.5.2 Evolution of the temperature distribution

The spatial temperature distribution at the end of a single fs-laser pulse, before heat diffusion sets in, reproduces the shape of the free-electron distribution of figure 8. Hence, the diameter of the initial temperature distribution ($1/e^2$ -values) amounts to 336 nm, the length to 806 nm (section 3.3.2). **Figure 10** shows the calculated temperature evolution at the center of the laser focus when series of 800-nm, 100-fs pulses are focused into water at different repetition rates (80 MHz and 1 MHz) and numerical apertures ($NA = 1.3$ and $NA = 0.69$). It was assumed that with each pulse an energy density of 1 J cm^{-3} at the center of the initial temperature distribution is deposited. For other values of the volumetric energy density, the shape of the temperature vs time curve will be the same but the absolute values of the temperature varies proportional to the peak density of absorbed power, A . For comparison, we also calculated the temperature evolution during cw irradiation with the same average power as for the pulsed irradiation (dotted lines in a) – c). For 80 MHz repetition rate, pulsed and continuous energy deposition differ significantly only during the first 100 ns.

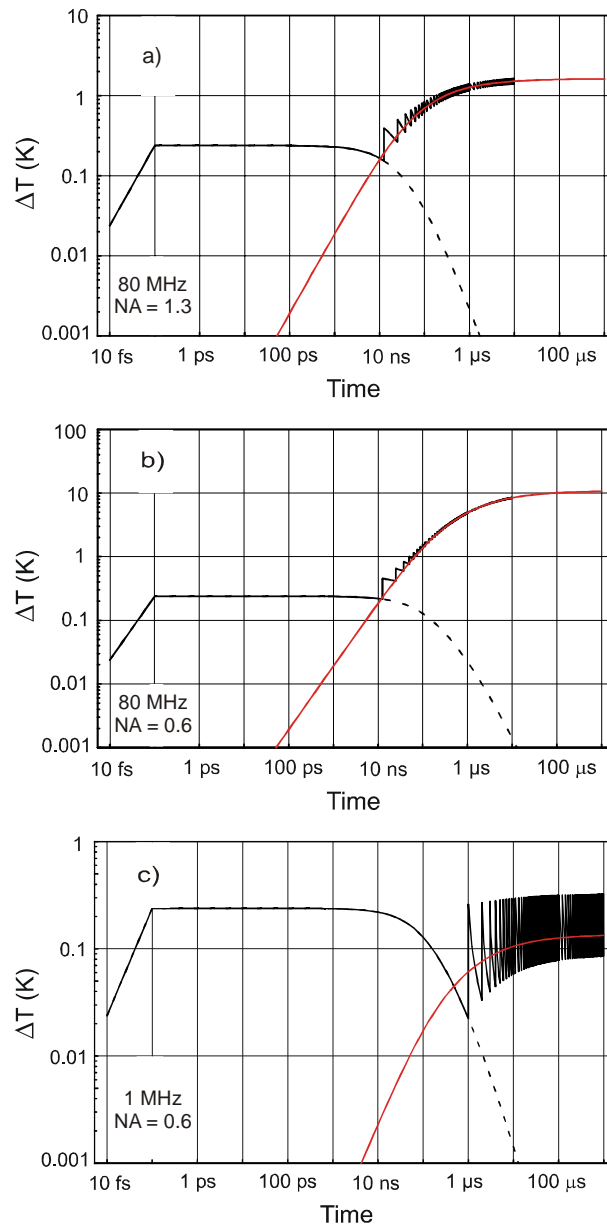


Figure 10: Temperature evolution at the center of the laser focus produced by a series of 800 nm, 100 fs pulses focused into water. a) 80 MHz repetition rate, $NA = 1.3$; b) 80 MHz repetition rate, $NA = 0.6$; c) 1 MHz repetition rate, $NA = 0.6$. The volumetric energy density deposited per pulse is always 1 J cm^{-3} at the focus center. The dashed lines represent the temperature decay after a single pulse. For comparison, the temperature evolution during cw irradiation with the same average power as for the pulsed irradiation is also shown.

The calculations in figure 10a for tightly focused irradiation with 80 MHz repetition rate reveal that the temperature is only 6.8 times larger after a few microseconds than the temperature increase caused by a single pulse. This implies that only a moderate heat accumulation occurs during plasma-mediated cellular surgery. However, when the numerical aperture is reduced from $NA = 1.3$ to $NA = 0.6$, such as in figure 10b, a 45-fold temperature increase is predicted. Temperature accumulation can almost entirely be avoided if, at the same NA, the repetition rate is lowered to 1 MHz (Fig. 10c). In this case, the peak temperature in a long pulse series is only 1.36 times larger than after a single pulse. For $NA = 1.3$ and 1 MHz repetition rate, this factor reduces to 1.024.

When laser surgery is performed with 80 MHz pulse series focused at $NA = 1.3$, the boiling temperature of 100°C will, due to the 6.8-fold temperature accumulation, be reached when each individual pulse produces a temperature rise of 11.8°C (starting from 20°C room temperature). For 800-nm, 100-fs pulses this temperature rise requires a free-electron density of $\rho_e = 2.1 \times 10^{19} \text{ cm}^{-3}$, which is reached at an irradiance of 0.51 times the value required for optical breakdown ($\rho_{cr} = 10^{21} \text{ cm}^{-3}$).

The evolution of the temperature distribution in the vicinity of the laser focus during application of 80-MHz pulse series is presented in **figure 11** for different numerical apertures. The distribution arising from the ellipsoidal focus volume is plotted both in radial and axial direction. For $NA = 1.3$, the temperature distribution remains fairly narrow (FWHM $\approx 600 \text{ nm}$) even after a few milliseconds when a dynamic equilibrium between energy deposition and heat diffusion has been established. The rapid decrease of the temperature with increasing distance from the laser focus is related to the small size of the focal volume which allows for rapid heat diffusion in all directions. By contrast, for $NA = 0.6$ the steady-state temperature distribution is more broadened compared to the single pulse distribution, in addition to the stronger increase of the peak temperature. Both, temperature accumulation and broadening of the temperature distribution can be avoided with repetition rates $\leq 1 \text{ MHz}$.

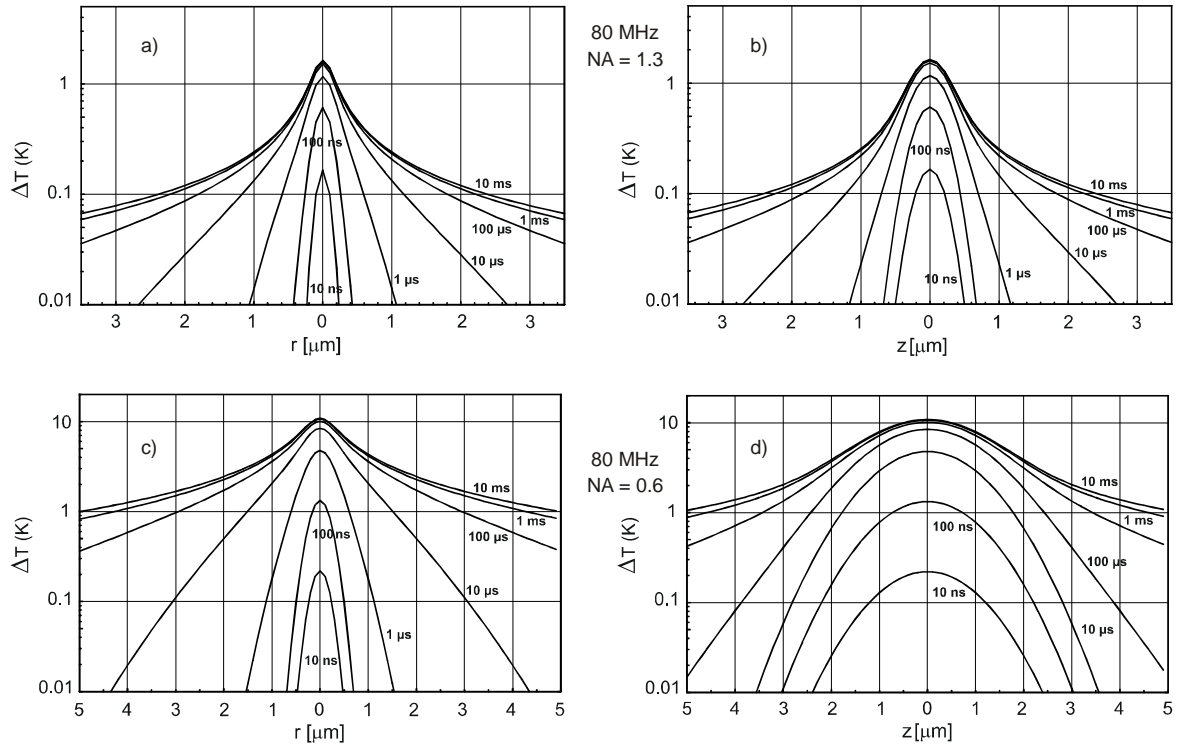


Figure 11: Temperature distribution in radial direction (a,c) and axial direction (b, d) produced by series of 800-nm, 100-fs pulses focused into water at numerical apertures of $NA = 1.3$ (a,b) and $NA = 0.6$ (c,d). The pulse repetition rate was 80 MHz in both cases, and the volumetric energy density deposited at the focus center was 1 J cm^{-3} for each pulse.

At first sight, the results of our temperature calculations might suggest that an irradiance range below the optical breakdown threshold exists where predominantly thermal effects in biological media can be produced. However, one needs to consider that about 10^6 free electrons *per pulse* are generated in the focal volume at the irradiance which creates a temperature difference of 11.8°C per pulse and a peak temperature of 100°C after a pulse series of several microseconds (for $NA = 1.3$). Any thermal denaturation of biomolecules will thus always be mixed with free-electron-induced chemical effects, and the latter will probably dominate.

3.5.3 Comparison with cw irradiation of linear absorbers

Since various researchers have produced cellular microeffects using long-pulsed or continuous wave irradiation [Pal96, Schn02, Pat05, Ber69, Ber71, Sto89] it is of interest to compare the widths of the temperature distributions produced by series of ultrashort laser pulses and cw irradiation.

Figure 12 shows the evolution of the temperature distribution when cw irradiation of 514 nm wavelength is focused into a linearly absorbing aqueous medium at NA = 1.3. The temperature distribution is slightly broader (FWHM 850 nm) than that in Fig. 11a arising from nonlinear absorption of 80-MHz IR femtosecond pulse trains (FWHM 600 nm). The temperature distribution produced by femtosecond pulse trains is narrower because it originates from the free-electron distribution (Eq. 17) rather than from the irradiance distribution (Eq. 16) which is relevant for linear energy deposition. However, the spatial resolution of femtosecond laser surgery is not determined by the steady-state temperature distribution but by the width of the *free-electron* distribution itself, as we shall see in section 7.1. Therefore, the spatial resolution of fs laser surgery is considerably better than that of a cw microbeam.

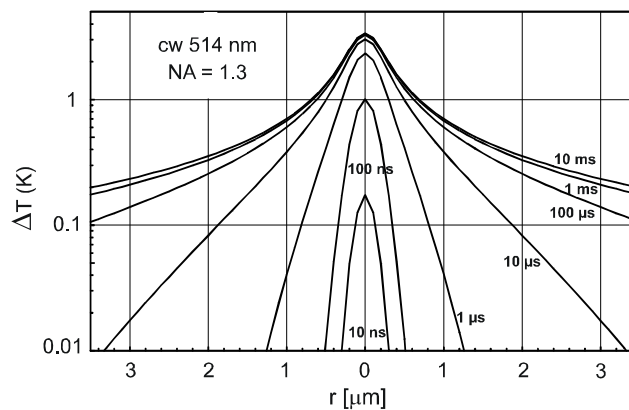


Figure 12: Evolution of the temperature distribution in radial direction produced by continuous energy deposition in a linearly absorbing aqueous medium at a laser wavelength of 514 nm. The calculations were performed for the same absorbed average power as in the case of pulsed, nonlinear energy deposition presented in Fig. 11.

3.6 THERMOELASTIC STRESSES AND STRESS-INDUCED BUBBLE FORMATION

3.6.1 Calculation of stress distribution and bubble formation

The temperature rise in the focal volume occurs during thermalization of the energy carried by the free electrons, i. e. within a few picoseconds to tens of picoseconds (see section 3.5.1). This time interval is much shorter than the acoustic transit time from the center of the focus to its periphery. Therefore, no acoustic relaxation is possible during the thermalization time, and the thermoelastic stresses caused by the temperature rise stay confined in the focal volume, leading to a maximum pressure rise [Vog03, Pal99, Pal03]. Conservation of momentum requires that the stress wave emitted from a finite volume within an extended medium must contain both compressive and tensile components such that the integral of the stress over time vanishes [Pal99, Sig78]. The tensile stress wave may induce fracture of the material even after a temperature rise too small to produce thermal damage [Pal96]. In water, it will cause the formation of a cavitation bubble when the tensile strength of the liquid is exceeded. For cell surgery, the threshold for bubble formation defines the onset of disruptive mechanisms contributing to dissection.

To determine the evolution of the thermoelastic stress distribution in the vicinity of the laser focus, we solved the three-dimensional thermoelastic wave equation. A starting point for the calculation of the thermoelastic stress wave propagation is the temperature distribution at the end of a single femtosecond laser pulse that reproduces the free-electron distribution described by Eq. (17). In the following calculations, this temperature distribution is characterized by T_{max} , the temperature in °C in the center of the focal volume. From this temperature distribution the initial thermoelastic pressure (right after the laser pulse, before the acoustic wave has started to propagate) was calculated using

$$p(\vec{r}) = \int_{T_1}^{T_2(\vec{r})} \frac{\beta(T)}{K(T)} dT, \quad (19)$$

where $T_1 = 20^\circ\text{C}$ is the temperature before the laser pulse, and $T_2(\vec{r})$ the temperature of the plasma after the laser pulse, which depends on the location within the focal volume. The temperature dependence of the thermal expansion coefficient β and the compressibility K was taken into account, using values for metastable water from Ref. [Skr88]. The time- and space-dependent pressure distribution $p(\vec{r}, t)$ due to the relaxation of the initial thermoelastic pressure was calculated using a k -space (spatial frequency) domain propagation model [Kös01, Cox05].

Because the heated volume is very small ($\approx 0.07 \mu\text{m}^3$) and the region subjected to large tensile stress amplitudes is even smaller (see Fig. 14, below), the presence of inhomogeneous nuclei that could facilitate bubble formation is unlikely. Therefore, we have to consider the tensile strength of *pure* water to estimate the bubble formation threshold in femtosecond optical breakdown. Traditionally, the rupture of a liquid achieved by tensile stress under isothermal conditions is called “cavitation” while bubble formation due to heating under isobaric conditions is called “boiling” [Bre95]. Such a distinction becomes obscure when targets are both heated and stretched under conditions of stress confinement. We use the crossing of the “kinetic spinodal” as defined by Kiselev (1999, 2001) as threshold criterion for bubble formation. In the thermodynamic theory of phase transitions, the locus of states of infinite compressibility $(\partial p / \partial V)_T = 0$, the spinodal, is considered as a boundary of fluid metastable (superheated) states. Physically, however, the metastable state becomes short-lived due to statistical fluctuations well before the spinodal is reached [Ski88, Deb96]. The “kinetic spinodal” is the locus in the phase diagram where the lifetime of metastable states becomes shorter than a relaxation time to local equilibrium. If the surface tension is known, the physical boundary of metastable states in this approach is completely determined by the equation of state only, i.e. by the equilibrium properties of the system [Kis99, Kis01]. This feature distinguishes the kinetic spinodal from the homogeneous nucleation limit derived earlier by Fisher, which depends on the size of the volume under consideration and the duration of the applied stress [Fis48]. Unlike Fisher’s equation, the kinetic spinodal reproduces the shape of the spinodal and is applicable in the entire temperature range from room temperature to the critical point. Nucleation threshold in cells will probably resemble those in pure water because the biomolecules are too small to serve as boundaries for heterogeneous nucleation.

Figure 13a presents the saturated liquid/vapor curve (binodal), the spinodal, the kinetic spinodal, and the homogeneous nucleation limit derived by Fisher in a p vs T projection of the thermodynamic phase diagram for water. For comparison, experimental data by Skripov et. al. on the empirical limit of the metastable region and by Zheng et. al. on the tensile strength of water are also shown [Ski88, Zhe91]. In **figure 13b**, the kinetic spinodal is plotted together with the peak compressive and tensile thermoelastic stresses in the focus center that are produced when an 800-nm, 100-fs pulse is focused into water at $\text{NA} = 1.3$. The temperature at which the tensile stress curve reaches the kinetic spinodal is defined as bubble formation threshold. For larger laser pulse energies, the kinetic spinodal will be reached in an increasingly large part of the focal region.

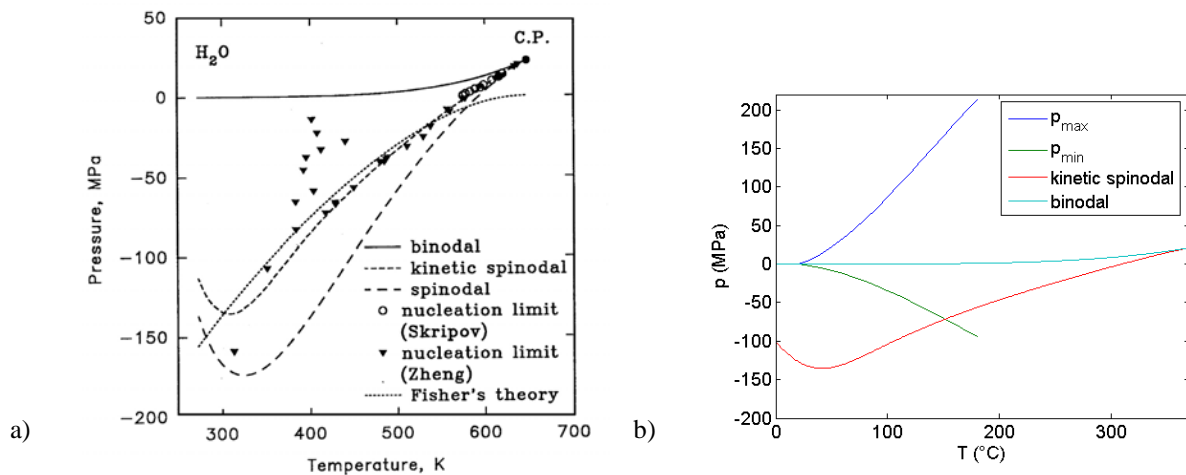


Figure 13: a) Binodal, spinodal, kinetic spinodal of water as a function of temperature, calculated with the analytic equation of state of Saul and Wagner ()1989. The dotted curve corresponds to the homogeneous nucleation limit in Fisher’s theory (1948), the circles indicate experimental data of Skripov and Chukanov (1988), and the triangles indicate the experimental data of Zheng et. al. (1991) recalculated in p - T coordinates. Figure reproduced with permission from Ref. [Kis99]. Copyright 1999 Elsevier Science B.V. b) Peak compressive and tensile thermoelastic stresses in the focus center produced by a 800-nm, 100-fs pulse focused into water at $\text{NA} = 1.3$, plotted together with the binodal and the kinetic spinodal.

To calculate the dynamics of the cavitation bubble produced after crossing the kinetic spinodal, first the size of the bubble nucleus was determined. It was identified with the extent of the region in which the negative pressure exceeds the kinetic spinodal limit $p(\vec{r}, t) < p_{ks}(\vec{r})$. The initial radius of a spherical bubble with the same volume was taken as the starting nucleus for the cavitation bubble. The heated and stretched material within the nucleus commences to expand instantaneously (within less than 1 ps) once the kinetic spinodal is reached [Gar03]. As driving force for the expansion only the negative part of the time-dependent stress in the center of the focal volume was considered, because the nucleus does not exist before the tensile stress arrives. This is in contrast to simulations of heterogeneous cavitation where pre-existing gas bubbles interact with a time-varying pressure wave [Pal96]. Only cases were simulated in which the temperature in the center of the focal volume slightly exceeds the phase transition threshold and the size of the resulting nucleus is small compared with the focal volume. This justifies using the tensile stress amplitude in the center of the undisturbed focal volume as driving force for the bubble expansion. For larger laser pulse energies one would need to consider that the tensile stress is diminished by the rupture of the liquid.

After the passage of the tensile stress transient, the vapor pressure p_v inside the bubble continues to drive the bubble expansion. The initial vapor pressure is calculated for a temperature averaged over all volume elements within the nucleus. During bubble growth, it will drop due to the cooling of the expanding bubble content. This cooling is counteracted by heat diffusion from the liquid surrounding the bubble. The temperature of this liquid, on the other hand, drops because of heat diffusion out of the focal volume as depicted by the dashed lines in Fig. 10. To quantify the temporal evolution of the driving pressure, we consider two limiting cases:

Case 1: bubble size \ll focal volume. We assume that the bubble initially expands adiabatically until the average temperature of the bubble content has fallen to the temperature of the liquid at the nucleus wall. Afterwards, heat flow from the surrounding liquid maintains the temperature of the bubble content at the same level as that of the surrounding liquid. The bubble pressure $p_v(t)$ thus equals the equilibrium vapor pressure corresponding to the temperature at the nucleus wall, which, for NA = 1.3, decays within about 20 ns to 1/e of its initial value (Fig. 10a). Justifications for this hypothesis are the small bubble size and the fact that the bubble nucleus is not empty but contains material that is initially at liquid density and has a relatively large heat capacity.

Case 2: Bubble size comparable to or larger than the focal volume. When the size of the nucleus becomes comparable to the size of the focal volume, the bubble expands more rapidly. In this case, the heated liquid shell surrounding the bubble is rapidly thinned, which leads to an accelerated heat dissipation into adjacent liquid. The heat flow into the bubble is probably small compared with the amount of heat contained in the material within the bubble nucleus. Therefore, the entire bubble dynamics is modeled as an adiabatic expansion. As a consequence, the vapor pressure drops much faster than in case 1. In both cases, the ongoing phase transition in the bubble was neglected to obtain tractable expressions for $p_v(t)$. This simplification enabled us to use the Gilmore model to describe the bubble dynamics [Pal96, Gil52, Kna71]. The pressure drop is in case 1 slower and in case 2 faster than the pressure decay corresponding to the actual phase transitions of the bubble content. Therefore, these cases represent upper and lower limits for the evolution of the actual bubble size after femtosecond optical breakdown.

3.6.2 Evolution of the stress distribution

The thermalization time of the energy carried by the free electrons was assumed to be 10 ps. For NA = 1.3, and $\lambda = 800$ nm, and a sound velocity in water of $c_0 = 1500$ m/s, the acoustic transit time to the periphery of the heated region with 168 nm radius is 112 ps. Thus the dimensionless thermalization time (thermalization time divided by acoustic relaxation time) is $t_p^* = 0.09$, which corresponds to a very high degree of stress confinement. The "thermalization pulse" was assumed to have a Gaussian temporal shape, with the peak at $t = 0$. By comparison with an exponential "thermalization pulse" we found that for short dimensionless pulse durations t_p^* , the pulse shape has little influence on the shape and amplitude of the stress wave.

Figure 14 shows the spatial stress distribution in radial and axial direction for various points in time after the release of the laser pulse, and **figure 15** presents the temporal evolution of the stress amplitude in the center of the focal volume. All pressure amplitudes are normalized to the peak compressive stress created in the focal volume.

The compressive stress generates a stress wave traveling into the surrounding medium. When the thermal expansion comes to a rest, inertial forces lead to the generation of a relaxation wave that propagates from the periphery of the focal volume towards its center and is focused in the center of symmetry. Because of the geometrical focusing, it turns into a tensile stress wave that achieves maximum amplitude at the center of symmetry.

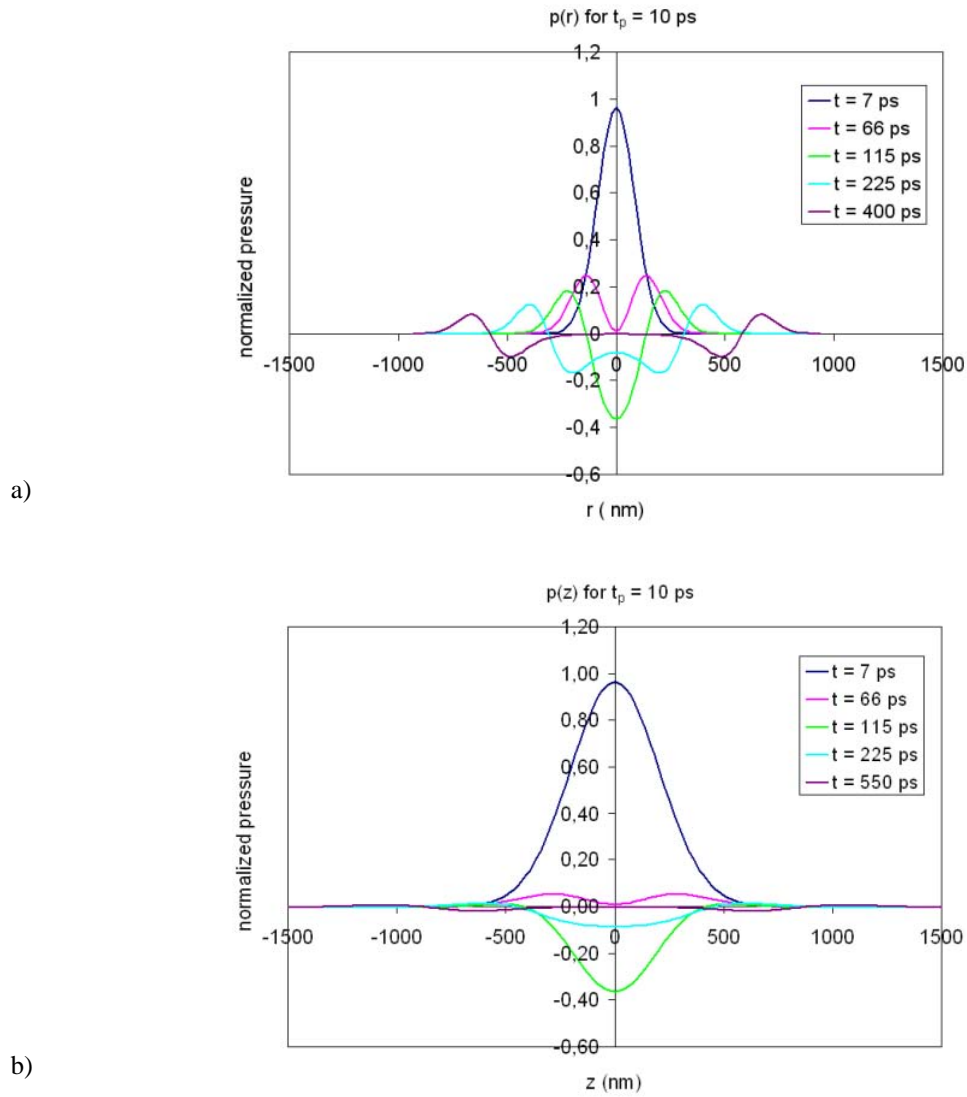


Figure 14: Stress distribution produced by a single femtosecond pulse of 800 nm wavelength focused into water ($NA = 1.3$), for various times after the release of the laser pulse; (a) in radial direction, (b) in axial direction. The thermalisation time of the energy carried by the free electrons was assumed to be 10 ps. The dimensionless thermalisation time (thermalization time divided by acoustic relaxation time) was $t_p^* = 0.09$. The "thermalization pulse" was assumed to have a Gaussian temporal shape, with the peak at $t = 0$. The pressure amplitudes are normalized to the peak compressive stress created in the focal volume.

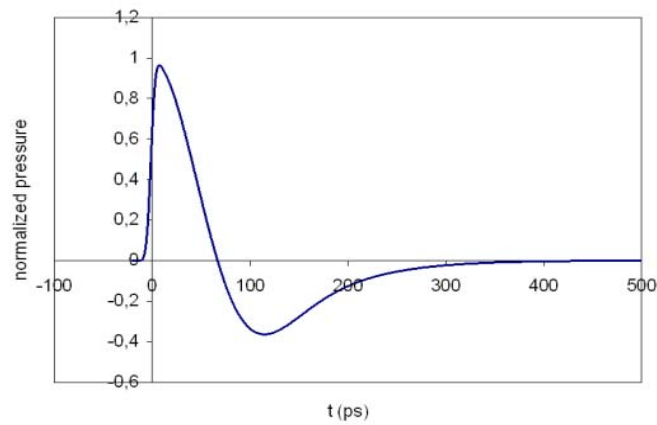


Figure 15: Temporal evolution of the stress amplitude in the center of the focal volume for the same conditions as in Fig. 14.

The peak tensile stress amplitude depends strongly on the shape of the heated volume. It is largest for a spherical shape [Pal99] and much smaller in the present case of an elongated ellipsoid. The dependence of the compressive stress amplitude on the degree of stress confinement t_p^* was relatively strong, but the amplitude of tensile stress waves remained approximately constant when the duration of the thermalization “pulse” was varied between 5 ps, 10 ps, and 20 ps.

A comparison of Figures 14a and 14b shows that the stress wave amplitudes outside the focal region are considerably larger in radial than in axial direction. This is a consequence of the elongated shape of the focal volume. The stress transients emitted in both directions have a bipolar shape as expected for thermoelastic waves. The amplitude of stress transient when it leaves the heated region in radial direction amounts to 25% of the peak compressive pressure. This differs from the previously analyzed case of a top hat distribution where the amplitude of the compressive wave just outside the heated volume amounts to 0.5 times the peak compressive pressure inside that volume [Vog02].

Experimental data on stress wave emission

Measurements of the stress waves produced by femtosecond optical breakdown at large NA and close to the breakdown threshold are very challenging because of the sub-micrometer size of the breakdown volume and the sub-nanosecond duration of the stress transients (Figs. 14, 15). Hydrophones with sufficiently small detector size to resolve the shape of the transient close to their source are not available, and optical techniques [Vog96b, Stau93, Pal97, Noa98b] do also not provide the necessary spatial resolution. Therefore, we performed measurements at smaller numerical aperture ($NA = 0.2$) to assess the stress amplitudes arising during femtosecond optical breakdown.

Investigations for irradiances well times above the breakdown threshold were done by means of streak photography and subsequent digital image analysis of the streak recordings [Noa98a,b,c]. Differentiation of the stress wave propagation curves $r(t)$ obtained from the streak recordings yielded the stress wave velocity that is related to the pressure amplitude by the known Rankine-Hugoniot-relationship for water [Rice57] if the stress wave has shock wave properties. The analysis yielded the entire pressure vs distance curve in the immediate vicinity of the breakdown region perpendicular to the optical axis as shown in **figure 16**, together with the corresponding streak recording.

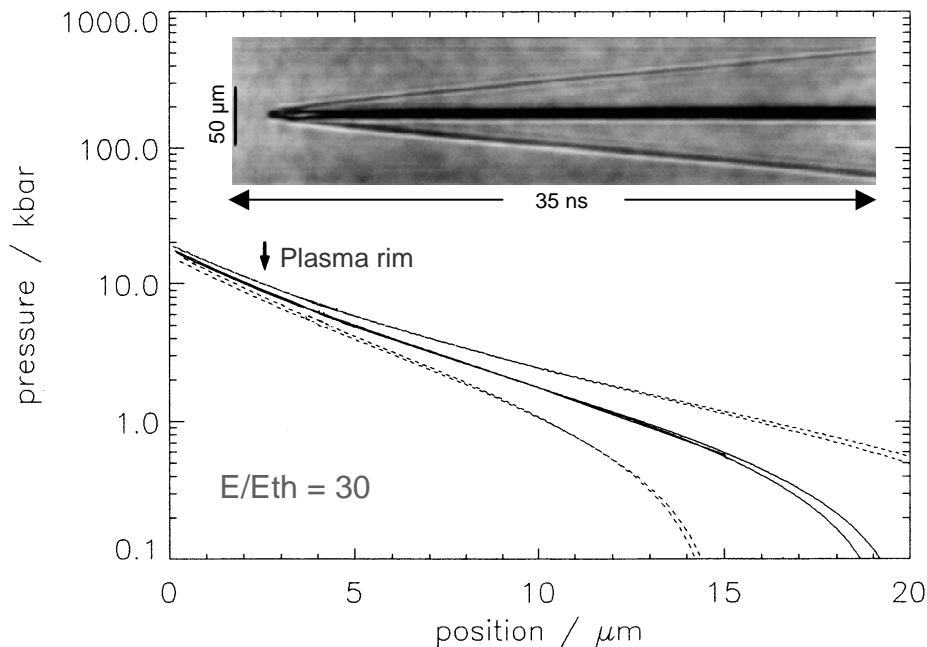


Figure 16: Measured pressure vs propagation distance curve for a stress wave produced by a 100-fs pulse of 5 μ J energy ($E/E_{th} = 30$) focused into distilled water at $NA = 0.2$ (16° full focusing angle). The laser wavelength was 580 nm. The arrow represents the location of the plasma rim as determined from plasma photographs in side view. The $p(d)$ curve was determined from the streak recording of the stress wave emission shown in the insert.

The determination of the shock wave pressure becomes inaccurate for pressure amplitudes below 100 MPa where the deviation of the propagation velocity from the sonic velocity becomes too small to be measured accurately with the streak technique [Noa98b]. Therefore, the streak technique could only be applied for shock wave measurements at energies 15-150 times above the breakdown threshold. Stress wave amplitudes closer to the optical breakdown threshold were determined indirectly by hydrophone measurements at 6 mm distance from the focus [Noa98c] and extrapolation of these data to the plasma rim. We used a PVDF hydrophone (Ceram) with a rise time of 12 ns, an active area of 1 mm², and a sensitivity of 280 mV/MPa (calibrated by the manufacturer up to a frequency of 10 MHz). A distance of 6 mm between detector and laser focus was required to avoid measurement errors arising from the intersection of a spherical shock wave with a plane detector [Vog96b]. Measurement results for energies from close to the breakdown threshold up to 80 times threshold are shown in **figure 17**.

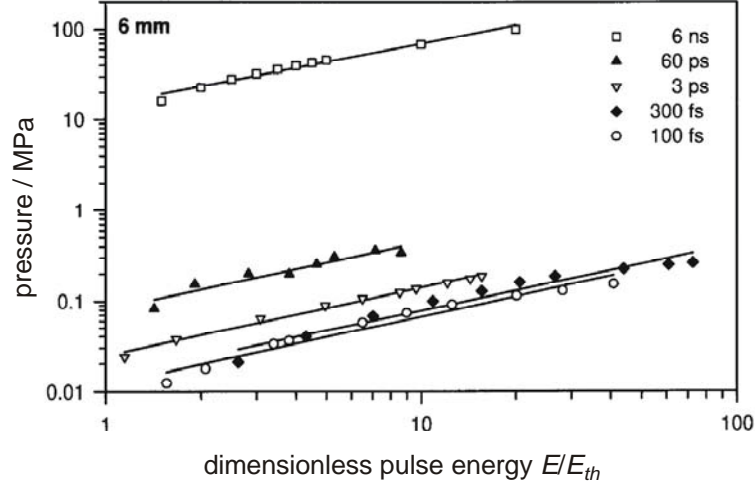


Figure 17: Stress wave amplitude for 100-fs pulses as a function of the dimensionless laser pulse energy E/E_{th} . The pressure amplitudes were measured by means of a hydrophone at 6 mm distance from the laser focus.

The results of far-field hydrophone measurements can be extrapolated to the boundary of the focal region if the decay constant n of the pressure decay $p \propto r^{-n}$ with increasing propagation distance r is known. The decay constant was estimated by comparing pressure values at the plasma rim and in the far-field that were measured at a larger laser pulse energies. For example, for $E = 30 \times E_{th}$, the pressure at the plasma rim ($r = 2.2 \mu\text{m}$) is 900 MPa (Fig. 16), and the pressure measured at 6 mm distance is 0.12 MPa (Fig. 17). The resulting decay constant is $n = 1.13$. Previous investigations of complete $p(r)$ curves for spherical shock waves produced by 30-ps pulses of 50 μJ energy yielded a very similar constant of $n = 1.12$ over a large range of propagation distances [Vog96b].

An estimate of the pressure value at 6 mm distance produced by a 100-fs pulse with threshold energy was obtained by extrapolating the data for $E/E_{th} \geq 1.5$ in Fig. 17 to $E = E_{th}$. It is about 0.008 MPa. The plasma radius at E_{th} was identified with the focal radius of $2.2 \mu\text{m}$ measured using a knife edge technique [Noa98c]. A pressure of $p = 0.008 \text{ MPa}$ at 6 mm distance corresponds to a pressure value of 61 MPa at the plasma rim when a decay constant $n = 1.13$ is assumed, and to a value of 56 MPa with a decay constant of $n = 1.12$, respectively. Our calculations of the thermoelastic stress generation predict a peak pressure of 168 MPa at the bubble formation threshold (see section 3.6.3 below). According to figure 14, the stress transient that leaves the heated region in radial direction has a peak pressure of $\approx 25\%$ of the maximum compressive amplitude *within* the focal volume. We thus obtain a theoretical prediction of 42 MPa for the amplitude of the thermoelastic stress wave at the plasma rim. Considering the uncertainties in the location of the plasma rim and the differences in numerical aperture between experiment and calculation, the agreement between experimental results (56-61 MPa) and calculated data (42 MPa) is very good.

Both experiments and calculations reveal that stress confinement in femtosecond optical breakdown results in the generation of high pressure values even though the temperature rise is only relatively small. In a purely thermal process, a temperature rise to, for example, 200°C starting from room temperature would produce a saturation vapor pressure of 1.6 MPa. The compressive pressure transient produced by a temperature rise of 180 °C under stress confinement conditions has an amplitude of 220 MPa which is more than two orders of magnitude larger than the vapor pressure.

The situation is different for optical breakdown at longer pulse durations where the stress confinement condition is not fulfilled. Here, high pressures are always associated with high temperatures and plasma energy densities. For pulses which are considerably longer than the thermalization time of the free-electron energy, a dynamic equilibrium between generation of free electrons and thermalization of their energy is established during the laser pulse [Noa99]. This leads to a high value of the plasma energy density [Vog99a] and a temperature of several thousand degrees Kelvin [Bar68, Sto95, Cha97], which, in turn, drives the emission of a strong shock wave [Vog96b]. The duration of this shock wave is determined by the time it takes for the high pressure within the plasma to decrease during the plasma expansion [Vog96b], which for $NA = 0.9$ was found to be about 25-40 ns [Ven02]. By contrast, the duration of the thermoelastic stress transients is determined by the geometric dimensions of the breakdown volume which are in the sub-micrometer range. This leads to a duration of the stress transients in the order of less than 300 ps (Fig. 15). The short duration of these stress waves is correlated with a small energy content (see also section 3.6.4).

3.6.3 Threshold for stress-induced bubble formation

A specific feature of the stress transients generated during fs optical breakdown is their tensile component that is related to the high degree of stress confinement during energy deposition. The tensile stress makes it possible that a cavitation bubble can be generated by a relatively small temperature rise in the liquid. The threshold for bubble formation is defined by the temperature rise leading to a crossing of the kinetic spinodal, as shown in figure 13. For $\lambda = 800$ nm, $NA = 1.3$, and a room temperature of 20°C , the critical temperature rise and the corresponding critical tensile stress are $\Delta T = 131.5^\circ\text{C}$, and $p = -71.5$ MPa, respectively. The corresponding compressive pressure is 168 MPa.

The temperature rise of 131.5°C at the threshold for bubble formation corresponds to an increase in energy density of 551 J cm^{-3} which, according to eq. (18), is produced by a free-electron density of $\rho_e = 0.236 \times 10^{21} \text{ cm}^{-3}$. This electron density is less than the breakdown criterion of $\rho_{cr} = 10^{21} \text{ cm}^{-3}$ assumed in our numerical calculations and in most other theoretical studies of plasma formation. The discrepancy between the threshold values relying on different breakdown criteria needs to be kept in mind when comparing the results of experimental studies, where bubble formation serves as breakdown criterion, with those of numerical simulations.

The fact that femtosecond optical breakdown is associated with only a relatively small temperature rise explains why plasma luminescence is no longer visible for pulse durations shorter than about 10 ps [Ham96, Ken97, Noa98a]. For pulse durations longer than the thermalization time, large amounts of energy are transferred from the free electrons to the heavy particles during the laser pulse [Noa99], resulting in a temperature of several thousand degrees Kelvin, bubble formation, and a bright plasma luminescence [Bar68, Sto95, Cha97]. By contrast, a peak temperature of 151.5°C reached at the threshold for bubble formation with 100-fs pulses is too low to produce blackbody radiation in the visible range of the optical spectrum. Moreover, the recombination radiation of femtosecond-laser-produced plasmas is weak because only one “set” of free electrons is produced that recombines after the end of the laser pulse. The energy density will remain small also at energies above the threshold for bubble formation because of the shielding of the focal region by plasma formation upstream of the focus [Vog99a, Nah96, Ham97, Fan02a,b, Ray05] (see section 3.3.2). Therefore, bubble formation is a more useful breakdown criterion for ultra-short laser pulses than plasma luminescence.

Experimental data on breakdown thresholds

A comparison between experimental threshold data from various researchers and threshold values predicted by our model is presented in **table 1**. Note that calculated values refer to the peak power in the laser pulse and in the focal spot while experimental data are often calculated using the average power in the laser pulse and within the focal area.

Our numerical predictions lie within the range of experimental data for all pulse durations. However, that does not mean very much considering the fact that the experimental data scatter within a range of one order of magnitude for femtosecond and nanosecond pulses, and only slightly less for picosecond pulses. These large variations reflect the difficulty of performing precise threshold measurements in the bulk of water. Ideally, high-quality laser beams and diffraction limited focusing optics should be employed, the spot size should be measured to control the beam quality, and I_{th} should be calculated using the measured spot size. However, in various studies, the quality of the laser beam and focusing optics were far from optimal, and, nevertheless, the diffraction limited spot size has been used for the calculation of I_{th} . In the presence of aberrations, this leads to erroneously large threshold values. Even when the spot size is measured, aberrations will lead to false results because breakdown occurs in hot spots within the focal region that are smaller than the measured spot size. The threshold values determined this way are therefore

Pulse duration	Wavelength (nm)	NA or focusing angle	Gaussian (G) top hat (T)	Measured spot diameter (μm)	Diffraction limited spot (μm)	Bd criterion Bubble (B) Luminescence (L)	E_{th} (μJ)	F_{th} (J/cm ²)	$I_{th} \times 10^{11}$ W/cm ²)	$I_{rate} \times 10^{11}$ W/cm ²)	Source	Factors influencing the measured threshold value
10 ns	1064	14°	G		4.0	L	400	3200	3.2		[178]	Spherical aberrations, Ps spikes because of longitudinal mode beating
7 ns	1064		G		75	L		245	0.35		[99, 100]	Longitudinal mode beating, self-focusing
6 ns	1064	32°	G	5.4		L	89.9	396	0.66	1.79	[15]	Longitudinal mode beating
6 ns	532	22°	G	5.3		L	38.5	174	0.29	6.06	[15]	Longitudinal mode beating
6 ns	1064	NA0.9	T		1.44	L	18.3	1122	1.87		[3]	Longitudinal mode beating; absorption in microscope objective not considered
6 ns	532	NA0.9	T		0.72	L	1.89	462	0.77		[3]	Longitudinal mode beating; absorption in microscope objective not considered
220 ps	1064		G		37	L		64.9	2.95	1.81 (100ps)	[99, 100]	Self focusing
200 ps	800	NA0.65	T		1.50	B	4.0	90.4	4.52	2.90 (100ps)	[179, 180]	Spherical aberrations
60 ps	532	16.7	T	7.2		L	10.0	24.4	4.07	6.63 (100ps)	[136]	Moderate spher. aberrations
40 ps	1064	14°	G		4.0	B	1.6	64.0	16		[178]	Spherical aberrations
30 ps	1064		G		37	L		19.2	6.41		[99, 100]	Self-focusing
30 ps	1064	22	G	4.7		L	2.38	13.6	4.53	2.67 (10ps)	[15]	
30 ps	532	22	G	3.4		L	1.01	11.3	3.75	6.19 (10ps)	[15]	
3 ps	580	16.7	TG	10.8		B	1.1	1.25	4.15		[136]	Moderate spher.aberrations
3 ps	580	16	G	5.0		B	0.51	2.6	8.5	15.3 (1ps,532nm)	[80, 81]	
300 fs	580	16.7	TG	10.8		B	1.0	1.1	36.0		[136]	Moderate spher. aberrations, Self-focusing
300 fs	580	16	G	5.0		B	0.29	1.4	47.6		[15]	Self-focusing
150 fs	620			5.0		B		0.87	58.0		[181]	Self-focusing
150 fs	620			5.0		B		1.3	86.7		[181]	Self-focusing
125 fs	580	16.7	TG	10.8		B	0.35	0.4	30.6		[136]	Moderate spher.aberrations, self-focusing
100 fs	580	16	G	4.4		B	0.17	1.1	111.0	55.9(532nm)	[80, 81]	Self-focusing
100 fs	800	NA0.65	T		1.50	B	≈ 0.1	5.64	564	65.4	[182]	Spherical aberrations
44 fs	810	≈16	G	≈10		B	0.19	0.22	50		[183]	Strong self-focusing

Table 1: Comparison of experimental optical breakdown thresholds for water, together with calculated threshold values obtained using the criterion $\rho_{cr} = 10^{21} \text{ cm}^{-3}$. Whenever the spot size was determined in the experiment, the measured spot size is quoted and used for the threshold calculations. Measured spot sizes refer to the ‘linear’ size, without the influence of self-focusing. When the spot diameter was not measured, the diffraction limited spot size is quoted and used for calculating the thresholds. Spot sizes refer to the $1/e^2$ values of the intensity for irradiation with a Gaussian beam profile, and to the first minimum of the Airy function for irradiation with a top-hat beam profile. Factors compromising the accuracy of the measured threshold data are listed in the column on the far right of the table.

smaller than the actual values [Vog99b]. Many breakdown experiments were performed by focusing a laser beam into a glass cell by means of an external focusing optics. Even when this optics is of high quality, the glass cell itself will introduce spherical aberrations. This source of error can be avoided by using water immersion microscope objectives built into the wall of the cell [Ven02].

For nanosecond pulses, longitudinal mode beating in the laser resonator will usually produce intensity spikes of picosecond duration with amplitudes up to 4-5 times as large as the averaged intensity. Such statistical fluctuations of the peak irradiance are a major cause of the wide statistical distribution of optical breakdown thresholds and substantially reduce their absolute values [Gle84, Efi04]. Therefore, single-frequency lasers providing a temporally Gaussian pulse shape should be used for threshold measurements. However, to date all measurements of nanosecond optical breakdown thresholds in water have been performed with longitudinally multimode laser beams.

To avoid a change of the focal spot size by nonlinear beam propagation, sufficiently large focusing angles must be used [Sch01, Vog96a, Soi89]. While this is easy to achieve for nanosecond pulses, a numerical aperture $NA \geq 0.9$ is required for a pulse duration of 100 fs to be sure to exclude a diminution of the spot size by self-focusing and the corresponding apparent reduction of the breakdown threshold [Sch01]. To date, hardly any threshold data obtained with such large NAs are available for ultrashort laser-induced breakdown in water. We must conclude that the present experimental data basis is not reliable enough to perform a thorough comparison with theoretical predictions. Future measurements with aberration-free temporally Gaussian laser pulses focused at large NA will have to fill this gap.

In addition, a better adjustment of the numerical breakdown criterion to the experimental criterion of bubble formation is needed to enable a meaningful comparison of experimental data with model predictions. While bubble formation requires an approximately constant energy density within the focal volume for all laser pulse durations and wavelengths, the energy density associated with a fixed value of the free electron density, such as $\rho_{cr} = 10^{21} \text{ cm}^{-3}$, varies considerably with pulse duration. Thus the assumption of a constant free electron density as breakdown criterion is quite arbitrary, especially for cases where the threshold is smooth, i.e. where ρ_{max} increases continuously with irradiance. In these cases it seems more reasonable to relate the critical free electron density to the energy density within the medium that leads to bubble formation. Equation (17) provides the required link between electron and energy density, and an analysis of $\rho_{max} (I/I_{rate})$ curves (Figs 3 and 5) then yields the corresponding threshold irradiance.

The new threshold definition for the numerical model will yield a better match between the experimentally observed and numerically predicted wavelength dependence of breakdown thresholds than the values in table 1. Experimentally, the thresholds for ns- and ps- pulses decrease with decreasing wavelength [Ven02, Vog96a], but values calculated with a constant ρ_{cr} show the opposite trend. Previous calculations revealed a relatively smooth threshold for ns- and ps- breakdown with visible and UV wavelengths, in contrast to the sharp threshold for IR wavelengths shown in Fig. 3c [Vog01]. Calculated threshold values based on the new definition will for IR wavelengths thus be the same as those obtained with $\rho_{cr} = 10^{21} \text{ cm}^{-3}$, but they will be lower for visible and UV wavelengths, in accord with experimental observations.

3.6.4 Cavitation bubble dynamics

Figure 18 shows a 2-D representation of the evolution of the thermoelastic stress wave and of the region in which the kinetic spinodal is surpassed (bubble nucleus) for a peak temperature of 200°C, slightly above the threshold for bubble formation. The subsequent bubble dynamics calculated for cases 1 and 2 described in section 3.6.1 is presented in **figure 19**. It turned out that for a vapor pressure that changes adiabatically with bubble size (case 2 in Fig. 19b) the bubble motion is very similar to the case where the vapor pressure is not taken into account at all and only the negative pressure pulse drives the bubble expansion. **Figure 20** shows the maximum bubble radii for case 1 and case 2 as a function of the maximum temperature achieved in the center of the focal volume, together with the radius of the nucleus, R_0 . Close to threshold, the actual bubble radius will probably resemble case 1 in which the bubble nucleus is assumed to be much smaller than the focal region. For energies well above threshold, the predictions obtained for case 2 become more realistic.

The most prominent feature of the transient bubbles produced close to the threshold of femtosecond optical breakdown is their small size and short lifetime. The bubble radius amounts to only about 200 nm in water, and will be even smaller in a visco-elastic medium such as the cytoplasm. This makes a dissection mechanism associated with bubble formation compatible with intracellular nanosurgery, in contrast to nanosecond optical breakdown where the smallest bubble radius in water observed detected for $NA = 0.9$ was $R_{max} = 45 \mu\text{m}$ [Ven02].

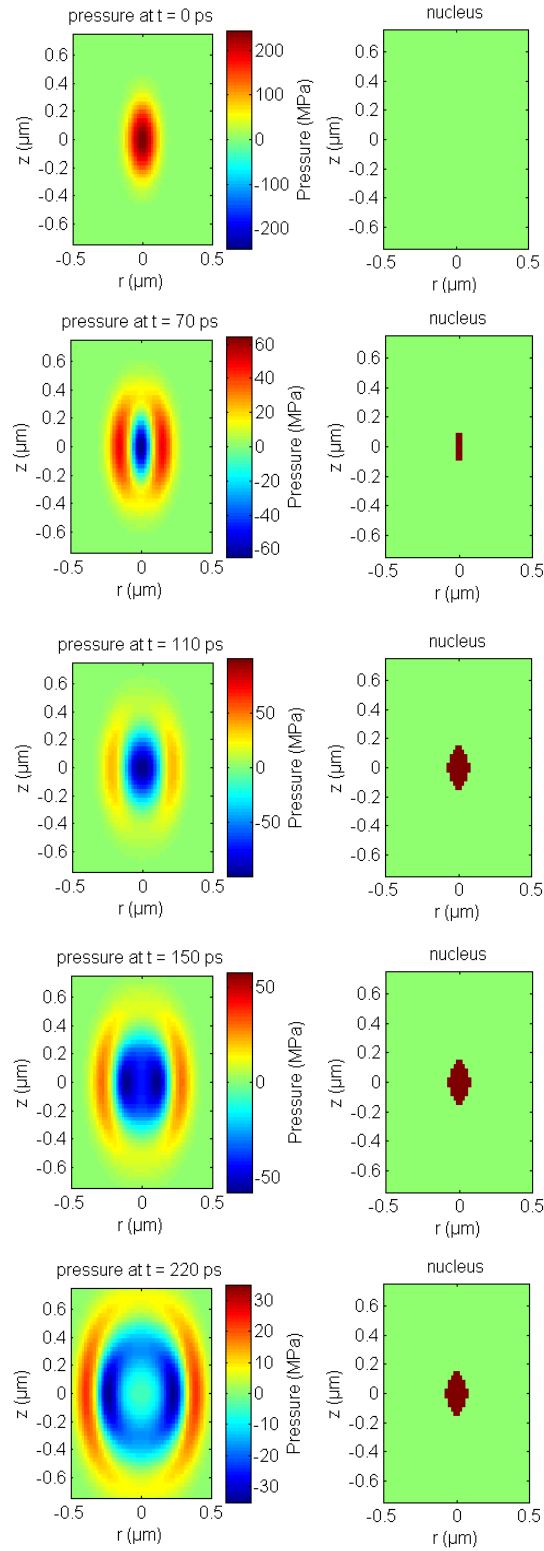


Figure 18: 2-D Plots of thermoelastic stress evolution (left), and of the region in which the kinetic spinodal limit is exceeded (right). This region demarcates the size of the bubble nucleus that is then expanded by the thermoelastic tensile stress wave.

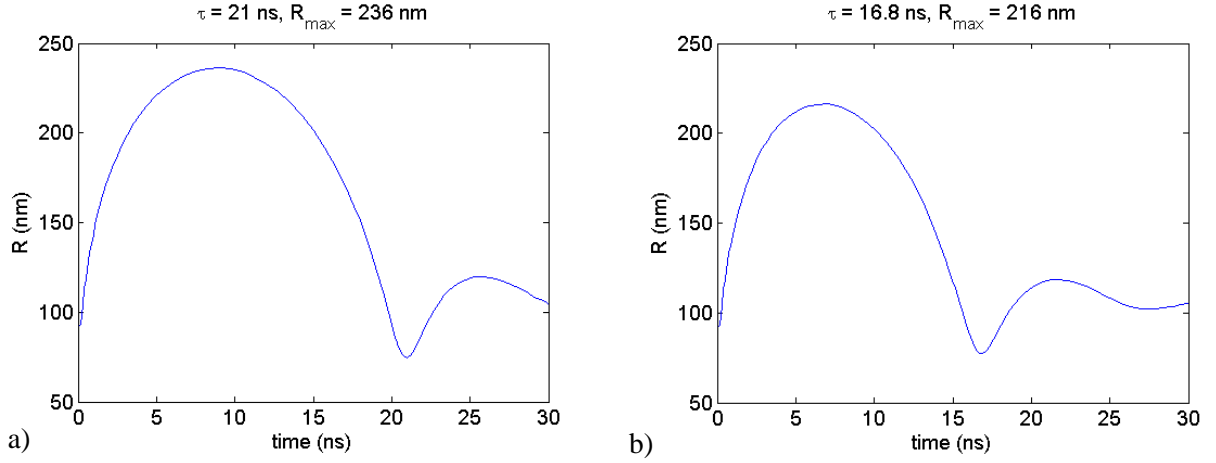


Figure 19: Radius time curve of the cavitation bubble produced by a single femtosecond laser pulse focused at $NA = 1.3$ that leads to a peak temperature rise of $T_{\max} = 200$ °C at the focus center. The radius of the bubble nucleus is $R_0 = 91.1$ nm. The temperature at the wall of the nucleus is $T_{\text{wall}} = 145$ °C, and the mean temperature averaged over all volume elements within the bubble nucleus is $T_{\text{mean}} = 168$ °C. The $R(t)$ curve in a) was calculated under the assumption that the vapor pressure within the bubble is given by mean temperature within nucleus and decays due to heat diffusion (case 1, see text). The curve in b) was calculated assuming that the vapor pressure drops adiabatically during bubble expansion (case 2).

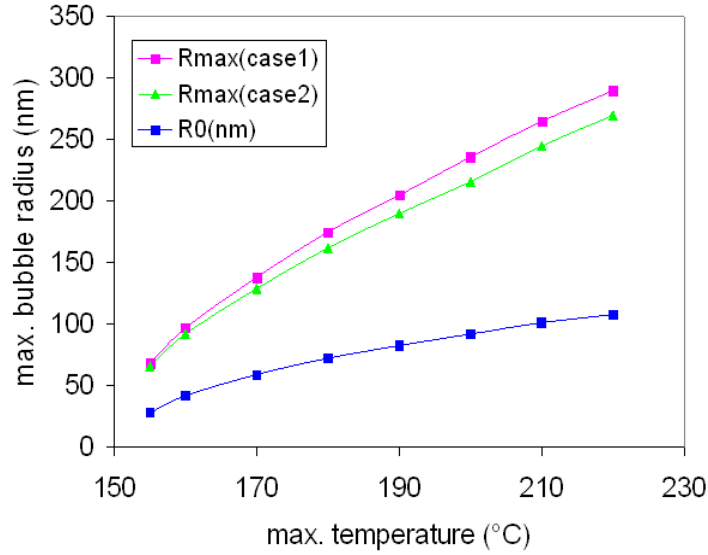


Figure 20: Maximum bubble radii for cases 1 and 2 as a function of the maximum temperature achieved in the center of the focal volume, together with the radius of the nucleus, R_0 . The slight undulations in the curves are numerical artifacts due to the limited size of volume elements representing the nucleus size.

The small bubble size corresponds to a small energy

$$E_B = \frac{4\pi}{3} (p_\infty - p_v) R_{\max}^3 \quad (20)$$

of the expanded bubble. For the case presented in Fig 19a, it amounts to 5.3×10^{-15} J (5.3 femtojoule). The smallness of the bubble energy is partly explained by the small energy content of the stress transient creating the bubble. This energy is equals to the energy stored in thermoelastic compression of the heated fluid volume [Pal03],

$$E_{TE} = \frac{1}{2\rho_0 c_0^2} \int p_0^2 dV, \quad (21)$$

where p_0 is the initial thermoelastic pressure generated under conditions of stress confinement and the integration goes over the entire volume that is heated by the laser pulse. For a temperature rise in the center of the focal volume

of 180°C that leads to a maximum pressure p_0 of 221 MPa, E_{TE} amounts to 7.8×10^{-14} J. For comparison, the total heat content of the plasma is

$$E_{tot} = \rho_0 C_p \int \Delta T dV, \quad (22)$$

giving $E_{tot} = 1.66 \times 10^{-11}$ J under the same conditions. The energetic conversion efficiency from heat into the thermoelastic wave is therefore $E_{TE}/E_{tot} = 0.46\%$, and the conversion efficiency from thermoelastic energy into bubble energy is 6.8%. This result of a low conversion efficiency from absorbed laser energy into mechanical energy for femtosecond pulses is in agreement with experimental results [Vog99b, Noa98a]. By contrast, for nanosecond optical breakdown with NA = 0.9 the conversion efficiency was experimentally found to be 12.7 % for $\lambda = 1064$ nm, and 3.3% for $\lambda = 532$ nm at the breakdown threshold, and it reached values of 53% and 33.5 %, respectively, for energies 10-fold above threshold [Ven02].

Experimental data in the literature on cavitation bubble dynamics

Time-resolved investigations of the effects of transient femtosecond-laser-induced bubbles on cells are not yet available. However, Dayton et. al. investigated the oscillations of 1.5- μm radius bubbles that were phagocytosed by leukocytes and stimulated by a rarefaction-first one-cycle acoustic pulse with 440 ns duration [Day01]. By means of streak photography and high-speed photography with 100 Mill. f/s they observed that phagocytosed bubbles expanded about 20-45% less than free microbubbles in response to a single acoustic pulse of the same intensity. The difference is due to the viscosity of the cytoplasm and the elastic modulus of the cytoskeleton. Bubbles subjected to a tensile stress amplitude of 0.9 MPa would expand to a radius of 6 μm without rupturing the cell membrane. Larger oscillations would cause immediate cell lysis. The viability of the non-lysed cells after insonation was not tested, but it is evident that the bubble oscillations strain the cell membrane and deform or even rupture the cytoskeleton. In the case of femtosecond optical breakdown, the radius of the bubble nucleus is much smaller (≈ 90 nm compared to 1.5 μm), and the tensile stress transient acting on the bubbles is much shorter than in the case investigated by Dayton (≈ 100 ps compared to 220 ns). Therefore, the resulting bubbles cause little structural damage within a cell and do not affect cell viability.

Lin et. al. investigated the thresholds for cell death produced by cavitation induced around absorbing microparticles irradiated by nanosecond laser pulses [Lin99, Les01]. They observed that an energy of 3 nJ absorbed by a single particle of 1 μm diameter produced sufficiently strong cavitation to kill a trabecular meshwork cell after irradiation with a single laser pulse. Pulses with 1 nJ absorbed energy produced lethality after several exposures [Lin99]. Viability was lost even when no morphologic damage was apparent immediately after the collapse of the transient bubble with less than 1 μs life time (according to the Rayleigh equation [Vog96b, Ray17], 1 μs lifetime corresponds to $R_{\text{max}} = 5.5$ μm). Nuclear staining of nonviable cells by ethidium bromide confirmed that cell death was associated with membrane damage. According to Neumann and Brinkmann (2005), a bubble radius of 3 μm within a cell of 7.5 μm radius is sufficient to cause an enlargement of the membrane by 4% that will result in membrane rupture [Nee90]. The results of our calculations in Fig. 20 demonstrate that the radius of fs-laser-produced transient bubbles remains well below this damage threshold. This applies even for laser pulse energies of a few nanojoule because for $\rho_{\text{cr}} = 10^{21} \text{ cm}^{-3}$ and 1 μm plasma length about 99% of the incident energy is transmitted through the focal region [Noa99]. The heated volume is much smaller than the volume of the microparticles investigated by Lin et. al. (1999), and the deposited heat energy corresponding to a peak temperature of $T_{\text{max}} = 200^\circ\text{C}$ or 300°C is only 16.6 or 25.8 pJ, respectively, much less than in Lin's case.

Bubbles around gold nanoparticles are of interest in the context of nanoparticle cell surgery (section 3.1.1). When particles with 4.5 nm radius were irradiated by 400 nm, 50 fs pulses, bubbles of up to 20 nm radius were observed by means of X-ray scattering techniques [Kot05]. The small size of these bubbles which is one order of magnitude less than for those produced by focused femtosecond laser pulses is consistent with the fact that the collective action of a large number of nanoparticles is required to produce the desired surgical effect.

Membrane damage can also be induced by bubble oscillations that occur largely outside of the cell [Lok01] such as in laser-optoporation [Sou00]. Rupture (or at least poration) of the cell membrane requires strains larger than 2-3% [Nee90, Boa02]. Again, no time-resolved investigations of the laser-based procedure are yet available, but cell poration and lysis induced by the dynamics of pressure-wave-excited bubbles has been already studied [Wol02]. These effects are of interest in the context of transient membrane permeabilisation of cells for the transfer of genes or other substances.

So far, we have only discussed the transient bubbles produced by single laser pulses. These bubbles can only be detected by very fast measurement schemes. However, during high-repetition rate pulse series accumulative thermal effects and chemical dissociation of biomolecules come into play (sections 3.3.4 and 3.5.2) that can produce long-lasting bubbles that are easily observable under the microscope [Sup05, Koe02, Rie05]. Dissociation of

biomolecules may provide inhomogeneous nuclei that lower the bubble formation threshold below the superheat limit defined by the kinetic spinodal. Even though thermoelastic forces may still support the bubble growth, it is mainly driven by boiling of cell water and by chemical or thermal decomposition of biomolecules into small volatile fragments. After the end of the fs pulse train, the vapor will rapidly condense but the volatile decomposition products will disappear only by dissolution into the surrounding liquid and thus form a longer-lasting bubble.

Long-lasting ‘residual’ bubbles have also been observed after pulse series of 3.8 kHz repetition rate where, according to our results in section 3.5.2, accumulative thermal effects can be excluded, but they were seen only when fairly large pulse energies of ≥ 180 nJ were applied [Zoh05]. The experiments were performed using a numerical aperture of $NA = 0.6$. Our temperature calculations revealed that, at this NA, the energy required to produce any specific temperature rise is 22.7 times larger than for $NA = 1.3$. Therefore, the thermal and chemical effects of single pulses are sufficiently strong to produce a certain amount of noncondensable gas by disintegration of the biomolecules, and rectified diffusion of dissolved air into the oscillating transient bubbles will further contribute to the formation of residual, long lasting bubbles [Cru84, Lei94, Vog01 Chapter 6].

3.6.5 Experimental determination of the bubble formation threshold and bubble size

Time-resolved investigation of fs laser induced optical breakdown in water at large NA is very challenging. A large numerical aperture (about $NA=0.9$) has to be used to avoid artifacts by nonlinear beam propagation. However, diffraction limited focusing of fs pulses at large NA is associated with breakdown threshold energies of only a few nanojoules. This makes it difficult to detect the transient bubbles indicating the occurrence of optical breakdown because theory (section 3.6.4) predicts that the bubble size is well below the optical resolution limit. Because of this difficulty, we can not apply flash photography for bubble detection but have to resort to light scattering technique. We developed a method in which the bubble size is inferred from the bubble oscillation time that is determined by analysis of light scattering from a cw probe laser beam. To validate this technique, we compared the results obtained for $R_{\max} \geq 1 \mu\text{m}$ with the corresponding photographically determined bubble sizes.

Experimental setup

Femtosecond laser pulses are generated by a Yb:glass laser system IC-1045-30-fs Reg Amp/SHG/THG (High Q Laser Production). This laser system delivers amplified pulses with pulse duration of 315 fs, a center wavelength of $\lambda = 1040$ nm, and 30 μJ pulse energy at 1 kHz repetition rate. Frequency doubling and frequency tripling create laser irradiation with $\lambda = 520$ nm center wavelength and 14 μJ pulse energy, and $\lambda = 348$ nm center wavelength and 1.5 μJ pulse energy, respectively. With a combination of two fast shutters, single pulses can be selected out of the 1 kHz repetition rate signal. The oscillator leakage is suppressed by means of an external pockels cell. Precise energy adjustment is achieved by combinations of $\lambda/2$ plates and thin film polarizers.

The femtosecond pulses are focused into the water cell through a 63x or 40x long-distance UV-VIS-IR water immersion microscope objective that was built into the wall of the cell (**Figure 21**). For the detection of bubbles with sizes below the optical resolution limit a cw probe beam (658 nm, 25 mW) is aligned collinear with the fs-pump beam and delivered through the focusing objective. The transmitted light is collected by a second microscope objective built into the opposite cell wall. Larger bubbles could be photographed through a third microscope objective (20x) oriented perpendicular to the optical axis of the pump and probe beams. When the 40x objective was used to focus the fs-pulses, we could achieve a confocal arrangement with the 20x objective at correct working distance for all objectives. This was not possible with the 63x objective. For illumination of the focal region, we used a Nanolite flash lamp with 18 ns pulse duration. To be able to image very small bubbles near the optical resolution limit, the image formed by the 20x objective and tube lens was further magnified using a Nikkor objective (63mm/1:2.8) corrected for 8x magnification. This way, we achieved a total magnification factor of 162.

We found that for larger bubbles, the optimal signal to noise ratio of the scattering signal is achieved when the beam waist of the probe beam is slightly smaller than the bubble size. This is, of course, not possible to achieve when the bubbles are smaller than the optical resolution limit. Here, the optimum signal to noise ratio is obtained when the waist of the probe laser beam is as small as possible. This was achieved by spatial filtering of the probe laser beam and by expanding it to a diameter much larger than the optical pupil of the microscope objective. This way the probe laser beam exhibited a nearly flat beam profile over the aperture of the focusing microscope objective, resulting in the minimum possible spot size. An adjustable aperture for the probe laser beam behind the collecting objective served to optimize the signal to noise ratio for bubble detection.

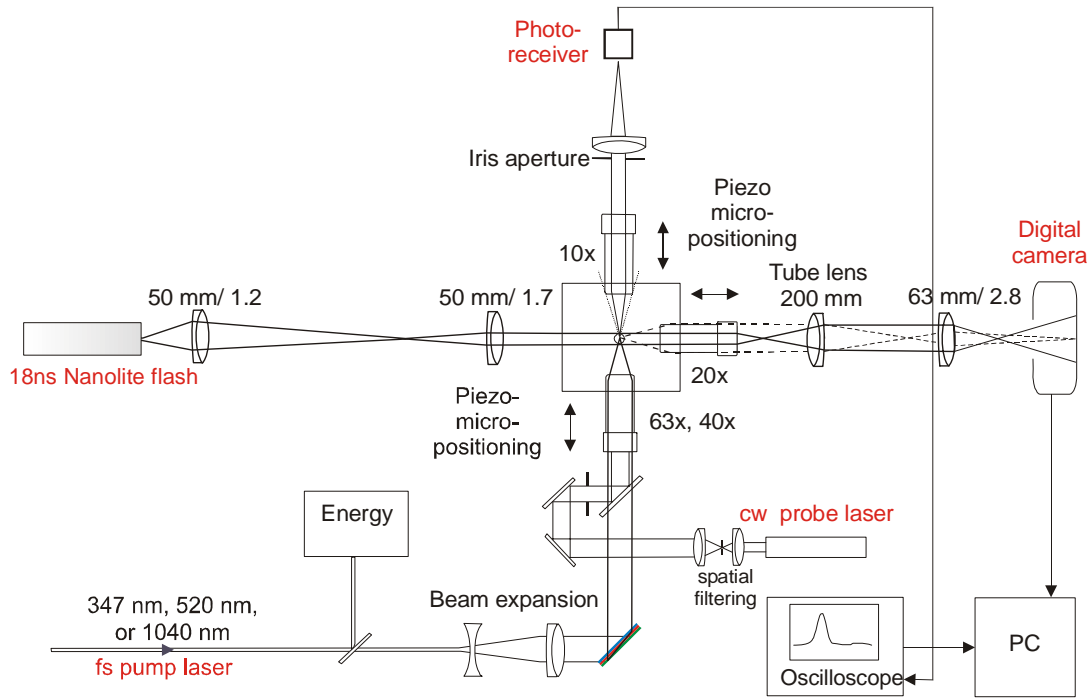


Figure 21: Experimental setup for the time-resolved investigation of bubble formation induced by 315-fs laser pulses. The setup is designed for simultaneous flash photography of the laser induced bubbles in side view and detection of the scattering signal of the probe laser along the optical axis of the pump laser.

The scattering signal is detected by an AC-coupled high speed photoreceiver (FEMTO, HCA-S) with a signal bandwidth from 25 kHz to 200 MHz and an additional monitor output of the DC signal that is important for the basic alignment of the entire setup. When the bubble size is much smaller than the focus of the probe laser beam, the scattering signal is much smaller than the total amount of the light transmitted through the focal volume. AC coupling is very useful to remove this bias. The duration of the scattering signal equals the oscillation time of the bubble in the focal volume.

Determination of bubble size through time-resolved scattering measurements

Figure 22 presents time-resolved signals from bubbles produced by 315-fs laser-induced optical breakdown in water. The 1040-nm fs pump laser pulse and a 658-nm cw laser were focused with the 63x objective (NA:0.9), and the probe laser light was collected with the 10x objective (NA:0.3). An additional aperture with 4 mm diameter behind the 10x objective reduced the effective aperture to an NA of approximately 0.1, corresponding to $\alpha = 4,3^\circ$. We found empirically that the sensitivity of bubble detection is best at this NA. The reason for this finding is not yet completely understood but must be related to the Mie scattering characteristics [Mie08, Ker69] of the bubbles, as discussed in detail in [Linz 2006].

Figure 22 shows that the measured scattering signal from the first bubble oscillation is symmetrical. The entire oscillation time can, therefore, be easily identified for all bubble sizes. For larger pulse energies, one or several rebounds of the oscillating bubble are observed after the first collapse.

How can we calculate the bubble radius from the bubble oscillation time? The simplest calculation is given by the well known Rayleigh formula [Ray17]:

$$R_{\max} = \frac{T_{\text{osc}}}{1.83} \sqrt{\frac{p_{\infty} - p_v}{\rho_0}} \quad (23)$$

where p_v is the vapor pressure inside the bubble (2330 Pa at 20°C). However, the Rayleigh formula was derived without consideration of surface tension, which exerts a pressure $p = 2\sigma/R$ in addition to the hydrostatic pressure. The pressure by surface tension can be neglected for large bubbles but becomes important for bubble radii of a few μm or below. In water at room temperature, the surface tension against air is 0.073 N/m, and the corresponding pressure acting on bubbles of for example 100 nm radius is 1.46 MPa. Since this value is much larger than the hydrostatic pressure of 0.1 MPa, surface tension will considerably alter the relationship between bubble oscillation

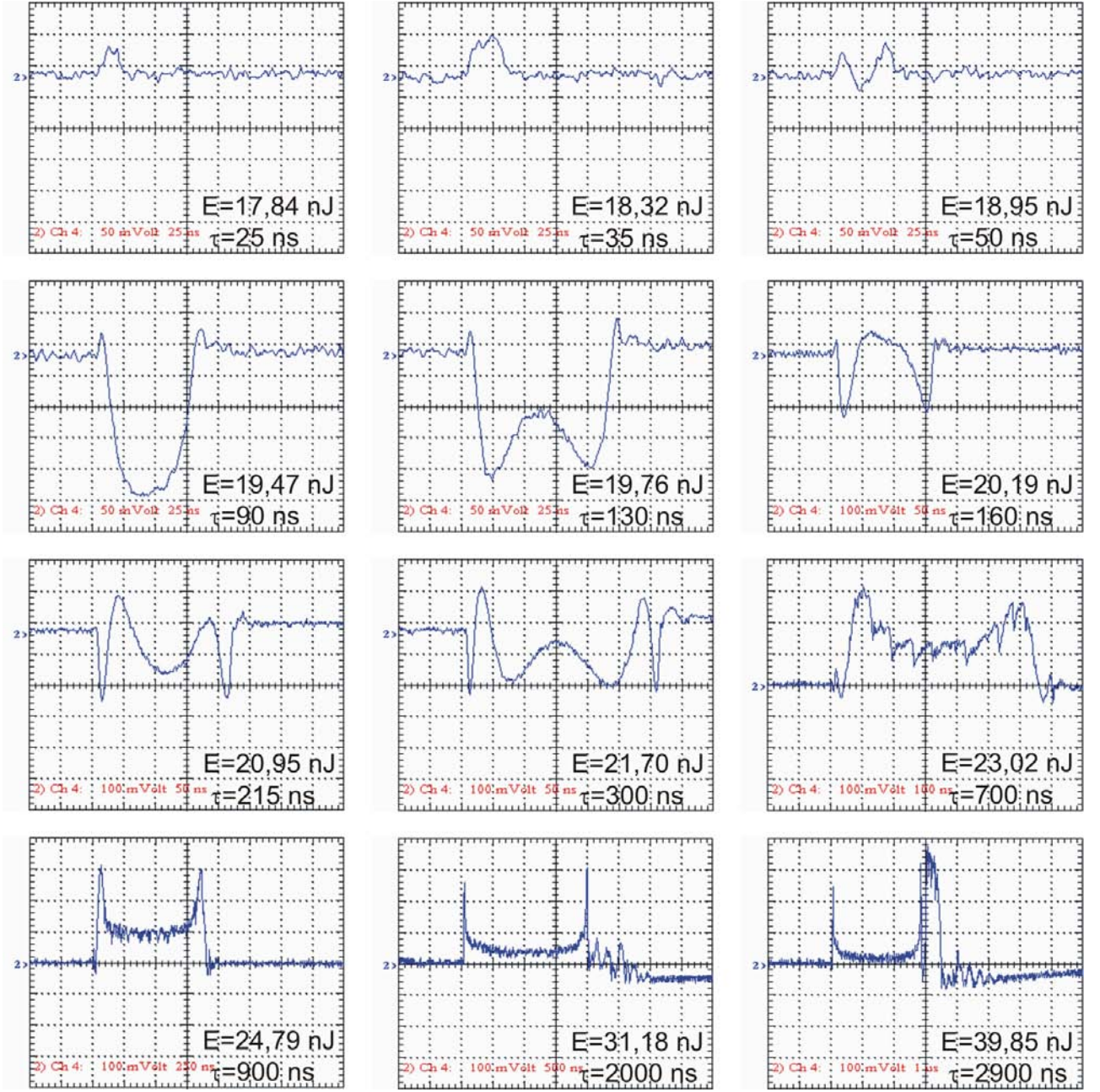


Figure 22: Time-resolved scattering signals of 315-fs laser pulses with 1040 nm wavelength induced bubbles in water. Pump- and probe laser are focused with the 63x objective (NA=0.9) and collected with the 10x objective (effective NA=0.1). The scattering signals provide information about the bubble oscillation time. Both pump laser pulse energy and the corresponding bubble oscillation time are given in each plot.

time and maximum radius. Rough estimates of bubble size and bubble energy considering the surface tension can be obtained by the following approximations:

$$R_{\max\sigma} = \frac{T_{osc}}{1.83} \sqrt{\frac{(p_{\infty} - p_v) + p_{\sigma}(R_{\max})}{\rho_0}} \quad (24)$$

$$E_{B\sigma} = \frac{4}{3} \pi [(p_{\infty} - p_v) + p_{\sigma}(R_{\max\sigma})] R_{\max\sigma}^3 \quad (25)$$

Here, $R_{\max\sigma}$ must be determined in an iterative fashion, starting with the p_σ -value based on R_{\max} obtained with the Rayleigh equation (23). The correct R_{\max} -value is then again inserted into equation (24) and after a few iterations of this kind, the found $R_{\max\sigma}$ value is obtained.

Equation (24) is a simplification since it neglects the temperature dependence of surface tension that is important because the focal volume is heated during optical breakdown. Moreover, the pressure exerted by surface tension is not constant as suggested by the term $p_\sigma(R_{\max})$ but is a function of time: $p_\sigma[R_{\max}(t)]$. Note that the errors made by both simplifications will partly compensate each other because the first simplification leads to an overestimation of p_σ (σ decreases with increasing temperature), and the second simplification results in an underestimation of p_σ (it is larger than $p_\sigma(R_{\max})$ during bubble growth and collapse). Therefore, equations (24) and (25) are useful as zero-order approximations for a determination of $R_{\max\sigma}$ and $E_{B\sigma}$ under consideration of surface tension.

To increase the precision of the determination of R_{\max} , we established a refined method based on the model of bubble formation described above in section 3.6.1 and the Gilmore model of bubble dynamics already used in those calculations. Unlike the Rayleigh model, the Gilmore model takes the surface tension, viscosity and compressibility of the liquid into account. **Figure 23a)** shows the relationship between maximum bubble radius and oscillation time for the full model calculations (case 1 and case 2, such as in section 3.6.1 and 3.6.4), the Gilmore model with constant σ , and the Rayleigh model. The bubble size in the Gilmore model was varied by using increasingly large equilibrium radii R_n with constant initial radius R_0 . This leads to bubble oscillations with increasing amplitude. It turns out, that the Gilmore model yields a good approximation to the $R_{\max} = f(T_{\text{osc}})$ relation obtained by our full numerical model, whereas the Rayleigh model leads to a marked underestimation of the bubble sizes, especially for short oscillation times. **Figure 23b)** shows that the discrepancy between Gilmore and Rayleigh modeling becomes smaller with increasing bubble size and is negligible for bubble oscillation times $\geq 7\mu\text{s}$, corresponding to bubble radii $\geq 35\mu\text{m}$.

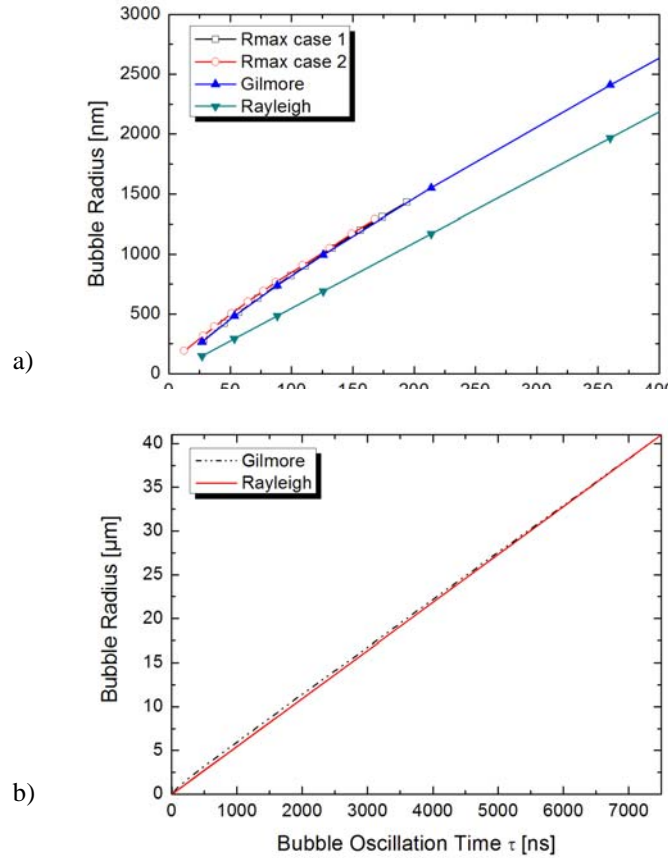


Figure 23: (a) Relationship between bubble oscillation time and maximum bubble radius predicted by our full model of thermoelastic bubble generation (case 1 and case 2) [Vog05], the Gilmore model of cavitation bubble dynamics [Gil52, Kna71, Pal96], and the Rayleigh equation (equation (7)). (b) Comparison between Gilmore and Rayleigh modeling for oscillation times up to $7\mu\text{s}$ and bubble radii up to $40\mu\text{m}$. The discrepancy due to the neglect of surface tension in the Rayleigh equation diminishes with increasing bubble size.

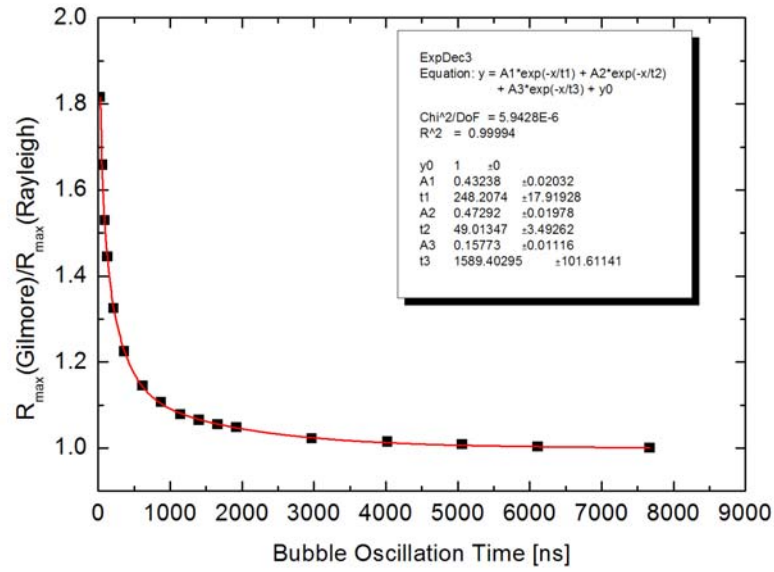


Figure 24: Ratio of the maximum bubble radius calculated with the Gilmore model to the maximum bubble radius calculated with the Rayleigh model for different bubble oscillation times. An analytic function was plotted to these values. This allows us, to calculate the maximum bubble radius of the Gilmore model by use of the simple Rayleigh model in combination with the correction factor for specific oscillation times. As expected from figure 14, the correction factor for bubble oscillation times $\geq 7\mu s$ is 1 and increases with decreasing bubble oscillation time. For $T_{osc} \rightarrow 0$, the correction factor converges against 2.063. Therefore, the Gilmore model predicts bubbles that are maximal 2 times larger than expected with the Rayleigh model.

For practical purposes, we simplify the determination of R_{max} from T_{osc} by using the Rayleigh equation (23) together with a correction factor $R_{Gilmore} / R_{Rayleigh}$ that is plotted in **figure 24**. The correction factor can be approximated by the analytical equation:

$$f(T_{osc}) = 0,43238 * e^{\frac{-T_{osc}}{248,2074}} + 0,47292 * e^{\frac{-T_{osc}}{49,01347}} + 0,15773 * e^{\frac{-T_{osc}}{1589,40295}} + 1. \quad (26)$$

To verify our measurement, we compared the results obtained with the time-resolved light scattering technique to the results obtained by flash photography, as described in [Linz 2006]. We generally found a very good agreement between the results of both measurement techniques. However, for very small bubbles, the bubble radii determined by means of the Gilmore model agree better with the photographic results than the values calculated using the Rayleigh equation that neglects surface tension.

3.6.6 Comparison between experimentally determined and calculated bubble size

Theoretical predictions on laser-induced bubble radii obtained by the model described in section 3.6.1 and experimental results obtained by the technique described in section 3.6.5 are compared in figure 26 for fs pulses of 1040 nm wavelength focused at NA = 0.8. For comparison with the experimental data, we identify the measured irradiance threshold I_{th} with the calculated temperature threshold for bubble formation, $T_{th} = 167.9^\circ C$. Since a room temperature of $20^\circ C$ was assumed for all calculations, T_{th} corresponds to a temperature rise $\Delta T_{th} = T_{th} - 20^\circ C = 147.9^\circ C$. Using the equations $\varepsilon = \Delta T \rho_0 C_p$ and $\rho_{th} = \varepsilon / (9/4) \tilde{\Delta}$ from section 3.5.1, we calculate the corresponding value for the threshold free electron density ρ_{th} . Here ε denotes the plasma energy density, ρ_0 the mass density of the medium, C_p the heat capacity and $\tilde{\Delta}$ the ionization potential of the medium ($\tilde{\Delta} = 6.78$ eV for laser pulses with $\lambda = 1040$ nm, $\tau = 315$ fs, focused through an objective with NA = 0.8). The threshold free electron density amounts to $\rho_{th} = 2.54 \cdot 10^{20} \text{ cm}^{-3}$. Using the $\rho = \rho(I/I_{th})$ – curve of figure 5, we obtain from ρ_{th} a reference point for the experimental irradiance threshold for bubble formation. From this starting point, we can by means of the $\rho(I/I_{th})$ curve and the above equations translate the experimental irradiance values into temperature values. This enables us to plot the comparison between measured bubble radii and numerical predictions shown in **figure 26**.

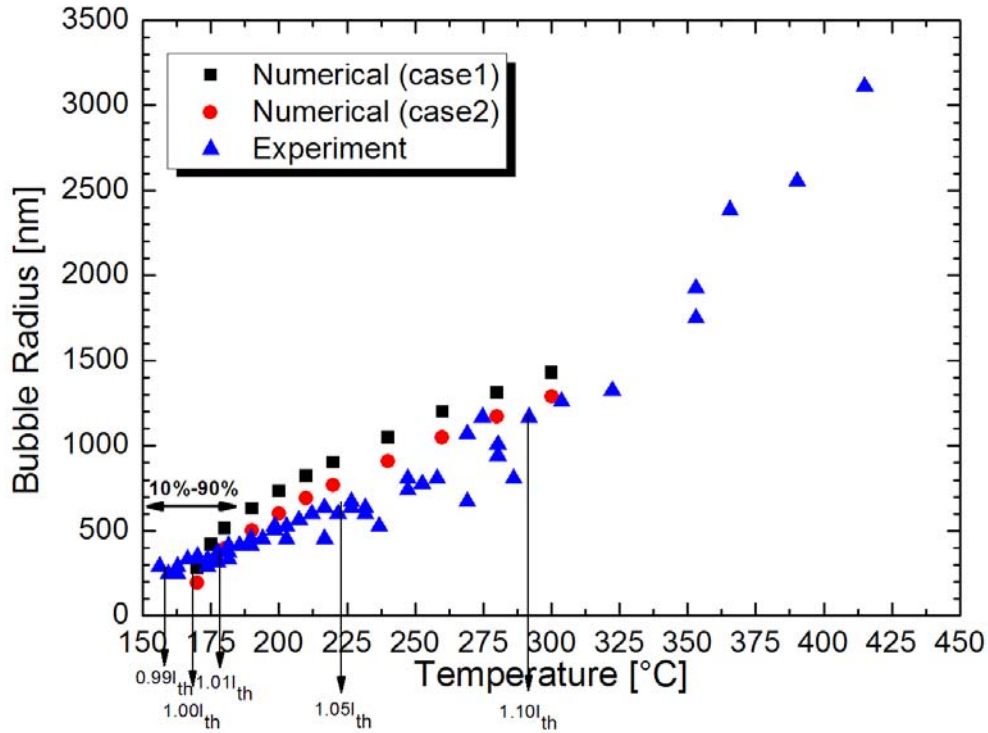


Figure 26: Comparison of model predictions for fs-laser-induced bubble formation [Vog05] with experimental results. All data refer to breakdown in water produced by 315-fs, 1040-nm pulses focused at $NA = 0.8$. Cases 1 and 2 stand for isothermal and adiabatic conditions of the bubble content with respect to the surrounding liquid. To indicate the width of the experimental threshold region, the energy range from 10 % to 90 % breakdown probability is marked by arrows.

We obtain an excellent agreement between predicted and measured bubble radii at the bubble formation threshold (190-280 nm for case 1 and case 2, respectively, compared to measured values of ≈ 300 nm). With increasing temperature, the theoretically predicted values grow, at first, slightly faster than the measured values. This may be due to two reasons: First, the model neglects the clipping of the tensile stress amplitude upon rupture of the liquid. Secondly, the Gilmore model used to calculate the bubble dynamics assumes a radially symmetric stress distribution around the spherical bubble. The time evolution of this stress distribution is identified with the $p(t)$ curve in the focus center. The actual stress distribution is non-isotropic, with larger stress amplitudes in radial direction than in axial direction (Fig. 14). Both theoretical assumptions lead to an overestimation of the maximum bubble size. However, the general agreement between calculated and measured data is very good, confirming our theory of thermoelastic bubble formation for energy values close to the breakdown threshold.

Interestingly, a steep increase of the bubble size is observed for temperature values larger than about 300 °C. This coincides with the spinodal limit at ambient pressure [Vog03]. For $T > 300$ °C, no tensile stress is required to induce a phase transition in pure water, and bubble formation will progress as explosive vaporization supported by the thermoelastic stresses. It has been found previously, that this regime is much more efficient for stress-confined surface ablation than the “spallation” regime at lower temperatures [Pal03, Vog03]. Thus, it is not surprising to obtain similar results for stress-confined optical breakdown. Bubble formation for temperatures above 300 °C is further addressed in the next section (section 4) of this report.

4 FEMTOSECOND BREAKDOWN IN THE HIGH DENSITY PLASMA REGIME

4.1 CAVITATION BUBBLE RADIUS AND CONVERSION OF LASER ENERGY INTO BUBBLE ENERGY

The size of the laser-produced cavitation bubbles is a good measure for the precision achievable in laser surgery and for the possible extent of collateral effects. Moreover, the conversion efficiency of laser energy into bubble energy is linked to the plasma energy density which allows to draw conclusion on the free electron density and temperature within the plasma. Therefore, we investigated the cavitation bubble size in an energy range from the bubble formation threshold to about 7x threshold.

Bubble radii produced by laser pulses of all investigated wavelengths focused through the 63x, NA=0.9 objective are presented in figure 27 a), and an enlarged view of the energy range very close to the breakdown threshold is shown in figure 27 b). In the enlarged view, the radii are plotted as a function of the dimensionless pulse energy $\beta = E/E_{th}$ to facilitate the comparison of the effects arising from different laser wavelengths.

While figure 27 b) portrays the variation of individual bubble sizes, an average over many measurements is required to identify the dependence of the bubble size at threshold on NA and wavelength. Measurement data averaged over the energy range from 10 % to 90 % breakdown probability are summarized in table 2.

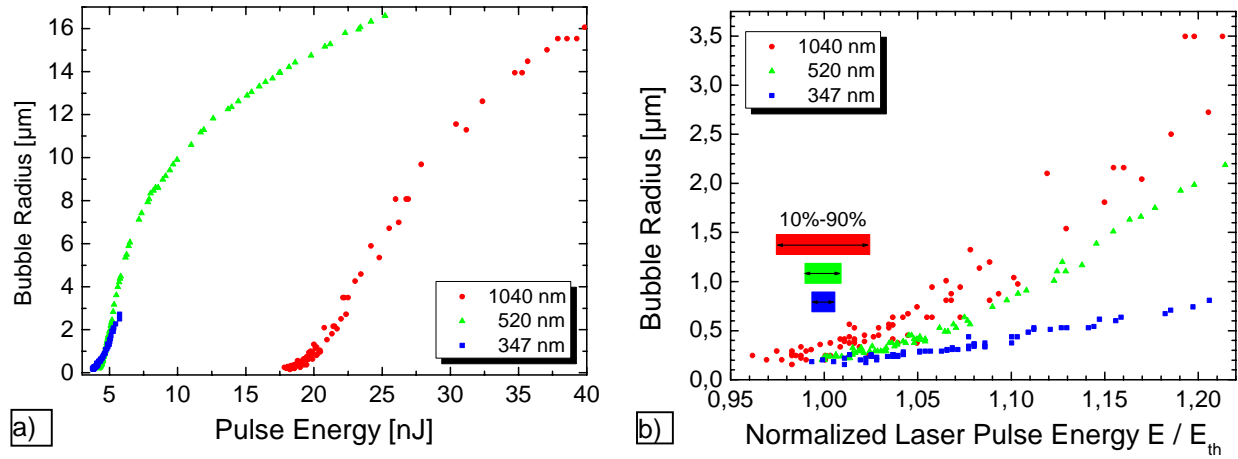


Figure 27: a) Bubble radius as a function of pulse energy for 315-fs laser pulses of 1040 nm, 520 nm, and 347 nm wavelength focused into water through the 63x (NA=0.9) microscope objective. b) Enlarged view from a) of the energy range very close to the breakdown threshold. The actual pulse energy is normalized by the threshold energy, yielding a dimensionless energy value $\beta = E/E_{th}$. The bars indicate the width of the energy range between 10 % and 90 % breakdown probability.

focusing objective	Bubble Radius $R_{B E10-E90}$ [nm]					
	$\lambda = 1040$ nm		$\lambda = 520$ nm		$\lambda = 355$ nm	
	Bubble radius [nm]	Diffr. limited spot radius [nm]	Bubble radius [nm]	Diffr. limited spot radius [nm]	Bubble radius [nm]	Diffr. limited spot radius [nm]
40x (NA=0.8)	328 ± 44	793	288 ± 28	397	216 ± 17	264
63x (NA=0.9)	322 ± 96	705	232 ± 17	353	190 ± 9	235

Table 2: Average values of the bubble radii at breakdown threshold for various wavelengths and NA. The measurement data were averaged over the energy range from 10 % to 90 % breakdown probability. For comparison, the diffraction limited spot radii $r = 0.61 \cdot \lambda / NA$ are also presented.

Close to the breakdown threshold, the laser-produced bubbles are in the nanometer range and considerably smaller than the diffraction limited spot size. However, the bubble radius increases quite rapidly with laser pulse energy, and for pulse energies twice the breakdown energy, it is already in the order of the size of a biological cell. The energy range between 10% and 90% breakdown probability is smallest for UV pulses, i.e. the threshold is here very well defined. Moreover, the increase of bubble size is also slowest for UV wavelengths, consistent with the comparatively weak dependence of free electron density on irradiance that is predicted by our rate equation model (see Fig. 5). Even for energies 20% larger than the bubble formation threshold, the maximum bubble radius is still as small as 700 nm, which is well compatible with cellular nanosurgery. By contrast, bubbles produced using IR laser pulses with energies 20% above threshold already have a radius of 3.5 μm .

While the cavitation bubble size is a good measure for the possible precision of the laser effects, the conversion efficiency of laser energy into bubble energy presented in figure 28 provides information about the underlying physical mechanisms and phase transitions. The principle picture is similar as for the dependence of bubble radius

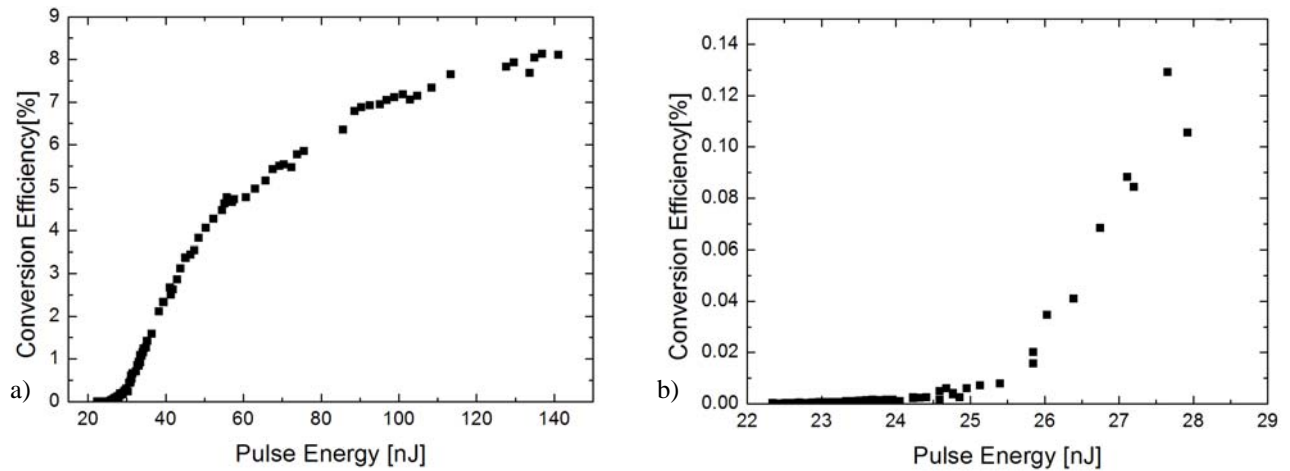


Figure 28: Conversion efficiency of laser pulse energy into bubble energy for 315-fs laser pulses with a wavelength of 1040 nm focused with the 40x Leica water immersion objective (NA=0.8). a) Energy interval up to 6 times breakdown threshold energy $E_{\text{th}}=22.65$ nJ. b) Energy interval close to the threshold energy.

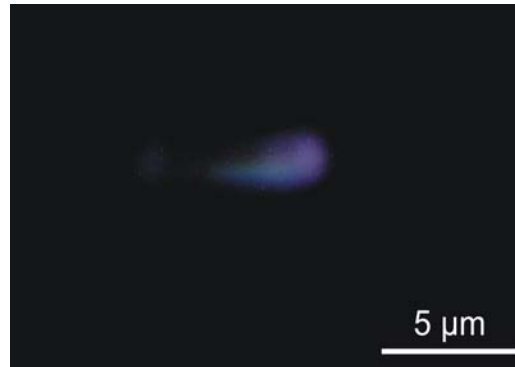
on laser pulse energy (figure 27), but due to the proportionality $E_B \sim R_B^3$ the separation into two interaction regimes becomes even more obvious. Close to the breakdown threshold, the conversion efficiency is extremely small, ranging from 0.0002 % up to about 0.01 %. In this regime, bubble formation relies mainly on thermoelastic tensile stress as describe in detail in section 3. For $E/E_{\text{th}} \geq 1.1$, the conversion efficiency increases rapidly until it eventually converges towards a limit of about 10 % for large pulse energies. Here, tensile stress is not any more required to rupture the liquid but the temperatures in the focal volume are sufficiently high to induce explosive vaporization.

The steep rise of energy density with increasing irradiance explains, in turn, why the threshold for cavitation in water presented in this study are so close to the threshold for void formation in glass [Sch01]. Since the large conversion efficiency into bubble energy indicates a well localized energy deposition. This feature is very important for corneal intrastromal refractive surgery, fs-laser mediated cutting of flaps for excimer laser refractive surgery, and the creation of photonic structures in glass. It cannot be achieved with lower NA where plasma formation is more strongly influenced by nonlinear beam propagation and by shielding effects. Our investigational techniques (flash photography combined with determination of the maximum bubble size through measurement of its oscillation time as well as the Schlieren techniques described in section 5) are well suited to investigate the borders (minimum NA) of the regime of localized energy deposition and the transition to filamentation.

4.2 LUMINESCENT FEMTOSECOND PLASMAS WITH LARGE ENERGY DENSITY

A large conversion efficiency of optical energy into mechanical energy correlates with large energy densities and temperatures in the focal region. Figure 29 shows that plasma luminescence can be detected when 1040-nm fs laser pulses with energies of approximately 165 nJ (7 time above the breakdown threshold) are focused into water at a numerical aperture of 0.8. This finding is very remarkable because plasma luminescence has never been observed when fs pulses were focused at smaller numerical apertures ($NA \leq 0.3$) and beam propagation was strongly influenced by nonlinear beam propagation and shielding effects.

Figure 29: Plasma luminescence after deposition of 1040-nm fs laser pulses with energies of approximately 165nJ, corresponding to 7x breakdown threshold energy focused with the 40x objective. The picture is integrated over more than 150 laser pulses.



We observed a plasma luminescence only at large pulse energies ($E = 165$ nJ, $\beta = 7$) and after integration over more than 150 laser pulses, even though the light emitted by the plasma was collected with a numerical aperture of $NA = 0.5$. Since the emission is too weak for a spectral analysis to be performed, we are not yet sure whether it is blackbody radiation or some kind of recombination radiation. We can exclude direct recombination radiation with photon energy of approximately 6.5 eV because such radiation would be immediately reabsorbed. However, in water, recombination is usually not a one-step process but consists in hydration of a free electron within about 300 fs and subsequent decay of the hydrated state that has an average lifetime of approximately 300 ns [Nik83]. Recombination radiation emitted during the decay of the hydrated state has a larger wavelength that may be able to leave the water cell. However, it seems unlikely that it is bright enough to be detected by the CCD chip of the digital camera. Moreover, if it could be detected, it should also be observable at smaller NAs, in contrast to previous experimental findings. A specific feature of the focusing at large NA, for which plasma luminescence was now first observed, is the highly localized energy deposition, leading to a highly compact plasma shape (the luminescent plasma in figure 24 is only 4 μm long and 2 μm wide) The combination of compact plasma shape and large conversion efficiency into bubble energy suggests that the plasma energy density at large pulse energies must be fairly high. Therefore, it seems likely, that the radiation presented in figure 24 is blackbody radiation.

In fs breakdown, a large plasma energy density must be associated with a large free electron density because only one “set” of free electrons is produced the energy of which is thermalized during a few ps after the end of the pulse. By contrast, in ns breakdown a dynamic equilibrium between free electron generation and recombination evolves during the laser pulse which results in a given energy density at much lower values of free electron density and temperature. In fs breakdown, the temperatures of several thousand Kelvin required to produce visible plasma radiation can only be achieved with free electron densities of approximately 10^{22} cm^{-3} (A free electron density of $1.0 \cdot 10^{22} \text{ cm}^{-3}$ corresponds to a temperature of 6000 K for 1040 nm and $NA=0.8$, assuming a constant value of the heat capacity C_p). This is a very interesting finding because some researchers state that above the critical density for which the plasma frequency exceeds the light frequency, the plasma becomes 100% reflecting and further coupling into the plasma is completely impaired [Fei04]. For $\lambda = 1040$ nm, the critical free electron density amounts to approximately $1.0 \cdot 10^{21} \text{ cm}^{-3}$. Our results, even though still preliminary, indicate that the free electron density produced in the bulk of transparent dielectrics, can be at least one order of magnitude larger. This conjecture is also supported by the fact that hardly any plasma luminescence is observed behind the laser beam waist. Most of the incoming laser light must thus be absorbed within the length of the luminescent plasma which is $< 5 \mu\text{m}$. The corresponding large absorption coefficient through inverse bremsstrahlung absorption requires a large free-electron density. Possible explanations of the phenomenon of efficient laser plasma coupling at free electron densities exceeding the critical density have previously already been discussed in the context of laser fusion and plasma formation at material surfaces [God72, 79, 95].

Thus, fs optical breakdown phenomena in bulk media at large NA span a large range: from nanocavitation induced by a temperature rise of less than 200 °C for energies at the bubble formation threshold to laser plasma coupling features similar to those in laser fusion when energies well above the breakdown threshold are employed.

4.3 FUTURE EXPERIMENTAL WORK AND MODELING

Modeling of the bubble formation for temperatures above 300 °C requires a different approach from that appropriate close to threshold that was presented in section 3. When the amount of deposited energy and the plasma size are known, the subsequent hydrodynamic development can be modeled by hydrodynamic codes based on tabulated equation-of-state data. This has previously demonstrated on ps optical breakdown using the MESA code developed

at Los Alamos National Laboratories and measurement data from our laboratory [Cha97]. However, such calculations mostly require mainframe computers and are not easy to implement on a PC, and the codes are not easily accessible.

We intend to measure plasma transmission T and reflection R for energies well above threshold in a follow-up project to the present project. The corresponding values of the plasma volume will be determined from photographs of the plasma luminescence. From plasma absorption $A = 1 - T - R$ and plasma volume V we will then determine the energy density $\varepsilon = E_{\text{abs}} / V$. Knowledge of ε , the equation of state of water, and the Grüneisen coefficient may then allow to assess the temperature T after equilibration of electron and ion temperatures and the resulting thermoelastic pressure even on a PC when the plasma is assumed to be spherical. In a second step, the measured data on plasma volume (= initial cavitation bubble volume) and maximum bubble radius R_{max} will be implemented into the Gilmore model of cavitation bubble dynamics and used to calculate the initial plasma pressure averaged over the period of stress confinement and the time after relaxation of the thermoelastic stress. Comparison of both results will yield a picture of the stress evolution in the immediate plasma vicinity that is hard to obtain experimentally. We expect a scenario in which, owing to stress confinement, the initial peak pressure of the thermoelastic transients is much larger than the shock wave pressure arising from ns breakdown. However, because of the sub-nanosecond duration of the thermoelastic transients (Fig. 15), the ultrashort transients will be rapidly damped, and the dissipated energy will contribute to the emission of ‘normal’ shock waves similar to those arising from ns breakdown. Hence, the possible effects of the large thermoelastic pressure values will probably be confined to the immediate vicinity of the plasma and have no effect at larger distances. As a consequence, they will be hard to detect in liquid media but may be relevant for the formation of nanocavities or fractures in fs laser processing of glass or quartz with tightly focused pulses.

5 TIME-RESOLVED IMAGING OF FEMTOSECOND BREAKDOWN

5.1. SCHLIERN TECHNIQUES FOR THE VISUALIZATION OF LOW-DENSITY PLASMAS

Schlieren techniques serve to visualize phase objects by transforming phase gradients or phase shifts into intensity variations in the image [Set01, Lau03]. The phase changes result from refractive index variations in the object plane that, in turn, relate to variations of pressure, temperature, or free-electron density. Schlieren techniques are thus well suited to investigate changes of these parameters in fs-laser induced low-density plasmas and stress waves. The experiments described in this section served to identify the optimum technique.

Figure 31 shows a schematic drawing of an optical setup suitable for Schlieren photography. The illumination part in a setup for Schlieren photography consisting of collimator and condensor usually resembles the Köhler microscope illumination that yields a bright and homogeneous light distribution in the object plane. An aperture located in the front focal plane of the condensor produces a well-defined light source with sharp edges that can be exactly matched by an appropriate Schlieren filter in the back focal plane of L_1 . The phase object is imaged into the observation plane either by one lens or, as shown in Fig. 30, by a combination of two lenses L_1 and L_2 . The back focal plane of L_1 (Fourier plane) contains the spatial frequency spectrum of the phase object and, at the same time, the image of the illuminating light source. Depending of the Schlieren technique used, a filter in the Fourier plane blocks the image of the light source either partially or completely. This way, phase information in the object plane is transformed into intensity information in the image plane [Set01, Lau03]. In each Schlieren technique, the shape of the light source in the front focal plane of the condensor, which is conjugate to the Fourier plane, must match the shape of the filter. Pairs of light sources and filters used in various Schlieren techniques are also shown in Fig. 30.

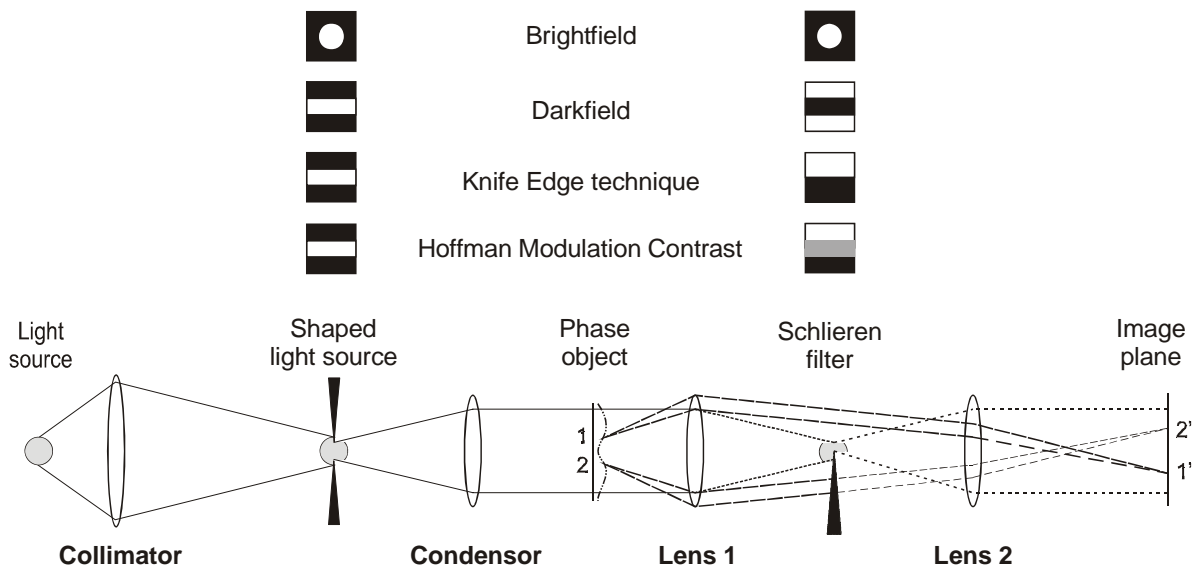


Figure 30: Setup for Schlieren photography, exemplified on Toepler's knife-edge technique.

Figure 30 illustrates the principle of Schlieren filtering on the example of the classical knife-edge technique. The knife edge blocks more than half of the image of the light source, producing a grey background in the observation plane. Light from point 1 of the phase object is deflected upwards, passes the knife edge and produces a bright spot 1' in the observation plane. Light from point 2 of the phase object is deflected downwards and blocked by the knife edge, leaving point 2' of the observation plane darker than the background illumination. The brightness of each point in the observation plane depends on the deflection angle at the corresponding point of the object plane (i.e. on the local phase gradient). The brightness thus depends both on the direction and the steepness of the phase gradient. The use of an extended light source allows for a certain measurement range in which the intensity variation in the object plane is proportional to the phase gradient. For very large gradients, the intensity reaches a saturation level. For a horizontal knife edge, the vertical size of the light source image in the Fourier plane relative to the size of the spatial frequency spectrum determines both measurement range and sensitivity. A large light source corresponds to a large measurement range and low sensitivity, and a small source vice versa.

Laser light sources are usually point-like due to the small divergence of the laser radiation. The filter matched to a laser light source will thus be very small and cover only a small part of the spatial frequency spectrum. Therefore, they are not well suited for Schlieren imaging when a large measurements range is desired because a

small deflection will already produce maximum brightness or darkness (i.e. saturation) in the observation plane. By contrast, incoherent light sources mostly have a finite size, and their use additionally avoids a distortion of the image by laser speckles. However, in cases where maximum sensitivity is more important than a large measurement range, laser light sources combined with appropriate small Schlieren filters are the best choice. If only laser sources are available for illumination (for example in applications where the pulse duration of incoherent sources is too long or their brightness too low), graded filters can improve the performance of the knife-edge technique and allow for a larger measurement range ([Set01], section 5.1.1, p. 112-114, and section B.3, p. 345-347).

We investigated the performance of all Schlieren techniques presented in Fig. 30. In the bright field technique, the aperture of imaging lens L_1 serves as Schlieren filter. High sensitivity requires a small numerical aperture of the imaging system and, because of diffraction effects, it is coupled with poor resolution in the Schlieren image. The classical knife-edge technique has been described above. Hoffman modulation contrast (HMC) [Hof75] is a modification of the knife-edge method that allows to produce a grey background for the intensity modulations portraying phase gradients in the object without completely blocking a part of the light source. Instead, the entire image of the light source is covered by a grey filter with 15% transmission. The advantage is that a much larger part of the spatial frequency spectrum is transmitted than with the knife-edge technique at equal sensitivity. As a result, the optical resolution is better with HMC because more diffraction orders contribute to the filtered image. The dark field technique has a similar advantage because all higher diffraction orders can pass the Schlieren filter. However, since the filter is symmetric, the Schlieren image contains no information about the direction of the phase gradients. Phase contrast and differential interference contrast (Nomarski) techniques were not included in our experimental comparison because they are difficult to realize on an optical bench and are thus not well suited to be integrated into the setup of Fig. 30.

For the bright field, knife-edge, and HMC techniques, we used a plasma spark from an electric discharge as extended, incoherent light source (Nanolite K-L, High-speed photo systems, Wedel, Germany). The duration of this spark is 18 ns and thus too long to image the short-lived low-density plasmas produced by femtosecond laser pulses with sufficient contrast. Therefore, we will later use femtosecond-laser-produced continuum generation to illuminate the Schlieren photographs (see Fig. 30). For the dark-field setup we used a frequency-doubled Nd:YAG laser as light source to achieve maximum sensitivity in the visualization of phase objects. To achieve speckle-free illumination, the laser light was coupled into a 300 m long multimode optical fiber with a 160 μm core diameter. Since the path length differences among the various fiber modes are larger than the coherence length of the laser pulse, no interference phenomena are observed at the fiber end. The duration of the illumination pulse at the end of the fiber is 20 ns. Maximum sensitivity is achieved when the Schlieren filter is very small compared to the size of the spatial frequency spectrum. Therefore, we imaged the fiber tip onto a small slit aperture and used a thin wire as Schlieren filter.

We used the example of an ablation plume produced by Q-switched Er:YAG laser ablation of water to compare the performance of the various Schlieren techniques. The images were recorded by means of a high-resolution digital camera (Nikon D 100). The results are shown in Figure 31, and advantages and disadvantages of the various techniques are summarized in Table 3. The optical resolution of the bright-field image in Fig. 31a is good because of the large aperture used for imaging, but the sensitivity is poor. The dark field image in Fig. 31b exhibits a very high sensitivity, but it is not easy to identify the physical structures in this image. Leading edge and trailing edge of a shock wave both appear as bright lines separated by a black line originating from the pressure peak of the shock wave where no light deflection occurs. Thus one might interpret the leading and trailing edge of the shock waves as separate entities instead as parts of one physical structure. This problem does not arise with the knife-edge technique and HMC. The knife-edge technique has a good sensitivity but produces images with poor resolution (Fig. 31c). The optical resolution is much better with HMC (Fig. 31d) because more diffraction orders contribute to the filtered image.

To increase the sensitivity of HMC without sacrificing dynamic range or resolution, we introduced a modification of the Hoffman technique [Vog06]. Now, the grey part covers only 87 % of the image of the light source leaving 13% free, and the border of the grey part acts as knife edge. With this combination of Hoffman modulation contrast and knife-edge technique, the fractions of light transmitted through the grey filter and passing it contribute exactly equally to the background intensity in the filtered image (15% transmission through the grey filter covering 87% of the relevant area corresponds to 13% of the incident light, the same percentage as transmitted through the uncovered region). The knife-edge part of the combined technique is very sensitive because the uncovered part of the light source image is narrow. Small deflections shifting the image of the light source by only $\approx 1/7$ part of the width of the grey filter suffice to double the intensity in the filtered image or to reduce it by 50%. Light modulation by the grey

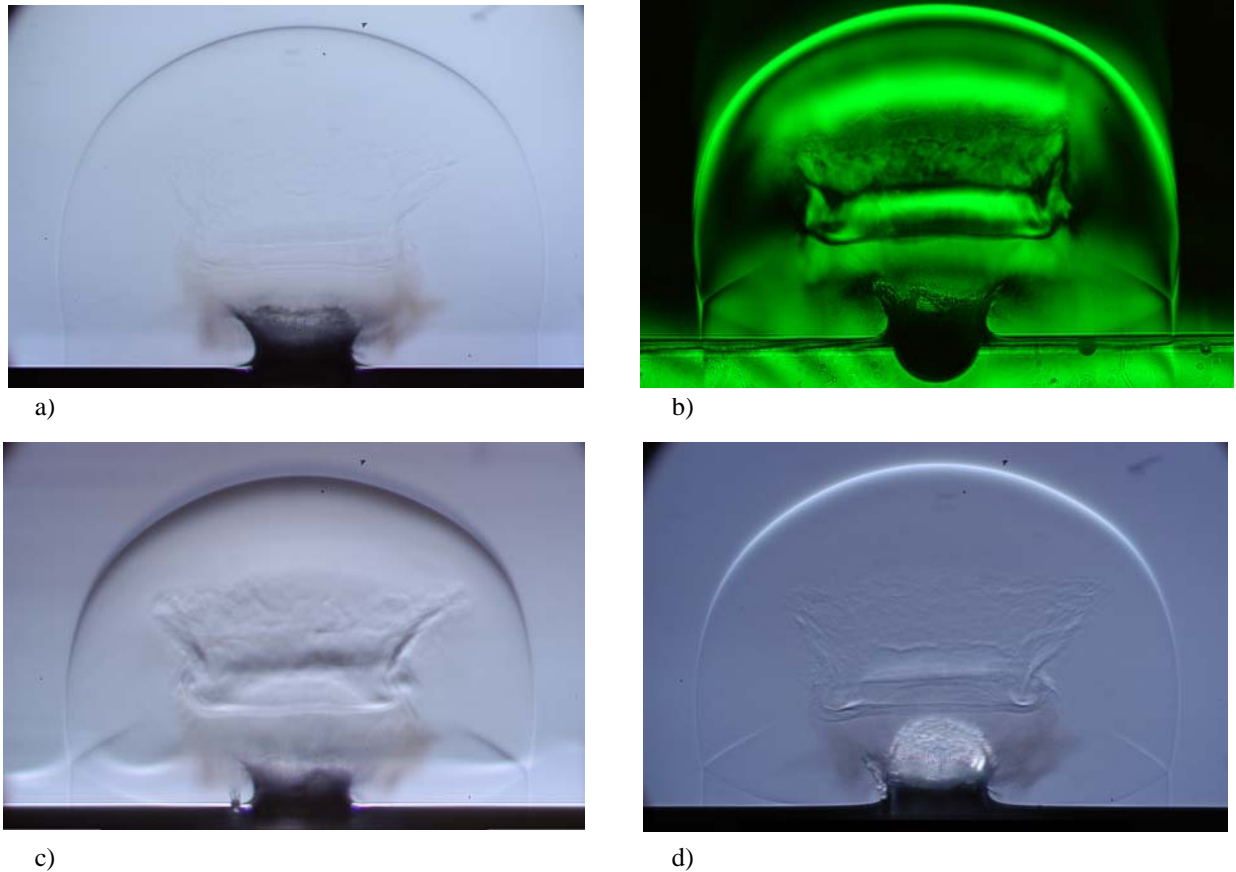


Figure 31: Visualization of a phase object by means of different Schlieren techniques: Diameter of irradiated spot: 0.5 mm. (a) Bright field image recorded with $F = 2.5$, (b) Dark field image, (c) Knife-edge technique, with filter blocking the lower part of the Fourier plane as shown in Fig. 6, (d) Hoffmann modulation contrast with filter blocking the upper part of the Fourier plane. The object shown is an ablation plume produced by Q-switched Er:YAG laser ablation of water. The plume consists of water vapor (top) and a mixture of vapor and droplets (bottom). The plume expansion has resulted in the formation of an external shock wave propagating into the surrounding air, and the collision between plume and ambient air has produced also an internal shock wave that travels through the plume towards the water surface.

filter, in turn, provides a 7 times larger dynamic range than the knife edge part of the filtering. The results are documented in Fig. 33. The dependence between light deflection and intensity change in the filtered image in Fig. 33 is nonlinear, stronger for small deflections and weaker for large deflections, which results in improved contrast for regions with small refractive index gradients. Resolution is not compromised because the transmitted part of the spatial frequency spectrum is even larger than with the regular Hoffman technique. The resolution of modified HMC is much better than that of the knife-edge technique especially for the regime with largest sensitivity in which a large part of the light source is covered by the knife edge or the grey part of the filter, respectively (Fig. 32).

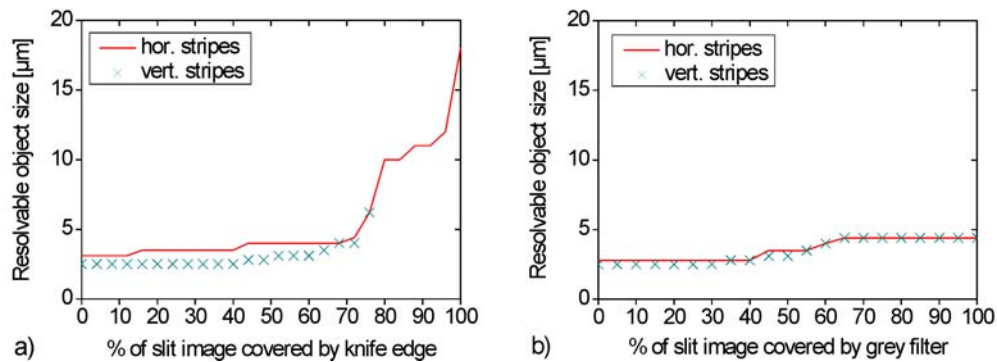


Fig. 32 Relation between optical resolution and % cutoff for the knife-edge technique (a) and modified Hoffman modulation contrast (b). The resolution was determined using a US Air Force test plate. In a), no vertical stripes could be resolved for more than 75% cutoff.

	Brightness change in image depends on	Sensitivity	Measurement range	Image resolution	Constant sensitivity for all directions of phase-gradients	Info on direction of phase-gradient	False structures
Bright field	phase-gradient, for gradients exceeding an NA - dependent threshold	low	large	good, but deteriorates with increasing sensitivity	yes	no	no
Dark field (slit-like light source and bar-like filter)	phase-gradient	High to very high (with laser light source)	small	good	no	no	yes
Dark field (round light source and filter)	phase-gradient	High to very high (with laser light source)	small	good	yes	no	yes
Knife edge	phase-gradient	moderate to high	large to moderate	poor for high sensitivity	no	yes	no
Hoffman Modulation Contrast	phase-gradient	moderate to high	large to moderate	good even at high sensitivity	no	yes	no
Hoffman + knife edge	phase-gradient	Increased for small phase-gradients	large to moderate	good even at high sensitivity	no	yes	no
Phase contrast	phase shift	Very high	small	good	yes	no	Halos in regions of large phase-gradients
DIC (Differential interference contrast)	phase-gradient	high	moderate	good	no	yes	no, but not suited for imaging through birefringent container walls

Table 3: Comparison of the performance of various Schlieren techniques. Hoffman modulation contrast combined with knife-edge filtering has an excellent performance (see Figs. 31 and 33) and is well suited for a realization on an optical bench.

It is important to note that for a given width of the grey part of the Hoffman filter the sensitivity of the Schlieren method can be increased by choosing an imaging lens L_3 with large focal length. In that case, the spatial frequency spectrum is large compared to the filter width, and light is deflected off the filter already by weak phase objects. When L_1 of the setup in Fig. 30 is a microscope objective, the back focal plane is usually located within the objective and thus not directly accessible. Therefore, the image formed by the microscope objective L_1 and tube lens L_2 (a tube lens is required in infinity-corrected optical systems) must be imaged by another lens possessing an accessible back focal plane to perform the Schlieren filtering (not shown in Fig. 30). In this case the focal length of L_5 must be sufficiently large to provide high sensitivity.

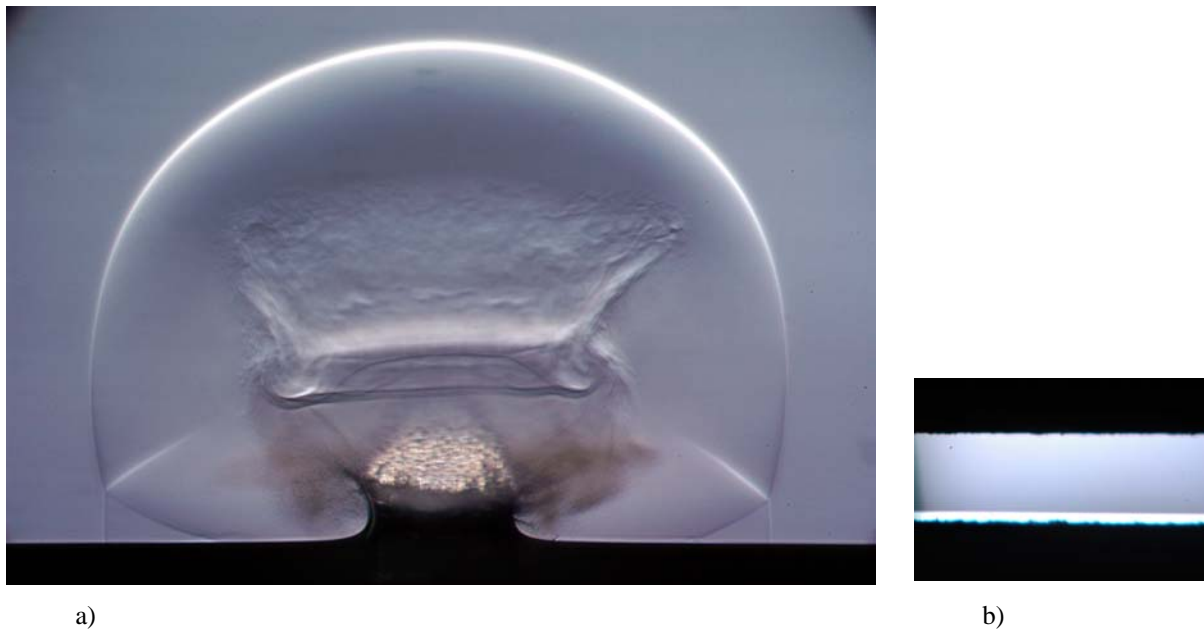


Figure 33: (a) Visualization of the same phase object as in Fig. 31 by means of a modified Hoffmann modulation technique. Diameter of irradiated spot: 0.5 mm. (b) Position of the Hoffman filter with respect to the image of the light source. About 1/5 of the area of the light source remains uncovered by the grey part of the Hoffman filter.

Conclusion: The modified Hoffmann modulation technique is a speckle-free, sensitive Schlieren technique with high spatial resolution and a relatively large measurement range for different refractive index gradients. The laser-based dark-field technique features the highest sensitivity.

5.2. TEST OF HOFFMAN CONTRAST AND DARK-FIELD TECHNIQUE ON LASER-INDUCED PRESSURE TRANSIENTS IN AIR

The modified Hoffmann modulation technique and the laser-based dark-field technique were tested on the visualization of plasma-induced pressure transients in air produced by a 10- μ J N_2 laser pulse focused onto a dissected histologic specimen on a glass slide. The laser pulse serves for contamination-free catapulting of the specimen into a vial for subsequent proteomic or genomic analysis. The results obtained using the modified Hoffman modulation contrast are presented in figure 34, and a picture series taken using the laser-based dark-field technique is shown in figure 35. The Hoffman technique yields a good representation of structural features of the probe and of the laser-produced plasma but a visualization of the acoustic transients could not be achieved. However, using the dark-field technique, the shock wave generated by the plasma expansion could be visualized, and the shock wave velocity and pressure could be determined.

The sensitivity of the Hoffman technique is determined by the width of the partially transmitting part of the Hoffman filter, and by the width of that part of the image of the light source that is not covered by the filter (see section 5.1 above). The partially transmitting part of commercially available Hoffman filters has a width of 1.4 mm, and the corresponding width of the non-covered image of the light source (15% of the total width) amounts to 210 μ m. By contrast, with the dark-field technique, a 50 μ m thin filter wire could be used. The smaller size of the filter results in an increase of the sensitivity by a factor of at least 4.2. Moreover, the signal to noise ratio for the detection of weak phase object is much better when phase variations appear as bright structures on a dark background rather than as variations of brightness on a bright background. Further improvements of the SNR were achieved by subtraction of a reference image that had been taken before release of the laser pulse from the actual image showing the acoustic transient. The subtraction eliminates background noise caused by diffraction, scattering or reflection of illuminating light by other objects than the transient structures of interest.

This way, we were able to visualize transients produced by a 10- μ J laser pulse even though the pressure-induced refractive index change is much smaller in air than in water and the shock wave propagation with an initial velocity of 26 km/sec caused a marked blur on the photographs during the 20-ns exposure time.

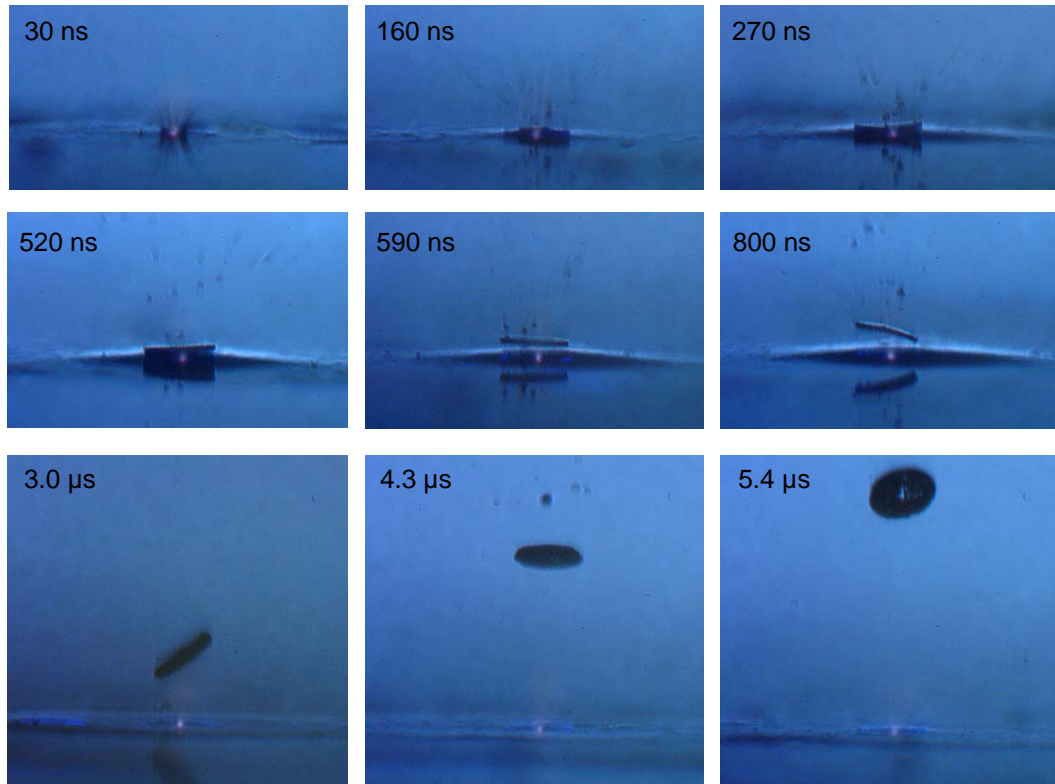


Figure 34: Catapulting of dissected histologic specimens with 40 μm radius and 5 μm thickness. 10- μJ N_2 -laser pulses focused through a 40 \times long-distance microscope objective (NA = 0.6) were used for catapulting. Time-resolved photographs were taken using the modified Hoffman modulation contrast described in section 5.1.

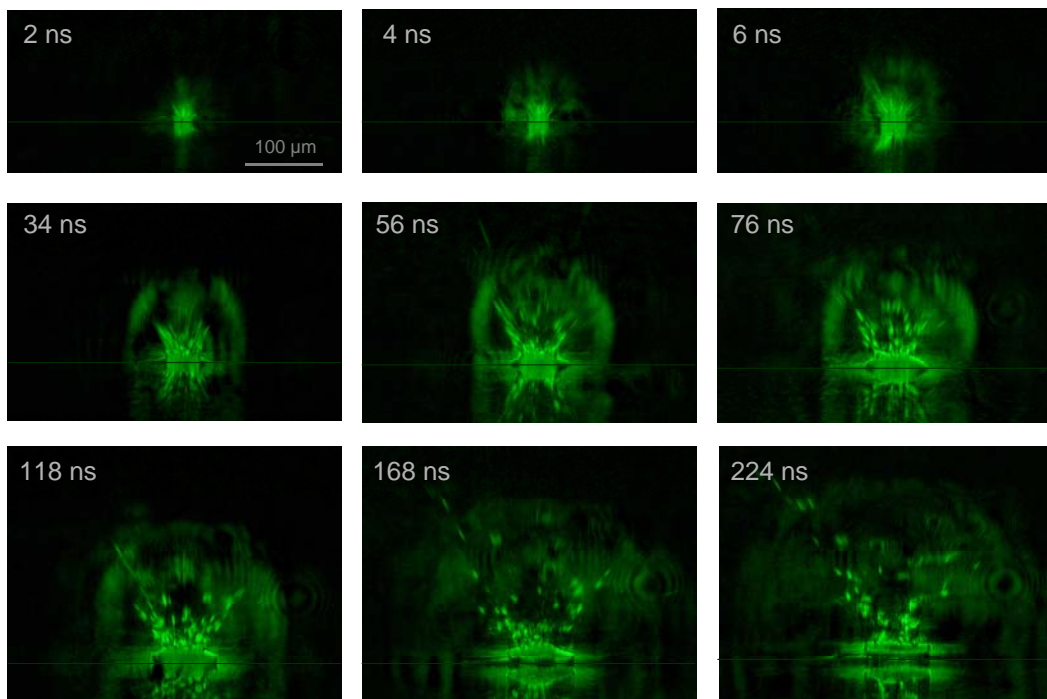


Figure 35: Time-resolved photographs of the initial phase of catapulting of dissected histologic specimens taken with a laser-based dark-field Schlieren technique. The catapulting parameters were the same as for figure 34. The shock wave emitted by the expanding laser plasma can clearly be identified on the photographs. The initial shock wave pressure has a similar magnitude (670 MPa for 10 μJ pulse energy) as observed previously for plasma formation in water (1300 MPa produced by a 50- μJ 30-ps pulse [Vog96b]).

5.3. INVESTIGATION OF FEMTOSECOND LASER-INDUCED LOW DENSITY PLASMAS

We showed that the laser-based dark-field technique is well suited for the documentation of low-density plasmas. When femtosecond laser pulses are used for illumination of the photographs, the blur can be eliminated, and an even higher sensitivity than in the present images can be expected. However, for the large NAs used in cell surgery and addressed in our modelling and experiments, the region with refractive index changes is smaller than the diffraction limited resolution of any optical imaging system. Therefore, we will in future use the developed Schlieren methods for investigating the transition of breakdown dynamics from large NA to smaller NAs. Here, the breakdown region is larger than the resolution of the diffraction limited imaging setup with large NA ($NA = 0.5$) that were developed in our project. This work will be performed in the project FA 8655-05-1-3010.

6 INFLUENCE OF LINEAR ABSORPTION ON OPTICAL BREAKDOWN

Even though biological cells and soft tissues consist largely of water (55-99% of the mass), their content of biomolecules (Proteins, DNA, RNA, glycosaminoglycans, lipids, etc.) will also influence the dynamics of optical breakdown. Therefore, it is a rather crude approximation to simply use water properties for modeling optical breakdown in tissue, as done in section 3 and by all other researchers to date. An empirical justification for this simplification is that the breakdown thresholds in water and in transparent tissues such as cornea were found to be very similar for laser wavelengths exhibiting small linear absorption in those tissues [Doc86]. However, for laser wavelengths that are highly absorbed in tissue, the dynamics will change. For example, the plasma formation threshold in cornea or skin for the ArF excimer laser wavelength ($\lambda = 193$ nm, optical penetration depth in tissue ≈ 0.3 μm) is about 6 times higher than the ablation threshold [Ven95, Vog03], which indicates that plasma formation must be supported by linear absorption. The interaction of linear and nonlinear absorption will be relevant for most UV wavelengths because they are well absorbed in biomolecules and for mid IR wavelengths because they are well absorbed in water and, for $6 \mu\text{m} < \lambda < 10 \mu\text{m}$, also in collagen. Therefore, it would be desirable to include linear absorption into the optical breakdown model.

Linear absorption can influence the breakdown dynamics in two ways: Heating of the material in the laser focus results in thermionic emission of free electrons, and the additional energy levels associated with linear absorption can facilitate the generation of seed electrons for cascade ionization by multiphoton ionization. In the present project, we have focused attention on the inclusion of thermionic emission into the breakdown model because this can be done by a general approach that links free electron generation to the temperature rise in the focal volume, which, in turn, is related to the optical absorption coefficient. By contrast, the influence of linear absorbing chromophores on multiphoton ionization depends on the specific structure of the energy levels of each individual chromophore together with its number density in the tissue. Therefore, the modeling must be very specific, and the general explanatory value of such specific models is questionable.

In this chapter, we first describe the changes of the optical breakdown dynamics in nominally transparent media when thermal electron emission is included into the breakdown model (section 6.1), and then explore the additional influence of linear absorption (section 6.2). We shall see that the inclusion of thermal emission destroys the self-consistency of any breakdown model that merely addresses the temporal evolution of free electron density but ignores the plasma-induced hydrodynamic effects. In this limited framework, plasma can be formed but will never disappear because in a hot plasma recombination of free electrons is permanently counteracted by thermal emission. That circle can only be broken by incorporating adiabatic cooling of the expanding plasma into the model, i.e. by considering the coupling of free electron evolution and hydrodynamic effects. This task poses a formidable challenge on future modeling efforts.

6.1. EXTENSION OF THE NUMERICAL MODEL OF OPTICAL BREAKDOWN TO INCLUDE THERMAL ELECTRON EMISSION

6.1.1 Modeling approach

In *transparent dielectrics*, free-electron generation by the incident light relies primarily on multiphoton ionization and cascade ionization. However, once the energy carried by the primary free electrons is thermalized, thermal emission of free electrons comes into play as a secondary process. In order to include thermal emission into the model described in section 3, we look at the electronic energy distribution in thermal equilibrium and consider those electrons to be „free“ that possess energies larger than the band gap energy. We assume that the energy distribution of thermal electrons resembles a Boltzmann distribution. The Boltzmann statistics applies, strictly speaking, only to ensembles of particles with little mutual interaction (gases, or the electron ‘gas’ within metals), and not to solids characterized by discrete energy bands. However, the structure of the solid breaks down in the temperature regime where thermal emission yields a considerable contribution to free-electron generation. Therefore, we consider application of the Boltzmann statistics to be an appropriate first-order approximation. We further assume that the ‘activation energy’ required to produce a (quasi-) free electron in dielectric solids is given by the energy gap between ground state and exciton band at low temperatures and remains constant with increasing temperature.

For *materials with strong linear absorption*, thermal emission of free electrons will be the primary process triggering plasma formation if it provides seed electrons at a lower irradiance than what would be required for multiphoton ionization. This will be the case primarily for long pulse durations, because the radiant exposure producing a temperature leading to thermal emission of seed electrons is the same for all pulse durations, as long as

heat diffusion can be neglected, while the irradiance corresponding to this radiant exposure decreases with increasing pulse duration, and so does the probability for multiphoton effects.

With increasing pulse duration, linear absorption will provide not just seed electrons but also an ever-larger fraction of the free electrons contributing to breakdown. The pulse energy must increase to maintain the irradiance level required to drive the ionization cascade up to the critical free-electron density. The larger pulse energy will, at the same time, produce higher temperatures and more thermal electrons.

From the above it is obvious that consideration of thermal ionization is necessary to obtain a consistent picture of the evolution of the free electron density during optical breakdown. Surprisingly, this process was, to the best of our knowledge, not included in any of the previously published models of optical breakdown in transparent media.

6.1.2 Results

The results of our calculations of plasma formation in pure water using the extended numerical model for pulse durations of 6 ns, 30 ps, and 100 fs and wavelengths of 1064 nm, 532 nm, and 355 nm are presented in Figures 36-38. The calculations were performed for NA = 0.5, with two values of the critical electron density, $\rho_{cr} = 10^{20} \text{ cm}^{-3}$, and $\rho_{cr} = 10^{21} \text{ cm}^{-3}$. In the figures we present for 6 ns pulse duration only the results for $\rho_{cr} = 10^{20} \text{ cm}^{-3}$, and for 30 ps and 100 fs pulse duration only results for $\rho_{cr} = 10^{21} \text{ cm}^{-3}$ because these assumptions yielded the best agreement between numerically predicted and experimentally determined breakdown thresholds [Noa99]. In Table 4, however, all results are summarized. The start temperature assumed in all calculations was 293°K, and the heat capacity was assumed to be constant, regardless of the peak temperature reached.

36a) 6ns/1064nm, $\rho_{cr} = 10^{20} \text{ cm}^{-3}$

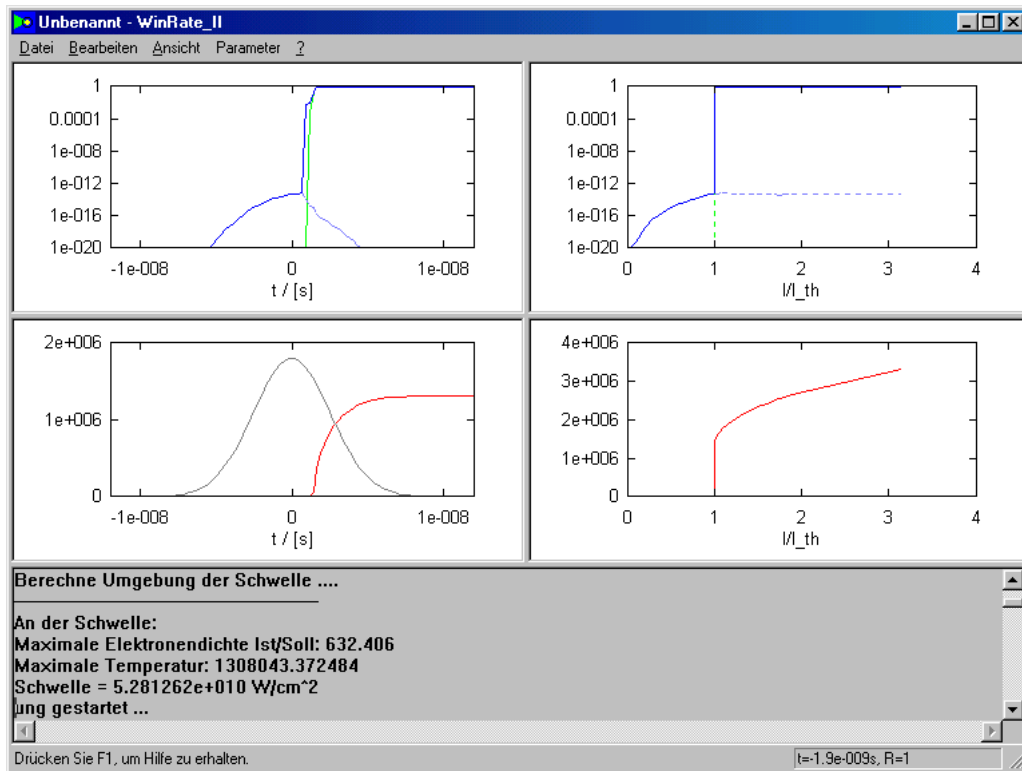
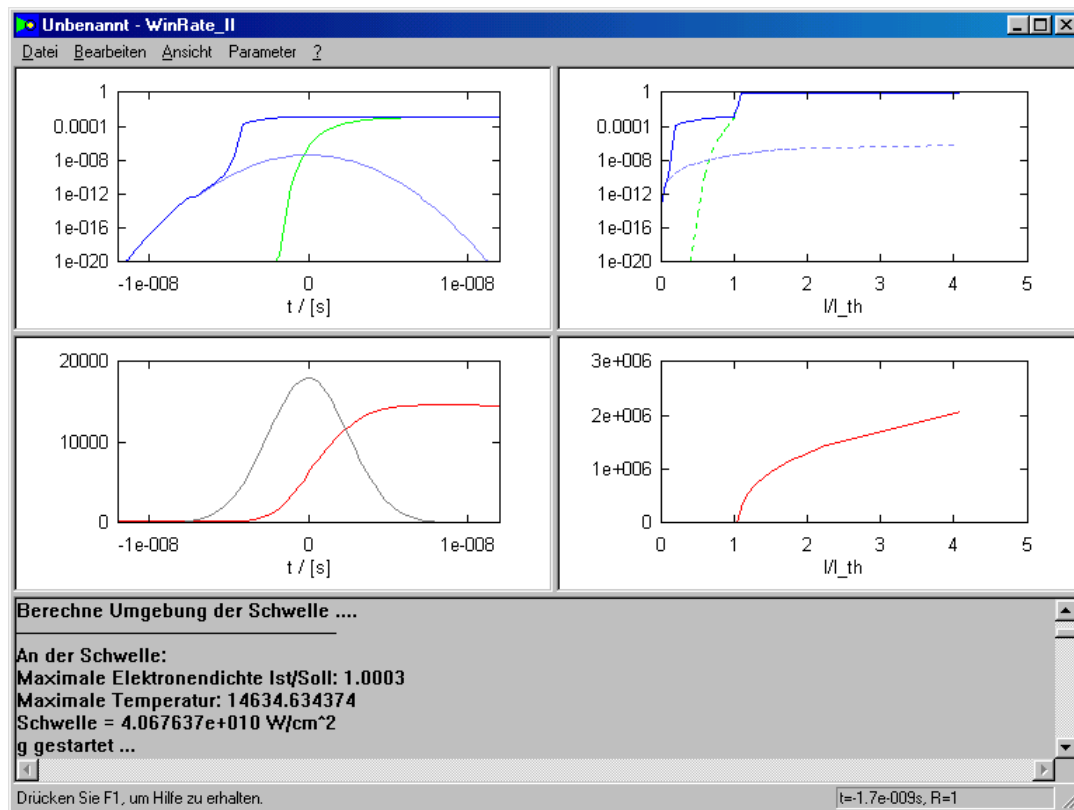
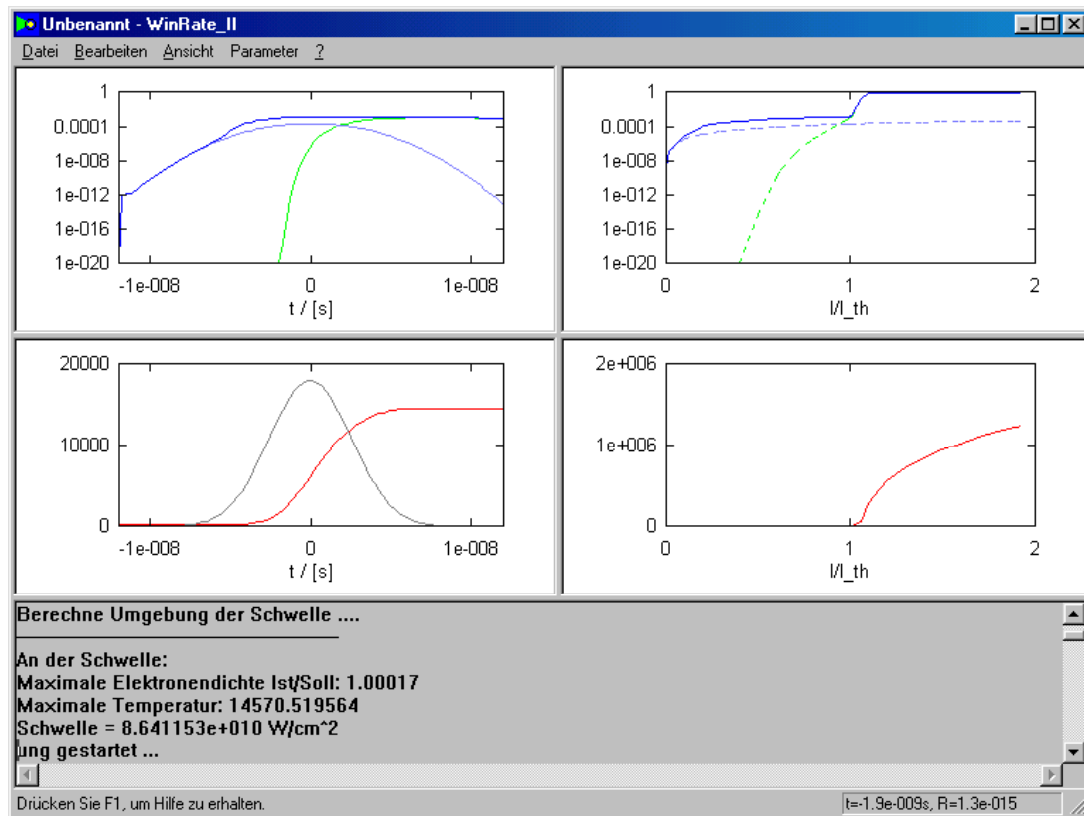


Figure 36: Screenshots with the results of the numerical simulations of plasma formation by 6-ns pulses at wavelengths of (a) 1064 nm, (b) 532 nm, and (c) 355 nm (see next page). In each screenshot, the upper left graph portrays the evolution of the ionization degree as a function of time. Full ionization (i.e. a degree of 1.0) corresponds to a free-electron density of $6.68 \times 10^{22} \text{ cm}^{-3}$. The dark blue line represents the total degree of ionization, the bright blue line the part produced by MP-effects, and the green line the part arising from thermal emission of electrons. The upper right graph presents the maximum ionization degree produced during a laser pulse as a function of irradiance. Besides the total ionization degree, the parts arising from MPI and thermal emission are also plotted. The lower left graph shows the temporal evolution of the plasma temperature (red) in relation to the temporal shape of the laser pulse (grey). The lower right graph show the peak temperature reached during breakdown as a function of irradiance.

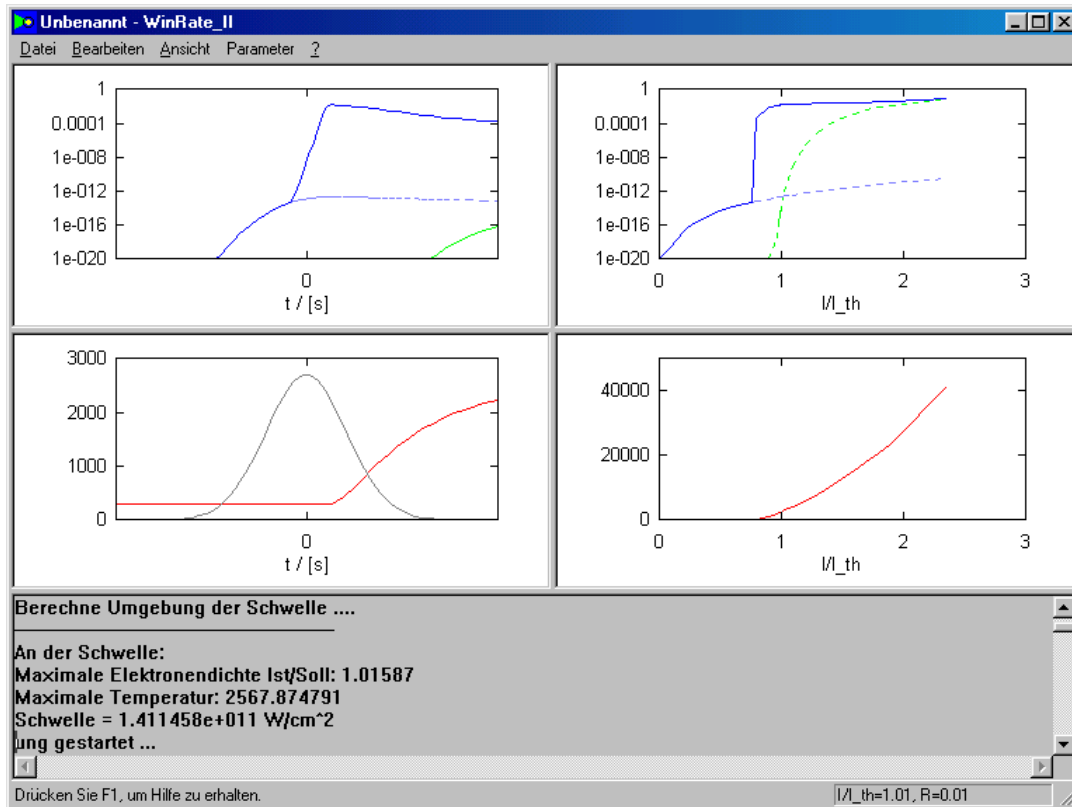
36b) 6ns / 532nm, $\rho_{cr} = 10^{20} \text{ cm}^{-3}$



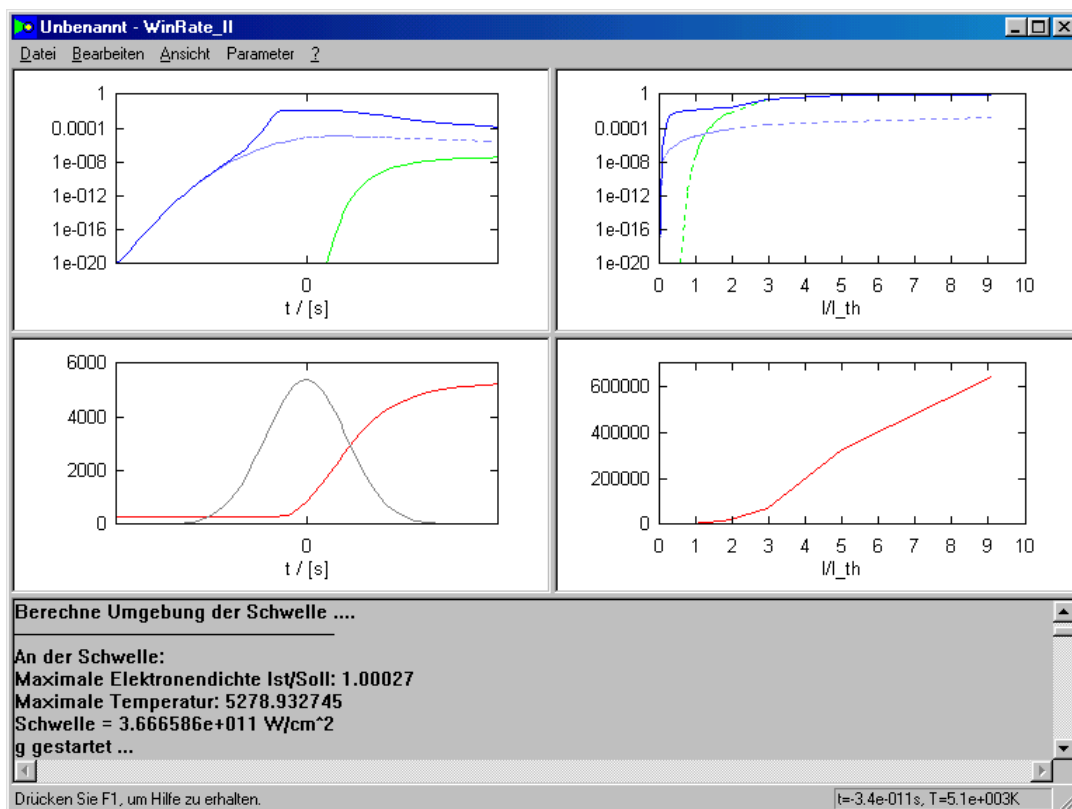
36c) 6ns / 355 nm, $\rho_{cr} = 10^{20} \text{ cm}^{-3}$



37a) 30ps/1064nm, $\rho_{cr} = 10^{21} \text{ cm}^{-3}$



37b) 30ps/532nm, $\rho_{cr} = 10^{21} \text{ cm}^{-3}$



37c) 30ps/355nm, $\rho_{cr} = 10^{21} \text{ cm}^{-3}$

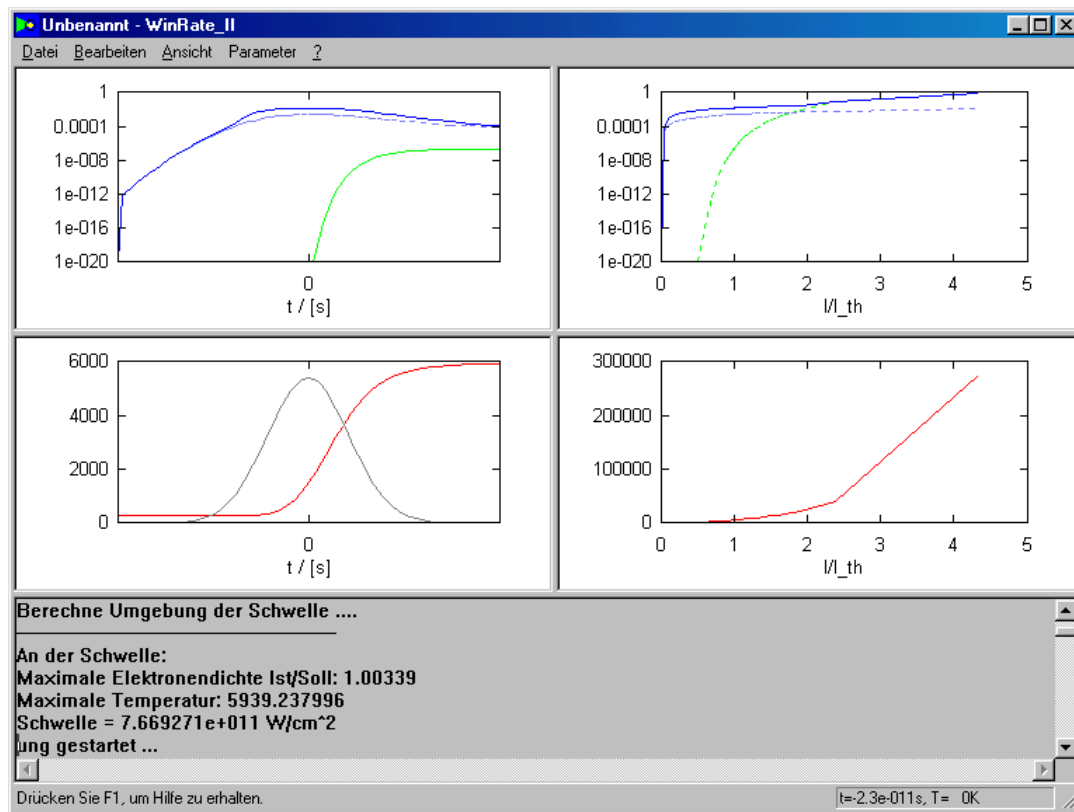
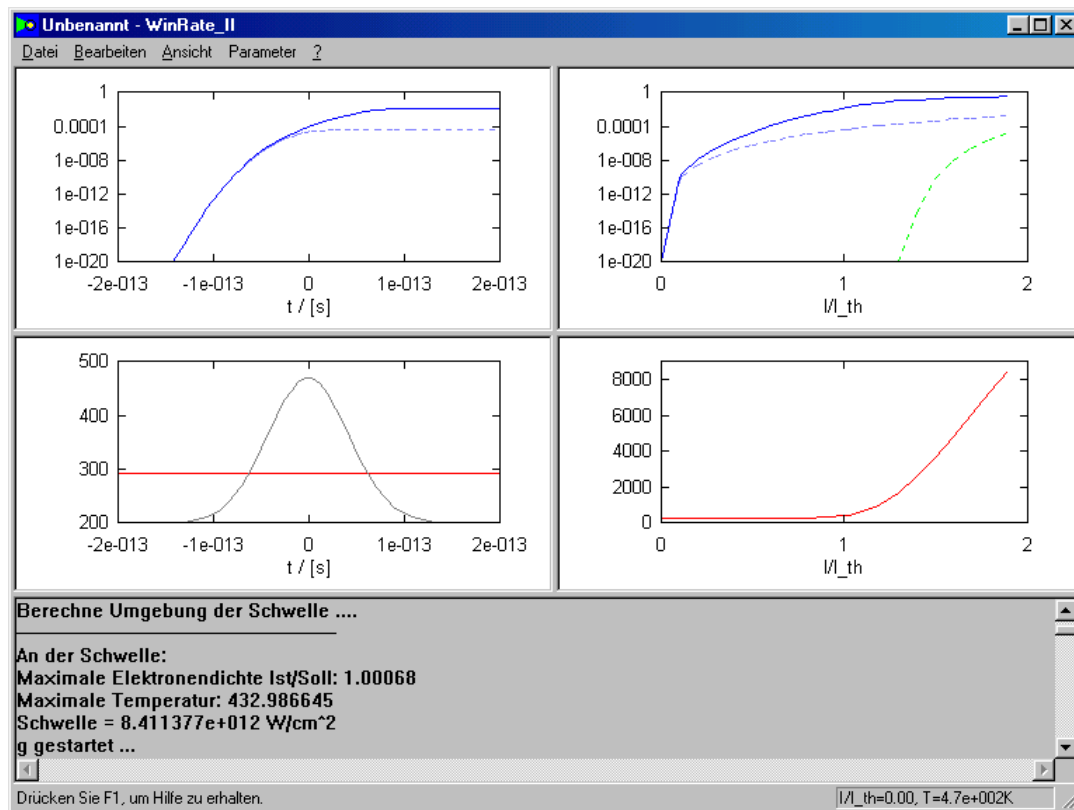
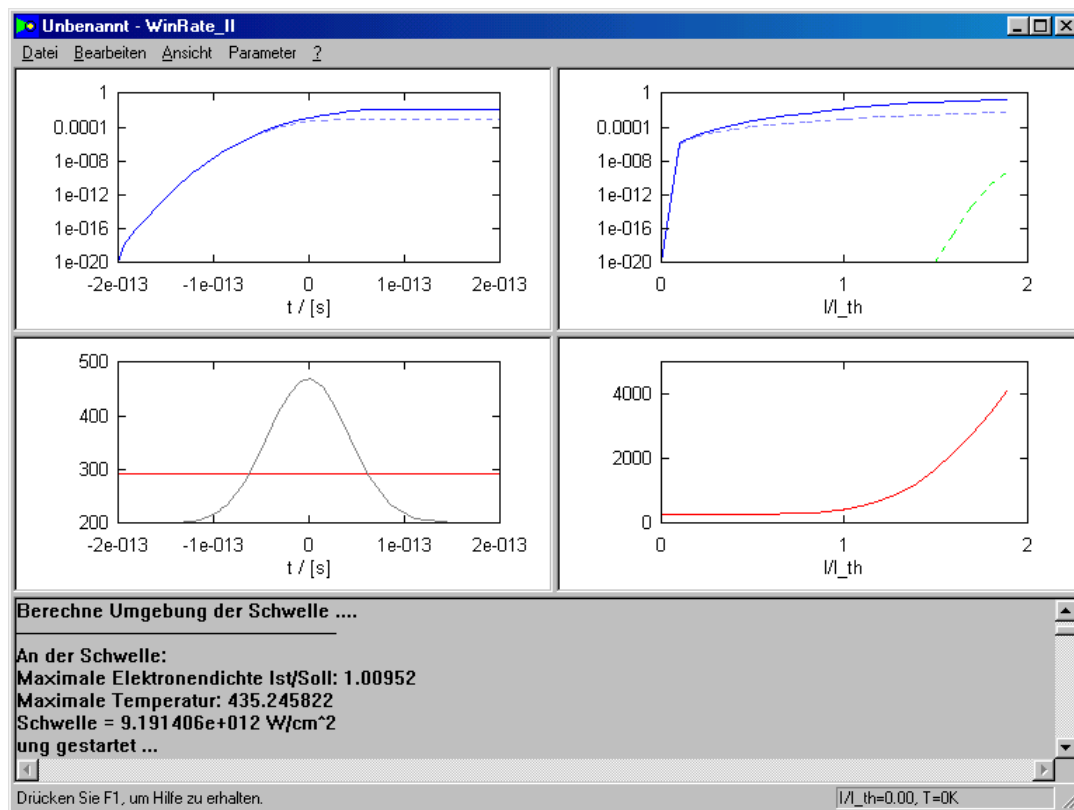


Figure 37: Results of the numerical simulations of plasma formation by 30-ps pulses at wavelengths of (a) 1064 nm, (b) 532 nm, and (c) 355 nm.

38a) 100fs/1064nm, $\rho_{cr} = 10^{21} \text{ cm}^{-3}$



38b) 100fs/532nm, $\rho_{cr} = 10^{21} \text{ cm}^{-3}$



38c) 100fs/355nm, $\rho_{cr} = 10^{21} \text{ cm}^{-3}$

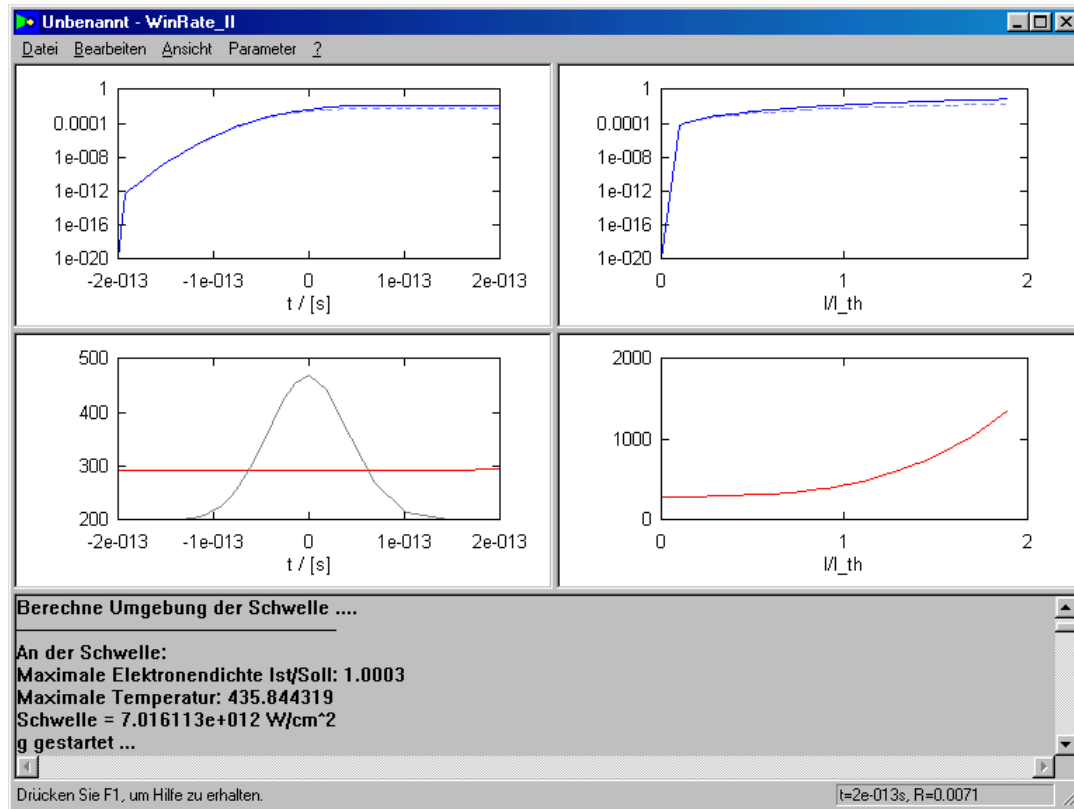


Figure 38: Results of the numerical simulations of plasma formation by 100-fs pulses at wavelengths of (a) 1064 nm, (b) 532 nm, and (c) 355 nm.

NA = 0.5	$10^{20}/\text{cm}^3$			$10^{21}/\text{cm}^3$		
	1064 nm	532 nm	355 nm	1064 nm	532 nm	355 nm
6 ns	5.28×10^{10} 1.31×10^7 Thermal	4.07×10^{10} 1.46×10^4 Cascade	8.64×10^{10} 1.46×10^4 Cascade	5.28×10^{10} 1.3×10^6 Thermal	4.25×10^{10} 2.45×10^4 Thermal	9.02×10^{10} 2.45×10^4 Thermal
30 ps	1.15×10^{11} 328 Cascade	9.39×10^{10} 335 Cascade	1.06×10^{11} 348 MP/Cascade	1.41×10^{11} 2568 Cascade/ Thermal	3.67×10^{11} 5278 Cascade	7.67×10^{11} 5939 Cascade
100 fs	6.59×10^{12} 306 Cascade	5.83×10^{12} 305 MP/Cascade	2.82×10^{12} 305 MP/Cascade	8.41×10^{12} 433 Cascade	9.19×10^{12} 435 Cascade	7.01×10^{12} 436 MP/Cascade

Table 4: Overview of the results of simulations of plasma formation for various pulse durations and wavelengths, assuming free-electron densities at the breakdown threshold of $\rho_{cr} = 10^{20}/\text{cm}^3$ and $10^{21}/\text{cm}^3$, respectively. For each parameter set, the upper values denotes the irradiance threshold for optical breakdown (W/cm^2), and the lower value denotes the maximum temperature reached at threshold (K). Also listed is the process that contributes the largest number of free electrons.

6.1.3 Discussion

Nanosecond pulses

Because zero linear absorption is assumed in all simulations, the first seed electron(s) in the focal volume can only be produced by multiphoton ionization, regardless of wavelength.

For long wavelengths (1064 nm), multiphoton-generation of the seed electron is the main hurdle for optical breakdown to occur. Once a free electron is generated, cascade ionization becomes the dominant process, leading to an increase of the free-electron density by 10 orders of magnitude within a fraction of the laser pulse. For large free-electron densities, recombination processes slow the cascade down because recombination is proportional to ρ^2 while cascade ionization is proportional only to ρ . However, collisional transfer of kinetic energy of the free electrons to heavy particles results in a rapid heating of the plasma volume that, in turn, leads to a massive thermal emission of free electrons and to full ionization of the focal volume at the end of the laser pulse.

Full ionization of the plasma volume corresponds to a free-electron density that is much larger than the critical electron density assumed for breakdown (i.e. $\rho_{cr} = 10^{20} \text{ cm}^{-3}$, or $\rho_{cr} = 10^{21} \text{ cm}^{-3}$, respectively). This is a consequence of the very high irradiance required for multiphoton-initiation of the first free electron at $\lambda = 1064 \text{ nm}$. As a consequence, the cascade becomes so vigorous that it is stopped by recombination only at free electron densities considerably larger than ρ_{cr} . Thermalization of the large amount of energy carried by these free electrons then causes a temperature rise to $\approx 10^6 \text{ K}$ that is sufficiently high to produce full ionization.

In reality, such high temperatures have never been observed close to the optical breakdown threshold. Instead, it was observed that for $\lambda = 1064 \text{ nm}$ the plasma size at the breakdown threshold was considerably larger than the focal volume, in contrast to optical breakdown at shorter wavelengths [Vog96a, Ven02]. The enlargement of the plasma can be explained by two mechanisms: 1. If the free electron density in the focal volume is high enough that the plasma frequency equals or exceeds the frequency of the incident light, the bulk of the light will be reflected and contribute to nonlinear absorption in the vicinity of the focus. 2. UV-photons emitted in recombination events occurring in the focal volume may contribute to the formation of additional quasi-free electrons in the plasma vicinity that act as seed electrons for cascade ionization. Optical breakdown will occur wherever the local irradiance is sufficient to produce the critical electron density. These mechanisms reduce the amount of light reaching the focus center and spread the volume into which the energy is deposited, this way limiting the peak temperature. The fact that they are not considered in our model is responsible for the wrong predictions at $\lambda = 1064 \text{ nm}$.

For shorter wavelengths in the visible and UV region of the optical spectrum, multiphoton ionization plays an increasingly important role in producing the critical electron density. Therefore, seed electrons produced by MPI are readily available at the irradiance level required for the ionization cascade to reach the critical electron density, and the cascade does, at the breakdown threshold, not overshoot this value. Due to the reduced number of free electrons, collisional energy transfer to the medium is diminished, and the calculated peak temperatures are much smaller than for 1064 nm. The predicted temperatures of about 15000°K for $\lambda = 532 \text{ nm}$ and $\lambda = 355 \text{ nm}$ agree well with spectroscopically determined plasma temperatures of 10000°K for 5-ns pulses at $\lambda = 1064 \text{ nm}$ [St095] and 15000°K for a 30-ns pulse at $\lambda = 694 \text{ nm}$ [Bar68]. Note, however, that the experimental values were obtained well above the breakdown threshold while the numerical predictions refer to the temperature rise at threshold where the actual values are expected to be somewhat smaller than experimental values quoted above. The model simulations overestimate the temperatures produced by nanosecond breakdown, because the adiabatic cooling due to the hydrodynamic expansion of the plasma during the laser pulse is not considered. Experimental and theoretical investigations of plasma-induced cavitation bubble generation suggest that the hydrodynamic expansion sets in after a few nanoseconds [Vog96b]. It is thus relevant for the temperatures reached in nanosecond optical breakdown but plays no role for picosecond or femtosecond pulses.

The model predictions for the plasma temperatures at superthreshold irradiances are too high for all laser parameters because the model does neither consider the plasma growth towards the incoming laser beam and the resulting shielding effect for the focal region, nor does it consider adiabatic cooling by plasma expansion.

Pico- and femtosecond pulses

As expected, cascade ionization plays a much smaller role for pulse durations in the picosecond and nanosecond range than for nanosecond pulses. Due to the thermalization time of a few picoseconds for the energy carried by free electrons, the temperature rise and the thermal emission of free electrons exhibit a delay with respect to the laser pulse both for picosecond and nanosecond pulses. For femtosecond pulses they occur outside the time window shown in the graphs. To obtain the correct peak temperatures and $T_{\max}(I/I_{th})$ curves, all simulations were continued

throughout a time interval given by twice the pulse duration plus 10 times the thermalization time. The peak temperatures are summarized in table 4.

Both for picosecond and femtosecond breakdown, the calculated peak temperatures agree surprisingly well with experimental data and/or temperature values obtained by completely different theoretical approaches. Chapyak and Godwin used measured data for plasma size and absorbed laser energy together with the equation of state of water to calculate the temperature after breakdown produced by 30-ps, 1064 nm laser pulses [Cha97]. They obtained a value of 2160°K, close to the value of 2568°K predicted in the present calculations. Spectroscopic measurements by Stolarski and coworkers yielded higher values of 6000-7000°K well above threshold [Sto95]. However, since thermal equilibrium is established only towards the end or after the laser pulse, the plasma radiation consists largely of bremsstrahlung and recombination radiation, and contains only a fraction attributable to blackbody radiation. The spectroscopic data from picosecond breakdown in terms of blackbody thus do not simply reflect the equilibrium temperature in the plasma but are largely influenced by the electron temperatures before thermalization. Their interpretation in terms of blackbody radiation will, most likely, lead to an overestimation of the plasma temperature.

For femtosecond breakdown, our model predicts a temperature rise of 140°K – 143 °K at the breakdown threshold, with little variation for different wavelengths. This result agrees well with the threshold for bubble formation by thermoelastic tensile stress (temperature rise of 105°K) that was obtained by the calculations presented in section 3.

6.2. MODELING OF OPTICAL BREAKDOWN CONSIDERING BOTH THERMAL ELECTRON EMISSION AND LINEAR ABSORPTION

6.2.1 Results

In the following, the extended breakdown model including thermal electron emission is applied to study *breakdown in linearly absorbing media*. Figure 39 presents breakdown thresholds and maximum temperatures as a function of the linear absorption coefficient for a laser pulse duration of 1 ns and wavelengths of 355 nm and 1064 nm, respectively. In figures 40 and 41, the corresponding data for the time evolution of free-electron density and temperature at threshold are presented, together with the maximum free-electron densities and temperatures as a function of irradiance. The calculations were performed for $NA = 0.5$, $\Delta E = 6.5$ eV (such as for water), and $\rho_{cr} = 10^{20} \text{ cm}^{-3}$. A critical electron density of $\rho_{cr} = 10^{20} \text{ cm}^{-3}$ was assumed because for 6-ns-pulses this assumption yields the best agreement between numerically predicted and experimentally determined breakdown thresholds [Noa99]. The start temperature used for all calculations was 293°K, and the heat capacity was assumed to be constant and equal to the value for liquid water at room temperature.

For large linear absorption coefficients, the optical penetration depth becomes smaller than the focal length. For $NA = 0.5$, $\lambda = 1064$ nm, this is the case when $\alpha > 1000 \text{ cm}^{-1}$, and for $\lambda = 355$ nm it applies for $\alpha > 3000 \text{ cm}^{-1}$. Under such conditions, the breakdown process resembles plasma formation at a target surface more than breakdown in a bulk medium. In this case, the values for electron density and temperature quoted below refer to a disk with diameter of the laser focus and thickness of the optical penetration depth rather than to the entire focal volume. This applies also to the calculation of electron diffusion losses during the laser pulse.

For both wavelengths the irradiance threshold decreases monotonically with increasing linear absorption in a similar fashion. The overall decrease amounts to a factor of 46 for $\lambda = 355$ nm, and to a factor of 34 for $\lambda = 1064$ nm. However, the dependence of the maximum temperature at threshold on the linear absorption coefficient is quite different for UV and IR breakdown. The temperature increases monotonically with linear absorption for UV pulses (from regime 1 to regime 2) but for IR pulses it decreases first (from regime 1 to 2) before it rises again (regime 3). While the dependence of the breakdown threshold on the absorption coefficient is expected, the strikingly different dependence of temperature on linear absorption for both wavelength is, at first sight, hard to understand. Here the detailed presentation of the results in Figures 40 and 41 provides better insight.

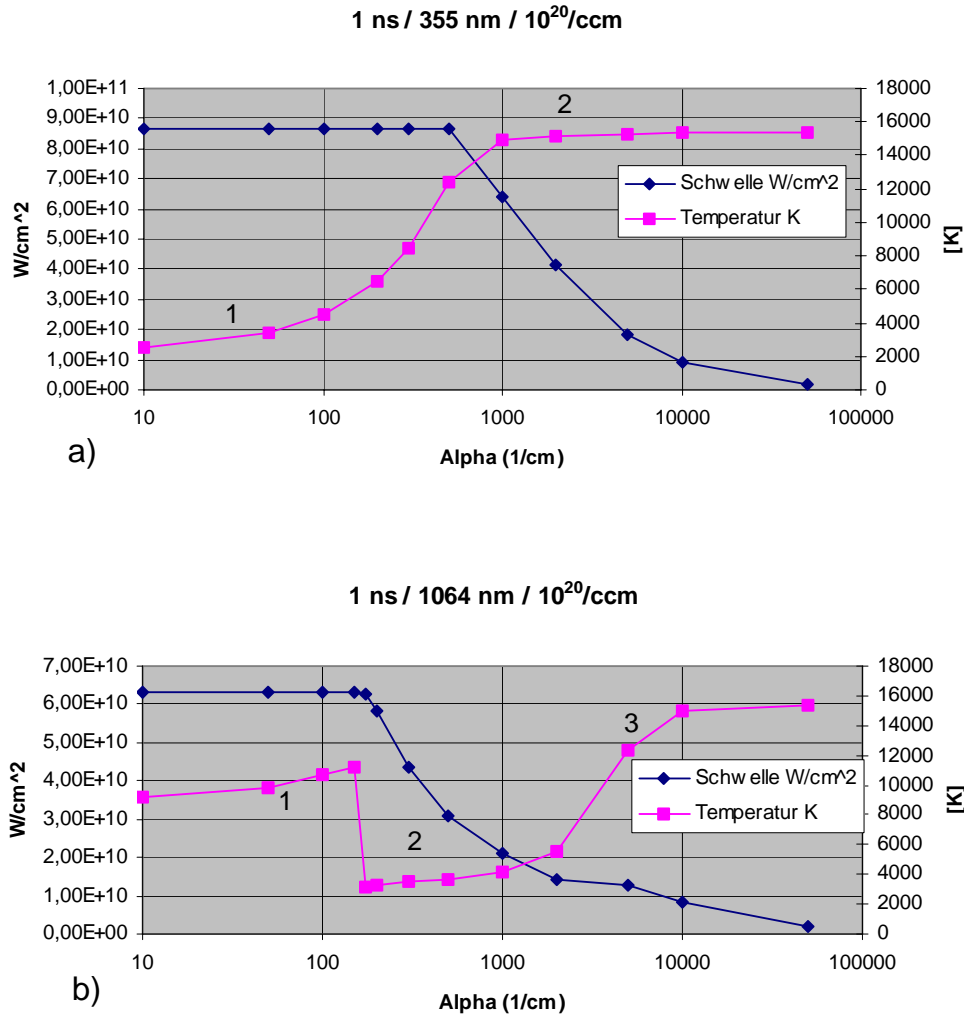


Figure 39: Breakdown threshold (“Schwelle”) and maximum temperature as a function of the linear absorption coefficient (Alpha) for 1 ns pulse duration and wavelengths of (a) 355 nm, and (b) 1064 nm. The calculations were performed for $NA = 0.5$, $\Delta E = 6.5$ eV (such as for water), and $\rho_{cr} = 10^{20} \text{ cm}^{-3}$. The numbers in the figures denote different regimes discussed in the text.

IR pulses (1064 nm)

Figure 40 (next 3 pages): Screenshots with the results of the numerical simulations of plasma formation by 1-ns pulses at 1064 nm wavelength. In each screenshot, the upper left graph portrays the evolution of the ionization degree as a function of time. Full ionization (i.e. a degree of 1.0) corresponds to a free-electron density of $6.68 \times 10^{22} \text{ cm}^{-3}$. The dark blue line represents the total degree of ionization, the bright blue line the part produced by MP-effects, and the green line the part arising from thermal emission of electrons. The upper right graph presents the maximum ionization degree produced during a laser pulse as a function of irradiance. Besides the total ionization degree, the parts arising from MPI and thermal emission are also plotted. The lower left graph shows the temporal evolution of the plasma temperature (red) in relation to the temporal shape of the laser pulse (grey). The lower right graph shows the peak temperature reached during breakdown as a function of irradiance.

Fig 40a) $\lambda = 1064 \text{ nm}$, 1 ns , $\rho_{\text{cr}} = 10^{20} \text{ cm}^{-3}$, $\alpha = 50 \text{ cm}^{-1}$

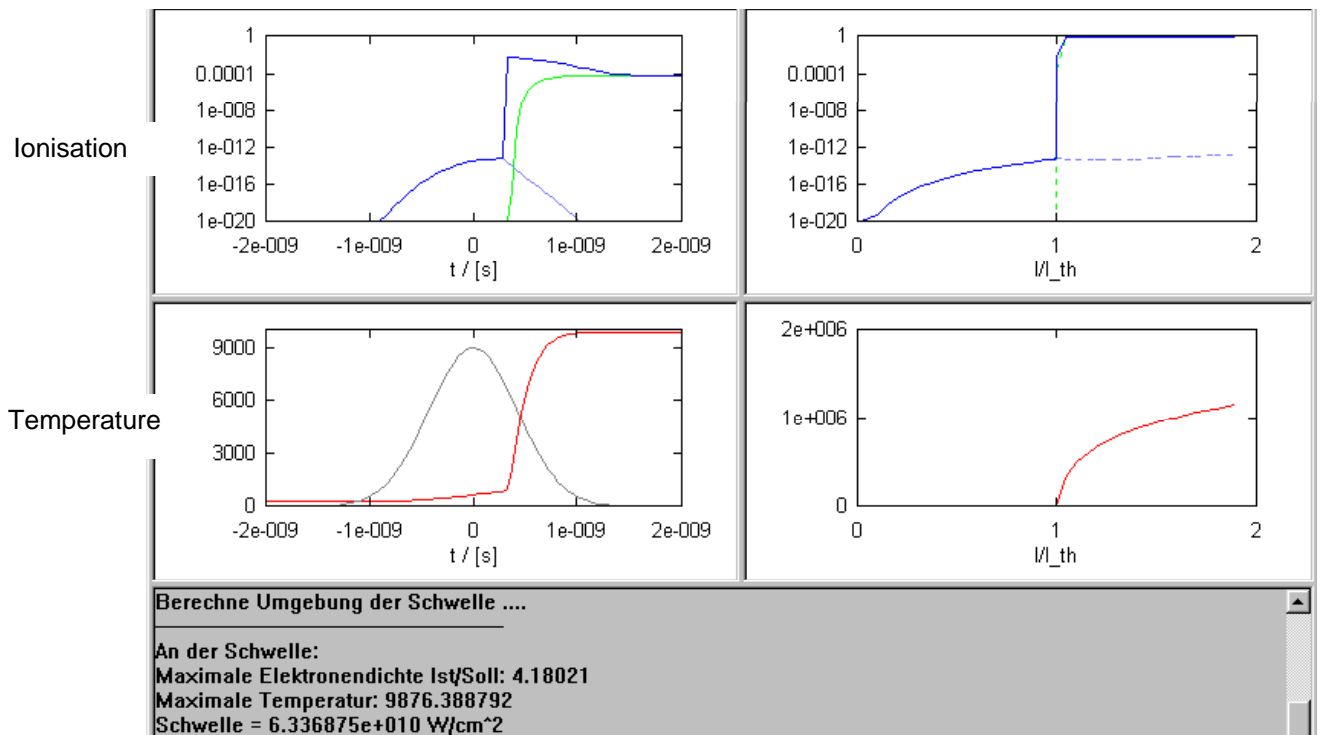


Fig 40b) $\lambda = 1064 \text{ nm}$, 1 ns , $\rho_{\text{cr}} = 10^{20} \text{ cm}^{-3}$, $\alpha = 150 \text{ cm}^{-1}$

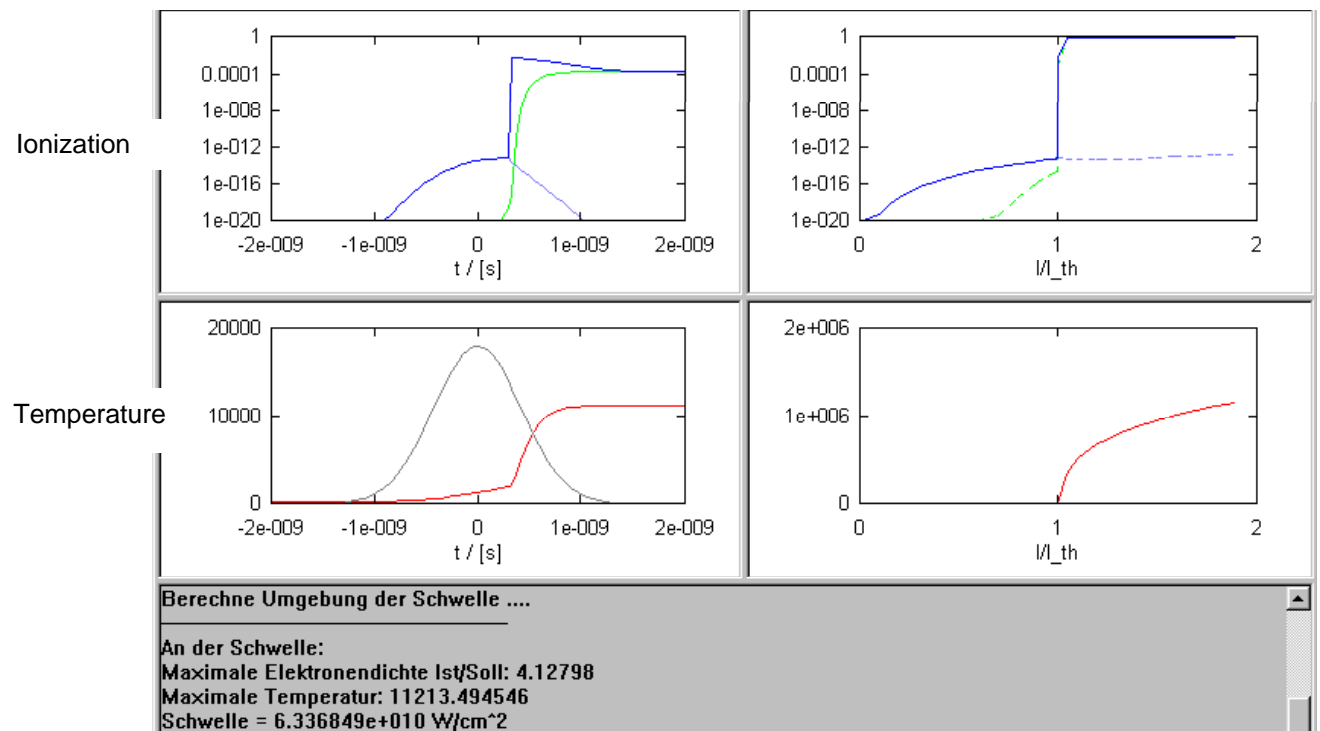


Fig 40c) $\lambda = 1064 \text{ nm}$, 1 ns , $\rho_{\text{cr}} = 10^{20} \text{ cm}^{-3}$, $\alpha = 175 \text{ cm}^{-1}$

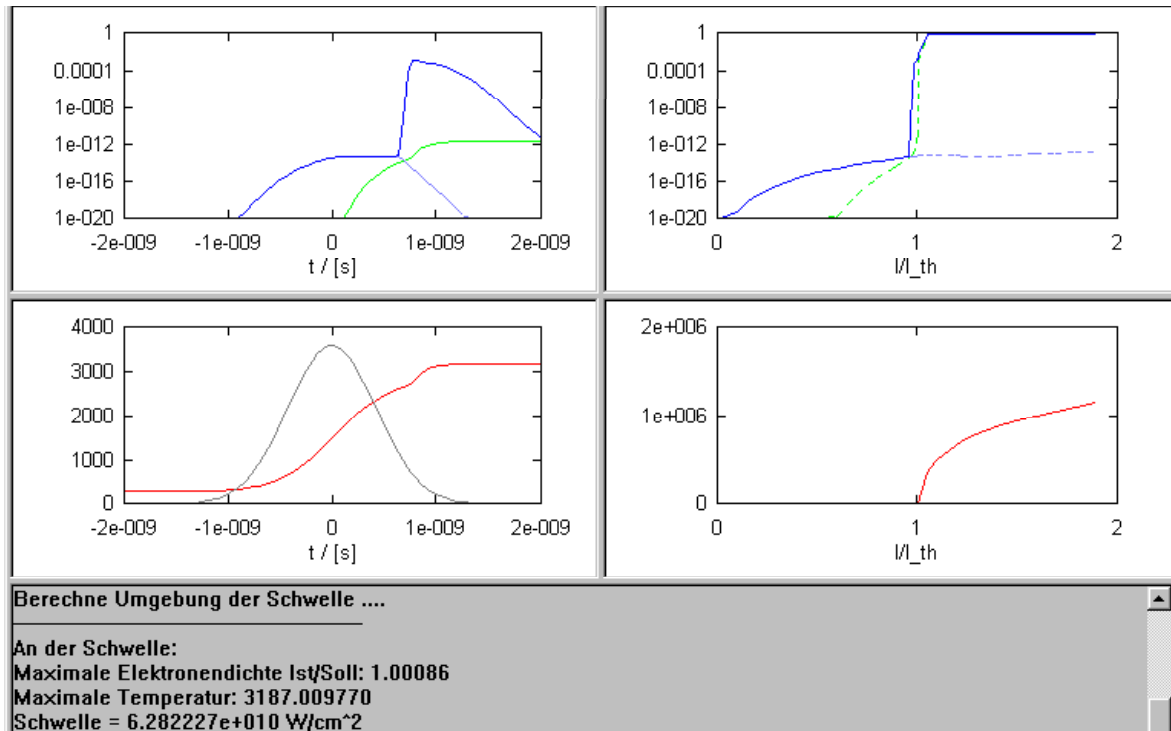


Fig 40d) $\lambda = 1064 \text{ nm}$, 1 ns , $\rho_{\text{cr}} = 10^{20} \text{ cm}^{-3}$, $\alpha = 500 \text{ cm}^{-1}$

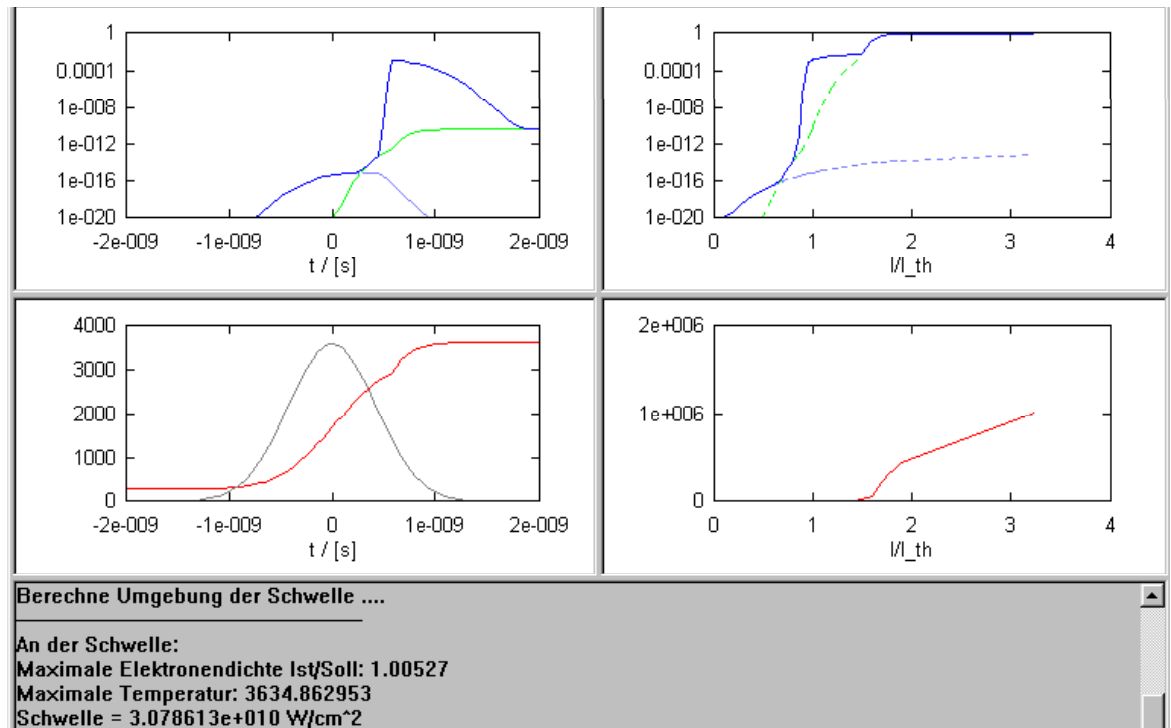


Fig 40e) $\lambda = 1064 \text{ nm}$, 1 ns , $\rho_{\text{cr}} = 10^{20} \text{ cm}^{-3}$, $\alpha = 5000 \text{ cm}^{-1}$

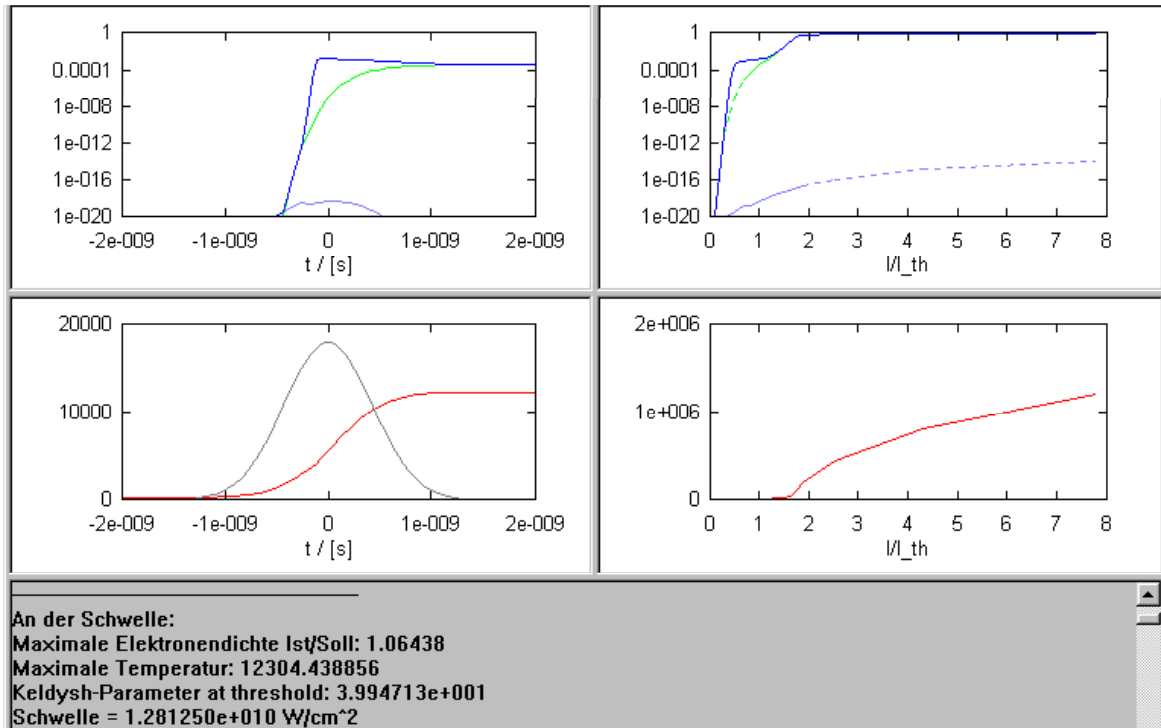
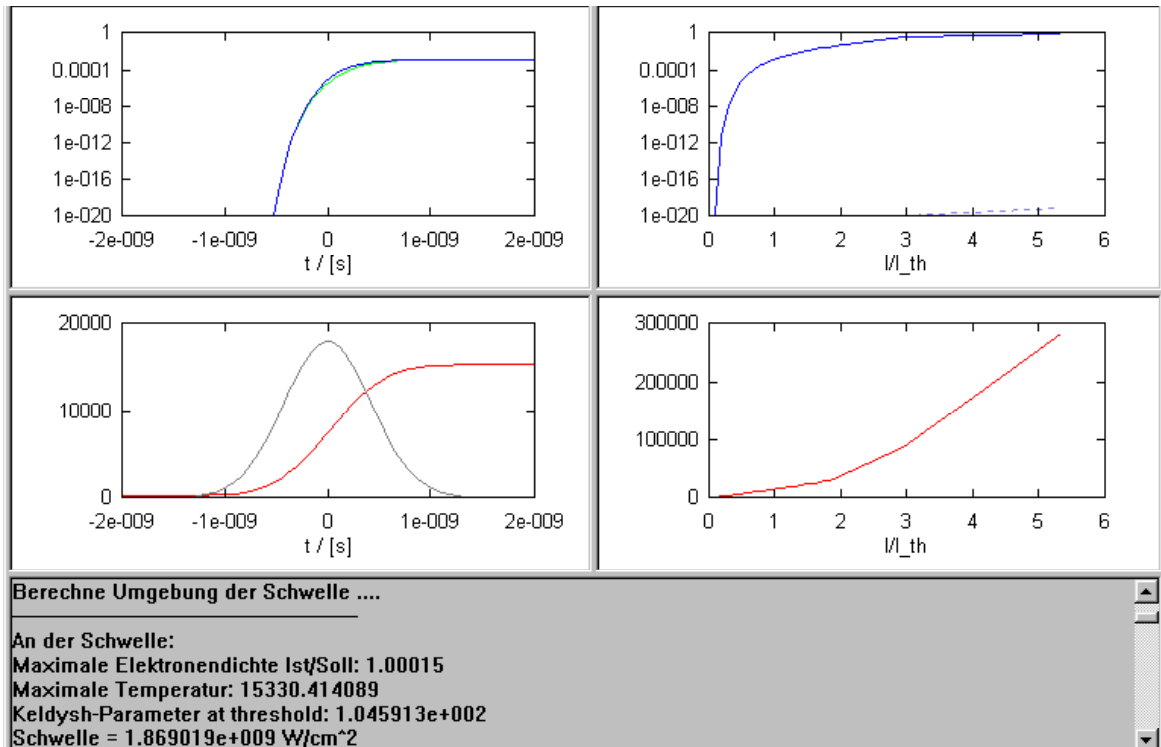


Fig 40f) $\lambda = 1064 \text{ nm}$, 1 ns , $\rho_{\text{cr}} = 10^{20} \text{ cm}^{-3}$, $\alpha = 50\,000 \text{ cm}^{-1}$



For long wavelengths (1064 nm) and transparent media, multiphoton-generation of the seed electron is the main hurdle for the occurrence of optical breakdown. Once a free electron is generated, cascade ionization becomes the dominant process, leading to an abrupt increase of the free-electron density by 10 orders of magnitude within a fraction of the laser pulse. For large free-electron densities, recombination processes stop the cascade down because

recombination is proportional to ρ^2 while cascade ionization is proportional to ρ . Nevertheless, the ionization avalanche overshoots the critical electron density $\rho_{cr} = 10^{20} \text{ cm}^{-3}$ by a factor of ≈ 4 . Subsequently, collisional transfer of kinetic energy of free electrons to heavy particles results in a rapid heating of the plasma volume that, in turn, leads to a massive thermal emission of free electrons and to full ionization of the focal volume at the end of the laser pulse (section 6.1).

The above scenario changes only slightly for linear absorption coefficient of $\alpha = 50 \text{ cm}^{-1}$ and $\alpha = 150 \text{ cm}^{-1}$ (Figs. 40a and b). An important difference is that linear absorption has led to temperatures of 850 K and 1750 K, respectively, when the avalanche starts. The probability of thermal excitation of an electron into the conduction band is low at these temperatures, but the probability of MPI at IR wavelengths is also low. Thus thermal excitation starts to compete in generating the seed electron for the avalanche, and this is the reason why the highest likelihood for the start of the avalanche is now found after the peak of the laser pulse when the temperature is larger than right at the peak where the probability for MPI is largest. Note that the contribution of MPI to the heating of the focal region is negligible compared to linear absorption and to CI. One can assess the contribution of the nonlinear absorption mechanisms to heating by looking at the respective number density of free-electrons produced. It is almost 10^{11} times larger for CI than for MPI.

With increasing linear absorption, it becomes ever more likely that the seed electron is produced via thermal excitation. For $\alpha = 175 \text{ cm}^{-1}$, linear absorption seems to be strong enough to produce a seed electron by thermal excitation, as indicated by a slight reduction of the irradiance threshold below the value required for MPI generation of the initial electron. The temperature at the start of the avalanche is here about 2700 K. Due to the decrease of the threshold irradiance, the avalanche does not overshoot the critical electron density any more (Fig 40c). Moreover, since the thermal seed electron is produced late during the pulse, the avalanche starts so late, that it can “extract” only a small portion of the laser pulse energy. Therefore, the nonlinear absorption via CI and the corresponding additional temperature rise are suddenly much smaller than for weaker linear absorption (Fig. 39b). While for $\alpha \leq 150 \text{ cm}^{-1}$ (regime 1 in Fig. 39b) the temperature rise is mostly caused by nonlinear absorption, for $\alpha \geq 175 \text{ cm}^{-1}$ heating by linear absorption is the dominant process (regimes 2 and 3 in Fig. 39b).

The temperature at the start of the avalanche is about 2700 K for all investigated absorption coefficients between 175 cm^{-1} and 5000 cm^{-1} (Figs. 40c-e). Plasma formation via nonlinear absorption is thus “ignited” by linear absorption – a typical scenario, for example, for laser lithotripsy [Ten87, Vog97]. The increasing linear absorption coefficient reduces the energy required for producing the heat generating the seed electron. Therefore, the breakdown threshold decreases with increasing absorption coefficient. With decreasing threshold irradiance, the ionization avalanche progresses more slowly and thus has to start earlier during the laser pulse to reach the critical electron density (Figs. 40c-e).

For large absorption coefficients, the threshold is not any more determined by the irradiance required to produce a thermal seed electron but rather by the irradiance to generate the critical free-electron density via CI and thermal ionization. With increasing linear absorption, an ever larger fraction of the free electrons is produced thermally (regime 3 in Fig. 39b). For $\alpha = 5000 \text{ cm}^{-1}$, CI still dominates but for $\alpha = 50\,000 \text{ cm}^{-1}$, it has entirely lost its dominant role (Figs. 40e-f). The temperature obtained at the end of the laser pulses increases with linear absorption until a limiting value is reached where the critical free electron density can be produced by thermal ionization alone which is almost the case for $\alpha = 50\,000 \text{ cm}^{-1}$. The corresponding temperature is 15330 K.

Compared to the case of a completely transparent target, linear absorption leads to a reduction of the maximum free electron density and peak temperatures for irradiances at or slightly above the breakdown threshold. The irradiance range for which this reduction applies reaches up to about $1.5 \times I_{th}$ for $\alpha = 175 \text{ cm}^{-1}$, and up to about $3 \times I_{th}$ for $\alpha = 50\,000 \text{ cm}^{-1}$. Farther above the breakdown threshold, the model predicts full ionization and very high temperatures like for transparent media. Such values are not reached in reality. The discrepancy arises because the model does neither consider the plasma growth towards the incoming laser beam and the resulting shielding effect for the focal region at superthreshold irradiances nor the expansion of the plasma during the laser pulse that would both reduce the free electron densities and peak temperatures reached. Another unrealistic outcome of the model is that the temperature and free electron density predicted for the focal region remain constant after the end of the laser pulse because the plasma expansion leading to adiabatic cooling is not considered. In spite of these limitations, the model is a valuable tool for the prediction of breakdown thresholds and the analysis of the breakdown dynamics for irradiances below and slightly above the breakdown threshold.

UV Pulses (355 nm)

Fig 41a) $\lambda = 355 \text{ nm}$, 1 ns , $\rho_{\text{cr}} = 10^{20} \text{ cm}^{-3}$, $\alpha = 50 \text{ cm}^{-1}$

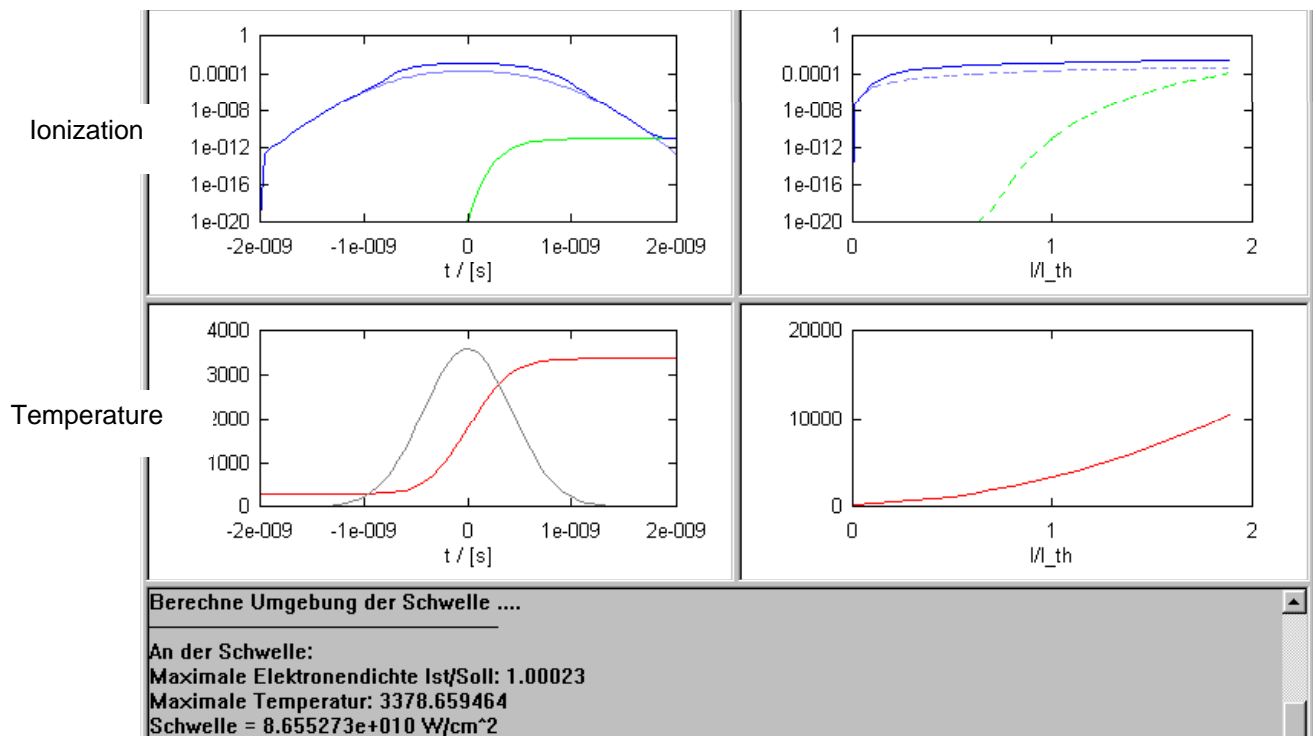


Fig 41b) $\lambda = 355 \text{ nm}$, 1 ns , $\rho_{\text{cr}} = 10^{20} \text{ cm}^{-3}$, $\alpha = 500 \text{ cm}^{-1}$

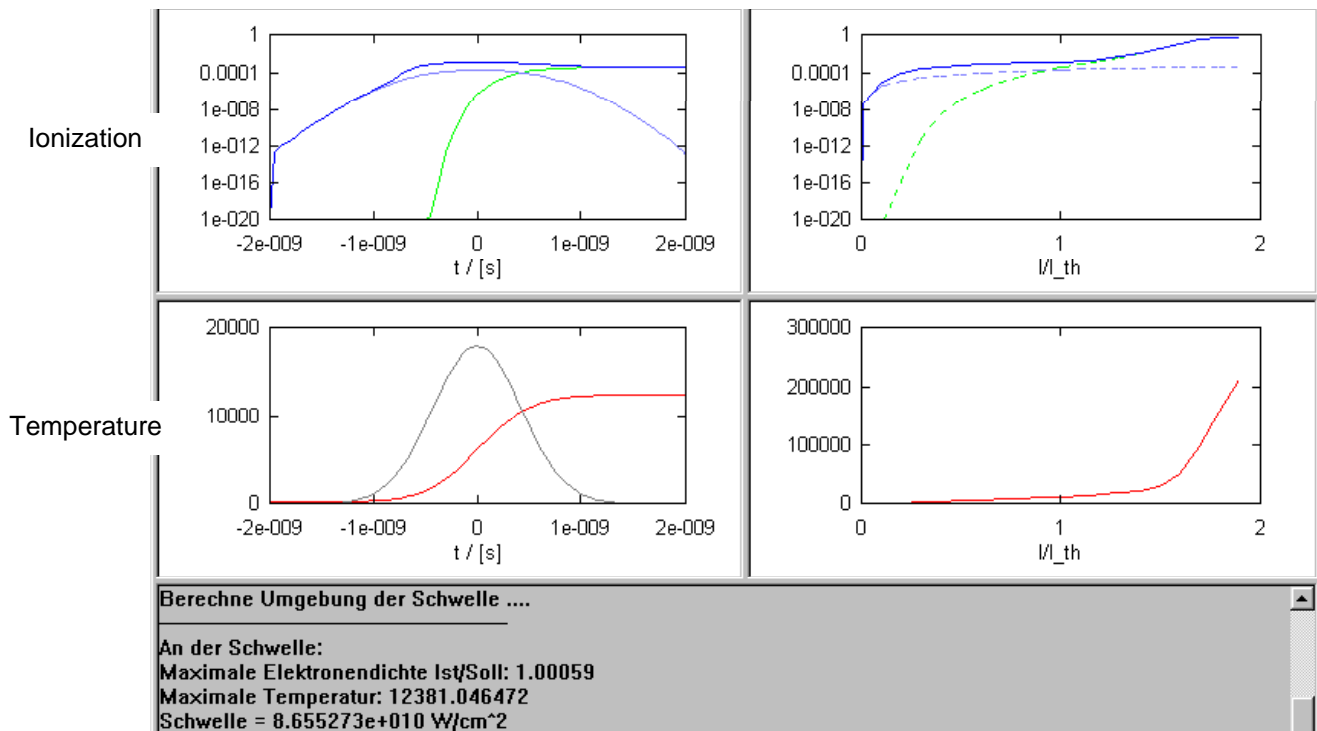


Fig 41c) $\lambda = 355 \text{ nm}$, 1 ns , $\rho_{\text{cr}} = 10^{20} \text{ cm}^{-3}$, $\alpha = 5000 \text{ cm}^{-1}$

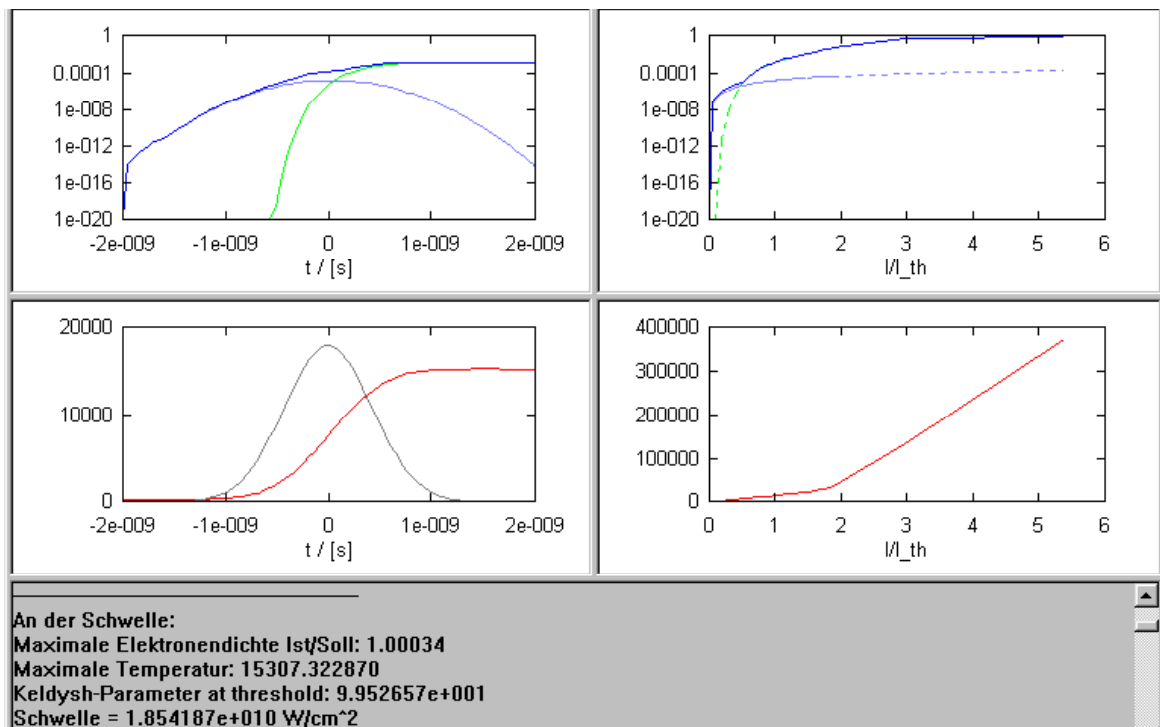


Fig 41d) $\lambda = 355 \text{ nm}$, 1 ns , $\rho_{\text{cr}} = 10^{20} \text{ cm}^{-3}$, $\alpha = 50\,000 \text{ cm}^{-1}$

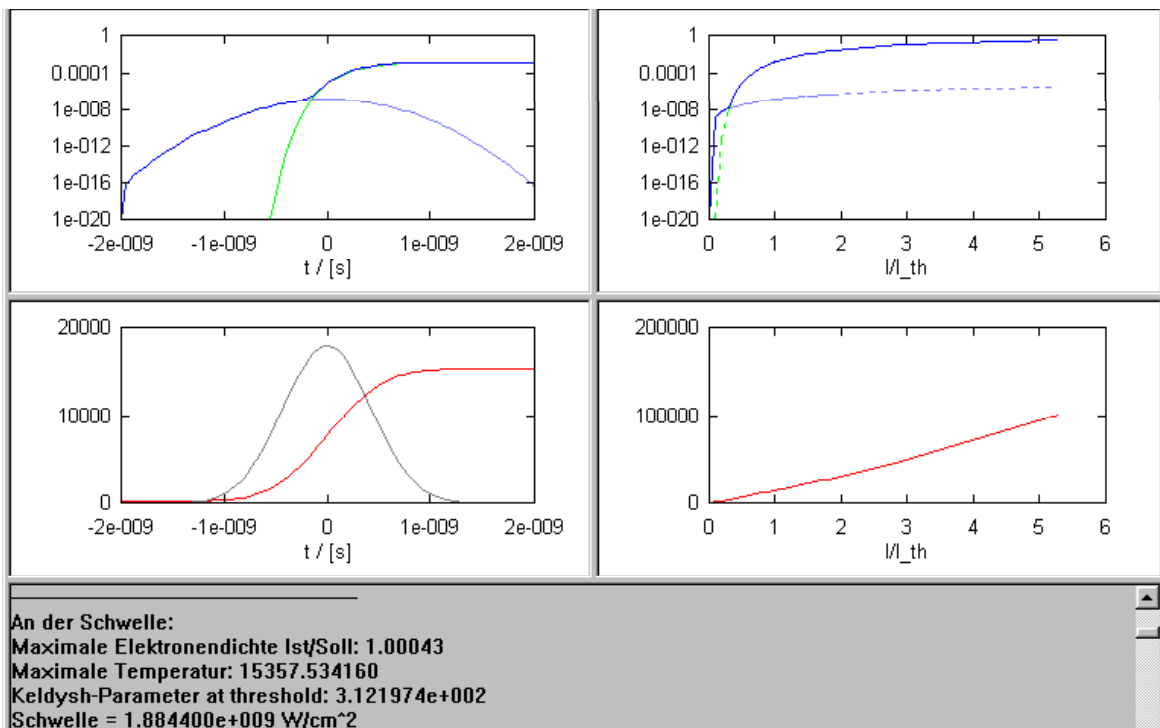


Figure 41 (previous two pages): Screenshots with the results of the numerical simulations of plasma formation by 1-ns pulses at 355 nm wavelength. The upper left graph portrays the evolution of the ionization degree as a function of time. The dark blue line represents the total degree of ionization, the bright blue line the part produced by MP-effects, and the green line the part arising from thermal emission of electrons. The upper right graph presents the maximum ionization degree produced during a laser pulse as a function of irradiance. Besides the total ionization degree, the parts arising from MPI and thermal emission are plotted as dashed blue and green lines, respectively. The lower left graph shows the temporal evolution of the plasma temperature (red) in relation to the temporal shape of the laser pulse (grey). The lower right graph shows the peak temperature reached during breakdown as a function of irradiance.

For short wavelengths in the UV region of the optical spectrum, seed electrons produced by MPI are always readily available at the irradiance level required for the ionization cascade to reach the critical electron density ρ_{cr} . Therefore, the ionization cascade at the breakdown threshold does not overshoot ρ_{cr} , such as predicted for IR breakdown in media with weak linear absorption (Figs 40a,b).

Although MPI plays a much larger role at short wavelengths, the irradiance breakdown threshold for 355-nm irradiation is similar to the threshold at 1064 nm. The reason is that CI is less efficient for UV wavelengths than for IR wavelengths because the cross section for inverse bremsstrahlung absorption is proportional to λ^2 . The opposite wavelength dependences of MPI and CI approximately balance one another, and this explains why the overall wavelength dependence of the breakdown threshold is relatively weak.

In spite of the similar breakdown thresholds, the temporal evolution of plasma formation at 355 nm differs strongly from that at 1064 nm. Due to the early generation of seed electrons by MPI, a large electron density is achieved already before the intensity peak of the laser pulse is reached. This produces a significant temperature rise through collisional transfer of kinetic energy from the free electrons to heavy particles already early during the laser pulse. Even for a small absorption coefficient of 10 cm^{-1} , a temperature of about 1400 K is reached already at the peak of the pulse, and T increases to 2510 K until the end of the pulse (Fig. 41a). With increasing absorption coefficient, an ever larger temperature rise is observed (transition from regime 1 to 2 in Fig. 39a). The additional heating can almost exclusively be attributed to linear absorption of laser energy.

Let us now consider how heating by linear absorption influences the process of plasma formation. The number of thermally generated free electrons is given by

$$N_{therm} = N_0 \frac{kT}{\Delta E} e^{-\frac{\Delta E}{kT}}, \quad (27)$$

where N_0 denotes the number of electrons in the valance band, ΔE is the band gap energy, T the temperature, and k the Boltzmann constant. The equation shows that the number of thermal electron grows very rapidly with increasing temperature. We know from the above discussion of IR breakdown that thermal generation of seed electrons for CI becomes relevant for $T \geq 2700 \text{ K}$ which is reached at $\alpha = 175 \text{ cm}^{-1}$ for $\lambda = 1064 \text{ nm}$. For $T = 5400 \text{ K}$, the rate of thermal ionization is already 7 orders of magnitude larger than for $T = 2700 \text{ K}$. Thus, with increasing linear absorption of the target, thermal ionization does not only seed the ionization cascade but provides an rapidly increasing number of electrons feeding the cascade, in addition to the contribution of MPI. This explains the decrease of the irradiance threshold for breakdown observed for large absorption coefficients. The threshold drops for absorption coefficients larger than $\alpha = 500 \text{ cm}^{-1}$ for which a temperature exceeding 6000 K is reached at the peak, and 12,280 K at the end of the laser pulse.

For $\alpha \leq 500 \text{ cm}^{-1}$, when MPI still provides the majority of the of the free electrons feeding CI, the maximum of the free electron density coincides with the peak of the laser pulse. By contrast, for $\alpha = 5000 \text{ cm}^{-1}$ (Fig. 41c), the electron density continues to increase until the end of the pulse because the cascade is feed by an increasing number of thermal electrons produced through linear absorption. Towards the end of the pulse the plasma temperature is so high (about 15 000 K) that thermal ionization becomes the dominant mechanism of free-electron generation.

In summary: With increasing linear absorption, the breakdown threshold decreases both for IR and UV pulses, and an ever larger fraction of the free electrons is produced thermally. The temperature obtained at the end of the laser pulses increases until a limiting value is reached where the critical free electron density can be produced by thermal ionization alone. This seems to be the case for $\alpha > 5\,000 \text{ cm}^{-1}$. For the largest absorption coefficients investigated, plasma formation is largely a thermal process regardless of laser wavelength. Thus it is not surprising that the predicted breakdown thresholds and maximum temperatures for UV and IR breakdown at $\alpha = 50\,000 \text{ cm}^{-1}$ are almost the same: the thresholds are $1.884 \times 10^9 \text{ W/cm}^2$ for 355 nm and $1.869 \times 10^9 \text{ W/cm}^2$ for 1064 nm, and the respective temperatures are 15357 K and 15330 K.

Differences between UV and IR breakdown in linear absorbing media

In IR breakdown, a reduction of the irradiance threshold occurs once seed electrons for CI are produced by heating through linear absorption instead of MPI. In UV breakdown, a decrease of the breakdown threshold requires as well that thermally generated free electrons become as numerous or more abundant than electrons produced by MPI. However, since MPI occurs much more easily at UV wavelengths, much higher temperatures than in IR breakdown must be produced through linear absorption to fulfill this requirement.

In both wavelength regions, heating in the focal region can be largely attributed to nonlinear absorption for absorption coefficients up to about $100\text{--}150\text{ cm}^{-1}$. For media with larger absorption coefficients, heating through linear absorption dominates. The transition from one heating regime to the other is for UV wavelengths associated with a temperature rise because of the increasing contribution of linear absorption. However, for IR wavelengths it is first associated with a temperature drop occurring as a consequence of the transition, and only for larger absorption coefficients with a temperature rise.

6.2.2 Discussion

Low-density plasmas produced by ns pulses

The plots of ionisation vs I/I_{th} in Fig 40 reveal that in IR breakdown in weakly absorbing media ($\alpha \leq 200\text{ cm}^{-1}$), the maximum electron density ρ_{max} increases by more than 10 orders of magnitude at threshold. This means that no low-density plasmas are formed below the breakdown threshold. However, for large absorption coefficients ($\alpha > 1000\text{ cm}^{-1}$), a relatively high free-electron density is produced not only at threshold but also in a narrow irradiance range below threshold. In this regime, the free electrons are mostly generated by CI even if for larger irradiances thermal ionization dominates. Only for $\alpha = 50\,000\text{ cm}^{-1}$ free electrons are also below threshold largely produced by thermal ionization.

For UV breakdown, the situation is quite different. The plots in Fig. 41 predict that low-density plasmas are produced by in a broad irradiance range below threshold even in weakly absorbing media ($\alpha \leq 10\text{ cm}^{-1}$). For $\alpha \leq 500\text{ cm}^{-1}$, the dominant process leading to low-density plasma formation is MPI or MPI-supported CI. For very large absorption coefficients, however, thermal ionization plays a major role above and below the breakdown threshold. Nevertheless, for sufficiently small irradiance there is still a regime where MPI dominates.

Role of linear absorption in femtosecond breakdown

The energy deposited into the electronic system of atoms or molecules either through linear or nonlinear absorption needs to be dissipated via electron-phonon coupling before a thermodynamic “temperature” is reached and thermal electron emission can occur. Because thermalization lasts a few picoseconds to a few tens of picoseconds, thermal ionization based on linear absorption can occur only long after the end of a femtosecond laser pulse, and will not influence the breakdown threshold.

However, linear absorbing molecules in an aqueous medium may influence the rate of free electron generation through multiphoton processes and thus alter the breakdown threshold., as discussed in section 6.3.

Procedures in which plasma formation is influenced by thermal ionization

Pulsed laser lithotripsy is usually performed with lasers emitting in the visible and IR range of the optical spectrum, with wavelengths ranging from 532 nm (frequency doubled Nd:YAG laser) to $2.1\text{ }\mu\text{m}$ (holmium laser). With the exception of the effects caused by the free-running holmium laser [Cha99], laser lithotripsy always relies on plasma formation at the stone surface mediated by linear absorption [Ten87, Vog97]. Since usually microsecond pulses are used, plasma formation is initiated by heating of the target [Ten87]. Unfortunately, no reliable data on the absorption coefficients of urinary and biliary calculi are available; in most publications only data on optical breakdown thresholds are reported. It can be assumed that the absorption coefficient of the bulk material is usually below 200 cm^{-1} corresponding to regime 1 in Figs. 39a and b, while the absorption coefficient in highly absorbing regions of pigmented stones may be somewhat larger and belong to regime 2 (the attenuation coefficient of melanin in skin at $\lambda = 500\text{ nm}$ is $\approx 600\text{ cm}^{-1}$ [Vog03, Sad01]). Therefore, changes of the breakdown characteristics by linear absorption are expected already for nanosecond laser pulses. They will probably be even more pronounced for the longer pulses of about $1\text{ }\mu\text{s}$ duration that are frequently employed for lithotripsy. The model calculations presented here for $\tau = 1\text{ ns}$ would need to be repeated for $1\text{ }\mu\text{s}$ pulse duration to obtain quantitative results relevant for lithotripsy.

Cell surgery using nonosecond pulses. A very important biomedical application of plasma formation supported by linear absorption is *cellular surgery* such as optoinjection of cells or separation of cells from histologic specimens by laser microdissection and subsequent laser catapulting of the dissecta into a vial for proteomic and genomic analysis (see section 2). Sometimes pulses from a frequency doubled Nd:YAG ($\tau = 3$ ns, $\lambda = 532$ nm) laser are used for optoinjection [Kra98]. Since the linear absorption of cellular structures is small in the visible region of the optical spectrum ($\alpha < 100$ cm⁻¹), breakdown is governed by nonlinear absorption and occurs somewhere in regime 1 of Fig. 39. This is confirmed by the good agreement between experimental work on optoinjection [Kra98] and experimental studies on optical breakdown in water at large NA [Ven02].

Commercial microbeam systems mostly employ a nitrogen laser emitting 3-ns pulses at 337 nm wavelength. At this wavelength, the attenuation coefficient for unstained cells can reach 1000 cm⁻¹, while it amounts to about 5000 cm⁻¹ for stained histologic specimens, and to 40 000 cm⁻¹ for the polyethylene-naphthalate polymer foil used for laser pressure catapulting [Lor04]. This means that breakdown occurs in regime 2 of Fig. 39a where plasma formation is strongly supported by linear absorption. Here, the temperatures predicted for the breakdown threshold are between 12 000 and 15 000 K (see Figs. 41b-d), and temperatures larger than 1000 K are still predicted for irradiances as small as $0.3 I_{th}$. Since biological materials and polymers thermally disintegrate at temperatures around 1000 K, it is expected that the ablation threshold in regime 2 is considerably lower than the breakdown threshold. This agrees with experimental results from our group showing that the ablation threshold for nitrogen laser pulses focused on histologic specimens is 2-4 times below the plasma formation threshold [Lor04]. However, the pulse energies and irradiances that are actually used for microdissection and laser pressure catapulting are above the breakdown threshold [Lor04]. We can thus conclude that these processes involve the formation of fully developed plasmas with free-electron densities above 10^{20} cm⁻³.

Femtosecond laser dissection of cell organelles. It was reported that Giemsa-stained chromosomes have a smaller ablation threshold than unstained chromosomes when pulses from a fs oscillator were used for dissection [Koe01]. Different threshold were also observed when model-locked ps pulse trains were used for intracellular dissection of cell organelles and strands of the cytoskeleton that were stained with fluorescent dyes of different absorption coefficients [Bot04]. The lowering of the ablation threshold is most likely due to the facilitation of multiphoton processes by the one-photon electronic excitation into an intermediate energy level. Such processes will play a role mainly when mode-locked pulses with high repetition rate are used for which ablation occurs in the low-density plasma regime (see section 7 below). In this regime, most free electrons are produced by photoionization (MPI or tunneling), and changes of the MPI dynamics has a large effect. By contrast, when amplified fs pulses are used, dissection relies on bubble formation induced by thermoelastic tensile stress (see section 7 below), and much larger free electron densities are required to produce the bubble. For this, avalanche ionization must occur within the entire focal volume and thus the energy levels in water become more important than the levels in the scattered chromophores. Therefore, linear absorbing chromophores play a smaller role when amplified fs pulses rather than oscillator pulses are used for material processing.

Ocular laser safety. Here, the linear absorption in the retinal pigment epithelium is very large. In a certain range of pulse durations, where the damage threshold is determined by thermal effects, this leads to a constant radiant exposure threshold for ocular damage [ANSI93]. For ultrashort laser pulses, however, the irradiance at this radiant exposure value becomes so high that nonlinear absorption effects exceed the linear absorption, and the damage threshold decreases [Cai99]. Modifications of the nonlinear absorption process produced by linear light absorption in the RPE in this range of pulse durations will be due to the facilitation of multiphoton ionization.

Pulsed laser surface ablation of strongly absorbing materials at large radiant exposures well above the ablation threshold. Here plasma formation in the target often ignites plasma formation in the ambient atmosphere and thus results in an unwanted shielding effect.

In biological media, UV-pulses at wavelengths around 200 nm and IR pulses at wavelengths around 3 μ m are strongly absorbed. However, the mechanism triggering plasma formation differs depending on the wavelength of the laser irradiation. For wavelengths in the mid-IR, only thermal emission can provide the seed electrons for avalanche ionization. The experimental threshold for plasma formation at $\lambda = 3$ μ m is about 5.5 J/cm² [Api04], i.e. 55 times larger than the ablation threshold of about 0.10 J/cm². For strongly absorbed UV wavelengths, where multiphoton processes come into play, the plasma formation threshold is only about 6 times larger than the ablation threshold [Ven95]. The fact that both thresholds are much closer together for UV wavelengths indicates that multiphoton processes supported by linear absorption are more efficient for triggering plasma formation than thermal emission.

Conclusions

The extended model of plasma formation is useful to assess changes of the breakdown threshold by linear absorption. However, it yields false results for the plasma lifetime because the plasma expansion leading to adiabatic cooling is not considered. Neglect of the plasma expansion also leads to unrealistically high plasma temperatures for plasmas produced by nanosecond pulses. Another factor contributing to the unrealistically high plasma temperatures is the lack of consideration of shielding and reflection of the incoming laser pulse by dense plasmas. This shortcoming also affects the modeling of plasma formation at superthreshold energies. Future modeling thus needs to refine the treatment of energy deposition into the plasma and to combine simulations of the plasma formation with simulations of the hydrodynamic response. For picosecond and femtosecond plasmas, simulations of the hydrodynamic response need to incorporate thermoelastic effects. Combined simulations of the plasma formation and the hydrodynamic response could, for the first time, provide a unified picture of the optical and mechanical breakdown events in aqueous media and tissue. However, such an effort requires the availability of advanced hydrodynamic codes and mainframe computers.

6.3. INFLUENCE OF LINEAR ABSORPTION ON MULTIPHOTON IONIZATION

In the introduction of section 6 we mentioned the possibility to model the influence of linear absorption on multiphoton ionization by introducing an intermediate energy level between the ground state and exciton state that can be reached by one-photon absorption, and to consider multiphoton processes both for electrons in the ground state and the intermediate state. However, this scenario will be realistic only for very few chromophores and wavelengths, and it does not make sense to establish a complex extension of the model that is valid only for specific, rare cases.

The excitation pathways of electronic, vibrational and rotational energy levels in organic molecules are generally very complex, differ from chromophore to chromophore, and depend on the duration of the laser pulse compared to relaxation times of the excited states. A global solution that relates the degree of ionization at the end of the laser pulse to the laser parameters and the concentration and the absorption cross section of chromophores in an aqueous solution must therefore disregard the specific energy levels involved in the photophysical process.

Many researchers have assumed a certain background energy density in the target material to account for impurities, localized electronic states, or chromophores that facilitate photionization. However, this approach completely neglects the irradiance dependence of the photophysical processes and the temporal evolution of the free-electron density created during the laser pulse by such processes.

A better approach for a global modeling of ionization through photophysical processes is provided by the rate equation

$$\left(\frac{d\rho}{dt}\right)_{pp} = AKI^m, \quad m < k \quad (28)$$

where K denotes the concentration (number density) of the chromophores, A their absorption cross section, m is the order of the one- or multiphoton process involved in free-electron generation from chromophores, and k the order of the multiphoton process in the pure medium. The parameters A and m allow to adjust Eq. (2) to the properties of specific chromophores in solution or to a desired value of $(\rho_{\max})_{pp}$. Separate monitoring of $(d\rho/dt)_{pp}$ throughout the calculations will provide $(\rho_{\max})_{pp}$ and thus allow to keep track of the contribution of photophysical ionization of chromophores compared to photoionization and avalanche ionization in the pure medium.

7 IMPLICATIONS FOR LASER EFFECTS ON BIOLOGICAL CELLS AND TISSUES

Two parameter regimes have been established for femtosecond laser nanosurgery: One technique uses long pulse series from fs oscillators with repetition rates in the order of 80 MHz and pulse energies well below the optical breakdown threshold [Koe99a, Koe01a, Tir02, Zei03, Sac05, Sup05, Rie05, Smi01, Oeh008]. From 40000 pulses [Koe99a] to several million pulses [Tir02, Sac05] have been applied at one specific location to achieve the desired dissection or membrane permeabilisation. The other approach uses amplified pulse series at 1 kHz repetition rate with pulse energies slightly above the threshold for transient bubble formation [Yan04, Wat04, Hei05]. Here the number of pulses applied at one location varied between 30 [Wat04] and several hundred [Yan04, Hei05].

Based on the discussion of the physical effects associated with femtosecond laser induced plasma formation in the previous sections, we now proceed to explain the working mechanisms of both modalities for cell surgery. For this purpose, the different low-density plasma effects and physical breakdown phenomena are summarized in **figure 42**, together with experimental damage, transfection and dissection thresholds on cells. The different effects are scaled by the corresponding values of free-electron density and irradiance.

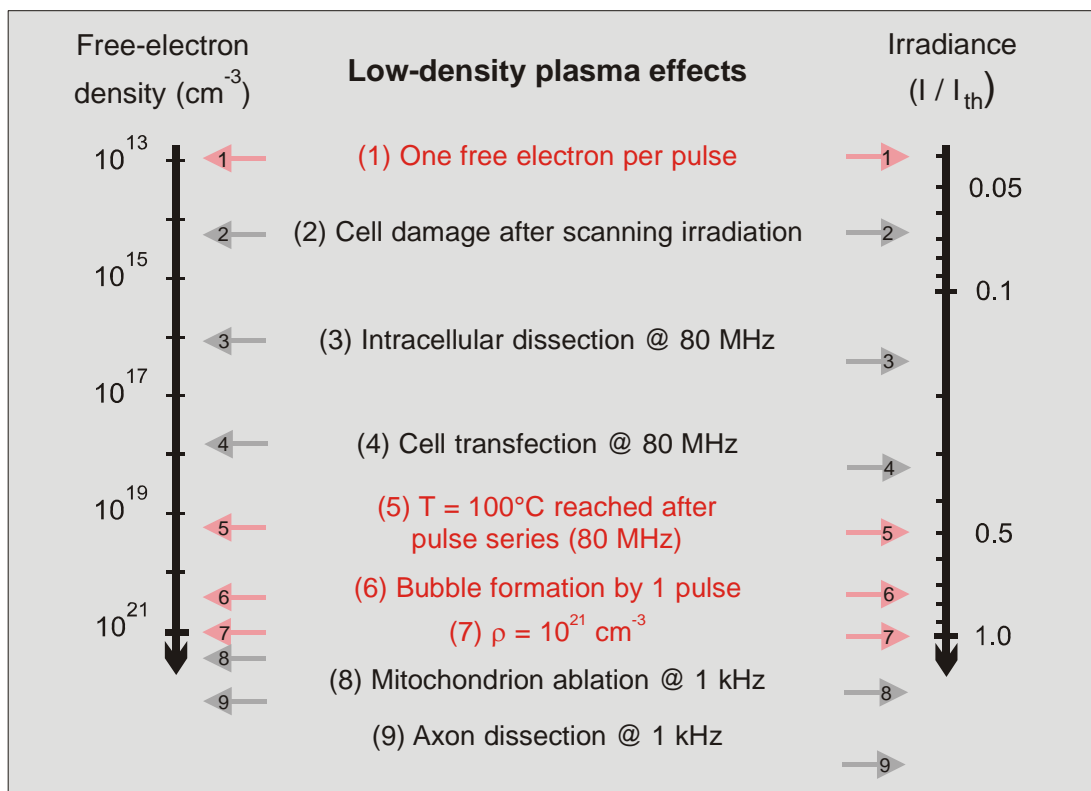


Figure 42: Overall view of physical breakdown phenomena induced by femtosecond laser pulses, together with experimental damage, transfection and dissection thresholds on cells. The different effects are depicted together with the corresponding values of free-electron density and irradiance. The irradiance values are normalized to the optical breakdown threshold I_{th} defined by a critical electron density of $\rho_{cr} = 10^{21} \text{ cm}^{-3}$. All data refer to plasma formation in water with femtosecond pulses of about 100 fs pulses and 800 nm wavelength; the exact pulse durations are given in table 2.

Chemical cell damage (2) refers to membrane dysfunction and DNA strand breaks leading to apoptosis-like cell death observed after scanning irradiation of PtK2 cells with 800-nm pulses at 80 MHz repetition rate [Tir01]. Chromosome dissection (3) relates to the intranuclear chromosome dissection [4], and (4) to cell transfection by transient membrane permeabilisation [Tir02], both performed using 80-MHz pulse trains from a femtosecond oscillator. Mitochondrion ablation (8) refers to the ablation of a single mitochondrion in a living cell using 1-kHz pulse trains [She05], and axon dissection (9) applies to axotomy in life C-elegans worms carried out with sequences of pulses emitted at 1 kHz repetition rate from a regenerative amplifier [Yan04]. Points (1), (5), (6) and (7) stand for physical events or threshold criteria. The respective laser parameters, and the absolute values of irradiance and free-electron density for each point are listed in **table 5**.

Effect	Pulse duration (fs) NA	Energy (nJ)	Repetition rate	Dwell time (ms) Average power	Number of pulses per spot	Electron density (cm ⁻³)	Volum. Energy density (Jcm ⁻³)	Irradiance (×10 ¹² W cm ⁻²)	Normalized irradiance I / I _{rate}
(1) One free electron per pulse	100 1.3		single pulse	-	1	2.1×10 ¹³	4.9×10 ⁻⁵	0.26	0.04
(2) Chemical cell damage after scanning irradi. [144]	90 1.3	0.0875	80 MHz	0.6 per cell 7 mW	4.8 × 10 ⁴ per cell	1.5×10 ¹⁴	3.5×10 ⁻⁴ for 1 pulse	0.44	0.067
(3) Intranuclear chromosome dissection @ 80 MHz [4]	170 1.3	0.38	80 MHz	0.5 per chromosome dissection 30 mW	4 × 10 ⁴	2.0×10 ¹⁶	4.7×10 ⁻² for 1 pulse	0.10	0.15
(4) Cell transfection @ 80 MHz [53]	170 1.3	0.6-1.2	80 MHz	12 50-100 mW	9.6 × 10 ⁵	5-200 ×10 ¹⁷	1.2-47 for 1 pulse	1.6-3.1	0.25-0.48
(5) ΔT of 100°C after many pulses	100 1.3		80 MHz	≥ 0.1	≥0.8 × 10 ⁴	2.1×10 ¹⁹	50 for 1 pulse	3.3	0.51
(6) Bubble formation in pure water	100 1.3		single pulse	-	1	2.36×10 ²⁰	551	5.1	0.78
(7) Bd-threshold in numerical models	100			-	1	1.0×10 ²¹	2.6×10 ³	6.54	1
(8) EYFP tagged mitochondrion ablation @ 1 kHz [85]	100 1.4	2	1 kHz	>100	Several hundred	≥10 ²¹	≥2.6×10 ³	10.5	1.6
(9) Axon dissection in C.elegans @ 1 kHz [79]	200 1.4	10	1 kHz	400	400	≥10 ²¹	≥2.6×10 ³	52	8.0

Table 5: Numerical values of the data presented in Figure 21. All data refer to a laser wavelength of $\lambda = 800$ nm, and water as breakdown medium. The experimental irradiance values assume diffraction limited focusing conditions and a perfect laser beam. They refer to the peak irradiance in the laser focus ($\approx 2 \times$ average irradiance within the spot diameter) to make them comparable to the calculated values. The actual irradiance in the experiments is probably somewhat smaller than the values calculated under these assumptions. For superthreshold irradiance values, the plasma will grow in size, and plasma shielding and reflection will limit the growth of the free electron density. Therefore no exact values of the electron density and energy density are given.

7.1 FEMTOSECOND PULSE TRAINS AT MHZ REPETITION RATES WITH ENERGIES BELOW THE THRESHOLD FOR BUBBLE FORMATION

The irradiance threshold (2) for cell death induced by laser pulse series of 80 MHz repetition rate scanned over the entire cell volume ($0.067 \times I_{\text{rate}}$) is lower than the irradiance threshold for intracellular dissection. However, this does not imply that intracellular dissection with 80-MHz pulse series must lead to severe cell damage because locally confined irradiation does not affect cell viability in the same way as scanning irradiation.

The threshold for intranuclear chromosome dissection with 80-MHz pulse series (3) is almost 4 times as large as the irradiance (1) producing one free electron per pulse in the focal volume ($0.15 \times I_{\text{rate}}$ vs $0.04 \times I_{\text{rate}}$). In fact,

about 1000 free electrons per pulse are produced with the parameters used for dissection. Therefore, it is very likely that the intracellular ablation produced by long trains of femtosecond pulses in the low-density plasma regime relies on cumulative free-electron-mediated chemical effects. This hypothesis is supported by the facts that the individual pulses produce a thermoelastic tensile stress of only ≈ 0.014 MPa, and a pulse series of 100 μ s duration results in a temperature rise of only $\approx 0.076^\circ\text{C}$. These values for tensile stress and temperature rise are by far too small to cause any cutting effect or other types of cell injury. The breaking of chemical bonds, as described in section 4, may first lead to a disintegration of the structural integrity of biomolecules and finally to a dissection of subcellular structures. Bond breaking may be initiated both by resonant interactions with low-energy electrons, and by multiphoton processes of lower order that do not yet create free electrons [Koe99a, Koes99, Hop01, Egg05].

Interestingly, transient membrane permeabilisation for gene transfer (4) requires a considerably larger laser dose than chromosome dissection. Not only the irradiance is larger, but the number of applied pulses ($\approx 10^6$) also exceeds by far the quantity necessary for chromosome dissection ($\approx 4 \times 10^4$). Chromosome dissection may be facilitated by the DNA absorption around 260 nm enabling nonlinear absorption through lower-order multiphoton processes. Moreover, while breakage of relatively few bonds is sufficient for chromosome dissection, the creation of a relatively large opening is required for diffusion of a DNA plasmid through the cell membrane. The corresponding laser parameters are still within the regime of free-electron-mediated chemical effects but already quite close to the range where cumulative heat effects start to play a role (5).

At larger laser powers, bubbles with a lifetime in the order of a few seconds were observed that probably arise from dissociation of biomolecules into volatile, non-condensable fragments [Sup05, Koe02, Rie05, Mas04]. This dissociation of relatively large amounts of biomaterials can be attributed both to free-electron-chemical and photochemical bond breaking as well as to accumulative thermal effects. The appearance of the bubbles is an indication of severe cell damage or cell death within the targeted region and defines an upper limit for the laser power suitable for nanosurgery. A criterion for successful intratissue dissection at lower energy levels is the appearance of intense autofluorescence in perinuclear cell regions [Sup05, Koe02] that is likely due to the destruction of mitochondria at the rim of the laser cut [Oeh00].

7.2 FEMTOSECOND PULSES AT KHZ REPETITION RATES WITH ENERGIES ABOVE THE BUBBLE FORMATION THRESHOLD

When pulse trains of 1 kHz repetition rate are employed for nanosurgery, pulse energies ranging from 2-40 nJ are used [Yan04, Wat04, Hei05, She05]. Examples are the ablation of single mitochondria (8) by several hundred 2-nJ pulses [She05] and the severing of axons in a live C-elegans worm (9) with a similar number of 10-nJ pulses [Yan04]. These energies are above the threshold for thermo-elastically induced formation of minute transient cavitation bubbles (6), and are thus associated with mechanical disruption effects. The tensile thermoelastic stress waves enable dissection of cellular structures at low volumetric energy densities, and the small size of the heated volume (Fig. 8) correlates with a radius of the expanded bubble in the order of only 120-300 nm (Fig. 20). This explains why fs-laser induced bubble formation does not necessarily lead to cell damage whereas ns-laser-induced bubble generation is usually associated with cell death [Pit03, Lin99, Les01, Neu05b, Roe04].

Due to the contribution of mechanical effects to dissection, the total energy required for nanosurgery with kHz pulse series is less than the total energy necessary with MHz pulse trains. For example, ablation of a mitochondrion using 1-kHz pulses required a total energy of less than 1 μ J [She05] while for intranuclear chromosome dissection with 80-MHz pulses an energy of 15 μ J was needed [Koe99].

For sufficiently large pulse energies, bubble expansion and shock wave pressure can cause effects far beyond the focal volume which lead to cell death [Wat04, Zoh05, Wat05]. To avoid unwanted side effects, irradiances should be used that are only slightly above the bubble formation threshold. Useful techniques for an on-line monitoring of the ablation threshold during laser surgery are to detect the onset of photobleaching, or of light scattering by bubbles generated at the laser focus. Heisterkamp et. al. found that the threshold for photobleaching is just below the ablation threshold [Hei05]. Neumann and Brinkmann described a light scattering technique for an on-line detection of micrometer-sized bubbles produced by pulsed laser irradiation [Neu05a].

We conclude that, depending on the repetition rate of the fs laser pulses, nanosurgery relies on two very different mechanisms. With oscillator pulse trains at MHz repetition rates, dissection is due to accumulative chemical effects in low-density plasmas. In this regime, no transient bubbles with submicrosecond lifetime are produced, and the formation of long-lived bubbles by accumulative chemical and thermal effects must be avoided. With pulse trains at kHz repetition rate, the accumulative creation of chemical effects would take too long to be

practical. Therefore, the pulse energies are raised to a level where the thermo-elastic generation of minute transient bubbles enables to achieve nanodissections. Due to their short lifetime of less than 100 ns and the long time intervals between the laser pulses, no cumulative bubble growth occurs as long as pulse energies close to the bubble formation threshold are used.

7.3 COMPARISON WITH LONG-PULSED AND CW IRRADIATION

In their pioneering work, Berns et. al. [Ber69, Ber71] used high-power argon laser irradiation in multiline operation (with wavelengths of 488 nm and 514 nm) applied in 25-30 μ s pulses. Other researchers employed longer exposure times of 0.25 s [Pal96] and 1 to 2.5 s [Schn02] at smaller laser power. Berns et. al. (1981) related the spatial extent of their laser effects simply to the irradiance distribution in the focal region. However, with the exposure times used, the energy deposition is broadened by thermal diffusion. For large numerical apertures the focal volume has an almost spherical shape, and the characteristic thermal diffusion time t_d is approximately given as [Car59]

$$t_d = d^2 / 8\kappa \quad (29)$$

where κ is the thermal diffusivity and d the focal diameter. Thermal confinement of the energy deposition requires that the laser exposure is shorter than the thermal diffusion time [Vog03]. For a focal spot diameter of 480 nm in aqueous media ($\lambda = 514$ nm, NA = 1.3), this is the case only for laser pulse durations < 210 ns; for longer laser exposures such as used by Berns et al (1981) the temperature distribution is broadened. We have seen in section 5.3 (Fig. 12) that the distribution close to the focus center becomes stationary after about 10 μ s. This implies that the spatial extent of effects from laser pulses longer than 10 μ s is similar to that of lesions arising from cw laser irradiation. However, the temperature distribution is very narrow even for cw irradiation because from a point-like source the heat can diffuse in all spatial directions and, therefore, the temperature drops very quickly with growing distance from the source.

Effects created by long-pulsed or cw irradiation usually rely on linear (one photon) absorption. For argon laser irradiation at wavelengths of 488 nm and 514 nm that can be well transmitted into a cell, the laser power needed for surgery in unstained cells exceeds 1 W [Ber71]. It is thus considerably higher than the average power of about 30 mW necessary with femtosecond laser pulse trains at 800 nm [Koe99a, Koe01a] for which plasma formation induced by the ultrashort laser pulses results in a dramatic local increase of the absorption coefficient at the focus, regardless of the linear absorption coefficient. Berns et. al. speculated that high-power argon laser cell surgery is most likely a multiphoton mechanism [Ber81]. However, even though two-photon excited visible fluorescence was observed in experiments with a 760-nm cw laser beam [Koe95], multiphoton absorption is unlikely to be the dominant absorption mechanism considering the fact that the focal irradiance for 1 W laser power (5.5×10^8 Wcm⁻²) is 3 orders of magnitude less than the irradiance required for intracellular dissection with 800-nm, 170-fs pulses. The focal irradiance used for quasi-cw cell surgery is also much lower than the irradiances used for multiphoton microscopy [Koe00, Koe01b]. Thus there is little doubt that quasi-cw cell surgery is based on the linear absorption of the target structures whereas ultrashort-pulsed surgery relies on nonlinear absorption.

It was shown above that no purely thermal effects can be produced using ultrashort laser pulses. All thermal effects are accompanied by free-electron mediated chemical effects and thermoelastic mechanical effects. By contrast, quasi-cw cell surgery is mediated by local thermolysis and the formation of minute vapor bubbles. The temperatures required for thermolysis depend on the heat exposure time [Pea95], and are well above 100 °C for heat exposure durations in the millisecond or microsecond range [Hue99, Sim05]. The bubble nucleation threshold by thermolysis of strongly absorbing biomolecules such as melanin was found to be about 150 °C for pulse durations between 12 ns and 1.8 μ s [Neu05a]. This seems to be the lower temperature limit of cell surgery using microsecond pulses. The upper limit of a localized temperature rise without bubble formation is given by the threshold for explosive vaporization in the entire focal volume that for nonpigmented cells was found to be about 220°C [Sim05]. This threshold is lower than the superheat limit of water at ambient pressure ($\approx 300^\circ\text{C}$) above which homogeneous nucleation and spinodal decomposition will result in a phase explosion [Vog03, Skri88, Kis99]; probably because of the heterogeneous structure of the cells.

The temperatures required for quasi-cw cell surgery are considerably higher than those involved in femtosecond laser dissection by high-repetition-rate fs pulse trains that relies on photochemical and free-electron mediated chemical effects (section 7.1). They are in a similar range than the temperatures needed for femtosecond laser surgery at repetition rates below 1 MHz that is based on bubble formation by tensile thermoelastic stress (section 7.2).

The spatial resolution of quasi-cw cell surgery is related to the temperature distribution arising from a continuous deposition of laser energy via linear absorption that was presented in figure 11. Interestingly, it is not much broader than the temperature distribution arising from nonlinear absorption of femtosecond pulse trains shown in figure 10. However, as the spatial resolution of femtosecond laser surgery is given by the width of the free-electron distribution rather than by the temperature distribution, the precision of the energy deposition in fs laser surgery is considerably better than for cw or long-pulsed irradiation. The half-width of the free-electron distribution shown in Fig. 8b for $\lambda = 800$ nm and $NA = 1.3$ is only 190 nm in radial direction (without consideration of electron diffusion), compared to the half-widths of 590 nm and 730 nm of the temperature distributions in Fig. 11 resulting from irradiation with pulse durations of 10 μ s and 10 ms, respectively. It should be mentioned, however, that thermal damage is not directly proportional to the temperature elevation but to the damage integral that is an exponential function of temperature [Pea95]. The thermally damaged region can therefore be narrower than the half-width of the temperature distribution [Rin96, Des98]. Because of this reason, the gain of spatial resolution achievable by use of ultrashort laser pulses instead of quasi-cw irradiation is less than often assumed. Using fs-pulses, extracellular chromosomes could be completely dissected with an FWHM cut size of about 300 nm which amounts to 40% of the diffraction limited focal spot size [Koe01a]. Berns et al. produced chromosomal lesions of less than 1 μ m size using argon laser irradiation [Ber81]. Thus the spatial resolution achieved by IR femtosecond laser surgery is by a factor of about three better than that of the classical technique introduced more than 30 years ago [Ber69].

A major advantage of femtosecond laser surgery is that it can be performed at arbitrary locations even in media that are transparent at low irradiances, and with much less average power. The use of low-power argon lasers requires staining of the target structures [Ber81, Pal96, Schn02, Ber69]. The need for staining reduces the versatility of the technique compared to femtosecond laser surgery that can be performed at any arbitrary location. Another important advantage of ultrashort laser irradiation is the option to combine material modification with high-resolution nonlinear imaging modalities.

Recently, Paterson et. al. reported that cell wall permeabilisation is possible with a low-power blue diode laser ($\lambda = 405$ nm) using 0.3 mW irradiation and 40 ms exposure time [Pat05]. Owing to the short laser wavelength, the energy used (13 μ J) was three orders of magnitude less than the energy required for membrane permeabilisation with 488-nm irradiation [Schn02]. It was more than one order of magnitude larger than the energy of 0.5 μ J needed with ns pulses [Kra98], but the transfection process with millisecond pulses avoids mechanical disruptions extending beyond the region of the laser focus that are a problem with ns pulses [Ven02]. Mechanical disruption was also avoided in the study by Tirlapur and König who used 80-MHz femtosecond pulse trains of 800 nm for membrane permeabilisation [Tir02], but the total energy employed was here about 50 times larger than with the blue diode laser. Considering the fact that a blue laser diode is less costly than a femtosecond laser, the practical advantages of ultrashort laser pulses for membrane permeabilisation still have to be proven. However, ultrashort laser pulses are the tool of choice for intracellular and intratissue nanosurgery at arbitrary locations and/or in conjunction with nonlinear imaging.

7.4 POTENTIAL HAZARDS FROM LOW-DENSITY PLASMAS IN MULTIPHOTON MICROSCOPY AND SECOND HARMONIC IMAGING

A matter of concern is that low-density plasmas could be a potential hazard in multiphoton microscopy [Hop01, Koe00, Den90, So98, Koe99b] and higher harmonic imaging [Sup05, Guo97, Mor00, Chu03, Fu05]. Multiphoton imaging of cells is usually done using femtosecond laser pulses of about 700 – 1100 nm wavelength emitted at \approx 80 MHz from an oscillator with mean powers of 100 μ W up to several milliwatts [Koe00, Koe01b]. Similar mean powers are required for second harmonic imaging [Chu03]. These laser powers are close to the threshold for cell damage reported to be between 2 mW and 10 mW depending on the damage criterion used, the pulse duration, and the number of applied pulses [Koe99a, Mel03, Oeh00, Tir01, Koes99, Hop01]. It is also close to the values used for intracellular and intratissue dissection that range from 4 mW – 100 mW, depending on target structure [Koe99a, Tir02, Zei03, Sac05, Sup05, Koe02]. This suggests that the mechanisms underlying laser cell surgery may also contribute to the side effects in nonlinear imaging.

Our results indicate that thermal damage can be ruled out as cause of cell damage in multiphoton microscopy as even dissection with oscillator pulses does not involve thermal effects (Fig 21), and previous studies confirm this finding [Den95, Schoe98]. In the literature, photodamage produced by short laser pulses is mostly ascribed to multiphoton-induced photochemistry [Bes71, Mel03, Ber00]. However, a comparison of the irradiance thresholds for photodamage with the corresponding free electron densities in figure 21 shows that the formation of low-density plasmas may contribute considerably to the observed damage or even dominate its creation, especially in non-

stained targets. An exception is the work by Berns et al. (2000) who achieved gene manipulation by exposing chromosomes that were sensitized with a dye absorbing at 530 nm wavelength to 100-ps pulses of 1064 nm wavelength. The peak irradiance used in these experiments was $\approx 10^7 \text{ W/cm}^2$, far below the threshold for plasma formation, and it is quite clear that in this case the laser effects relied on two-photon-induced photochemical changes without the involvement of free electrons. By contrast, the irradiance required to induce localized DNA damage in nonstained chromosomes or cell nuclei was $\approx 1 \times 10^{11} \text{ W/cm}^2$ for 5.7-ns pulses of 532 nm wavelength [Cal83], and $1.9 \times 10^{11} \text{ W/cm}^2$ for 120-fs pulses of 750 nm wavelength [Mel03]. The first irradiance value is larger than the optical breakdown threshold in water at the same pulse duration that was measured to be $0.77 \times 10^{11} \text{ W/cm}^2$ [Ven02]. In the second case, a three-photon interaction can provide the energy required for molecular excitation at the DNA absorption peak around 260 nm, but the irradiance required for photodamage will generate also a free-electron density of $\approx 10^{13} \text{ cm}^{-3}$ which borders the region in which chemical changes may be induced by pulse series. Eggeling et. al. (2005) showed that the photobleaching kinetics with femtosecond laser pulses usually involves excitation into higher electronic states close to the ionization threshold followed by photolysis, unlike for longer pulse durations where photobleaching occurs via the triplet state. Heisterkamp et. al. (2005) found that slightly larger irradiance values than those required for photobleaching already lead to ablation, a process mediated by plasma formation. Together these findings indicate that low-density plasmas may be involved in the generation of ultrashort-laser-induced effects that were traditionally exclusively attributed to direct photochemical reactions, and may also contribute to photodamage in nonlinear microscopy. With increasing irradiance, free-electron mediated chemical effects become ever more important compared to direct photochemical reactions because the rate of free electron generation increases very fast with irradiance due to its high-order nonlinearity.

We saw that multiphoton fluorescence excitation bears a trade-off between low off-focus and severe in-focus photobleaching [Egg05]. This raises the question which laser pulse duration, repetition rate and wavelength is best suited to minimize the detrimental effects. It was found that at the same level of photodamage pulses with 3-4 ps duration provide the same signal or even an increase in signal compared to femtosecond pulses [Koes99, Hop01, Koe99b]. The increase in signal is due to the fact that, at constant irradiance, longer pulses produce a larger fluorescence excitation yield. The smaller fluorescence yield associated with the use of shorter pulses could be readily compensated for by an increase in peak power if the irradiance dependences of photodamage and multiphoton ionization were the same because the distance from the damage threshold would, under these conditions, remain constant. However, the irradiance dependence of photodamage is usually steeper than that of multiphoton excitation [Bes71, Koes99, Hop01] because photodamage often involves higher-order photochemical effects or even ionization. Therefore, the use of very short high-intensity femtosecond pulses for nonlinear imaging involves a larger risk of photodamage and seems to be neither essential nor advantageous. A prolongation of the pulse duration is, on the other hand, associated with an increase of average power because the peak power of the individual pulses cannot be reduced without loss of multiphoton excitation efficiency. The upper limit of useful pulse durations is set by the average power level leading to cumulative thermal damage. However, in aqueous media with low absorption coefficient in the wavelength range around 800 nm this is not the case for power levels up to at least 100 mW [Ber71, Schoe98].

Similar considerations apply for the selection of optimum repetition rates for nonlinear imaging. The limit for the maximum useful repetition rate is defined by the rate of energy deposition for which thermal damage starts to occur. It depends on the NA of the microscope objective (Figs. 10, 11), and on the linear absorption coefficient of the cells or tissues investigated. The limit is especially low in pigmented tissues such as skin [Mas04], but in non-pigmented tissues and cells even GHz repetition rates may be used. If for pulses of constant peak power of the individual pulses the laser repetition rate is increased from 80 MHz to 2 GHz, a much better signal to noise ratio can be achieved within the same image acquisition time [Chu03]. GHz repetition rates can also be employed to achieve the same signal strength with considerably smaller pulse peak power than with 80 MHz. This increases the safety margin with respect to photodamage [Chu03] and is thus of special interest for in-vivo nonlinear microscopy.

In second- and third harmonic imaging, the use of longer IR wavelengths than 800 nm was found to be advantageous because with a longer wavelength more photons are required for ionization and thus the safety margin increases [Sup05, Chu03]. With regard to multiphoton microscopy, it is advantageous to use fluorophores with long excitation wavelengths that enable the use of longer laser wavelengths. This way, the order of the multiphoton process can remain the same for imaging while the number of photons required for ionization increases. However, if a specific fluorophore with a given excitation wavelength must be employed, the order of the nonlinearities involved in image formation and photodamage increase in a similar fashion with increasing wavelength. Therefore, the optimum wavelength must in these cases be determined for each individual fluorophore [Sac05].

8. SUMMARY AND CONCLUSIONS

Femtosecond laser pulses enable the creation of spatially extremely confined chemical, thermal and mechanical effects in biological media and other transparent materials via free-electron generation through nonlinear absorption. Because of the nonlinear nature of plasma formation and the deterministic relationship between free electron density and irradiance, effect sizes well below the diffraction limit can be achieved. Precision and versatility are better than with cw irradiation for which the energy deposition relies on one-photon absorption and vital stains are often required to create the necessary absorption.

Free electrons are produced in a fairly large irradiance range below the optical breakdown threshold. This *low-density plasma regime* provides a 'tuning range' in which the nature of the laser-induced effects can be deliberately changed by gradually varying the irradiance. Chemical effects induced by the free electrons and direct multiphoton interactions dominate at the lower end of this irradiance range, whereas at the upper end they are mixed with thermal effects and modified by thermo-elastic stresses. For a sufficiently strong temperature rise, the thermo-elastic tensile stress leads to bubble formation, and the laser-induced effects become more disruptive. The threshold for bubble formation defines the experimental breakdown threshold in aqueous media. In our numerical calculations performed for a numerical aperture of $NA = 1.3$ and a wavelength of 800 nm, this threshold corresponds to a temperature rise of 131.5°C and an end temperature of 151.5°C, well below the superheat threshold (spinodal limit) at ambient pressure. It is predicted to be reached with a free-electron density of $\rho_e = 0.236 \times 10^{21} \text{ cm}^{-3}$, which is below the threshold criterion of $\rho_{cr} = 10^{21} \text{ cm}^{-3}$ often used in the modeling of plasma formation.

Although it is convenient to distinguish between chemical, thermal and thermo-mechanical effects, a clear separation between these regimes does not exist for femtosecond laser effects. Because free-electron generation precedes any thermal or thermo-mechanical effects, the latter are never independent from free-electron-induced chemistry or multiphoton-induced photochemical effects. Temperatures that would usually lead to thermal denaturation are associated with millions of free electrons in the focal volume that produce chemical changes.

The stress-confinement of the energy deposition in femtosecond-laser-induced material processing is responsible for the generation of large compressive and tensile stress amplitudes already at moderate temperature rise. Therefore, a small temperature rise is sufficient for bubble generation in a liquid without any pre-existing nuclei, and the bubbles at threshold are very small. For $NA = 0.8$ and $\lambda = 1040 \text{ nm}$, we experimentally observed a bubble size at threshold of only $\approx 300 \text{ nm}$, in excellent agreement with the numerical predictions (190 nm – 280 nm, depending on the assumption made for the thermal exchange between bubble content and surrounding liquid). The low volumetric energy density required for thermoelastically induced cavity formation (only about 1/5 of the vaporization enthalpy) is a reason for the lack of thermal side effects in femtosecond laser dissection and the small conversion rate of laser energy into mechanical energy. Moreover, it explains, why at the bubble formation threshold the bubble size is much smaller than for "conventional" phase transitions without stress confinement.

While close to threshold, the laser-produced bubbles are in the nanometer range and considerably smaller than the diffraction limited spot size, the bubble radius increases quite rapidly with laser pulse energy, and for pulse energies twice the breakdown energy, it is already in the order of the size of a biological cell. Here, tensile stress is not any more required to rupture the liquid but the temperatures in the focal volume are sufficiently high to induce explosive vaporization. When fs laser pulses with energies 7 times above the breakdown threshold were focused into water at $NA = 0.8$, a luminescent plasma was observed, indicating a large plasma energy density and free electron density, and an efficient laser plasma coupling even for free electron densities exceeding the critical density of $\rho \approx 10^{21} \text{ cm}^{-3}$.

Based on the analysis of the laser-induced chemical and physical effects, we investigated the working mechanisms of femtosecond laser nanoprocessing in biomaterials with oscillator pulses of 80 MHz repetition rate and with amplified pulses of 1 kHz repetition rate and revealed that they belong to two different regimes. Dissection at 80 MHz repetition rate is performed in the low-density plasma regime at subnanjoule energies well below the optical breakdown threshold and less than one order of magnitude higher than those used for nonlinear imaging. It is mediated by free-electron-induced chemical decomposition (bond breaking) in conjunction with multiphoton-induced chemistry, and hardly related to heating or thermoelastic stresses. Dissection with 1 kHz repetition rate is performed using about 10-fold larger pulse energies (a few nanojoule) and relies on thermoelastically-induced formation of minute transient cavities that is probably facilitated by the free-electron-induced decomposition of biomolecules and by direct photochemistry.

Unwanted side effects in femtosecond laser surgery are usually related to the formation of long-lasting bubbles in the high-repetition rate mode that are produced by accumulative heating and tissue dissociation into volatile fragments, and to excessively large transient bubbles in the low-repetition rate mode. Future experiments must

explore the specific hazards of each side effect and define the respective “therapeutic range” for each surgical modality.

The use of oscillator pulse trains is technically simpler and offers the possibility of combining nonlinear material modification with nonlinear imaging. Amplified pulses allow not only to perform nanosurgery but are also suited for tasks requiring larger cutting rates and pulse energies such as the precise dissection of individual cells from histologic specimens and their subsequent separation by laser catapulting, or the nondestructive isolation of single cultured cells [Hos04, Bar04, Ring04]. They are probably also more suitable for high-throughput cell transfection. However, their use poses the challenge to control the cavitation bubble size in order to remain close to the bubble formation threshold because the bubble size increases rapidly with increasing laser pulse energy, and well above threshold the bubble oscillation may cause unwanted mechanical side effects.

Short wavelengths seem to be especially well suited for the manipulation of cellular events because the dependence of the free-electron density on irradiance is weak and the tuning range between chemical, thermal and mechanical effects is thus broader than for longer wavelengths. Short wavelengths in the visible or UVA portion of the optical spectrum, provide, furthermore, better spatial resolution than infrared wavelengths. However, if simultaneous nonlinear material modification and nonlinear imaging is desired, one needs to use IR wavelengths because they have a larger optical penetration depth and enable to produce multiphoton-induced fluorescence, SHG or THG within a well-detectable wavelength range. The largest safety margin for nonlinear imaging without deleterious side effects for the specimen exists when the difference in the order of the multiphoton effects used for imaging and ionisation is as large as possible, which is the case for IR wavelengths > 1000 nm.

The principle mechanisms of femtosecond laser interaction with biomaterials described above are not only relevant for nanosurgery with tightly focused laser pulses but also for applications such as intrastromal corneal refractive surgery [Rat03, Hei03, Juh99, Han04] or presbyopia treatment [Rip05] where the laser pulses are focused at smaller numerical apertures. In the latter cases, nonlinear beam propagation must be taken into account, and one needs to bear in mind that the thermoelastic tensile stress amplitude produced by energy deposition into cylindrical volumes differs from those arising from spherical or ellipsoidal volumes [Pal99]. Similar considerations also apply for the analysis of intraocular lesions from ultrashort laser pulses in the context of laser safety [Cai04, Toth97, Roc99]. Besides for nanoprocessing of biological materials, low density plasmas can also be used to modify other transparent materials and enable, for example, the generation of optical waveguides, couplers, or even lasers in bulk glass and fused silica [Sch01, Min01, Wat03, Tac04].

We conclude that with the advent of compact and reliable femtosecond laser technology, nanoprocessing of biological cells and tissues has gained new exciting perspectives. A deeper understanding of the working mechanisms will help to further optimize this technique, to open new avenues for micro- and nanomanipulation, and to find new applications for functional studies on cells and small organisms.

Important challenges for future research are the establishment of a real-time monitoring of the laser-induced events, especially for those cases where bubble formation is involved in dissection, and the assessment of the consequences of the bubbles oscillations for the integrity, metabolisms and viability of the affected cells. For online dosimetry, techniques for a real-time assessment of the size of transient bubbles with lifetimes below $1\ \mu\text{s}$ must be established. For surgery using oscillator pulses at MHz repetition rates, bubble oscillations are probably not relevant. Here, bubble growth is a much slower process driven by the cumulative production of noncondensable gas and can more easily be monitored.

A significant shortcoming of all present models of optical breakdown in biomaterials is the lack of consideration of the specific absorption properties of the biomolecules or stains contained in the aqueous medium. We made first attempts to consider the role of heating by linear absorption and the modification of multiphoton processes by intermediate energy levels located within the band gap for water. The extended model probably yields reasonable predictions for breakdown thresholds in the presence of linear absorption. However, the inclusion of thermal emission destroys the self-consistency of a breakdown model that merely addresses the temporal evolution of free electron density but ignores the hydrodynamic effects leading to plasma expansion. Therefore, the predicted plasma energy densities and temperatures are by far too high. Consistency of the model can be restored only by consideration of the coupling between free electron evolution and hydrodynamic effects, which remains a challenge for future work.

9 PUBLICATION YIELD OF THE PROJECT

Publications in peer-reviewed Journals

1. **Vogel A, Noack J, Hüttmann G, Paltauf G** (2005) Mechanisms of femtosecond laser nano surgery of biological cells and tissues. *Appl. Phys B* **81**:1015-1047 (Invited paper)
2. **Vogel A, Apitz I, Freidank S, Dijkink R** (2006) Sensitive high-resolution white-light Schlieren technique with a large dynamics range for the investigation of ablation dynamics. *Opt. Lett.* **31**:1812-1814

Book chapters

1. **Vogel A, Noack J, Hüttmann G, Paltauf G** (2006) Femtosecond plasma-mediated nanosurgery of cells and tissues. In: Phipps C (ed.) *Laser Ablation*, Springer, Heidelberg, pp 217-262

Conference proceedings

1. **Vogel A, Noack J, Hüttmann G, Paltauf G** (2002) Low-density plasmas below the optical breakdown threshold - potential hazard for multiphoton microscopy, and a tool for the manipulation of intracellular events. *Proc SPIE* **4620** "Multiphoton Microscopy in the Biomedical Sciences II," 202-216
2. **Vogel A, Noack J, Hüttmann G, Paltauf G** (2002) Femtosecond-laser-produced low-density plasmas in transparent biological media: a tool for the creation of chemical, thermal and thermomechanical effects below the optical breakdown threshold. *Proc SPIE* **4633** "Commercial and Biological Applications of Ultrafast Laser IV," 23-37
3. **Vogel A** (2003) Creation of chemical, thermal, and thermomechanical effects in transparent biological media by femtosecond-laser-produced low-density plasmas. *Proc. Korea Conference on Innovative Science and Technology 2003 "Femtoscience and Technology – Future Implications"*, 2. – 5. November 2003 in Jeju, Korean Federation of Science and Technology Societies, 295-312.
4. **Vogel A, Noack J, Hüttmann G, Paltauf G** (2006) Mechanisms of femtosecond laser nanoprocessing of biological cells and tissues. In: Herman P, Hess W (eds.) *Proc. COLA 2005*, Journal of Physics: Conference Series IX, Institute of Physics Publishing, (at press)
5. **Vogel A, Noack J, Hüttmann G, Linz N, Freidank S, Paltauf G** (2006) Femtosecond laser nano surgery of biological cells and tissues. *Proc. 4th Int. Congress on Laser Advanced Materials Processing (LAMP2006)*, 16. – 19. Mai 2006, Kyoto, Japan (at press).
6. **Vogel A, Noack J, Hüttmann G, Linz N, Freidank S, Paltauf G** (2006) Mechanisms of femtosecond laser nano surgery of biological cells and tissues. *Proc. 3rd Interna. Nanophotonics Symposium Handai, Osaka University*, 05. – 08. Juli 2006, Osaka, Japan (at press).

Manuscripts in preparation

1. **Vogel A, Linz N, Freidank S, Paltauf G** Femtosecond laser induced nanocavitation
2. **Vogel A, Noack J**: The role of linear absorption for femtosecond and nanosecond optical breakdown

10 REFERENCES

- J. R. Aist, H. Liang, M. W. Berns : Astral and spindle forces in PtK2 cells during anaphase B : a laser microbeam study. *J. Cell Sci.* 104, 1207-1216 (1993)
- M.V. Ammosov, N. B. Delone, V. P. Krainov: Tunnel ionization of complex atoms and of atomic ions in an alternating electromagnetic field. *Sov. Phys. JETP* 64, 1191-1194 (1986)
- American national standard for the safe use of lasers.** New York: American National Standards Institute, 1993. ANSI Standard Z136.1.
- R. L. Amy, R. Storb: Selective mitochondrial damage by a ruby laser microbeam: an electron microscopic study. *Science* 150, 756-758 (1965)
- S. Antinori, C. Panci, H.A. Selman, B. Caffa, G. Dani, C. Versaci: Zona thinning with the use of a laser: a new approach to assisted hatching in humans. *Hum Reprod.* 11, 590-594 (1996)
- I. Apitz, A. Vogel: Material ejection in nanosecond Er:YAG laser ablation of water, liver, and skin. *Appl. Phys. A* **81**, 329-338 (2004)
- C. L. Arnold, A. Heisterkamp, W. Ertmer, H. Lubatschowski: Streak formation as side effect of optical breakdown during processing the bulk of transparent Kerr media with ultrashort laser pulses. *Appl. Phys. B* 80, 247-253 (2005)
- D. Arnold, E. Cartier: Theory of laser-induced free-electron heating and impact ionization in wide-band-gap solids. *Phys. Rev. B* 46, 15102-15115 (1992)
- J. A. Barron, P. Wu, H. D. Ladouceur, B. R. Ringeisen : Biological laser printing: a novel technique for creating heterogeneous 3-dimensional cell patterns. *Biomed. Microdev.* **6**, 139-147 (2004).
- P. A. Barnes, K.E. Rieckhoff: Laser induced underwater sparks. *Appl. Phys. Lett.* **13**, 282-284 (1968)
- M. Bass (ed in chief): *Handbook of Optics Vol. II* (McGraw Hill, New York 1995)
- S. Beck, T. Sakurai, B. Eustace, G. Beste, R. Schier, F. Rudert, D. G. Jay: Fluorophore-Assisted Light Inactivation (FALI): a high-throughput tool for direct target validation of proteins. *Proteomics* **2**, 247-255 (2002)
- M. Bessis, G. Nomarski: Irradiation ultra-violette des organites cellulaires avec observation continue en contraste en phase. *J. Biophys. Biochem. Cytol.* **8**, 777-792 (1960)
- M. Bessis, F. Gires, G. Mayer, G. Nomarski: Irradiation des organites cellulaires à l'aide d'un laser à rubis. *Compt. Rend. Acad. Sci.* **255**, 1010 (1962)
- M. Bessis: Selective destruction of cell organelles by laser beam. Theory and practical applications. *Adv. Biol. Med. Phys.* **13**, 209-213 (1971).
- M. W. Berns, R. S. Olson, D. E. Rounds: In vitro production of chromosomal lesions with an argon laser microbeam. *Nature* **221**, 74-75 (1969)
- M. W. Berns, W. K. Cheng, A. D. Floyd, Y. Ohnuki: Chromosome lesions produced with an argon laser microbeam without dye sensitization. *Science* **171**, 903-905 (1971)
- M. W. Berns, J. Aist, J. Edwards, K. Strahs, J. Girton, P. McNeil, J. B. Kitze, M. Hammer-Wilson, L.-H. Liaw, A. Siemens, M. Koonce, S. Peterson, S. Brenner, J. Burt, R. Walter, P. J. Bryant, D. van Dyk, J. Coulombe, T. Cahill, G. S. Berns: Laser Microsurgery in cell and developmental biology. *Science* **213**, 505-513 (1981)
- M. W. Berns, W. H. Wright, R. Wiegand-Steubing: Laser-microbeams as a tool in cell biology. *Int. Rev. Cytol.* **129**, 1-44 (1991)
- M. W. Berns, Z. Wang, A. Dunn, V. Wallace, V. Venugopalan: Gene inactivation by multiphoton-targeted photochemistry. *Proc. Nat Acad. Sci Amer.* **97**, 9504-9507 (2000)
- V. R. Bhardwaj, P. B. Corkum, D. M. Rayner, C. Hnatowsky, E. Simova, R. S. Taylor: Stress in femtosecond-laser written waveguides in fused silica. *Opt. Lett.* **29**, 1312-1314 (2004)
- N. Bloembergen: Laser-induced electric breakdown in solids. *IEEE J. Quantum Electr.* **QE-10**, 375-386 (1974)
- D. Boal: *Mechanics of the cell* (Cambridge Univ. Press, Cambridge, UK 2002)
- M. Born, E. Wolf: *Principles of Optics* (Pergamon Press, Oxford 1970)
- E. L. Botvinick, V. Venugopalan, J. V. Shah, L. H. Liaw, M. Berns: Controlled ablation of microtubules using a picosecond laser. *Biophys. J.* **87**, 4203-4212 (2004)
- B. Boudaiffa, P. Cloutier, D. Hunting, M. A. Huels, L. Sanche: Resonant formation of DNA strand breaks by low-energy (3 to 20 eV) electrons. *Science* **287**, 1658-1660 (2000)

- C.E. Brennen: *Cavitation and Bubble Dynamics* (Oxford University Press, New York, Oxford 1995)
- C. S. Buer, K. T. Gahagan, G. S. Swartzlander Jr., P. J. Weathers: Insertion of microscopic objects through plant cell walls using laser microsurgery. *Biotechnol. Bioeng.* **60**, 348-355 (1998)
- N. M. Bulgakova, R. Stoian, A. Rosenfeld, I. V. Hertel, E. E. B. Campbell: Electronic transport and consequences for material removal in ultrafast pulsed laser ablation of materials. *Phys. Rev. B* **69**, 054102-1-12 (2004)
- S. A. Bustin: Absolute quantification of mRNA using real-time reverse transcription polymerase chain reaction assays. *J. Mol. Endocrinol.* **25**, 169-193 (2000)
- C. P. Cain, C. A. Toth, G. D. Noojin, V. Carothers, D. J. Stolarski, B. A. Rockwell: Thresholds for visible lesions in the primate eye produced by ultrashort near-infrared laser pulses. *Invest. Ophthalmol. Vis. Sci.* **40**, 2343-2349 (1999)
- C. P. Cain, R. J. Thomas, G. D. Noojin, D. J. Stolarski, P. K. Kennedy, G. D. Buffington, B. A. Rockwell: Sub-50 fs laser retinal damage thresholds in primate eye with group velocity dispersion, self-focusing and low-density plasmas. *Graefes Arch. Clin. Exp. Ophthalmol.* Published online (2004 Jul 7)
- P.P. Calmettes, M. W. Berns: Laser-induced multiphoton processes in living cells. *Proc. Nat. Acad. Sci. USA* **80**, 7197-7199 (1983)
- H. S. Carslaw, J. C. Jaeger: *Conduction of Heat in Solids*, 2nd ed. (Oxford University Press: Oxford 1959)
- K.F. Chan et al.: Holmium:YAG laser lithotripsy: a dominant photothermal ablative mechanism with chemical decomposition of urinary calculi. *Lasers Surg. Med.* **25**, 22-37 (1999)
- E. J. Chapyak, R. P. Godwin, A. Vogel: A comparison of numerical simulations and laboratory studies of shock waves and cavitation bubble growth produced by optical breakdown in water. *Proc. SPIE* **2975**, 335-342 (1997)
- S.-W. Chu, T. M. Liu, C.-K. Sun, C.-Y. Lin, H.-J. Tsai : Real-time second-harmonic generation microscopy based on a 2-GHz repetition rate Ti:sapphire laser. *Opt. Express* **11**, 933-938 (2003)
- S. H. Chung, D. A. Clark, C. V. Gabel, E. Mazur, A. D. T. Samuel: Mapping thermosensation to a dendrite in *C. elegans* using femtosecond laser dissection. *BMC Neuroscience* doi:10.1186/1471-2202-7-30 (2006)
- R. H. Cole: *Underwater Explosions* (Princeton University Press, Princeton 1948)
- J. Colombelli, S. W. Grill, E. H. K. Stelzer: Ultraviolet diffraction limited nanosurgery of live biological tissues. *Rev. Sci. Instrum.* **75**, 472-478 (2004)
- J. Colombelli, E. G. Reynaud, J. Rietdorf, R. Pepperkork, E. H. K. Stelzer: Pulsed UV laser nanosurgery: retrieving the cytoskeleton dynamics in vivo. *Traffic* **6**, 1093-1102 (2005).
- B. T. Cox, P. C. Beard: Fast calculation of pulsed photoacoustic fields in fluids using k-space methods. *J. Acoust. Soc. Am.* **117**, 3616-3627 (2005)
- L. A. Crum: Rectified diffusion. *Ultrasonics* **22**, 215-223 (1984)
- P. A. Dayton, J. E. Chomas, A. F. H. Lunn, J. S. Allen, J. R. Lindner, S. I. Simon, K. W. Ferrara: Optical and acoustical dynamics of microbubble contrast agents inside neutrophils. *Biophys. J.* **80**, 1547-1556 (2001)
- P. G. Debenedetti: *Metastable Liquids: Concepts and Principles* (Princeton University Press, Princeton 1996)
- W. J. Denk, J. H. Strickler, W. W. Webb: Two-photon laser scanning microscopy. *Science* **248**, 73-76 (1990)
- W. J. Denk, D. W. Piston, W. W. Webb: Two-photon molecular excitation laser-scanning microscopy. In *Handbook of Biological Confocal Microscopy*. J. B. Prawley, Ed., pp. 445-458 (Plenum Press: New York 1995)
- L. Descloux, S. Rastegar, G. Delacretaz, A. Hollis, K. Rink : Kinetics of zona pellucida thermo-dissolution in mouse zygotes. *Proc. SPIE* **3195**, 137-142 (1998)
- H. Dittlbacher, J. R. Krenn, A. Leitner, F. R. Aussenegg: Surface plasmon polariton based optical beam profiler. *Opt. Lett.* **29**, 1408-1410 (2004)
- F. Docchio, C. A. Sachhi, J. Marshall: Experimental investigation of optical breakdown thresholds in ocular media under single pulse irradiation with different pulse durations. *Lasers Ophthalmol.* **1**, 83-93 (1986)
- F. Docchio: Lifetimes of plasmas induced in liquids and ocular media by single Nd:YAG pulses of different duration. *Europhys. Lett.* **6**, 407-412 (1988)
- D. Du, J. Squier, R. Kurtz, V. Elner, X. Liu, G. Güttmann, G. Mourou: Damage threshold as a function of pulse duration in biological tissue. In P. F. Barbara et al. *Ultrafast Phenomena IX* (Springer: New York 1994) 254-255
- D. Du, X. Liu, G. Mourou: Reduction of multi-photon ionization in dielectrics due to collisions. *Appl. Phys. B* **63**, 617-621 (1996)

- O. M. Efimov, K. Gabel, S. V. Garnov, L. B. Glebov, S. Grantham, M. Richardson, and M. J. Soileau: Color-center generation in silicate glasses exposed to infrared femtosecond pulses. *J. Opt. Soc. Am. B* **15**, 193-199 (1998)
- O. M. Efimov: Self-optical breakdown and multipulse optical breakdown of transparent insulators in the femto-nanosecond region of laser pulse widths. *J. Opt. Technol.* **71**, 338-347 (2004)
- C. Eggeling, A. Volkmer, C. A. M. Seidel: Molecular photobleaching kinetics of Rhodamine 6G by one- and two-photon induced confocal fluorescence microscopy. *Chem. Phys. Chem.* **6**, 791-804 (2005)
- C. H. Fan, J. Sun, J. P. Longtin: Breakdown threshold and localized electron density in water induced by ultrashort laser pulses. *J. Appl. Phys.* **91**, 2530-2536 (2002)a
- C. H. Fan, J. Sun, J. P. Longtin: Plasma absorption of femtosecond laser pulses in dielectrics. *ASME J. Heat Transf.* **124**, 275-283 (2002)b
- M. D. Feit, A. M. Komashko, A. M. Rubenchik: Ultra-short pulse laser interaction with transparent dielectrics. *Appl. Phys. A* **79**, 1657-1661 (2004)
- Q. Feng, J. V. Moloney, A. C. Newell, E. M. Wright, K. Cook, P. K. Kennedy, D. X. Hammer, B. A. Rockwell, C. R. Thompson: Theory and simulation on the threshold of water breakdown induced by focused ultrashort laser pulses. *IEEE J. Quantum Electron.* **33**, 127-137 (1997)
- J. C. Fisher: The fracture of liquids. *J. Appl. Phys.* **19**, 1062-1067 (1948)
- L. Fu, X. Gan, M. Gu: Use of a single-mode fiber coupler for second-harmonic-generation microscopy. *Opt. Lett.* **30**, 385-387 (2005)
- U. Fuchs, U. D. Zeitner, A. Tünnermann: Ultra-short pulse propagation in complex optical systems. *Opt. Express* **13**, 3852-3863 (2005)
- B. C. Garret, D. A. Dixon, D. M. Camaioni, D. M. Chipman, M. A. Johnson, C. D. Jonah, G. A. Kimmel, J. H. Miller, T. N. Rescigno, P. J. Rossky, S. S. Xantheas, S. D. Colson, A. H. Laufer, D. Ray, P. F. Barbara, D. M. Bartels, K. H. Becker, K. H. Bowen, S. E. Bradforth, I. Carmichael, J. V. Coe, L. R. Corrales, J. P. Cowin, M. Dupuis, K. B. Eisenthal, J. A. Franz, M. S. Gutowski, K. D. Jordan, B. D. Kay, J. A. LaVerne, S. V. Lyman, T. E. Madey, C. W. McCurdy, D. Meisel, S. Mukamel, A. R. Nilsson, T. M. Orlando, N. G. Petrik, S. M. Pimblott, J. R. Rustad, G. K. Schenter, S. J. Singer, A. Tokmakoff, L. S. Wang, C. Wittig, T. S. Zwier: Role of water in electron-initiated processes and radical chemistry; issues and scientific advances. *Chem Rev.* **105**, 355-389 (2005)
- B. Garrison, T. E. Itina, L. V. Zhigilei : Limit of overheating and the threshold behavior in laser ablation. *Phys. Rev. E* **68**, 041501 (2003)
- F. R. Gilmore: Calif. Inst. Techn. Rep. **26-4** (1952)
- L. B. Glebov, O. M. Efimov, G. T. Petrovski, P. N. Rogovtsev: The effect of the modal composition of laser radiation on the optical breakdown threshold of silicate glasses. *Sov. J. Quantum Electron.* **15**, 226-?? (1984).
- E. N. Glezer, E. Mazur: Ultrafast-laser driven micro-explosions in transparent materials. *Appl. Phys. Lett.* **71**, 882-884 (1997)
- R. P. Godwin: Optical mechanism for enhanced absorption of laser energy incident on solid targets. *Phys Rev. Lett.* **28**, 85-87 (1972)
- R. P. Godwin, C. G. M. van Kessel, J. N. Olsen, P. Sachsenmaier, R. Sigel: Reflection losses from laser-produced plasmas. *Z. Naturforsch.* **32a**, 1100-1107 (1977)
- R. P. Godwin: Absorption in laser-produced plasma experiments: a personal view. *Appl Opt.* **18**, 3555-3561 (1979)
- R. P. Godwin: Multilayer optics provides laser-plasma coupling insight. *Appl Opt.* **34**, 572-580 (1995)
- S. Gohlke, E. Illenberger: Probing biomolecules: Gas phase experiments and biological relevance. *Europhys. News* **33**, 207-209 (2002)
- D. Grand, A. Bernas, E. Amouyal: Photoionization of aqueous indole; conduction band edge and enrgy gap in liquid water. *Chem. Phys.* **44**, 73-79 (1979)
- K. O. Greulich: *Micromanipulation by Light in Biology and Medicine* (Birkhäuser, Basel, Boston, Berlin 1999)
- S. Grill, E. H. K. Stelzer: Method to calculate lateral and axial gain factors of optical setups with a large solid angle. *J. Opt. Soc. Am. A* **16**, 2658-2665 (1999)
- S. W. Grill, J. Howard, E. Schäffer, E. H. K. Stelzer, A. A. Hyman: The distribution of active force generators controls mitotic spindle position. *Science* **301**, 518-521 (2003)
- Y. Guo, P. P. Ho, A. Tirkslunas, F. Liu, R. R. Alfano: Optical harmonic generation from animal tissues by the use of picosecond and femtosecond laser pulses. *Opt. Lett.* **22**, 1323-1325 (1997)

- D. X. Hammer, R. J. Thomas, G. D. Noojin, B. A. Rockwell, P. A. Kennedy, W. P. Roach: Experimental investigation of ultrashort pulse laser-induced breakdown thresholds in aqueous media. *IEEE J. Quantum Electr.* **QE-3**, 670-678 (1996)
- D. X. Hammer, E. D. Jansen, M. Frenz, G. D. Noojin, R. J. Thomas, J. Noack, A. Vogel, B. A. Rockwell, A. J. Welch: Shielding properties of laser-induced breakdown in water for pulse durations from 5 ns to 125 fs. *Appl. Opt.* **36**, 5630-5640 (1997)
- M. Han, L. Zickler, G. Giese, M. Walter, F. H. Loesel, J. F. Bille: Second-harmonic imaging of cornea after intrastromal femtosecond laser ablation. *J. Biomed. Opt.* **9**, 760-766 (2004)
- A. Heisterkamp, T. Ripken, H. Lubatschowski, T. Mamom, W. Drommer, H. Welling, W. Ertmer: Nonlinear side-effects of fs-pulses inside corneal tissue during photodisruption. *Appl. Phys. B* **74**, 419-425 (2002)
- A. Heisterkamp, T. Mamom, O. Kermani, W. Drommer, H. Welling, W. Ertmer, H. Lubatschowski: Intrastromal refractive surgery with ultrashort laser pulses: in vivo study on the rabbit eye. *Graefes Arch. Clin. Exp. Ophthalmol.* **241**, 511-517 (2003)
- A. Heisterkamp, I. Z. Maxwell, E. Mazur, J. M. Underwood, J. A. Nickerson, S. Kumar, D. E. Ingber: Pulse energy dependence of subcellular dissection by femtosecond laser pulses. *Opt. Expr.* **13**, 3690-3696 (2005).
- A. Hertwig, S. Martin, J. Krüger, W. Kautek: Surface damage and color centers generated by femtosecond pulses in borosilicate glass and silica. *Appl. Phys. A* **79**, 1075-1077 (2004)
- R. Hoffman and L. Gross, "Modulation contrast microscope," *Appl. Opt.* **14**, 1169 (1975).
- A. Hopt, E. Neher: Highly nonlinear photodamage in two-photon fluorescence microscopy. *Biophys. J.* **80**, 2029-2036 (2001)
- Y. Hosokawa, H. Takabayashi, S. Miura, C. Shukunami, Y. Hiraki, H. Masuhara: Nondestructive isolation of single cultured animal cells by femtosecond laser-induced shockwave. *Appl. Phys. A* **79**, 795-798 (2004)
- H. Hotop: Dynamics of low energy electron collisions with molecules and clusters. In: L.G. Christophorou, J.K. Olthoff (eds.): *Proc. Int. Symp. on Gaseous Dielectrics IX 22-25 May 2001, Ellicott City, MD, USA*, pp. 3-14 (Kluwer Academic/Plenum Press, New York 2001)
- M. A. Huels, B. Boudaiffa, P. Cloutier, D. Hunting, L. Sanche : Single, double, and multiple double strand breaks induced in DNA by 3-100 eV electrons. *J. Am. Chem. Soc.* **125**, 4467-4477 (2003)
- T. P. Hughes: *Plasmas and Laser Light* (Adam Hilger, Bristol 1975)
- G. Huettmann, R. Birngruber: On the possibility of high-precision photothermal microeffects and the measurement of fast thermal denaturation of proteins. *IEEE J. Sel. Topics Quantum Electron.* **5**, 954-962 (1999)
- G. Hüttmann, J. Serbin, B. Radt, B. Lange, R. Birngruber : Model system for investigating laser-induced subcellular microeffects. *Proc. SPIE* **4257**, 398-409 (2001)
- G. Isenberg, W. Bielser, W. Meier-Ruge, E. Remy: Cell surgery by laser micro-dissection: a preparative method. *J. Microsc.* **107**, 19-24 (1976)
- I. M. Jánosi, D. Chrétien, H. Flyvberg: Structural microtubule cap : stability, catastrophe, rescue, and third state. *Biophys. J.* **83**, 1317-1330 (2002)
- D. G. Jay, T. Sakurai: Chromophore-assisted laser inactivation (CALI) to elucidate cellular mechanisms of cancer. *Biochim. Biophys. Acta* **87452**, M39-M48 (1999)
- H. O. Jeschke, E. M. Garcia: Ultrafast structural changes induced by femtosecond laser pulses. In: B. W. Adams (ed.) *Nonlinear Optics, Quantum Optics and Ultrafast Phenomena with X-rays*, pp. 175-214 (Kluwer Academic Publishers, Boston, Dordrecht, London 2003)
- A. P. Joglekar, H. Liu, G. J. Spooner, E. Meyhöfer, G. Mourou, A. L. Hunt: A study of the deterministic character of optical damage by femtosecond laser pulses and applications to nanomachining. *Appl. Phys B* **77**, 25-30 (2003)
- A. P. Joglekar, H. Liu, E. Meyhöfer, G. Mourou, A. L. Hunt: Optics at critical intensity. Applications to nanomorphing. *Proc. Nat. Acad. Sci.* **101**, 5856-5861 (2004)
- T. Juhasz, G. A. Kastis, C. Suarez, Z. Bor, W. E. Bron : Time-resolved observations of shock waves and cavitation bubbles generated by femtosecond laser pulses in corneal tissue and water. *Lasers Surg. Med.* **19**, 23-31 (1996)
- T. Juhasz, F. H. Loesel, R. M. Kurtz, C. Horvath, J. F. Bille, G. Mourou: Corneal refractive surgery with femtosecond lasers. *IEEE J. Sel. Topics Quantum Electron.* **5**, 902-910 (1999)
- S. Juodkazis, K. Yamasaki, V. Mizeikis, S. Matsuo, H. Misawa: Formation of embedded patterns in glasses using femtosecond irradiation. *Appl. Phys. A* **79**, 1549-1553 (2004)

- A. Kaiser, B. Rethfeld, M. Vicanek, G. Simon: Microscopic processes in dielectrics under irradiation by subpicosecond pulses. *Phys. Rev. B* **61**, 11437-11450 (2000)
- J. Kasparian, J. Solle, M. Richard, J.-P. Wolf: Ray-tracing simulation of ionization-free filamentation. *Appl. Phys. B* **79**, 947-951 (2004)
- L. V. Keldysh: Kinetic theory of impact ionization in semiconductors. *Sov. Phys. JETP* **11**, 509-518 (1960)
- L. V. Keldysh: Ionization in the field of a strong electromagnetic wave. *Sov. Phys. JETP* **20**, 1307-1314 (1965)
- P. K. Kennedy: A first-order model for computation of laser-induced breakdown thresholds in ocular and aqueous media: Part I – Theory." *IEEE J. Quantum Electron.* **QE-31**, 2241-2249 (1995)
- P. K. Kennedy, D. X. Hammer, B. A. Rockwell: Laser-induced breakdown in aqueous media. *Progr. Quantum Electron.* **21**, 155-248 (1997)
- M. Kerker: The scattering of light and other electromagnetic radiation. *Academic*, New York (1969)
- A. Khodjakov, R. W. Cole, B. R. Oakley, C. L. Rieder: A synergy of technologies: combining laser microsurgery with green fluorescent protein tagging. *Cell Motil. Cytoskeleton.* **38**, 311-317 (1997)
- A. Khodjakov, R. W. Cole, C. L. Rieder: Centrosome-independent mitotic spindle formation in vertebrates. *Curr. Biol.* **10**, 59-67 (2000)
- S. B. Kiselev: Kinetic boundary of metastable states in superheated and stretched liquids. *Physica A* **269**, 252-268 (1999)
- S. B. Kiselev, J. F. Ely: Curvature effect on the physical boundary of metastable states in liquids. *Physica A* **299**, 357-370 (2001)
- R. T. Knapp, J. W. Daily, F. G. Hammitt: *Cavitation* (McGraw-Hill, New York 1971) pp. 117-131
- H. J. Koester, D. Baur, R. Uhl, S. W. Hell: Ca^{2+} fluorescence imaging with pico- and femtosecond two-photon excitation: signal and photodamage. *Biophys. J.* **77**, 2226-2236 (1999)
- M. Kolesik, E. M. Wright, J. V. Moloney: Dynamic nonlinear X-waves for femtosecond pulse propagation in water. *Phys. Rev. Lett.* **92**, 253901 (2004)
- K. Koenig, H. Liang, M. W. Berns, B. J. Tromberg: Cell damage by near-IR microbeams. *Nature* **377**, 20-21 (1995)
- K. Koenig, I. Riemann, P. Fischer, K. Halbhauer: Intracellular nanosurgery with near infrared femtosecond laser pulses. *Cell. Mol. Biol.* **45**, 195-201 (1999)a
- K. Koenig, T. W. Becker, P. Fischer, I. Riemann, K. J. Halbhauer: Pulse-length dependence of cellular response to intense near-infrared laser pulses in multiphoton microscopes. *Opt. Lett.* **24**, 113-115 (1999)b
- K. Koenig: Multiphoton microscopy in life sciences. *J. Microsc.* **200**, 83-104 (2000)
- K. Koenig, I. Riemann, W. Fritsche: Nanodissection of human chromosomes with near-infrared femtosecond laser pulses. *Opt. Lett.* **26**, 819-821 (2001)a
- K. Koenig: Cellular response to laser radiation in fluorescence microscopes. In: A. Periasamy: *Methods in cellular imaging* pp. 236-251 (Oxford University Press, Oxford 2001)b
- K. Koenig, O. Krauss, I. Riemann: Intratissue surgery with 80 MHz nanojoule femtosecond laser pulses in the near infrared. *Opt. Express* **10**, 171-176 (2002)
- K. P. Köstli, M. Frenz, H. Bebie, and H. P. Weber, "Temporal Backward Projection of Optoacoustic Pressure Transients Using Fourier Transform Methods," *Physics in Medicine and Biology* **46**, 1863-1872 (2001).
- V. Kotaidis, A. Plech : Cavitation dynamics on the nanoscale. *Appl. Phys. Lett.* **87**, 213102 (2005)
- T. B. Krasieva, C. F. Chapman, V. J. LaMorte, V. Venugopalan, M. W. Berns, B. J. Tromberg: Cell permeabilization and molecular transport by laser microirradiation. *Proc. SPIE* **3260**, 38-44 (1998)
- S.-I. Kurata, M. Tsukakoshi, T. Kasuya, Y. Ikawa: The laser method for efficient introduction of foreign DNA into cultured cells. *Exp. Cell Res.* **162**, 372-378 (1986)
- H. Kuchling:, *Taschenbuch der Physik 13th ed.* (Fachbuch-Verlag, Leipzig 1991)
- G. Lahr: RT-PCR from archival single cells is a suitable method to analyze specific gene expression. *Lab. Invest.* **80**, 1477-1479 (2000)
- W. Lauterborn, T. Kurz: „*Coherent Optics. Fundamentals and Applications*,“ Springer: Berlin, Heidelberg, New York, 2003 (346 pp).T. G. Leighton: *The Acoustic Bubble* (Academic Press, London 1994)
- M. Lenzner, J. Krüger, S. Sartania, Z. Cheng, Ch. Spielmann, G. Mourou, W. Kautek, F. Krausz: Femtosecond optical breakdown in dielectrics. *Phys. Rev. Lett.* **80**, 4076-4079 (1998)

- D. Leszczynski, C. M. Pitsillides, R. K. Pastila, R. R. Anderson, C. P. Lin : Laser-beam triggered microcavitation : a novel method for selective cell destruction. *Radiat. Res.* **156**, 399-407 (2001)
- H. Liang, W. H. Wright, S. Cheng, W. He, M. W. Berns: Micromanipulation of chromosomes in PTK2 cells using laser microsurgery (optical scalpel) in combination with laser-induced optical force (optical tweezers). *Exp. Cell Res.* **204**, 110-120 (1993)
- C. P. Lin, M. W. Kelly, S. A. B. Sibayan, M. A. Latina, R. R. Anderson: Selective cell killing by microparticle absorption of pulsed laser radiation. *IEEE J. Sel. Top. Quantum Electron.* **5**, 963-968 (1999)
- N. Linz, S. Freidank, A. Vogel: Roles of tunneling, multiphoton ionization, and cascade ionization for femtosecond optical breakdown in aqueous media. Second Interim Report of AFOSR International Research Initiative Project SPC 053010 / EOARD, Grant FA 8655-05-1-3010 (January 2006)
- W. Liu, O. Kosareva, I. S. Golubtsov, A. Iwasaki, A. Becker, V. P. Kandidov, S. L. Chin: Femtosecond laser pulse filamentation versus optical breakdown in H₂O. *Appl. Phys. B* **76**, 215-229 (2003)
- M. Lokhandwalla, B. Sturtevant: Mechanical haemolysis in shock wave lithotripsy (SWL): I. Analysis of cell deformation due to SWL flow-fields. *Phys. Med. Biol.* **46**, 413-437 (2001)
- K. Lorenz: Mechanismen des Katapultierens biologischer Strukturen mit UV-Laserpulsen. Diploma thesis, University of Applied Science Lübeck (in German), 2004. Accessible through vogel@bmo.uni-luebeck.de.
- E. Mantoudis, B. T. Podsiadly, A. Gorgry, G. Venkat, I. L. Craft: A comparison between quarter, partial, and total laser-assisted hatching in selected infertility patients. *Hum. Reprod.* **16**, 2182-2186 (2001)
- S. S. Mao, F. Quéré, S. Guizard, X. Mao, R. E. Russo, G. Petite, P. Martin: Dynamics of femtosecond laser interactions with dielectrics. *Appl. Phys. A* **79**, 1695-1709 (2004)
- A.F. Markham: The polymerase chain reaction: A tool for molecular medicine. *Brit. Med. J.* **306**, 441-447 (1993)
- B. R. Masters, P. T. C. So, C. Buehler, N. Barry, J. D. Sutin, W. W. Mantulin, E. Gratton: Mitigating thermal mechanical damage potential during two-photon dermal imaging. *J. Biomed. Opt.* **9**, 1265-1270 (2004)
- W. Meier-Ruge, W. Bielser, E. Remy, F. Hillenkamp, R. Nitsche, R. Unsöld: The laser in the Lowry technique for microdissection of freeze-dried tissue slices. *Histochem J.* **8**, 387-401 (1976)
- R. A. Meldrum, S. W. Botchway, C. W. Wharton, G. J. Hirst: Nanoscale spatial induction of ultraviolet photoproducts in cellular DNA by three-photon near-infrared absorption. *EMBO Rep.* **12**, 1144-1149 (2003)
- G. Mie: Beiträge zur Optik trüber Medien, speziell kolloidaler Metallösungen. *Ann. Phys. Leipzig* **25**, 377-445 (1908)
- K. Minoshima, A. M. Kowalevich, I. Hartl, E. Ippen, J. G. Fujimoto. Photonic device fabrication in glass by use of nonlinear materials processing with a femtosecond laser oscillator. *Opt. Lett.* **26**, 1516-1518 (2001)
- T. Mitchinson, M. Kirschner: Dynamic instability of microtubule growth. *Nature* **312**, 237-242 (1984)
- S. K. Mohanty, M. Sharma, P. Gupta: Laser-assisted microinjection into targeted animal cells. *Biotechnol. Lett.* **25**, 895-899 (2003)
- L. Moreaux, O. Sandre, J. Mertz: Membrane imaging by second-harmonic generation microscopy. *J. Opt. Soc. Am. B* **17**, 1685-1694 (2000)
- G. Moreno, M. Lutz, M. Bessis: Partial cell irradiation by ultraviolet and visible light: conventional and laser sources. *Int. Rev. Exp. Pathol.* **7**, 99-136 (1969)
- K. Nahen, A. Vogel: Plasma formation in water by picosecond and nanosecond Nd:YAG laser pulses - Part II: Transmission, scattering, and reflection. *IEEE J. Selected Topics Quantum Electron.* **2**, 861-871 (1996)
- D. Needham, R. S. Nunn: Elastic deformation and failure of liquid bilayer membranes containing cholesterol. *Biophys. J.* **58**, 997-1009 (1990)
- J. Neev, Y. Tadir, P. Ho, M. W. Berns, R. H. Asch, T. Ord: Microscope-delivered ultraviolet laser zona dissection: principles and practices. *J. Assist. Reprod. Genet.* **9**, 513-523 (1992)
- J. Neumann, R. Brinkmann: Boiling nucleation on melanosomes and microbeads transiently heated by nanosecond and microsecond laser pulses. *J. Biomed. Opt.* **10**, 024001 (2005)a
- J. Neumann, R. Brinkmann: Nucleation and dynamics of bubbles forming around laser heated microabsorbers. *Proc. SPIE* **5863**, 586307 (2005)b
- M. H. Niemz, T. P. Hoppeler, T. Juhasz, F. J. Bille: Intrastromal ablation for refractive corneal surgery using picosecond infrared laser pulses. *Lasers Light Ophthalmol.* **5**, 149-155 (1993)

- D. N. Nikogosyan, A. A. Oraevsky, V. Rupasov: Two-photon ionization and dissociation of liquid water by powerful laser UV radiation. *Chem. Phys.* **77**, 131-143 (1983)
- J. Noack, D. X. Hammer, G. D. Noojin, B. A. Rockwell, A. Vogel: Influence of pulse duration on mechanical effects after laser-induced breakdown in water. *J. Appl. Phys.* **83**, 7488-7495 (1998)a.
- J. Noack, A. Vogel: Single shot spatially resolved characterization of laser-induced shock waves in water. *Appl. Opt.* **37**, 4092-4099 (1998)b.
- J. Noack: *Optischer Durchbruch in Wasser mit Laserpulsen zwischen 100 ns und 100 fs* (PhD Disertation, University of Lübeck, Lübeck 1998)c.
- J. Noack, A. Vogel: Laser-induced plasma formation in water at nanosecond to femtosecond time scales: Calculation of thresholds, absorption coefficients, and energy density. *IEEE J. Quantum Electron.* **35**, 1156-1167 (1999)
- S. Nolte, C. Momma, H. Jacobs, A. Tünnermann, B.N.Chikov, B. Wellegehausen, H. Welling: Ablation of metals by ultrashort laser pulses. *J. Opt. Soc. Am. B* **14**, 2716-2722 (1997)
- H. Oehring, I. Riemann, P. Fischer, K.J. Halbhuber, K. König: Ultrastructure and reproduction behavior of single CHO-K1 cells exposed to near-infrared femtosecond laser pulses. *Scanning* **22**, 263-270 (2000)
- A. A. Oraevsky, L. B. Da Silva, A. M. Rubenchik, M. D. Feit, M. E. Glinsky, M. D. Perry, B. M. Mammini, W. Small IV, B. Stuart: Plasma mediated ablation of biological tissues with nanosecond-to-femtosecond laser pulses: relative role of linear and nonlinear absorption. *IEEE J. Sel. Top. Quantum Electron.* **2**, 801-809 (1996)
- G. Paltauf, H. Schmidt-Kloiber: Model study to investigate the contribution of spallation to pulsed laser ablation of tissue. *Lasers Surg. Med.* **16**, 277-287 (1995)
- G. Paltauf, H. Schmidt-Kloiber: Microcavity dynamics during laser-induced spallation of liquids and gels. *Appl. Phys. A* **62**, 303-311 (1996)
- G. Paltauf, H. Schmidt-Kloiber: Measurement of laser-induced acoustic waves with a calibrated optical transducer. *J. Appl. Phys.* **82**, 1525-1531 (1997)
- G. Paltauf, H. Schmidt-Kloiber: Photoacoustic cavitation in spherical and cylindrical absorbers. *Appl. Phys. A* **68**, 525-531 (1999)
- G. Paltauf, P. Dyer: Photomechanical processes and effects in ablation. *Chem Rev.* **103**, 487-518 (2003)
- G. Palumbo, M. Caruso, E. Crescenzi, M. F. Tecce, G. Roberti, A. Colasanti: Targeted gene transfer in eucariotic cells by dye-assisted laser optoporation. *J. Photochem Photobiol. B* **36**, 41-46 (1996)
- L. Paterson, B. Agate, M. Comrie, R. Ferguson, T. K. Lake, J. E. Morris, A. E. Carruthers, C. T. A. Brown, W. Sibbett, P. E. Bryant, F. Gunn-Moore, A. C. Riches, K. Dholakia: Photoporation and cell transfection using a violet diode laser. *Opt. Express* **13**, 595-600 (2005)
- J. Pearce, S. Thomsen: Rate process analysis of thermal damage. In: A. J. Welch, M. Van Germert (eds) *Optical-Thermal Response of Laser-Irradiated Tissue*, 561-606 (Plenum Press, New York 1995)
- C. M. Pitsillides, E. K. Joe, X. Wei, R. R. Anderson, C. P. Lin: Selective cell targeting with light absorbing microparticles and nanoparticles. *Biophys. J.* **84**, 4023-4032 (2003)
- B. Pommellec, L. Sudrie, M. Franco, B. Prade, A. Mysyrowicz: Femtosecond laser irradiation stress induced in pure silica. *Opt. Express* **9**, 1070-1079 (2003)
- I. Ratkay-Traub, I. E. Ferincz, T. Juhasz, R. M. Kurtz, R. R. Krueger: First clinical results with the femtosecond neodymium-glass laser in refractive surgery. *J. Refract. Surg.* **19**, 94-103 (2003)
- K. R. Rau, A. Guerra, A. Vogel, V. Venugopalan: Investigation of laser-induced cell lysis using time-resolved imaging. *Appl. Phys. Lett.* **84**, 2940-2942 (2004)
- Lord Rayleigh: On the pressure developed in a liquid during the collapse of a spherical cavity. *Philos. Mag.* **34**, 94-98 (1917)
- D. M. Rayner, A. Naumov, P. B. Corkum: Ultrashort pulse non-linear optical absorption in transparent media. *Opt. Expr.* **13**, 3208-3217 (2005)
- J. F. Ready: *Effects of High Power Laser Radiation*, pp. 261-262 (Academic Press, Orlando 1971)
- B. Rethfeld: Unified model for the free-electron avalanche in laser-irradiated dielectrics. *Phys. Rev. Lett.* **92**, 187401 (2004)
- M. H. Rice, J. M. Walsh: Equation of state of water to 250 kilobars. *J. Chem. Phys.* **26**, 824-830 (1957)

- B. K. Ridley: *Quantum Processes in Semiconductors* (Oxford University Press, Oxford, 1999)
- I. Riemann, T. Anhut, F. Stracke, R. Le Harzic, K. König: Multiphoton nanosurgery in cells and tissues. *Proc. SPIE* **5695**, 216-224 (2005).
- B. R. Ringeisen, H. Kim, J. A. Barron, D. B. Krizman, D. B. Chrisey, S. Jackman, R. Y. C. Auyeung, B. J. Spargo: Laser printing of pluripotent embryonal carcinoma cells. *Tiss. Eng.* **10**, 483-491 (2004)
- K. Rink, G. Delacretaz, R. Salathé, A. Senn, D. Nocera, M. Germond, P. De Grandi, S. Fakan: Non-contact microdrilling of mouse zona pellucida with an objective-delivered 1.48 μm diode laser. *Lasers Surg. Med.* **18**, 52-62 (1996)
- T. Ripken, U. Oberheide, C. Ziltz, W. Ertmer, G. Gerten, H. Lubatschowski: Fs-laser induced elasticity changes to improve presbyopic lens accommodation. *Proc. SPIE* **5688**, 278-287 (2005)
- B. A. Rockwell, D. X. Hammer, R. A. Hopkins, D. J. Payne, C. A. Toth, W. P. Roach, J. J. Druessel, P. K. Kennedy, R. E. Annotte, B. Eilert, S. Phillips, G. D. Noojin, D. J. Stolarski, C. Cain: Ultrashort laser pulse bioeffects and safety. *J. Laser Appl.* **11**, 42-44 (1999)
- J. Roegerer, R. Brinkmann, C. P. Lin: Pump-probe detection of laser-induced microbubble formation in retinal pigment epithelium cells. *J. Biomed. Opt.* **9**, 367-371 (2004)
- C. A. Sacchi: Laser-induced electric breakdown in water. *J. Opt. Soc. Am. B* **8**, 337-345 (1991)
- L. Sacconi, I. M. Tolic-Norrelyke, R. Antolini, F. S. Pavone: Combined intracellular three-dimensional imaging and selective nanosurgery by a nonlinear microscope. *J. Biomed. Opt.* **10**, 014002 (2005)
- D. K. Sader, M. L. Mayo, R. D. Glickman: Optical characterization of melanin. *J. Biomed. Opt.* **6**, 404-411 (2001)
- R. K. Saiki, D. H. Gelfand, S. Stoffel, S. J. Scharf, R. Higuchi, G. T. Horn, K. B. Mullis, H. A. Erlich: Primer-Directed Enzymatic Amplification of DNA with a Thermostable DNA Polymerase. *Science* **239**, 487-491 (1988)
- S. Sato, E. Higurashi, Y. Taguchi, H. Inaba: Achievement of laser fusion of biological cells using UV pulsed dye laser beams. *Appl. Phys. B* **54**, 531-533 (1992)
- A. Saul, W. Wagner: A fundamental equation for water covering the range from the melting line to 1273 K at pressures up to 25 000 MPa. *J. Phys. Chem. Ref. Data* **18**, 1537-1564 (1989)
- C. B. Schaffer, N. Nishimura, E. Mazur: Thresholds for femtosecond laser-induced breakdown in bulk transparent solids and water. *SPIE Proc.* **3451**, 2-8 (1998)
- C. B. Schaffer, A. Brodeur, J. F. García, E. Mazur: Micromachining bulk glass by use of femtosecond laser pulses with nanojoule energy. *Opt. Lett.* **26**, 93-95 (2001)
- C. B. Schaffer, N. Nishimura, E. N. Glezer, A. M.-T. Kim, E. Mazur: Dynamics of femtosecond laser-induced breakdown in water from femtoseconds to microseconds. *Opt. Express* **10**, 196-203 (2002)
- C. B. Schaffer, J. F. García, E. Mazur: Bulk heating of transparent materials using a high repetition-rate femtosecond laser. *Appl. Phys. A* **71**, 351-354 (2003)
- H. Schneckenburger, A. Hendiger, R. Sailer, W. S. L. Strauss, M. Schmitt: Laser-assisted optoporation of single cells. *J. Biomed. Opt.* **7**, 410-416 (2002)
- A. Schönle, S. Hell: Heating by absorption in the focus of an objective lens. *Opt. Lett.* **23**, 325-327 (1998)
- K. Schütze, A. Clement-Sengewald: Catch and move – cut or fuse. *Nature* **368**, 667-668 (1994)
- K. Schütze, H. Pösl and G. Lahr: Laser micromanipulation systems as universal tools in molecular biology and medicine. *Cell. Mol. Biol.* **44**, 735-746 (1998)
- K. Schütze, G. Lahr: Identification of expressed genes by laser-mediated manipulation of single cells. *Nat Biotechnol.* **16**, 737-742 (1998)
- G.S. Settles: “*Schlieren and Shadowgraph Techniques*,” Springer: Berlin, Heidelberg, New York, 2001 (376 pp). Y. R. Shen: *The Principles of Nonlinear Optics* (Wiley, New York 1984)
- N. Shen, D. Datta, C. B. Schaffer, P. LeDuc, D. E. Ingber, E. Mazur: Ablation of cytoskeletal filaments and mitochondria in live cells using a femtosecond laser nanocissor. *MCB Mech. Chem. Biosystems* **2**, 17-25 (2005)
- Y. Shirahata, N. Ohkohchi, H. Itagak, S. Satomi: New technique for gene tranfection using laser irradiation. *J. Invest. Med.* **49**, 184-190 (2001)
- M. W. Sigrist, F. K. Kneubühl: Laser-generated stress waves in liquids. *J. Acoust. Soc. Am.* **64**, 1652-1663 (1978)
- D. Simanovskii, M. Sarkar, A. Irani, C. O’Connel-Rodwell, C. Contag, A. Schwettman, D. Palanker: Cellular tolerance to pulsed heating. *Proc. SPIE* **5695**, 254-259 (2005)

- C. E. Sims, G. D. Meredith, T. B. Krasieva, M. W. Berns, B. J. Tromberg, N. L. Allbritton: Laser-micropipet combination for single-cell analysis. *Anal. Chem.* **700**, 4570–4577 (1998)
- V. P. Skripov, E. N. Sinitsin, P. A. Pavlov, G. V. Ermakov, G. N. Muratov, N. V. Bulanov, V. G. Baidakov: *Thermophysical properties of liquids in the metastable (superheated) state* (Gordon and Breach, New York 1988)
- N. I. Smith, K. Fujita, T. Kaneko, K. Katoh, O. Nakamura, S. Kawata, T. Takamatsu: Generation of calcium waves in living cells by pulsed laser-induced photodisruption. *Appl. Phys. Lett.* **79**, 1208–1210 (2001)
- P. T. C. So: Prospects of nonlinear microscopy in the next decades: an overview. *Opt. Express* **3**, 312–314 (1998)
- M. J. Soileau, W. F. Williams, N. Mansour, E. W. Van Stryland: Laser-induced damage and the role of self-focusing. *Opt. Eng.* **28**, 1133–1144 (1989)
- J. S. Soughayer, T. Krasieva, S. C. Jacobson, J. M. Ramsey, B. C. Tromberg, N. L. Albritton: Characterization of cellular optoporation with distance. *Anal. Chem.* **72**, 1342–1347 (2000)
- J. Staudenraus, W. Eisenmenger: Fibre-optic hydrophone for ultrasonic and shock wave measurements in water. *Ultrasonics* **31**, 267–273 (1993)
- R. F. Steinert, C. A. Puliafito: *The Nd:YAG Laser in Ophthalmology* (W. B. Saunders, Philadelphia 1986)
- D. Stern, R. W. Schoenlein, C. A. Puliafito, E. T. Dobi, R. Birngruber, J. G. Fujimoto: Corneal ablation by nanosecond, picosecond, and femtosecond lasers at 532 and 625 nm. *Arch. Ophthalmol.* **107**, 587–592 (1989)
- J. Stolarski, J. Hardman, C. G. Bramlette, G. D. Noojin, R. J. Thomas, B. A. Rockwell, W. P. Roach: Integrated light spectroscopy of laser-induced breakdown in aqueous media. *Proc. SPIE* **2391**, 100–109 (1995)
- O. G. Stonington, T. P. Spurck, J. A. Snyder, J. D. Pickett-Heaps: UV microbeam irradiations of the mitotic spindle I. The UV microbeam apparatus. *Protoplasma* **153**, 62–70 (1989)
- R. Storb, R. L. Amy, R. K. Wertz, B. Fauconnier, M. Bessis: An electron microscope study of vitally stained single cells irradiated with a ruby laser microbeam. *J. Cell. Biol.* **31**, 11–29 (1966)
- A. M. Streltsov, N. F. Borelli: Study of femtosecond-laser-written waveguides in glasses. *J. Opt. Soc. Am. B* **19**, 2496–2504 (2002)
- B. C. Stuart, M. D. Feit, S. Hermann, A. M. Rubenchik, B. W. Shore, M. D. Perry: Nanosecond to femtosecond laser-induced breakdown in dielectrics. *Phys. Rev. B* **53**, 1749–1761 (1996)
- Q. Sun, H. Jiang, Y. Liu, Z. Wu, H. Yang, Q. Gong: Measurement of the collision time of dense electronic plasma induced by a femtosecond laser in fused silica. *Opt. Lett.* **30**, 320–322 (2005)
- W. Supatto, D. Dèbarre, B. Moullia, E. Brouzés, J.-L. Martin, E. Farge, E. Beaurepaire: In vivo modulation of morphogenetic movements in *Drosophila* embryos with femtosecond laser pulses. *Proc. Nat. Acad. Sci. USA* **102**, 1047–1052 (2005)
- S. Taccheo, G. Della Valle, R. Osellame, G. Cerullo, N. Chiodo, P. Laporta, O. Svelto, A. Killi, U. Morgner, M. Lederer, D. Kopf: Er:Yb-doped waveguide laser fabricated by femtosecond laser pulses. *Opt. Lett.* **29**, 2626–2628 (2004)
- W. Tao, J. Wilkinson, E. Stanbridge, M. W. Berns: Direct gene transfer into human cultured cells facilitated by laser micropuncture of the cell membrane. *Proc. Natl. Acad. Sci. USA* **84**, 4180–4184 (1987)
- K. K. Thornber: Applications of scaling to problems in high-field electronic transport. *J. Appl. Phys.* **52**, 279–290 (1981)
- P. Teng, N.S. Nishioka, R. R. Anderson, T.F. Deutsch: Optical studies of pulsed-laser fragmentation of biliary calculi. *Appl. Phys. B* **42**, 73–78 (1987)
- A. C. Tien, S. Backus, H. Kapteyn, M. Murnane, G. Mourou: Short-pulse laser damage in transparent materials as a function of pulse duration. *Phys. Rev. Lett.* **82**, 3883–3886 (1999)
- U. K. Tirlapur, K. König, C. Peuckert, R. Krieg, K.-J. Halbhauer: Femtosecond near-infrared laser pulses elicit generation of reactive oxygen species in mammalian cells leading to apoptosis-like death. *Exp. Cell Res.* **263**, 88–97 (2001)
- U. K. Tirlapur, K. König: Targeted transfection by femtosecond laser. *Nature* **418**, 290–291 (2002)
- C. A. Toth, D. G. Narayan, G. D. Noojin, K. P. Winter, B. A. Rockwell, W. P. Roach: Pathology of macular lesions from subnanosecond pulses of visible energy. *Invest. Ophthalmol. Vis. Sci.* **38**, 2204–2213 (1997)
- S. Tschachotin: Die mikroskopische Strahlenstichmethode, eine Zelloperationsmethode. *Biol. Zentralbl.* **32**, 623–630, 1912.

- M. Tsukakoshi, S. Kurata, Y. Nomiya, Y. Ikawa, T. Kasuya: A novel method of DNA tranfection by laser-microbeam cell surgery. *Appl. Phys. B* **35**, 135-140 (1984)
- V. Venugopalan, N.S. Nishioka, B.B. Mikic: The thermodynamic response of soft biological tissues to pulsed ultraviolet laser radiation, *Biophys. J.*, **69**, 1259-1271 (1995)
- V. Venugopalan, A. Guerra, K. Nahen, A. Vogel: The role of laser-induced plasma formation in pulsed cellular microsurgery and micromanipulation. *Phys. Rev. Lett.* **88**, 078103 (2002)
- A. Vogel, W. Hentschel, J. Holzfuss, W. Lauterborn: Cavitation bubble dynamics and acoustic transient generation in ocular surgery with pulsed neodymium:YAG lasers. *Ophthalmology* **93**, 1259-1269 (1986)
- A. Vogel, M.R.C. Capon, M. N. Asiy-Vogel, R. Brngruber: Intraocular photodisruption with picosecond and nanosecond laser pulses: tissue effects in cornea, lens, and retina. *Invest. Ophthalmol. Vis. Sci.* **35**, 3032-3044 (1994).
- A. Vogel, K. Nahen, D. Theisen: Plasma formation in water by picosecond and nanosecond Nd:YAG laser pulses - Part I: Optical breakdown at threshold and superthreshold irradiance. *IEEE J. Selected Topics Quantum Electron.* **2**, 847-860 (1996)a
- A. Vogel, S. Busch, U. Parlitz: Shock wave emission and cavitation bubble generation by picosecond and nanosecond optical breakdown in water. *J. Acoust. Soc. Am.* **100**, 148-165 (1996)b
- A. Vogel: Nonlinear absorption: intraocular microsurgery and laser lithotripsy. *Phys. Med. Biol.* **42**, 895-912 (1997)
- A. Vogel, J. Noack, K. Nahen, D. Theisen, S. Busch, U. Parlitz, D. X. Hammer, G. D. Nojin, B. A. Rockwell, R. Birngruber: Energy balance of optical breakdown in water at nanosecond to femtosecond time scales. *Appl. Phys. B* **68**, 271-280 (1999)a
- A. Vogel, K. Nahen, D. Theisen, R. Birngruber, R. J. Thomas, B. A. Rockwell: Influence of optical aberrations on laser-induced plasma formation in water and their consequences for intraocular photodisruption. *Appl. Opt.* **38**, 3636-3642 (1999)b
- A. Vogel, J. Noack: Numerical simulation of optical breakdown for cellular surgery at nanosecond to femtosecond time scales. *Proc. SPIE* **4260**, 83-93 (2001)a
- A. Vogel: *Optical Breakdown in Water and Ocular Media, and its Use for Intraocular Photodisruption* (Shaker Verlag, Aachen 2001)
- A. Vogel, J. Noack, G. Hüttmann, G. Paltauf: Femtosecond-laser-produced low-density plasmas in transparent biological media: A tool for the creation of chemical, thermal and thermomechanical effects below the optical breakdown threshold. *Proc. SPIE* **4633**, 23-37 (2002)
- A. Vogel, V. Venugopalan: Mechanisms of pulsed laser ablation of biological tissues. *Chem Rev.* **103**, 577-644 (2003)
- A. Vogel, J. Noack, G. Hüttmann, G. Paltauf: Mechanisms of femtosecond laser nanosurgery of cells and tissues. *Appl Phys B* **81**, 1015-1047 (2005)
- A. Vogel, I. Apitz, S. Freidank, R. Dijkink: Sensitive high-resolution white-light Schlieren technique with a large dynamic range for the investigation on ablation dynamics. *Opt. Lett.* **31**:1812-1814 (2006)
- D. von der Linde, H. Schüler: Breakdown threshold and plasma formation in femtosecond laser-solid interaction. *J. Opt. Soc. Am. B* **13**, 216-222 (1996)
- W. Watanabe, T. Toma, K. Yamada, J. Nishii, K. Hayashi, K. Itoh: Optical seizing and merging of voids in silica glass with infrared femtosecond laser pulses. *Opt. Lett.* **25**, 1669-1671 (2000)
- W. Watanabe, T. Asano, K. Yamada, K. Itoh, J. Nishii: Wavelength division with three-dimensional coupler fabricated by filamentation of femtosecond laser pulses. *Opt. Lett.* **28**, 2491-2493 (2003)
- W. Watanabe, N. Arakawa, S. Matsunaga, T. Higashi, K. Fukui, K. Isobe, K. Itoh: Femtosecond laser disruption of subcellular organelles in a living cell. *Opt. Express* **12**, 4203-4213 (2004)
- W. Watanabe, S. Matsunaga, T. Shimada, T. Higashi, K. Fukui, K. Itoh: Femtosecond laser disruption of mitochondria in living cells. *Med Laser Appl.* **20**, 185-193 (2005)
- F. Williams, S. P., Varama, S. Hillenius: Liquid water as a lone-pair amorphous semiconductor. *J. Chem. Phys.* **64**, 1549-1554 (1976)
- B. Wolfrum, R. Mettin, T. Kurz, W. Lauterborn: Observations of pressure-wave-excited contrast agent bubbles in the vicinity of cells. *Appl. Phys. Lett.* **81**, 5060-5062 (2002)

- M. F. Yanik, H. Cinar, H. N. Cinar, A. D. Chisholm, Y. Jin, A. Ben-Yakar: Functional regeneration after laser axotomy. *Nature* **432**, 822 (2004)
- C. P. Yao, R. Rahmanzadeh, E. Endl, Z. Zhang, J. Gerdes, G. Hüttmann: Elevation of plasma membrane permeability by laser irradiation of selectively bound nanoparticles. *J. Biomed. Optics* **10**, 064012 (2005)
- E. Zeira, A. Manevitch, A. Khatchaturians, O. Pappo, E. Hyam, M. Darash-Yahana, E. Tavor, A. Honigman, A. Lewis, E. Galun: Femtosecond infrared laser – an efficient and safe in vivo gene delivery system for prolonged expression. *Mol. Ther.* **8**, 342-350 (2003)
- Q. Zheng; D. J. Durben, G. H. Wolf, C. A. Angell: Liquids at large negative pressures: Water at the homogeneous nucleation limit. *Science*, **254**, 829-832 (1991)
- M. J. Zhody, C. Tse, J. Y. Ye, M. O'Donnell: Optical and acoustic detection of laser-generated microbubbles in single cells. *IEEE Trans. Ultrason. Ferr.* **52** (2006) (at press)
- B. Zysset, J. G. Fujimoto, T.F. Deutsch: Time-resolved measurements of picosecond optical breakdown. *Appl. Phys. B* **48**, 139-147 (1989)

11 ACKNOWLEDGEMENTS

Partners in this project were Joachim Noack (formerly Medical Laser Center Lübeck) for the modelling of plasma formation, Gereon Hüttmann (Institute of Biomedical Optics, University of Lübeck) for the thermal modelling, Günther Paltauf (Institute of Physics, Karl-Franzens University Graz, Austria) for the modelling of thermoelastic stress effects and bubble formation, Ingo Apitz (Institute of Biomedical Optics, University of Lübeck) for Schlieren photography of low-density plasmas, and Norbert Linz and Sebastian Freidank (Institute of Biomedical Optics, University of Lübeck) for the experimental work on femtosecond-laser-induced cavitation.. We appreciate stimulating discussions on the modeling of plasma formation with Paul Kennedy (US Air Force Optical Research Laboratory, Brooks City Base, San Antonio, U.S.A.), Nadezhda Bulgakova (Institute of Thermophysics, SB RAS, Novosibirsk, Russia), Rieko Verhagen (Philips Research, Eindhoven, The Netherlands), and Cord Arnold (Laserzentrum Hannover, Germany). We thank S. B. Kiselev (Colorado School of Mines, Golden, U.S.A.) for providing tabulated data of the kinetic spinodal [Kis99] used for calculating the bubble formation thresholds in section 3.